CAPITAL UNIVERSITY OF SCIENCE AND TECHNOLOGY, ISLAMABAD

Analysis of Acoustic Problems with Different Boundary Conditions and Step Discontinuities

by

Sajid Shafique

A thesis submitted in partial fulfillment for the
degree of Doctor of Philosophy

in the
Faculty of Computing
Department of Mathematics

2021

Analysis of Acoustic Problems with Different Boundary Conditions and Step Discontinuities

By

Sajid Shafique

(DMT 143022)

Dr. Annie Gorgey, **Associate Professor**
Sultan Idris Education University, **Malaysia**
(Foreign Evaluator 1)

Dr. Hongyu Liu, **Professor**
City University of Hong Kong, Kowloon, **Hong Kong**
(Foreign Evaluator 2)

Dr. Muhammad Afzal
(Thesis Supervisor)

Dr. Muhammad Sagheer
(Head, Department of Mathematics)

Dr. Muhammad Abdul Qadir
(Dean, Faculty of Computing)

DEPARTMENT OF MATHEMATICS
CAPITAL UNIVERSITY OF SCIENCE AND TECHNOLOGY
ISLAMABAD
2021

DEDICATION

To

My Great Father (Late)

&

My Great Mother

CAPITAL UNIVERSITY OF SCIENCE & TECHNOLOGY
ISLAMABAD
Expressway, Kahuta Road, Zone-V, Islamabad
Phone:+92-51-111-555-666 Fax: +92-51-4486705
Email: info@cust.edu.pk Website: https://www.cust.edu.pk

CERTIFICATE OF APPROVAL

This is to certify that the research work presented in the thesis, entitled "**Analysis of Acoustic Problems with Different Boundary Conditions and Step Discontinuities**" was conducted under the supervision of **Dr. Muhammad Afzal**. No part of this thesis has been submitted anywhere else for any other degree. This thesis is submitted to the **Department of Mathematics, Capital University of Science and Technology** in partial fulfillment of the requirements for the degree of Doctor in Philosophy in the field of **Mathematics**. The open defence of the thesis was conducted on **May 25, 2021**.

Student Name : Sajid Shafique (DMT143022) Sajid Shafique

The Examining Committee unanimously agrees to award PhD degree in the mentioned field.

Examination Committee :

(a) External Examiner 1: Dr. Muhammad Ayub
Professor
HITEC University, Taxila

(b) External Examiner 2: Dr. Aftab Khan,
Professor
COMSATS University, Islamabad

(c) Internal Examiner : Dr. Rashid Ali
Associate Professor
CUST, Islamabad

Supervisor Name : Dr. Muhammad Afzal
Assistant Professor
CUST, Islamabad

Name of HoD : Dr. Muhammad Sagheer
Professor
CUST, Islamabad

Name of Dean : Dr. Muhammad Abdul Qadir
Professor
CUST, Islamabad

AUTHOR'S DECLARATION

I, **Sajid Shafique (Registration No. DMT-143022)**, hereby state that my PhD thesis entitled, '**Analysis of Acoustic Problems with Different Boundary Conditions and Step Discontinuities**' is my own work and has not been submitted previously by me for taking any degree from Capital University of Science and Technology, Islamabad or anywhere else in the country/ world.

At any time, if my statement is found to be incorrect even after my graduation, the University has the right to withdraw my PhD Degree.

Sajid Shafique

(Sajid Shafique)

Registration No : DMT-143022

Dated: May, 2021

PLAGIARISM UNDERTAKING

I solemnly declare that research work presented in the thesis titled "**Analysis of Acoustic Problems with Different Boundary Conditions and Step Discontinuities**" is solely my research work with no significant contribution from any other person. Small contribution/ help wherever taken has been duly acknowledged and that complete thesis has been written by me.

I understand the zero tolerance policy of the HEC and Capital University of Science and Technology towards plagiarism. Therefore, I as an author of the above titled thesis declare that no portion of my thesis has been plagiarized and any material used as reference is properly referred/ cited.

I undertake that if I am found guilty of any formal plagiarism in the above titled thesis even after award of PhD Degree, the University reserves the right to withdraw/ revoke my PhD degree and that HEC and the University have the right to publish my name on the HEC/ University Website on which names of students are placed who submitted plagiarized thesis.

Sajid Shafique

(**Sajid Shafique**)

Dated: May, 2021

Registration No : DMT-143022

List of Publications

It is certified that following publication(s) have been made out of the research work that has been carried out for this thesis:-

1. **S. Shafique**, M. Afzal, and R. Nawaz, "On mode-matching analysis of fluid-structure coupled wave scattering between two flexible waveguides", *Canadian Journal of Physics*, vol. 95, no. 6, pp. 581-589, 2017.
2. **S. Shafique**, M. Afzal, and R. Nawaz, "On the attenuation of fluid-structure coupled modes in non-planar waveguide", *Mathematics and Mechanics of Solids*, vol. 25, no. 10, pp. 1831-1850, 2020.
3. M. Afzal and **S. Shafique**, "Attenuation analysis of flexural modes with absorbent lined flanges and different edge conditions", *Journal of the Acoustical Society of America*, vol. 148, no. 1, pp. 85-99, 2020.
4. M. Afzal, **S. Shafique**, and A. Wahab, "Analysis of traveling waveform of flexible waveguides containing absorbent material along flanged junctions", *Communications in Nonlinear Science and Numerical Simulation*, vol. 97, pp. 105737, 2021.

(Sajid Shafique)
Registration No: DMT 143022

Acknowledgement

“Glory be to you, we have no knowledge except what you have taught us. Verily, it is You, the All-Knower, the All-Wise O’All-Knowing, grant me knowledge” (AL-QURAN).

First and foremost, I would like to thank Allah almighty for giving me the puissance, knowledge, competence and opportunity to undertake this research study and to get it out and complete it satisfactorily. Without his benison, this achievement would not have been attainable. I had not enough wisdom and strength to conquer this milepost. It is one of his infinite benedictions that He bestowed upon me with the potential and ability to complete the present research.

I wish to show my gratitude to all the people whose abetment was a milestone in the completion of this project, specially my righteous supervisor Dr. Muhammad Afzal, for his priceless suggestions, constant support, great patience and encouragement. I wish to express my sincere thank to the head of department Dr. Muhammad Sagheer, for valuable guidance and encouragement extended to me. I would like to thanks Capital University of Science and Technology, Islamabad, Pakistan, for providing suitable environment for research purpose. I express my thankful feelings to especially Dr. Rab Nawaz and Dr. Abdul Wahab for their constructive suggestions during my research time. I would also appreciate the positive concern of my all research fellows, who supported me at the time of stress when I was about to lose my heart.

Last but not the least, I cannot forget my whole family especially my beloved mother, mother in-law, brother in-law, my sister, sisters in-law for their prayers, continuous support, love and my brother Mr. Majid Shafique’s assistance technically in completion of thesis. Their prayers have lightened up my spirit to finish this thesis. Special thanks to my wife who encouraged me throughout to complete my degree. I would like to express gratitude to my beloved younger daughters Labiqa and Azbha for being such a good girls who always cheering me up.

(Sajid Shafique)

Abstract

The present thesis discusses a class of physical problems that contains the propagation and attenuation of fluid-structure coupled waves through discontinuous flexible waveguides which support structure-borne as well as fluid-borne vibrations. The modelled configurations of flexible waveguides comprise thin elastic elements such as elastic membranes and/or plates joined to the structural discontinuities with or without flanges. The associated boundary value problems are governed by Helmholtz's equation and have Dirichlet, Neumann, Robin and/or higher order boundary conditions. The Mode-Matching (MM) scheme is used to solve the governing boundary value problems. This technique relies on the eigenfunction ansatz, which are based on the eigenvalue problem corresponding to the given boundary value problems. The eigenvalue problems having rigid, soft or impedance types of boundary conditions reveal orthogonal eigenfunctions, and the resulted eigen-sub-systems undergo Sturm-Liouville (SL) category. However, if the eigenvalue problems involve higher order boundary conditions the eigenfunctions are non-orthogonal in nature and, the resulted eigen-sub-systems underlie non-Sturm-Liouville category. In such systems, the development and use of generalized orthogonal characteristics is indispensable to ensure the point-wise convergence of the solution. The orthogonal characteristics are incorporated in the process of conversion of differential systems to the linear algebraic systems. The application of generalized orthogonality relation (OR) governs additional constants that are found through application of appropriate edge conditions. The systems are truncated and inverted to explain physical characteristics of the modeled structures. The numerical computations are performed by using the truncated solutions to see how the choice of appropriate edge conditions, structural variations and bounding wall conditions affect acoustic attenuation for structure-borne as well as fluid-borne vibrations. Furthermore, the Low-Frequency Approximation (LFA) solution which is valid only in low frequency regime is developed. The performance of LFA is compared with the benchmark MM method and is found in a good agreement with relative merits.

Contents

List of Figures

List of Tables

Abbreviations

MM	Mode-Matching
LFA	Low-Frequency Approximation
WH	Wiener-Hopf
SL	Sturm-Liouville
STP	Standard Temperature Pressure
OR	Orthogonality Relation
TL	Transmission-Loss
HVAC	Heating Ventilation and Air-Conditioning

Symbols

p	Acoustic pressure
ω	Angular frequency
ρ_0	Density in equilibrium state
ρ_p	Density of the plate
f	Frequency
L	Half length of expansion chamber or cavity
F_ℓ	Incident forcing due to structure or fluid
ϕ_{inc}	Incident scalar field potential
δ_{mn}	Kronecker delta
ρ_m	Mass density
$\bar{W}\left(\bar{x}, \bar{y}, \bar{t}\right)$	Membrane displacement
μ	Membrane wavenumber in *vacuo*
α	Membrane fluid loading parameter
$\bar{W}_1\left(\bar{x}, \bar{y}, \bar{t}\right)$	Plate displacement
μ_1	Plate wavenumber in *vacuo*
α_1	Plate fluid loading parameter
B	Plate bending stiffness
υ	Poisson's ratio
P_i	Power incident
P_r	Power reflected
P_t	Power transmitted
P_{abs}	Power absorb
$P\rfloor_{\text{fluid}}$	Power through fluid

$P\rfloor_{\text{memb}}$	Power through membrane
$P\rfloor_{\text{plate}}$	Power through plate
ϕ_{ref}	Reflected scalar field potential
ϕ	Scalar field potential
Z	Specific impedance in dimension form
ς	Specific impedance in dimensionless form
c	Speed of sound
c_m	Speed of sound on membrane
T	Tension
t	Time
ϕ_{tran}	Transmitted scalar field potential
N	Truncation number
$\mathbf{v}$	Velocity vector
k	Wave number
E	Young's modulus

Chapter 1

Introduction

Today acoustic, “the science of sound” has become an interdisciplinary field. It embodies many disciplines such as physics, mathematics, mechanical engineering, speech and hearing sciences. Acoustic has provided many challenging and interesting problems to engineers and researchers [1–7]. The continued interest in the field is often motivated by the necessity to design objects or channels useful in the reduction of structural vibrations and the associated noises. Such noises are usually generated by the variety of mechanisms occurring in systems of automobiles, turbofan engines, aero-engines, heating ventilation and air-conditioning (HVAC) systems and other engineering designs [8–12]. The duct-like structure is a common component in all these systems. Their key objective is to distribute air flow from the buildings or exhausts to environment. But, many times the waveguide acts as a conduit for a plethora of annoying sounds to living and working environment.

To mitigate the noise level, the study of noise reduction problems has received considerable attention of scientific community. In many engineering applications, noise is mitigated by controlling the vibrations of boundaries and unsteady flow phenomena. The techniques are classified into active noise control and passive noise control. In the active noise control, mitigation is achieved by noise cancellation (see, for instance, [13–16]). In passive noise control, sound-reducing measures are incorporated into the original system designs or retrofitting is used. Passive treatments are commonly used, for example, for mitigation of rocket launch noise (refer, for instance, to [17, 18]).

Usually the length of the duct is long enough in the HVAC systems to attenuate the sound sufficiently and the produced radiation field is negligible at the duct termination. In contrast, the modern jet engines, for example, have relatively short lengths and therefore, the radiated field at the duct termination is not negligible. Accordingly, sound-absorbing materials are extensively used in noise attenuation and a variety of them is available for applications as duct liners. They can be grouped into three broad categories: porous materials with or without facings, sintered fiber metals with air cavity backing, and Helmholtz resonators which include perforated panels with air cavity backing. Generally, fiber metals and perforated panels are used more often [19–21].

The sound-absorbing material lined in a duct that allows little or no sound propagation parallel to the wall is called locally reacting and can be described by a wall impedance (see, for instance, [22–24]). These physical problems are usually governed by Helmholtz or Laplace's type equation and have rigid, soft or impedance type of boundaries. The mathematical form of impedance boundary condition as given in [25] is

$$\rho\phi_t + Z\mathbf{n}\cdot\nabla\phi = 0, \tag{1.1}$$

where $\mathbf{n}$ is unit normal vector directed into the surface, ϕ represents the field potential, ϕ_t denotes the derivative of field potential with respect to time and, ρ is the density of fluid. Here Z denotes the specific impedance of the bounding surface, When $Z \to \infty$ the surface is acoustically rigid but if $Z \to 0$ the surface is soft. The acoustics scattering through different physical configuration containing boundaries of the type (1.1) have been addressed by many authors, for instance, see [26–31]. Note that the boundaries defined in (1.1) do not support vibration along the surfaces.

However, if the bounding surfaces are dynamical in nature that support vibration such as elastic membranes or plates, the boundary conditions involve second or higher order derivatives and are referred as "higher order boundary conditions".

The general form of higher order boundary condition as given in [32] is

$$\mathcal{L}_p\left(\frac{\partial}{\partial x}\right)\frac{\partial \phi}{\partial y}+\mathcal{M}_p\left(\frac{\partial}{\partial x}\right)\phi=0, p\in\{0,a\}, \qquad y\in\mathbb{R}. \tag{1.2}$$

Here $\mathcal{L}_p\left(\frac{\partial}{\partial x}\right)$ and $\mathcal{M}_p\left(\frac{\partial}{\partial x}\right)$ are differential operators of the form

$$\mathcal{L}_p\left(\frac{\partial}{\partial x}\right)=\sum_{h=0}^{H_p}c_h^p\frac{\partial^{2h}}{\partial x^{2h}} \quad \text{and} \quad \mathcal{M}_p\left(\frac{\partial}{\partial x}\right)=\sum_{j=0}^{J_p}d_j^p\frac{\partial^{2j}}{\partial x^{2j}}, \tag{1.3}$$

where c_h^p and d_j^p are constants and H_p and J_p are non-negative integers. The aforementioned form of higher order boundary conditions (1.2) is more general and comprises particular forms as elastic membranes and plates type boundaries, that have been used in literature by several authors in different physical situations for instance see, [33–35].

For the structure involving sudden variations in duct geometry or change of material properties the use of Wiener-Hopf (WH) is inappropriate [36]. Nevertheless, this approach has noteworthy extensions such as, modified WH technique [37], matrix formulation [38] and WH in conjunction with mode matching [39], but for many cases the technique is not easily generalized. Albeit sometime a little variation in physical problem may result various complications in determining the solution of governing boundary value problem.

On the other hand, the Mode-Matching method [40–42] advanced recently to predict the scattering behavior of fluid-structure coupled waves in ducts or channels has proved a viable tool. This technique provides a convenient way to incorporate the variations of material properties and structural discontinuities. The approach is especially useful for the cases wherein there exist a coupling between the propagation of vibrational waves along the boundaries and the acoustic waves of the fluid medium.

For the envisage problems the role of edge conditions is important physically as well as mathematically. Physically “edge conditions” define how an elastic membrane or plate’s ends are connected to the other surface. The possible choice of such connections inelastic membrane case can be fixed free or spring-like, whereas, in elastic plate case these conditions are clamped, pin-jointed and pivoted type. Mathematically, the imposition of edge conditions ensures the uniqueness of obtained solution. It is worthwhile mentioning that the unique solutions of boundary value problems corresponding to waveguides bounded by elastic plates or membranes have not been obtained without imposing conditions at the edges of the plates. Lawrie [43] proved that the number of required edge conditions is half of the order of membrane or plate boundary conditions. In the context of modal series expansions, edge conditions are linked to the convergence rate. A δ-function (to be interpreted as a generalized function) type of spurious edge source generates a divergent series. Although its role remains in the usual engineering practice somewhat in the background, the edge condition is certainly important in the problems involving flexible boundaries. In various designs of ducts different edge conditions are incorporated and have impact on the acoustic scattering [44]. Therefore, the scattering analysis through different edge conditions is essential as well as important.

1.1 State of the Art

The acoustic problems involving waveguide with sudden area changes, such as expansions or contractions are important in noise reduction applications. These waveguide problems are well established in literature and have been extensively investigated for the last few decades. Peat [45] investigated the acoustic waves in a waveguide at a discontinuity and developed the equivalent impedance formulae for the junctions of extended inlet and outlet duct systems. Such formulae have practical importance at low-frequency for reactive silencer systems. Selamet and Ji [46–48] studied circular waveguide and introduced expansion chambers with extended inlet and outlet by an analytical approach. Lee [49, 50] tried to increase the performance of reactive silencers by way of internal partitioning through topological optimization. Wang and Mak [51] investigated the sound wave propagation in a lined duct through periodic resonators array. Seo and Kim [52] adjusted the resonator arrays for wider noise reduction band at low-frequency.

The concept of utilizing elastic membranes as a means of controlling low-frequency noise is by no means new. Dowell and Voss [53] studied the vibrations of a cavity-backed panel in the presence of mean ow. Ford and McCormick [54] presented an analysis of arrangements of thin membranes, such as 0.2 mm aluminum sheets, stacked at a certain distance from each other, that have applications in concert halls, broadcasting studios, etc. They showed that substantial sound absorption occurs only at narrow bands around a few resonance frequencies of the membrane-cavity system. Kang and Fuchs [55] investigated the effectiveness of cavity-backed micro perforated membranes as acoustic absorbers in the context of architectural acoustics. Huang [56] proposed another type of membrane absorber for low-frequency duct noise. He observed that the membrane experienced fluid-structure coupled waves with a phase speed less than the in vacuo wave speed, which in turn propagates with a speed much less than that of the speed of sound in air.

Theoretically, the fluid-structure coupled waves could be slowed down indefinitely by increasing the compliance of the membrane, but in practice there is a limit on the membrane thickness that may be used. Huang et al. [57] investigated the propagation of sound in a flexible duct, both theoretically and experimentally. They performed experiments on a duct with a finite section of tensioned membrane and compared the propagating modes with the relevant modes of the infinite membrane model. An agreement in results occurred for phase speeds ranging from 8.3 m/s to 1348 m/s. A suitably stretched thin membrane backed by a cylinder cavity channel, which achieved a satisfactory performance from low to medium frequencies over an octave band, was again discussed by Huang [58, 59]. Here, he focused on the modal behavior of the fully coupled membrane-cavity system and found three resonant peaks in the low-to-medium frequency range, while the transmission loss between adjacent peaks remained above 10 dB. For the first peak, almost complete sound reflection occurred, as a result of an out-of-phase combination of the first and second in vacuo modes of simply supported membranes.

In the past decades, significant analyses of the performance of acoustical waveguides with rigid, soft and absorbent linings have been performed. A non-exhaustive list includes, for example, works by, Galich et al. [60], Ayub at al. [61, 62], Scott [63], Demir and Buyukaksoy [64], and Nilsson and Brander [65–68]. Likewise, Buyukaksoy [69] studied the propagation of sound in an infinite rigid circular cylindrical duct with an inserted expansion chamber whose walls are treated with an acoustically absorbent and locally-reacting material using the WH technique. The influence of the radius of the expansion chamber, lining impedance, mean flow, and the acoustical impedance of the central perforated tube on the transmission-loss is elucidated.

The problems referred by [27, 61, 62, 64, 69–73] can also be portrayed as the applications of classical WH technique [74]. However, for the structural discontinuity due to sudden variations in waveguide or higher order boundary conditions, the WH technique is not appropriate [75]. Yet, this approach has noteworthy extensions, for instance, Abrahams and Wickham [76] formulated the boundary value problem as an explicit matrix Wiener-Hopf factorization and exhibited the difficulty of a scalar kernel comprising exponentially growing elements. Later, they resolved this difficulty by general Wiener-Hopf factorization with exponential phase factors and illustrated the method with three specific examples [77]. Abrahams [78, 79] introduced a new procedure for Wiener-Hopf problems whereby Pade approximants were employed to acquire an approximate but explicit noncommutative factorization of a matrix kernel. For complex boundary value problems, this procedure leads to coupled equations that form the matrix kernel. This method is applicable to a wide range of initial/boundary value problems.

More recently, Peake and Abrahams [80] considered the waveguide whose inner surfaces were assumed with Robin condition, whilst other surfaces were applied by Neumann conditions. This led a matrix Wiener-Hopf problem with factorization of a 3×3 matrix. Chung and Fox [81] obtained the solution of system of partial differential equations by Wiener-Hopf approach that was the extension of earlier research work of Evans and Davies [82]. For step discontinuity in waveguide structure due to presence of inserted expansion chamber, the work of Demir and

Buyukaksoy [64, 69] with WH approach is significant in literature. However, for several circumstances this technique is not easily generalized or adequate.

As an alternative, the MM method has proved a viable approach to investigate the acoustic waveguide boundary value problems. Hassan [83] considered three spaced waveguide problem by matching eigenfunction expansion method which has already been analyzed by Rawlins [84] with WH technique. He reported in his presented work that matching method is an alternative to WH method. It was because that the split functions/complicated factor was not involved in finding the solution. Moreover, Hassan et al. [85] investigated the scattering analysis in triple and pentafurcated spaced duct by using mode matching method. In problems [83, 85], the geometries were considered continuous in structure with symmetric in y-axis.

The scattering phenomena in acoustic waveguides with flexible boundaries (elastic membrane or plate) have been investigated extensively by many researchers. Warren et al. [36] applied a mode-matching approach to analyze the acoustic scattering phenomena in waveguides involving discontinuities in height with the material property. Nawaz et al. [35] investigated the acoustic wave propagation in a waveguide bounded by flexible membranes whereas Afzal et al. [86] analyzed the acoustic scattering in a duct with higher-order boundaries involving a step discontinuity. The solution of a scattering problem in rectangular waveguide bounded by a membrane with abrupt geometric changes was obtained by Afzal et al. [87] with the help of the MM technique. Recently, Lawrie and Afzal [88] studied the scattering of acoustic waves at the connection between two flexible ducts involving a height discontinuity by a vertical membrane. Also, the problems involving wave-bearing boundaries at a flanged junction have been undertaken in [88–90] and significant effects have been analyzed on the propagating noise.

Cummings and Chang [91] imposed continuity of pressure and velocity over the inlet and outlet planes of the silencer while using the eigenmodes in an analytic mode matching scheme. Peat [92], and later by Kirby [93], proposed more efficient alternative to Cummings and Changs method. They established closed form analytic solutions based on the attenuation of the fundamental mode only. The methods proposed by Peat and Kirby are, however, precise only over a limited frequency range for a given waveguide structure. Such restrictions apply also to other methods based on the fundamental mode, for example methods proposed by Panigrahi and Munjal [94]. Recently Afzal et al. [86, 87] and, Nawaz and Lawrie [34], included the second mode forcing term which aim to carry energy through fluid-borne instead of structure-borne mode. It is thus established that the numerical results contrast well for both, the fundamental mode and secondary mode incidents.

The fluid-structure interaction in a duct bounded by elastic membrane or plate with different types of edge conditions has challenging and mathematical riddles to scientific community. Without specification of the edge conditions, the lack of uniqueness in the boundary value problems is manifest in the occurrence of extra (non-integral) terms in the orthogonality relation. The non-uniqueness is, in general, resolved by applying the edge conditions. Lawrie and Guled [95] investigated the performance of a reactive silencer using a mode-matching method and low-frequency approximation for zero displacement membrane edge conditions. They revealed that the stop band produced by the silencer can be broadened or shifted by altering the position of an internal membrane.

In the case of elastic plates, the edges are usually considered to be clamped, pin-jointed or pivoted. Norris and Wickham [70] developed the general solution for the acoustic scattering and obtained the explicit formulae for the pressure transform by imposing the clamped or welded connection of the plates. Brazier-Smith [71] presented the solution for scattering field of co-planar plates by considering the three types of joints or edge conditions, namely, free-free, hinged and clamped. It was demonstrated that the scattered field was sensitive in nature in case of both, the thickness and the physical connections of the plates. Sahoo et al. [96] applied different edge conditions to examine the scattering of water waves by a semi-infinite floating elastic plate.

Among most of the current research works concerning scattering analysis for the waveguides bounded by elastic membrane or plate with or without flanges/lined flanges and different types of edge conditions, only a few have focused on acoustic ducts with inserted expansion chambers. Towards this end, the acoustic problems concerning scattering and propagation of acoustic waves in waveguides bounded by elastic plates or membranes with inserted expansion chamber containing acoustical materials along flanged junction are investigated in this thesis.

1.2 Avant-Garde

The current study presents the MM analysis of acoustic scattering and attenuation through flexible waveguides including different types of edge conditions, material properties and structural discontinuities. The work is continuation of the already available studies, for instance see [34, 35, 87, 89], in extended form and highlighted the following aspects.

1. The scattering analysis of discontinuous interface containing flanges of rigid front and soft backing in infinite rigid/flexible waveguide.
2. The attenuation of fluid-structure coupled acoustic waves in non-planar waveguide involving cavities and elastic membranes bounded walls.
3. The scattering and attenuation analysis through the elastic plate bounded waveguide comprising absorbent lined flanges and different edge conditions.
4. The analysis of travelling wave forms of flexible expansion chamber connected with extended elastic plate bounded inlet/outlet through the lined flanges.
5. The development of LFA solutions of the envisaged problems in low-frequency regime and its comparison with MM results.
6. The consideration of structure-borne as well as fluid-borne mode incident radiations and the attenuation analysis in all of the aforementioned studies.

In the next section, the outlines of the dissertation is explained.

1.3 Dissertation Outline

The dissertation outlines are as follows. Chapter-2 presents the fundamental concepts useful in understanding the mathematical modeling of physical problems and their solution schemes. Chapter-3 includes two problems involving flanges of different material properties at discontinuous interface in infinite waveguides. The bounding wall conditions in both of the problems are assumed different and MM solution is explained. Moreover, the second problem in this chapter with title "On mode-matching analysis of fluid-structure coupled wave scattering between two flexible waveguides" has been published in "*Canadian Journal of Physics*" in 2017.

In Chapter-4, the attenuation of fluid-structure coupled modes of non-planar waveguide involving cavities is discussed. The physical problem is modeled to illustrate the scattering behavior of acoustic waves in a flexible waveguide composed of thin elastic elements having edges or joints and structural discontinuities. The fluid-structure coupled waveforms scatter after interacting with the discontinuities and edges of the underlying structure. The mode-matching technique, together with low-frequency approximation, is used to determine velocity potentials. The guiding structure is then analyzed and validated through scattering energy functionals by varying the dimensions of the cavities and the wave frequency. The results are formulated and analyzed by tuning the device using an appropriate choice of edge conditions, dimension of cavities, and wave frequencies, thereby validating the obtained solutions. This chapter with title "On the attenuation of fluid-structure coupled modes in non-planar waveguide" has been published in journal "*Mathematics and Mechanics of Solids*" in 2020.

The analysis of fluid-structure coupled waveforms and their attenuation in a flexible waveguide is carried out in Chapter-5. The physical configuration is considered expansion chamber that is connected with extended inlet/outlet by means of vertical lined flanges. The numerical experiments are performed to analyze the effects of absorbent linings and edge conditions on the attenuation of flexural modes. The guiding structure is exited with the structure-born mode incident as well as the fluid-born mode incident. Moreover, the research work of this chapter with title "Attenuation analysis of flexural modes with absorbent lined flanges and different edge conditions" has been also published in "*Journal of the Acoustical Society of America*" in 2020.

Chapter-6 describes the traveling waveform in a flexible waveguide bounded by elastic plates with an inserted expansion chamber having flanges at two junctions and a finite elastic membrane is investigated. An acoustically absorbent lining is placed along the inner sides of the flanges at the junctions while their outer sides are kept rigid. Moreover, the edge conditions are imposed to define the physical behavior of elastic membrane and plates at finite edges. The configuration is exited with the structure as well as fluid-born mode. The influence of the imposed edge conditions at the connections of the plates and the prescribed incident forcing on the transmission-loss along the duct is elaborated. Specifically, the effects of edge conditions on the transmission-loss of structure-borne vibrations and fluid-borne noise are specified. This research work has been published with title "Analysis of traveling waveform of flexible waveguides containing absorbent material along flanged junctions" in journal "*Communications in Nonlinear Science and Numerical Simulation*" in 2021. Finally, a brief summary, concluding remarks and future work are presented in Chapter-7.

Chapter 2

Preliminaries

This chapter depicts the fundamental concepts that are relevant to understand the propagation and scattering of acoustic wave in waveguides containing different material properties. The acoustic problems are governed with linear acoustic wave equation and different types of boundary conditions. The boundary conditions are considered to be: rigid, soft, absorbent lining, elastic membrane and elastic plate. The physical problems are governed by Helmholtz's or Laplace equation and having boundary conditions rigid, soft or impedance type underlie SL category, thereby the appearing eigenfunctions are linearly independent and satisfy the standard orthogonality conditions (for more details, see for instance [97, 98]. The orthogonality conditions help to recast the differential system to linear algebraic system during the matching analysis which is discussed in ongoing chapters of the thesis. On the other hand if the problem is governed by Helmholtz's or Laplace equation and involve higher order boundary conditions such as membrane or plate, the governing eigenfunctions do not satisfy standard orthogonality conditions, and thus the generalized orthogonality conditions are discussed. In more general form the development of such orthogonality conditions is explained in [99]. The relevant eigenfunctions are linearly dependent and satisfy the generalized orthogonality conditions. These conditions are explained in this chapter.

This chapter is organized as: Section 2.1 is dedicated to the mathematical derivation of the acoustic wave equations. Non-dimensional settings are illustrated in

Section 2.2. The different types of boundary conditions are presented in Section 2.3. The travelling wave formulation is presented in Section 2.4. Three types of models such as; Impedance-Impedance model in Section 2.5. Rigid-Membrane model in Section 2.6 and Rigid-Plate model in Section 2.7. The Mode-Matching technique, Low-Frequency Approximation, energy fluxes and transmission loss are explained in Section 2.8, Section 2.9, Section 2.10 and Section 2.11, respectively.

2.1 Linear Acoustic Equation

The linear acoustic wave equation defines the propagation of pressure perturbations in the fluid medium. The mathematical description of the acoustic wave equation in a fluid can be obtained with following assumptions [101].

- The undisturbed fluid is stationary (there is no fluid flow).
- Fluid is compressible.
- The fluid is under adiabatic conditions (i.e., there is no flow of heat in or out of the system).

Conservation of mass: The mass is conserved that can be described through continuity equation

$$\frac{\partial \rho}{\partial t} + \nabla \cdot (\rho \mathbf{v}) = 0, \tag{2.1}$$

where ρ is the mass density and $\mathbf{v}$ be the velocity of moving mass.

Conservation of momentum: The conservation of linear momentum can be given by

$$\rho \left(\frac{\partial \mathbf{v}}{\partial t} + (\mathbf{v} \cdot \nabla)\mathbf{v} \right) = -\nabla p, \tag{2.2}$$

where p denotes the fluid pressure. To derive the acoustic equation, the small fluctuations in the medium can be expressed through the dynamical variables as

$$\begin{aligned} \rho^{'}(t) &= \rho - \rho_0, \qquad (2.3) \\ \mathbf{v}^{'}(t) &= \mathbf{v} \end{aligned}$$

and

$$p^{'}(t) = p - p_0. \tag{2.4}$$

Here *prime* variables denote fluctuations and 0 in subscript represents the mean value. On applying these assumption to (2.1) and (2.2) and neglecting the products of small dynamical quantities, we obtain

$$\frac{\partial \rho^{'}}{\partial t} + \rho_0 \nabla \cdot \mathbf{v}^{'} = 0, \tag{2.5}$$

$$\rho_0 \frac{\partial \mathbf{v}^{'}}{\partial t} + \nabla p^{'} = 0. \tag{2.6}$$

On differentiating (2.5) with respect to t, we get

$$\frac{\partial^2 \rho^{'}}{\partial t^2} + \rho_0 \nabla \cdot \frac{\partial \mathbf{v}^{'}}{\partial t} = 0 \tag{2.7}$$

and gradient of (2.6) leads to

$$\rho_0 \nabla \cdot \frac{\partial \mathbf{v}^{'}}{\partial t} + \nabla^2 p^{'} = 0. \tag{2.8}$$

Thus, the subtraction of (2.7) and (2.8) yields

$$\frac{\partial^2 \rho^{'}}{\partial t^2} - \nabla^2 p^{'} = 0. \tag{2.9}$$

Since, from the Taylor's series of p about ρ_0, we get

$$p = p_0 + \left(\frac{\partial p}{\partial \rho}\right)_{\rho=\rho_0} (\rho - \rho_0) + \frac{1}{2}\left(\frac{\partial^2 p}{\partial \rho^2}\right)_{\rho=\rho_0} (\rho - \rho_0)^2 + \dots\, . \tag{2.10}$$

On neglecting the second and higher order perturbation terms,

$$p - p_0 \approx \left(\frac{\partial p}{\partial \rho}\right)_{\rho=\rho_0} (\rho - \rho_0) \tag{2.11}$$

and on substituting (2.3) and (2.4) in (2.11), we have

$$p^{'} = c^2 \rho^{'}, \tag{2.12}$$

where $c = \sqrt{(\partial p/\partial \rho)_{\rho=\rho_0}}$ is the speed of sound and its value depends upon the thermodynamic properties of the fluid. Under adiabatic condition at standard temperature pressure (STP), the speed of sound in air is 343 m/s. On substituting the value of $\rho^{'}$ from (2.12) into equation (2.9), we obtain

$$\frac{1}{c^2}\frac{\partial^2 p}{\partial t^2} - \nabla^2 p = 0. \tag{2.13}$$

Equation (2.13) is the standard acoustic wave equation in terms of acoustic pressure. In dimensional setting, it can be written as

$$\frac{1}{c^2}\frac{\partial^2 \bar{p}}{\partial \bar{t}^2} - \bar{\nabla}^2 \bar{p} = 0. \tag{2.14}$$

It is mentioned that the superposed bars above and hereinafter show the dimensional quantities whilst the over bars are skipped from the non-dimensional counterparts. It is useful to express (2.14) in terms of dimensional field potential $\bar{\Phi}(\bar{x}, \bar{y}, \bar{t})$ having relations with pressure and velocity, respectively as

$$\bar{p} = -\rho_0 \frac{\partial \bar{\Phi}}{\partial \bar{t}} \tag{2.15}$$

and

$$\bar{\mathbf{v}} = \bar{\nabla}\bar{\Phi}. \tag{2.16}$$

On assuming harmonic time dependence, we have

$$\bar{\Phi}(\bar{x}, \bar{y}, \bar{t}) = \bar{\phi}(\bar{x}, \bar{y})e^{-i\omega\bar{t}}, \tag{2.17}$$

where ω is the angular frequency. On substituting (2.15) and (2.17) into (2.14), we obtain the Helmholtz's equation

$$\left(\frac{\partial^2}{\partial \bar{x}^2} + \frac{\partial^2}{\partial \bar{y}^2} + k^2\right)\bar{\phi}(\bar{x}, \bar{y}) = 0, \tag{2.18}$$

where $k = \omega/c$ denotes the wave number. In order to non-dimensionalize the physical quantities, the non-dimensional settings are defined in next section.

2.2 Non-Dimensional Setting

With the non-dimensional setting, the equations and boundary conditions of the boundary value problems are appeared in dimensionless form, where all mathematical laws and rules are easily applicable. Thus, for making the physical quantities dimensionless in the mathematical modeling of the physical problems, the dimensionless settings, with respect to the typical scale k^{-1} (length scale) and ω^{-1} (time scale), are framed in the following way

$$x = k\bar{x}, \qquad y = k\bar{y} \qquad \text{and} \qquad t = \omega\bar{t}. \tag{2.19}$$

On using the above transformation, we have

$$\frac{\partial^2}{\partial\bar{x}^2} = k^2\frac{\partial^2}{\partial x^2}, \quad \frac{\partial^2}{\partial\bar{y}^2} = k^2\frac{\partial^2}{\partial y^2} \quad \text{and} \quad \bar{\Phi}(\bar{x},\bar{y}) = \frac{1}{k^2}\phi(x,y). \tag{2.20}$$

By using non-dimensional settings, Helmholtz's equation (2.18) can be expressed in dimensionless form as

$$\left(\nabla^2 + 1\right)\phi(x,y) = 0. \tag{2.21}$$

Any solution of this equation has to comply with the acoustical properties of the boundary.

2.3 Boundary Conditions

The boundary conditions play an important role in determining the mathematical solutions of physical problems. The nature and types of boundary conditions depend on the conditions assumed while modeling the physical problems. In acoustic, "reaction of the surface to sound" can be expressed in terms of boundary conditions and that describes the behavior of sound in the neighborhood of a bounding surface. The present study describes acoustic analysis of waveguides having different geometrical and bounding characteristics. Following types of boundary conditions are considered.

2.3.1 Acoustic Impedance

It is the ratio of the acoustic pressure to the normal velocity acting on some surface [25]. It is usually denoted by Z, that is

$$Z = \frac{\text{Pressure}}{\text{Velocity}}. \tag{2.22}$$

By using (2.15) and (2.16), we may write (2.22) in terms of dimensional field potential as

$$\rho \frac{\partial \bar{\Phi}}{\partial \bar{t}} + Z\mathbf{n} \cdot \nabla \bar{\Phi} = 0, \tag{2.23}$$

where $\mathbf{n}$ is unit normal vector directed into the surface. By considering the harmonic time dependence and non-dimensional setting, (2.23) becomes

$$\phi + i\zeta\mathbf{n} \cdot \nabla\phi = 0, \tag{2.24}$$

where $\zeta = (\rho c)^{-1}Z$ represents the dimensionless specific impedance bounding surface. For mathematical convenience, we may write (2.24) into more simpler form by

$$\phi + \mathcal{Q}\mathbf{n} \cdot \nabla\phi = 0, \tag{2.25}$$

where $\mathcal{Q} = i\zeta$ is an arbitrary parameter whose value basically depends on the characteristic impedance of the surface. This is also known as impedance boundary conditions. Moreover, three boundary conditions such as, absorbent, rigid and soft are explained on the basis of acoustic impedance condition in following manners.

- **Absorbent Condition:** For absorbent linings, the specific impedance assumes value $\zeta = \xi + i\chi$, and that basically specifies two types of sheets [69, 100].

    i. Fibrous sheet when: $\xi = 0.5, -1 < \chi < 3$,

    ii. Perforated sheet when: $0 < \xi < 3, -1 < \chi < 3$.

- **Rigid Condition:** The given surface is acoustically rigid if $Z \to \infty$, and that reveals from (2.24), that can be written as

$$\mathbf{n}\cdot\nabla\phi = 0. \tag{2.26}$$

- **Soft Condition:** The given surface is acoustically soft if $Z \to 0$ which implies $\mathcal{Q} \to 0$, therefore (2.25) gives

$$\phi = 0. \tag{2.27}$$

2.3.2 Elastic Membrane Condition

To formulate the elastic membrane condition it is assumed that the tensile stress is same at every point on the membrane and at every orientation of the line element perpendicular to the membrane surface. Such membranes are deformable like a sheet of rubber and that contain wave behavior similar to the waves on assemblage of flexible strings. Therefore, the tensile stress of the membrane can be referred as tension (T), and the wave equation for membrane can be found in many text, for instance [101]. For membrane condition coupled with compressible fluid, the dimensional displacement $\bar{W}(\bar{x},\bar{y},\bar{t})$ satisfies the equation of motion.

$$\frac{\partial^2\bar{W}}{\partial\bar{x}^2} - \frac{1}{c_m^2}\frac{\partial^2\bar{W}}{\partial\bar{t}^2} = \frac{1}{T}[\bar{p}]_-^+, \tag{2.28}$$

where $c_m = \sqrt{T/\rho_m}$ specifies the sound's speed on membrane having mass density ρ_m. The quantity $[\bar{p}]_-^+ = [\bar{p}]^+ - [\bar{p}]^-$ on the right hand side of the (2.28) denotes the fluid pressure difference across the membrane surface. On assuming the harmonic time dependence, it is convenient to express the membrane displacement by

$$\bar{W}(\bar{x},\bar{t}) = \bar{\mathrm{w}}(\bar{x})e^{-i\omega\bar{t}}. \tag{2.29}$$

Thus, on using (2.15), (2.17) and (2.29) into (2.28), after little arrangement we get

$$\frac{\partial^2\bar{\mathrm{w}}}{\partial\bar{x}^2} + \frac{\omega^2}{c_m^2}\bar{\mathrm{w}} = \frac{i\omega\rho_0}{T}\left[\bar{\phi}\right]_-^+. \tag{2.30}$$

As the membrane displacement $\bar{W}$ is related to field potential through the relation, that is,

$$\frac{\partial \bar{w}}{\partial \bar{t}} = \frac{\partial \bar{\Phi}}{\partial \bar{y}}, \tag{2.31}$$

which for harmonic time dependence reveals

$$\bar{\mathrm{w}} = \frac{i}{\omega}\frac{\partial \bar{\phi}}{\partial \bar{y}}. \tag{2.32}$$

After substituting (2.32) into (2.30), we get

$$\left[\frac{\partial^2}{\partial \bar{x}^2} + \frac{\omega^2}{c_m^2}\right]\frac{\partial \bar{\phi}}{\partial \bar{y}} = \frac{\omega^2 \rho_0}{T}\left[\bar{\phi}\right]_-^+. \tag{2.33}$$

On non-dimensionalizing (2.33) and the transformation defined in Section. 2.2, we get

$$\left[\frac{\partial^2}{\partial x^2} + \mu^2\right]\frac{\partial \phi}{\partial y} - \alpha\left[\phi\right]_-^+ = 0, \tag{2.34}$$

where $\mu = c/c_m$ and $\alpha = c^2\rho_0/\left(kT\right)$ denote the membrane wave number and fluid loading parameters, respectively.

To describe the behavior of vibrating elastic membrane "edge conditions" are used. These conditions define the physical connections as well as ensure the uniqueness of the solution.

- **Edge Conditions for Membrane:** Following two types of edge conditions of elastic membrane are used in this thesis.

  Fixed Edges: For the fixed edge, the displacement of the membrane is assumed to be zero, that is

  $$\frac{\partial \phi(0,a)}{\partial y} = 0. \tag{2.35}$$

  Free Edges: In this case, the gradient is assumed to be zero, that is

  $$\frac{\partial^2 \phi(0,a)}{\partial x \partial y} = 0. \tag{2.36}$$

  It is also known as simply supported edge condition.

2.3.3 Elastic Plate Condition

A plate is a solid body bounded by two surfaces. The distance between the two surfaces defines the thickness of the plate, which is assumed to be small compared to the lateral dimensions, such as the length and width in the case of a rectangular plate and the diameter in the case of a circular plate. The vibration of plates play an important role in the study of structural acoustic. The theory of elastic plates is an approximation of the three-dimensional elasticity theory to two dimensions, and that permits a description of the deformation in the plate along the midplane of the plate. Moreover, it is assumed that Young's modulus, Poisson ratio and area density vary across the plate in one direction. The governing equation of the plate in the form of dimensional plate displacement $\bar{W}_1\left(\bar{x},\bar{y},\bar{t}\right)$ coupled with compressible fluid is expressed below while the details pertaining to the derivation of the plate equation is given in [75].

$$\frac{\partial^4\bar{W}_1}{\partial\bar{x}^4}+\frac{2B^{'}(\bar{x})}{B(\bar{x})}\frac{\partial^3\bar{W}_1}{\partial\bar{x}^3}+\frac{B^{''}(\bar{x})}{B(\bar{x})}\frac{\partial^2\bar{W}_1}{\partial\bar{x}^2}+\frac{\rho_p}{B(\bar{x})}\frac{\partial^2\bar{W}_1}{\partial\bar{t}^2}=-[\bar{p}]_-^+, \tag{2.37}$$

where ρ_p is the mass density of the plate, $[\bar{p}]_-^+$ is the fluid pressure difference across the plate and B is the bending stiffness. For constant bending stiffness and area density, (2.37) leads to

$$\frac{\partial^4\bar{W}_1}{\partial\bar{x}^4}+\frac{\rho_p}{B(\bar{x})}\frac{\partial^2\bar{W}_1}{\partial\bar{t}^2}=-[\bar{p}]_-^+. \tag{2.38}$$

On assuming harmonic time dependence, the plate displacement can be expressed as

$$\bar{W}_1(\bar{x},\bar{t})=\bar{\mathrm{w}}_1(\bar{x})e^{-i\omega\bar{t}}, \tag{2.39}$$

so, (2.37) yields

$$\frac{\partial^4\bar{\mathrm{w}}_1}{\partial\bar{x}^4}-\frac{\rho_p\omega^2}{B(\bar{x})}\bar{\mathrm{w}}_1=-[\bar{p}]_-^+. \tag{2.40}$$

As the plate displacement $\bar{\mathrm{w}}_1$ in term of velocity potential is related by the relation as

$$\frac{\partial\bar{\mathrm{w}}_1}{\partial\bar{t}}=\frac{\partial\bar{\Phi}}{\partial\bar{y}}. \tag{2.41}$$

On using (2.15), (2.17) and (2.41) into (2.40), we obtain the following equation in term of field potential $\bar{\phi}(\bar{x},\bar{y})$ form as

$$\left[\frac{\partial^4}{\partial\bar{x}^4}-\frac{\rho_p\omega^2}{B(\bar{x})}\right]\frac{\partial\bar{\phi}}{\partial\bar{y}}=\frac{\omega^2\rho_0}{B(\bar{x})}\bar{\phi}. \tag{2.42}$$

On using non-dimensional setting from (2.19) and (2.20), the equation (2.42) leads to

$$\left[\frac{\partial^4}{\partial x^4}-\mu_1^4\right]\frac{\partial\phi}{\partial y}=\alpha_1\phi, \tag{2.43}$$

where $\mu_1=\sqrt[4]{c^2h\rho_p/Bk^2}$ represents the plate wavenumber in *vacuo* and $\alpha_1=c^2\rho/Bk^3$ denotes the fluid loading parameter. Moreover, the bending stiffness of the plate can also be expressed as $B=Eh^3/12(1-\upsilon^2)$ in which E is Young's modulus, and υ is Poisson's ratio. The elastic plate along with its connections at corners also plays an important role in effective designing of silencers. These connections are now explained in terms of plate edges.

- **Edge Conditions for Plate:** In the case of elastic plates, the edges are usually considered to be clamped, pin-jointed or pivoted. These are illustrated in following manners.

  Clamped Edges: The displacement and gradient of the plate at edges are assumed zero, that is

  $$\frac{\partial\phi(0,a)}{\partial y}=0 \quad \text{and} \quad \frac{\partial^2\phi(0,a)}{\partial x\partial y}=0. \tag{2.44}$$

  Pin-Jointed Edges: In case of pin-jointed edge conditions, the displacement and the bending moment are considered zero, that is

  $$\frac{\partial\phi(0,a)}{\partial y}=0 \quad \text{and} \quad \frac{\partial^3\phi(0,a)}{\partial x^2\partial y}=0. \tag{2.45}$$

  Pivoted Edges: In this set of edge conditions, the gradient and bending moment are assumed to be continuous, that is

  $$\frac{\partial\phi_i^2(0,a)}{\partial x\partial y}=\frac{\partial\phi_j^2(0,a)}{\partial y\partial x} \text{ and } \frac{\partial\phi_i^3(0,a)}{\partial x^2\partial y}=\frac{\partial\phi_j^3(0,a)}{\partial y\partial x^2}, \quad i\neq j. \tag{2.46}$$

Note that, these conditions physically realistic to apply only for the waveguide continuous in structure.

In next section, the assumed solution of wave propagation problem is elaborated.

2.4 Travelling Wave Formulation

The travelling wave solution can be expressed ansatz

$$\phi(x,y)=\sum_{n=0}^{\infty}\mathcal{A}_nY_n(y)e^{\pm i\eta_nx}, \tag{2.47}$$

where $Y_n(y); n=0,1,2...$ denote the shape of propagating mode, η_n is the wavenumber of n^{th} propagating mode and $\mathcal{A}_n$ are the amplitudes of that n^{th} mode.

The physical problems considered in this thesis are governed by Helmholtz's equation together with different types of boundary conditions. Therefore, the mathematical properties of eigenfunctions are linked mainly with the bounding properties of the bounding walls. These properties may underlie in SL category or may belong to non-SL category. Following three types of models are considered in this thesis.

- Impedance-Impedance Model
- Rigid-Membrane Model
- Rigid-Plate Model

Firstly, we explain the eigen properties associated with these models in detail.

2.5 Impedance-Impedance Model

In this model, the lower and upper horizontal boundaries of the duct are considered to be the impedance type of boundary condition. As the model problem is governed by Helmholtz's equation (2.21) together with impedance condition (2.25), so the eigenfunctions $Y_n(y)$ for the considered model satisfy the following eigen-sub-system

$$Y_n''(y) + \gamma_n^2 Y_n(y) = 0, \tag{2.48}$$

$$Y_n(a) - \mathcal{Q}_a Y_n'(a) = 0, \tag{2.49}$$

$$Y_n(b) + \mathcal{Q}_b Y_n'(b) = 0, \tag{2.50}$$

where $(')$ denotes the differentiation with respect to y variable and the quantities $\mathcal{Q}_a$ and $\mathcal{Q}_b$ are arbitrary constants. Also, $\gamma_n = \sqrt{(1-\eta_n^2)}$ denote the eigenvalues. On solving (2.48)-(2.50), we obtain

$$Y_n(y) = \sin[\gamma_n(y-a)] + \mathcal{Q}_a \cos[\gamma_n(y-a)]. \tag{2.51}$$

The eigenvalues γ_n are the roots of the following characteristics equation that is deduced by using (2.50) and (2.51), that is

$$\mathcal{K}(\gamma) = (1 - \gamma_n^2 \mathcal{Q}_a \mathcal{Q}_b) \sin[\gamma_n(b-a)] + (\mathcal{Q}_a + \mathcal{Q}_b) \cos[\gamma_n(b-a)] = 0. \tag{2.52}$$

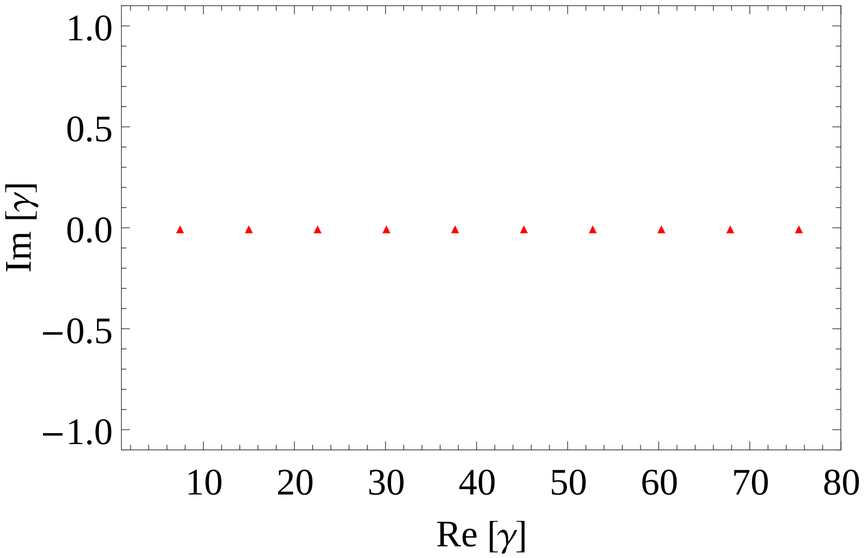

FIGURE 2.1: First 10 roots of the characteristic equations (2.52) at $f = 350$Hz with parameters $\mathcal{Q}_a = \mathcal{Q}_b = 1, \bar{a} = 0.02$m and $\bar{b} = 0.085$m.

The first ten real roots for $\mathcal{K}(\gamma) = 0$ are obtained by setting the parameters $\mathcal{Q}_a = \mathcal{Q}_b = 1, \bar{a} = 0.02\text{m}$ and $\bar{b} = 0.085\text{m}$ at $f = 350\text{Hz}$, which are shown in Fig. 2.1. These roots are arranged in ascending order. Now the orthogonality relation is demonstrated for the considered model problem in next section.

2.5.1 Orthogonality Relation

To derive the OR for this model, we multiply (2.48) by $Y_m(y)$ and integrate from a to b, then, we proceed as

$$\int_a^b Y_m(y)Y_n^{''}(y) + \gamma_n^2 \int_a^b Y_m(y)Y_n(y) = 0. \tag{2.53}$$

On integrating by parts, the first term in (2.53) together with (2.49) yields

$$\int_a^b Y_m(y)Y_n^{''}(y) = \Big[Y_m(y)Y_n^{'}(y)\Big]_a^b - \int_a^b Y_m^{'}(y)Y_n^{'}(y)dy,$$

$$= -\frac{1}{\mathcal{Q}_a}Y_m(a)Y_n(a) - \frac{1}{\mathcal{Q}_b}Y_m(b)Y_n(b) - \int_a^b Y_m^{'}(y)Y_n^{'}(y)dy, \tag{2.54}$$

after substituting (2.54) into (2.53), we get

$$-\frac{1}{\mathcal{Q}_a}Y_m(a)Y_n(a) - \frac{1}{\mathcal{Q}_b}Y_m(b)Y_n(b) - \int_a^b Y_m^{'}(y)Y_n^{'}(y)dy + \gamma_n^2 \int_a^b Y_m(y)Y_n(y) = 0. \tag{2.55}$$

Interchanging the indices m and n of (2.55), we find

$$-\frac{1}{\mathcal{Q}_a}Y_n(a)Y_m(a) - \frac{1}{\mathcal{Q}_b}Y_n(b)Y_m(b) - \int_a^b Y_n^{'}(y)Y_m^{'}(y)dy + \gamma_m^2 \int_a^b Y_n(y)Y_m(y) = 0. \tag{2.56}$$

On subtracting (2.56) from (2.55), we finally obtain

$$(\gamma_n^2 - \gamma_m^2)\int_a^b Y_n(y)Y_m(y) = 0. \tag{2.57}$$

For $m \neq n$, we get $\gamma_n^2 - \gamma_n^2 \neq 0$, so we have

$$\int_a^b Y_n(y)Y_m(y) = 0. \tag{2.58}$$

For $m = n$, we get $\gamma_n^2 - \gamma_n^2 = 0$, and we set

$$\int_a^b Y_n(y)Y_m(y) \neq 0.$$

The eigenfunctions $Y_n(y)$ are normalized as

$$\int_a^b Y_n(y)Y_m(y) = 1. \tag{2.59}$$

Hence, the property (2.58) and (2.59) is referred to as the orthogonality of the eigenfunctions $Y_n(y)$.

$$\int_a^b Y_n(y)Y_m(y)dy = D_n\delta_{mn}, \tag{2.60}$$

where δ_{mn} is the usual Kronecker delta. The eigenfunctions $Y_n(y)$ constitute a complete set. This completeness implies that an arbitrary function $f(y)$ can be represented to any desired accuracy as a linear combination of $Y_n(y)$

$$f(y) = \sum_n f_n Y_n(y). \tag{2.61}$$

Multiplying $f(y)$ by $Y_m(y)$ and integrating from a to b yields the expansion coefficient

$$f_n = \int_a^b f(y)Y_m(y)dx. \tag{2.62}$$

Hence, in order to match the modes of eigenfunctions expansion for the acoustic problems involving waveguide across the junctions between two regions, the orthogonality relation permits the problem to be reduced to solve an infinite system of linear algebraic equations. Now, the rigid-membrane model is discussed in next section.

2.6 Rigid-Membrane Model

In this model, we consider a flexible waveguide bounded below by a rigid wall and bounded above by an elastic membrane. The under consideration model is governed by Helmholtz's equation (2.21) together with boundary conditions (2.26) and (2.34) that leads to the following eigen-sub-system of equations

$$Y_n''(y) - \gamma_n^2 Y_n(y) = 0, \tag{2.63}$$

$$Y_n'(a) = 0, \tag{2.64}$$

$$(\gamma_n^2 + 1 - \mu^2)Y_n'(b) - \alpha Y_n(b) = 0. \tag{2.65}$$

The corresponding eigenvalues $\gamma_n = \sqrt{(\eta_n^2 - 1)}$ indicate the roots of the following characteristic equations

$$\kappa_1(\gamma) = (\gamma^2 + 1 - \mu^2)\gamma \sinh[\gamma(b-a)] - \alpha \cosh[\gamma(b-a)] = 0. \tag{2.66}$$

These roots are found numerically and have properties that are mentioned in the article [43]. These roots are ordered sequentially, real roots first and then by increasing imaginary part. Thus, γ_0 is always the largest real root.

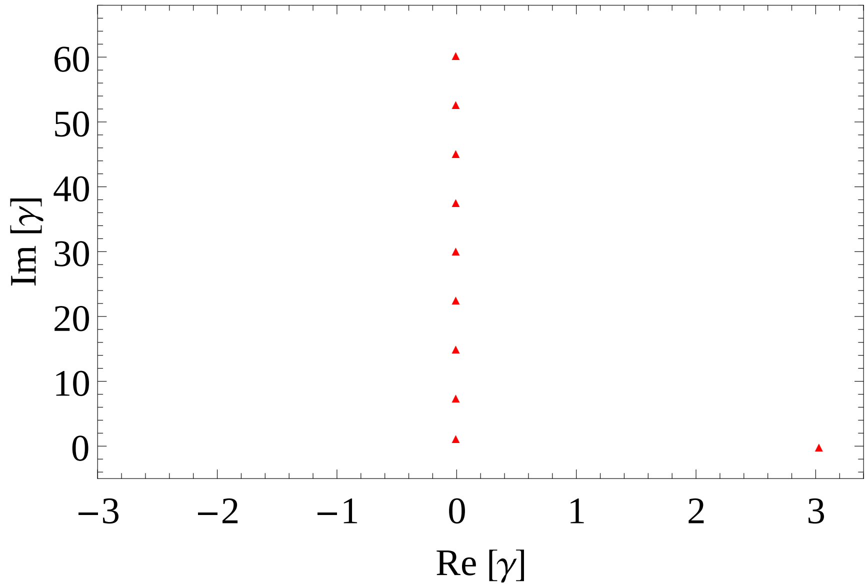

FIGURE 2.2: First 10 roots of the characteristic equations (2.66) at $f = 350$Hz with parameters $\mu = 2.74965,\ \alpha = 6.82942,\ \bar{a} = 0.02$m and $\bar{b} = 0.085$m.

The first ten roots are shown in Fig. 2.2 that are found numerically for the parameters: $\mu = 2.74965,\ \alpha = 6.82942,\ \bar{a} = 0.02$m and $\bar{b} = 0.085$m at $f = 350$Hz. Since, the resulting eigen system does not lead to SL system in which the standard orthogonality relation is not appropriate, the generalized orthogonality relations are developed [32].

2.6.1 Generalized Orthogonality Relation

We explore the generalized orthogonality relation for underlying eigen system. On multiplying (2.65) with $Y_m'(b)$, we get

$$(\gamma_n^2 + 1 - \mu^2)Y_n'(b)Y_m'(b) - \alpha Y_n(b)Y_m'(b) = 0, \tag{2.67}$$

after interchanging the indices m and n of (2.67), we obtain

$$(\gamma_m^2 + 1 - \mu^2)Y_m'(b)Y_n'(b) - \alpha Y_m(b)Y_n'(b) = 0. \tag{2.68}$$

On subtracting (2.68) from (2.67), we get

$$(\gamma_n^2 - \gamma_m^2)Y_n'(b)Y_m'(b) - \alpha[Y_n(b)Y_m'(b) - Y_m(b)Y_n'(b)] = 0. \tag{2.69}$$

Equation (2.69) together with (2.64) gives

$$(\gamma_n^2 - \gamma_m^2)Y_n'(b)Y_m'(b) - \alpha \int_a^b [Y_n(y)Y_m''(y) - Y_m(y)Y_n'(y)] = 0. \tag{2.70}$$

Consequently, from (2.63) that finally yields

$$(\gamma_n^2 - \gamma_m^2)\{Y_n'(b)Y_m'(b) + \alpha \int_a^b Y_n(y)Y_m(y)dy\} = 0, \tag{2.71}$$

for $m \neq n$, we have

$$\alpha \int_a^b Y_n(y)Y_m(y)dy + Y_n'(b)Y_m'(b) = 0, \tag{2.72}$$

for $m = n$, we get $\gamma_n^2 - \gamma_m^2 = 0$, thus we set

$$E_n := [Y_n'(b)]^2 + \alpha \int_a^b Y_n^2(y)dy. \tag{2.73}$$

Hence, the property (2.72) and (2.73) is concluded to generalized orthogonality relation as

$$\alpha \int_a^b Y_n(y)Y_m(y)dy + Y_n'(b)Y_m'(b) = E_n\delta_{mn}, \tag{2.74}$$

for the flexible waveguide bounded by membrane.

2.6.2 Properties of Eigenfunctions for Elastic Membrane

The class of eigen system in case of flexible membrane has well recognized properties [43] that are explained as

- The eigenfunctions $Y_n(y)$, $n = 0, 1, 2, 3...$, for flexible duct bounded by membrane are linearly dependent that satisfy

  $$\sum_{n=0}^{\infty} \frac{Y_n^{'}(b)Y_n(y)}{E_n} = 0, \qquad a \leq y \leq b. \tag{2.75}$$

  It is important to note that the number of linearly dependent sum is taken half of the order of the membrane partial differential equation.

- The eigenfunctions also satisfy the identities for membrane bounded duct, that is

  $$\sum_{n=0}^{\infty} \frac{[Y_n^{'}(b)]^2}{E_n} = 1. \tag{2.76}$$

2.7 Rigid-Plate Model

In this model, we consider a flexible waveguide bounded above by an elastic plate and bounded below by a rigid strip. The model problem is governed with Helmholtz's equation (2.21) together with boundary conditions (2.26) and (2.43) which yields

$$Y_n^{''}(y) - \gamma_n^2 Y_n(y) = 0, \tag{2.77}$$

$$Y_n^{'}(a) = 0, \tag{2.78}$$

$$\{(\gamma_n^2 + 1)^2 - \mu_1^4\} Y_n^{'}(b) - \alpha_1 Y_n(b) = 0. \tag{2.79}$$

The corresponding eigenvalues γ_n specify the roots of the dispersion relation, that can be written as

$$\kappa_2(\gamma) = \{(\gamma_n^2+1)^2 - \mu_1^4\}\gamma_n \sinh[\gamma_n(b-a)] - \alpha_1 \cosh[\gamma_n(b-a)] = 0. \qquad (2.80)$$

The first 10 roots of the characteristic equation ($\kappa_2(\gamma) = 0$) are plotted at $f = 350$Hz with parameters $\mu_1 = 7.52184,\ \alpha_1 = 370.914,\ \bar{a} = 0.02$m and $\bar{b} = 0.085$m, that are shown in Fig. 2.3.

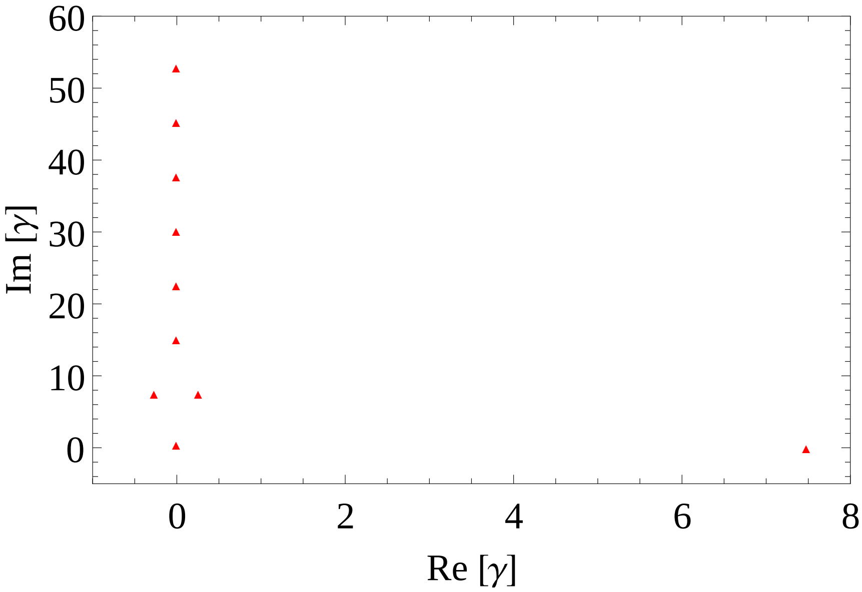

FIGURE 2.3: First 10 roots of the characteristic equations (2.80) at $f = 350$Hz with parameters $\mu_1 = 7.52184,\ \alpha_1 = 370.914,\ \bar{a} = 0.02$m and $\bar{b} = 0.085$m.

It is important to note that there exist finite real root, infinite imaginary roots and complex roots in pair form at certain frequency ranges. Such pairs are appeared, when the imaginary plate mode tends to cut-off duct modes. These complex pairs of γ can be obtained by solving the equation [34].

$$i\mu_1 = \sqrt{1 - \frac{n^2\pi^2}{k^2(\bar{b}-\bar{a})^2}}, \quad \text{for} \quad n = 1, 2, 3..., \qquad (2.81)$$

respectively. These roots are arranged according to the magnitude of imaginary part in ascending order such that γ^* is followed by $-\gamma^*$. Since the underlying eigen-system is non-Sturm-Liouville in nature, so it is indispensable to develop the generalized orthogonality relations.

2.7.1 Generalized Orthogonality Relation

The generalized orthogonality relation for plate bounded duct is derived as. On multiplying (2.79) with $Y_m^{'}(b)$, we get

$$\{(\gamma_n^2+1)^2-\mu_1^4\}Y_n^{'}(b)Y_m^{'}(b)-\alpha_1 Y_n(b)Y_m^{'}(b)=0, \tag{2.82}$$

after interchanging the indices m and n of (2.82), we find

$$\{(\gamma_m^2+1)^2-\mu_1^4\}Y_m^{'}(b)Y_n^{'}(b)-\alpha_1 Y_m(b)Y_n^{'}(b)=0. \tag{2.83}$$

On subtracting (2.83) from (2.82) that leads to

$$(\gamma_n^2-\gamma_m^2)(\gamma_n^2+\gamma_m^2+2)Y_n^{'}(b)Y_m^{'}(b)-\alpha_1[Y_n(b)Y_m^{'}(b)-Y_m(b)Y_n^{'}(b)]=0. \tag{2.84}$$

Equation (2.84) together with (2.78) provides

$$(\gamma_n^2-\gamma_m^2)(\gamma_n^2+\gamma_m^2+2)Y_n^{'}(b)Y_m^{'}(b)-\alpha_1\int_a^b[Y_n(y)Y_m^{''}(y)-Y_m(y)Y_n^{'}(y)]=0. \tag{2.85}$$

Consequently, from (2.77) that finally yields

$$(\gamma_n^2-\gamma_m^2)\{(\gamma_n^2+\gamma_m^2+2)Y_n^{'}(b)Y_m^{'}(b)+\alpha_1\int_a^b Y_n(y)Y_m(y)dy\}=0, \tag{2.86}$$

for $m\neq n$, we have

$$\alpha_1\int_a^b Y_n(y)Y_m(y)dy+(\gamma_n^2+\gamma_m^2+2)Y_n^{'}(b)Y_m^{'}(b)=0, \tag{2.87}$$

for $m=n$ we get $\gamma_n^2-\gamma_m^2=0$, thus we set

$$G_n:=2(\gamma_n^2+1)[Y_n^{'}(b)]^2+\alpha_1\int_a^b Y_n^2(y)dy. \tag{2.88}$$

Hence, the property of (2.87) and (2.88) is concluded to generalized orthogonality relation for the flexible waveguide bounded by plate, that can be expressed as

$$\alpha_1 \int_a^b Y_n(y)Y_m(y)dy + (\gamma_n^2 + \gamma_m^2 + 2)Y_n^{'}(b)Y_m^{'}(b) = G_n\delta_{mn}, \tag{2.89}$$

2.7.2 Properties of Eigenfunctions for Elastic Plate

The eigenfunctions $Y_j(\varrho_q, y),\ j = 1, 2$ are linearly dependent and their properties are mentioned below [43, 99]

$$\sum_{q=0}^{\infty} \Delta_{jq} Y_j(\varrho_q, y) = \sum_{q=0}^{\infty} \varrho_q^2 \Delta_j Y_j(\varrho_q, y) = 0, \qquad 0 \le y \le u \tag{2.90}$$

and

$$\sum_{q=0}^{\infty} \Delta_{jq}^2 \kappa_q = 0, \ \sum_{q=0}^{\infty} \varrho_q^2 \Delta_{jq}^2 \kappa_q = 1, \qquad 0 \le y \le u, \tag{2.91}$$

where

$$\Delta_{jq} = \frac{Y_j^{'}(\varrho_q, u)}{\kappa_q}. \tag{2.92}$$

The Green's function for the eigenfunctions can be constructed as [43]

$$\alpha_1 \sum_{q=0}^{\infty} \frac{Y_{jq}(\varrho_q, \upsilon)Y_{jq}(\varrho_q, y)}{\kappa_q} = \delta(y-\upsilon)+\delta(y+\upsilon)+\delta(y+\upsilon-2u), \qquad -u \le \upsilon,\ y \le u, \tag{2.93}$$

where $\delta(y)$ is the usual Dirac delta function and this result shows that the eigenfunction expansion representation of a suitably smooth function, say $f(y)$, converges point-wise to that functions. In order to obtain the solution of acoustic scattering problems in ducts or channels, Mode-Matching technique is presented in next section.

2.8 Mode-Matching Technique

Modal representation is generally opt to obtain the solution of acoustic waveguide problems. A single modal representation is only possible in segments of a duct with constant properties (diameter, wall impedance). When two segments of different properties are connected to each other, a modal representation can be used in each segment, but since the modes are different we have to reformulate the expansion of the incident field into an expansion of the transmitted field in the neighboring segment, using conditions of continuity of pressure and velocity. This is called: “MM”. Furthermore, these continuity conditions cannot be satisfied with a transmission field only, and a part of the incident field is reflected. Each mode is scattered into a modal spectrum of transmitted and reflected modes.

The first step in the MM method entails the eigenfunction expansion of unknown fields in the individual duct-regions in terms of their respective modes. Since the functional form of the modes is known, the problem reduces to that of obtaining modal amplitudes related with the field expansions in different duct-regions of waveguide. The modal representation is followed by the implementation of the continuity conditions for the fields at the interfaces in the junction regions. This method, in conjunction with the standard or generalized orthogonality relations of the modes, eventually leads to an infinite system of linear simultaneous equations for the unknown modal amplitudes. For further details on MM, we refer to [23].

In next section, we discuss the Low-Frequency Approximation technique.

2.9 Low-Frequency Approximation

LFA is found useful but valid only in low frequency regime. In this technique, we consider only a finite number of modes and the resulting finite systems can be solved simultaneously through inversion. The complete methodology of this method is presented in Chapters 4, 5 and 6.

2.10 Energy Flux

The energy flux or power (P) provides the understanding about the physical aspect of scattering as well as a check on the accuracy of obtained solution. The formula to obtain energy flux through fluid medium is given in [36] as

$$P\rfloor_{\text{fluid}} = \text{Re}\left\{ i\int_a^b \phi \left(\frac{\partial \phi}{\partial x}\right)^* dy \right\}, \tag{2.94}$$

where superposed asterisk ($*$) specifies for complex conjugate. Accordingly, the mathematical form of energy flux propagating via elastic membrane and plate are given by

$$P\rfloor_{\text{memb}} = \text{Re}\left\{ \frac{i}{\alpha}\left(\frac{\partial \phi}{\partial y}\right)\left(\frac{\partial^2 \phi}{\partial x \partial y}\right)^* \right\} \tag{2.95}$$

and

$$P\rfloor_{\text{plate}} = \text{Re}\left\{ \frac{i}{\alpha_1}\left[\left(\frac{\partial^2 \phi}{\partial x \partial y}\right)\left(\frac{\partial^3 \phi}{\partial x^2 \partial y}\right)^* - \left(\frac{\partial \phi}{\partial y}\right)\left(\frac{\partial^4 \phi}{\partial^3 x \partial y}\right)^* \right]\right\}, \tag{2.96}$$

respectively. Note that by using (2.94)-(2.96), we may construct a conserve power identity based upon the law of conservation of energy and that may serve as a physical check on the accuracy of truncated solution. As well, the accuracy of the silencer or waveguide are measured by transmission-loss (TL) that is expressed mathematically in next section.

2.11 Transmission-Loss

The performance of any acoustic waveguide is generally testified with the opt of transmission-loss [95], that is

$$\text{TL} = -10\log_{10}\left(\frac{P_t}{P_i}\right), \tag{2.97}$$

where, P_t stands for power transmitted, whilst P_i is for incident power through fluid.

Chapter 3

Acoustic Analysis in Discontinuous Waveguide with Different Boundaries

Two canonical problems are presented in this chapter. The first boundary value problem comprises waveguide whose boundary walls are assumed to be either rigid, soft or impedance in the presence of upper and lower flanges at matching interface between two duct regions with discontinuous structure. In second boundary value problem, the upper boundary walls are assumed to be elastic plates in waveguide with the presence of only lower flange at matching junction. The purpose of this chapter is to demonstrate the complete methodology to obtain the solution of both canonical problems by Mode-Matching technique.

3.1 Canonical Problem 1

The two-dimensional, rectangular infinite waveguide bounded below and above by two strips at $\bar{y} = \bar{0},\ \bar{a}$ and $\bar{y} = \bar{b}, \bar{d},\ -\infty < x < \infty$ respectively, where $\bar{d} > \bar{b} > \bar{a}$. Two vertical flanged strips at $\bar{x} = 0$, $0 \leq \bar{y} \leq \bar{h_1}$ and $\bar{h_2} \leq \bar{y} \leq \bar{d}$ are connected, forming the inlet and outlet duct region, respectively. The inside of the waveguide is filled with the compressible fluid of density ρ and sound speed c whilst the outer side is in *vacuo*. The physical configuration of the waveguide is shown in Fig. 3.1.

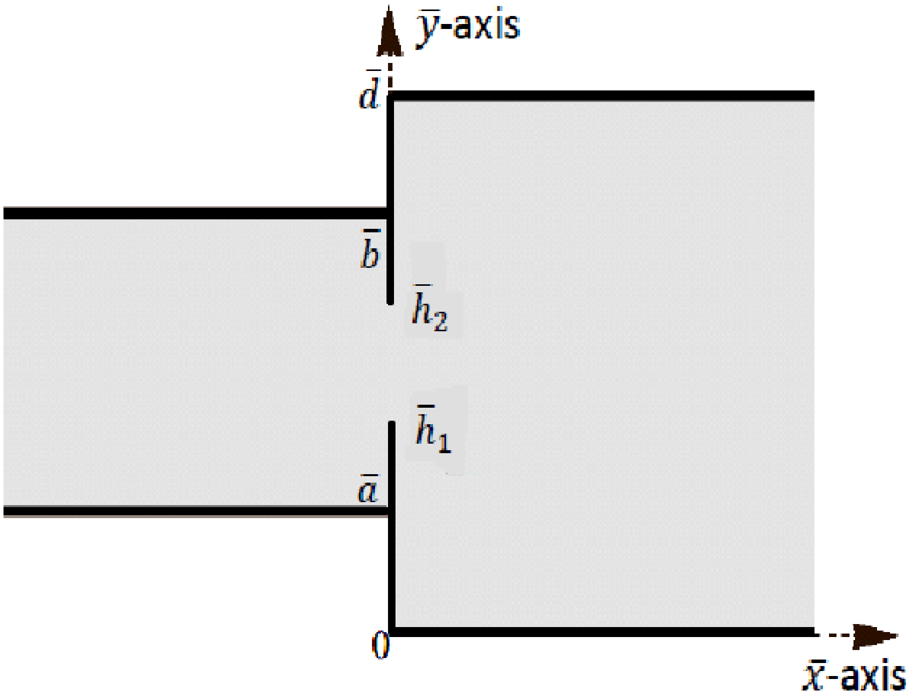

FIGURE 3.1: The physical configuration of the waveguide.

Since, the time independent non-dimensional fluid potential $\phi(x, y)$ satisfies the Helmholtz's equation (2.21) with unit wave number, that has been already derived in Section. 2.1, that is

$$\left(\nabla^2 + 1\right) \phi(x, y) = 0. \tag{3.1}$$

The rigid boundary conditions in non-dimensional form are given by

$$\frac{\partial \phi(x, a)}{\partial y} = 0, \quad \frac{\partial \phi(x, b)}{\partial y} = 0, \qquad x < 0, \tag{3.2}$$

the impedance boundary conditions for lower and upper strips can be written as

$$\phi(x, 0) - \mathcal{Q}_0 \frac{\partial \phi(x, 0)}{\partial y} = 0, \quad x > 0 \tag{3.3}$$

and

$$\phi(x, d) + \mathcal{Q}_1 \frac{\partial \phi(x, d)}{\partial y} = 0, \quad x > 0, \tag{3.4}$$

respectively. Moreover, the sides of upper and lower flanges lying at $\bar{x} = 0^-$ are acoustically rigid whilst the sides of both flanges aliened along $\bar{x} = 0^+$ are impedance that are expressed as

$$\frac{\partial \phi(0,y)}{\partial x} = 0, \quad \{a \leq y \leq h_1\} \cap \{h_2 \leq y \leq b\} \tag{3.5}$$

and

$$\phi(0,y) + \mathcal{Q}_2 \frac{\partial \phi(0,y)}{\partial x} = 0, \quad \{0 \leq y \leq h_1\} \cap \{h_2 \leq y \leq d\}, \tag{3.6}$$

respectively.

3.1.1 Mode-Matching Solution

In this section, the MM solution is developed for the underlying boundary value problem. Consider an incident wave of harmonic time dependence is propagating from inlet to outlet duct region. At interface $x = 0$, it is scattered into an infinite numbers of reflected and transmitted modes. So, the field potential $\phi(x,y)$ in respective inlet and outlet duct regions can be expressed as

$$\phi(x,y) = \begin{cases} \phi_1(x,y), & x < 0, \quad a \leq y \leq b, \\ \phi_2(x,y), & x > 0, \quad 0 \leq y \leq d. \end{cases} \tag{3.7}$$

On using Helmholtz's equation (3.1) together with (3.2) and (3.3)-(3.4) with the usual process of separation of variables, we obtain the eigenfunction expansion form in respective duct region, that is

$$\phi_1(x,y) = F_\ell Y_{1\ell}(y) e^{i\eta_\ell x} + \sum_{n=0}^{\infty} A_n Y_{1n}(y) e^{-i\eta_n x} \tag{3.8}$$

and

$$\phi_2(x,y) = \sum_{n=0}^{\infty} B_n Y_{2n}(y) e^{i\nu_n x}, \tag{3.9}$$

where $Y_{1n}(y) = \cos\{\gamma_n(y-a)\}, Y_{2n}(y) = \sin(\beta_n y) + \mathcal{Q}_0 \beta_n \cos(\beta_n y)$. The wave numbers $\eta_n = \sqrt{1-\gamma_n^2}$ denote in inlet duct region, whilst $\nu_n = \sqrt{1-\beta_n^2}$ represent the wave numbers of propagating modes in outlet duct regions. The first term in (3.8) denotes the multimodal incident for structural-borne ($\ell = 0$) and fluid-borne ($\ell = 1$) mode incident. Moreover, the eigenvalues $\gamma_n^2 = n\pi/(b-a), n = 0, 1, 2, ...$ and the eigenvalues β_n are found by the following characteristic equation.

$$(1 - \beta_n^2 \mathcal{Q}_0 \mathcal{Q}_1)\sin(\beta_n d) + (\mathcal{Q}_0 + \mathcal{Q}_1)\beta_n \cos(\beta_n d) = 0. \tag{3.10}$$

These roots are found numerically and having properties that have been discussed in Section. 2.5. Since the model problem is governed by Helmholtz's equation together with rigid, soft or impedance types boundary conditions leads to a SL system. The eigenfunctions $Y_{jn}(y),\ j = 1, 2$ in SL system are linearly independent and satisfy usual orthogonality relations, that is

$$\int_a^b Y_{1n}(y)Y_{1m}(y)dy = \frac{(b-a)}{2}\delta_{mn}\epsilon_m \tag{3.11}$$

and

$$\int_0^d Y_{2n}(y)Y_{2m}(y)dy = D_n\delta_{mn}, \tag{3.12}$$

where δ_{mn} is the kronecker delta and

$$\epsilon_m = \begin{cases} 2, & m = 0, \\ 1, & \text{otherwise.} \end{cases} \tag{3.13}$$

However, the coefficients A_n and B_n are called reflected and transmitted amplitudes in inlet and outlet duct regions respectively. These coefficients are found by using the continuity conditions of pressures and normal velocities at matching interfaces. Thus, the continuity condition of normal velocities at $x = 0$ are given by

$$\phi_{1x}(0, y) = \begin{cases} 0, & a \le y \le h_1, \\ \phi_{2x}(0, y), & h_1 \le y \le h_2, \\ 0, & h_2 \le y \le b, \end{cases} \tag{3.14}$$

hereinafter $\phi_{jx} = \dfrac{\partial \phi_j}{\partial x}$ $(j = 1, 2)$. Now the expression of reflected amplitudes are found by substituting (3.8)-(3.9) into (3.14) along with the usual orthogonality relation (3.13), that is

$$A_m = F_\ell \delta_{m\ell} - \frac{2}{(b-a)\eta_m \epsilon_m} \sum_{n=0}^{\infty} B_n \nu_n R_{mn}, \tag{3.15}$$

where

$$R_{mn} = \int_{h_1}^{h_2} Y_{1m}(y) Y_{2n}(y) dy. \tag{3.16}$$

Likewise, the continuity conditions of pressures at $x = 0$ are expressed as

$$\phi_2(0, y) = \begin{cases} -\mathcal{Q}_2 \phi_{2x}(0, y), & 0 \le y \le h_1, \\ \phi_1(0, y), & h_1 \le y \le h_2, \\ -\mathcal{Q}_2 \phi_{2x}(0, y), & h_2 \le y \le d. \end{cases} \tag{3.17}$$

Here, we obtain expression of transmitted amplitudes by substituting (3.8)-(3.9) into (3.17) along with the help of orthogonality relation (3.12), that is

$$B_m = \frac{F_\ell R_{m\ell}}{D_m} + \sum_{n=0}^{\infty} \frac{A_n R_{nm}}{D_m} - i\mathcal{Q}_2 \sum_{n=0}^{\infty} \frac{B_n \nu_n T_{mn}}{D_m}, \tag{3.18}$$

where

$$T_{mn} = \int_0^{h_1} Y_{2m}(y) Y_{2n}(y) dy + \int_{h_2}^{d} Y_{2m}(y) Y_{2n}(y) dy. \tag{3.19}$$

Hence the equations (3.15) and (3.18) form an infinite system of linear algebraic equations from which the unknown reflected amplitudes and transmitted amplitudes are determined.

3.1.2 Expression for Energy Flux and Power Balance

In this section, we determine the expressions of energy flux in the inlet and outlet duct regions of waveguide. As the boundaries of the waveguide are assumed rigid and impedance type so it is considered that no power will be lost and so the law of conservation law holds. Hence, it will be shown that incident power will be equal to sum of the reflected and transmitted power. In order to determine the incident power (P_i), the incident field, that is

$$\phi_{inc}(x,y) = F_\ell Y_{1\ell}(y)e^{i\eta_\ell x}, \tag{3.20}$$

is substituted in (2.94), to find the power propagating through fluid in the inlet duct region. So we get

$$P_i = \frac{1}{2}\mathrm{Re}\left[F_\ell F_\ell^* \eta_\ell^* e^{i(\eta_\ell-\eta_\ell^*)x}\int_a^b Y_{1\ell}(y)Y_{1\ell}(y)dy\right], \tag{3.21}$$

after simplification P_i reduces to

$$P_i = \frac{(b-a)}{2}F_\ell^2\eta_\ell. \tag{3.22}$$

Since $F_\ell = \sqrt{1/\eta_\ell}$, thus, we have

$$P_i = \frac{(b-a)}{2}. \tag{3.23}$$

To find the reflected power P_r, the reflected field in the inlet duct region is represented as

$$\phi_{ref}(x,y) = \sum_{n=0}^{\infty} A_n Y_{1n}(y)e^{-i\eta_n x}, \tag{3.24}$$

so, on substituting (3.24) into (2.94), we get

$$P_r = -\frac{1}{2}\mathrm{Re}\left[\sum_{n=0}^{\infty}\sum_{m=0}^{\infty} A_n A_m^* \eta_m^* e^{-i(\eta_n-\eta_m^*)x}\int_a^b Y_{1n}Y_{1m}dy\right]. \tag{3.25}$$

On using OR (3.11) into (3.25), we get

$$P_r = -\frac{(b-a)}{4}\mathrm{Re}\left[\sum_{n=0}^{\infty} \mid A_n \mid^2 \varepsilon_n \eta_n\right]. \tag{3.26}$$

Similarly, in order to obtain the transmitted power (P_t), the transmitted field in outlet duct region, that is expressed as

$$\phi_{tran}(x,y)=\sum_{n=0}^{\infty}B_nY_{2n}(y)e^{i\nu_nx}, \tag{3.27}$$

on substituting (3.27) in (2.94), we get

$$P_t=\frac{1}{2}\text{Re}\left[\sum_{n=0}^{\infty}\sum_{m=0}^{\infty}B_nB_m^*\nu_m^*e^{i(\nu_n-\nu_m^*)x}\int_0^d Y_{2n}(y)Y_{2m}(y)dy\right]. \tag{3.28}$$

On using OR (3.12) into (3.28), we obtain

$$P_t=\frac{1}{2}\text{Re}\left[\sum_{n=0}^{\infty}\mid B_n\mid^2 D_n\nu_n\right]. \tag{3.29}$$

For any enclosure, the power in inlet duct channel is equal to the power of outlet duct channel, that is

$$P_i+P_r=P_t. \tag{3.30}$$

To show the conserve power identity, we substitute (3.23), (3.26) and (3.29) into (3.30), we have

$$\frac{(b-a)}{2}-\frac{(b-a)}{4}\text{Re}\left[\sum_{n=0}^{\infty}\mid A_n\mid^2\varepsilon_n\eta_n\right]=\frac{1}{2}\text{Re}\left[\sum_{n=0}^{\infty}\mid B_n\mid^2 D_n\nu_n\right]. \tag{3.31}$$

Now by dividing $2/(b-a)$ on both sides of (3.31), we obtain

$$1=\frac{1}{2}\text{Re}\left[\sum_{n=0}^{\infty}\mid A_n\mid^2\varepsilon_n\eta_n\right]+\frac{1}{(b-a)}\text{Re}\left[\sum_{n=0}^{\infty}\mid B_n\mid^2 D_n\nu_n\right]. \tag{3.32}$$

We may scale (3.32) the incident power to unity, that is

$$1=P_r+P_t, \tag{3.33}$$

which is the conserved power identity, where

$$P_r=\frac{1}{2}\text{Re}\left[\sum_{n=0}^{\infty}\mid A_n\mid^2\varepsilon_n\eta_n\right] \tag{3.34}$$

and

$$P_t = \frac{1}{(b-a)}\mathrm{Re}\left[\sum_{n=0}^{\infty} \mid B_n \mid^2 D_n \nu_n\right]. \tag{3.35}$$

Note that (3.34) and (3.35) denote reflected and transmitted power's components respectively, for which the incident power is being scaled at unity.

3.1.3 Numerical Results and Discussions

In this section, numerical results are provided with discussion. The relevant heights of the inlet and outlet ducts are fixed as $\bar{a} = 0.2$m, $\bar{b} = 0.8$m, $\bar{d} = 1.0$m, $\bar{h_1} = 0.4$m and $\bar{h_2} = 0.6$m , whilst, the sound speed and density of the air are taken to be $c = 343.5$m/s and $\rho_a = 1.2$ kg/m^3, respectively, for all numerical assessments.

All the presented numerical results are obtained by truncating the mode-matching solutions with a truncation parameter referred to as N. The truncated solution can be used to check the accuracy of presented algebra and distribution of power or energy flux. The expressions for the reflected power (3.34) in the inlet duct and the transmitted power (3.35) in the outlet duct have been derived in Section. 3.1.2, whereas the incident power (3.33) is scaled at unity. The structural-borne vibration ($\ell = 0$) is only considered herein as an incident fields.

The purpose of the graphical results herein, is to analyze the scattering of powers or energies versus frequency (in hertz). The presented graphical figures are obtained for a fixed choice of rigid boundary conditions of all walls of the inlet duct section, whilst all boundaries of the outlet duct section are varying with following types of boundary conditions.

(a) Impedance Type:

For this type, the parameters are fixed as $\mathcal{Q}_0 = \mathcal{Q}_1 = \mathcal{Q}_2 = 1$.

(b) Soft Type:

For this case, the parameters are fixed as $\mathcal{Q}_0 = \mathcal{Q}_1 = \mathcal{Q}_2 = 0$.

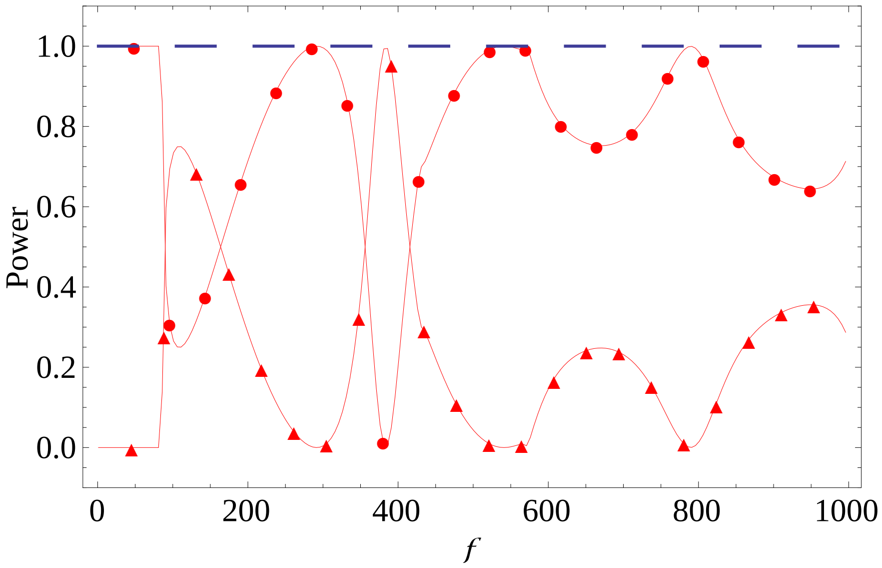

FIGURE 3.2: Power reflected (●), power transmitted (▲) and the law (3.33) of power balance (−−) against frequency for impedance type boundary conditions with flanges for $N = 90$.

(c) Rigid Type:

For this type, the parameters are taken as $1/\mathcal{Q}_0 = 1/\mathcal{Q}_1 = 1/\mathcal{Q}_2 = 0$.

Figs. 3.2-3.3 depict the distribution of power against frequencies in the domain 1Hz$\leq f \leq$ 1000Hz, for a fixed choice of rigid boundaries of the inlet duct wall and impedance boundary conditions (see, Type. (a)) assumed for the outlet duct walls. The Fig. 3.2 reveals that reflected and transmitted powers fluctuate at low frequency ranges ($f \leq$ 400Hz), but after $f =$ 400Hz, fluctuation in power reflection goes maximum in the presence of flanges. On the other hand, Fig. 3.3 depicts the powers scattering results in the absence of flanges by assuming the parameters $\bar{a} = \bar{h_1} =$ 0.2m and $\bar{b} = \bar{h_2} =$ 0.8m. It is observed that the reflection power goes minimum after $f =$ 400Hz than Fig. 3.2 because of the absence of the flanges. It is also noted that the conserved power identity (3.33) holds in both Figs. 3.2-3.3, which is displayed with dashed.

Figs. 3.4-3.5 depict the power propagation against frequency with soft type (see Type. (b)) boundary conditions imposed at the walls of the outlet duct section by keeping the boundaries of the wall of inlet duct as rigid. Fig. 3.4 reveals

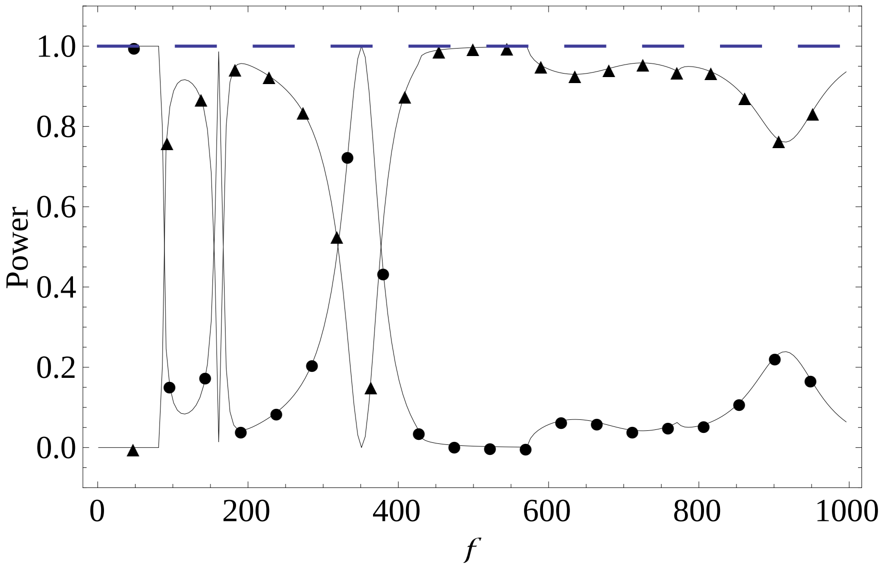

FIGURE 3.3: Power reflected (●), power transmitted (▲) and the law (3.33) of power balance (−−) against frequency for impedance type boundary conditions without flanges for $N = 90$.

the results of powers scattering with flanges, whilst Fig. 3.5 depicts the powers scattering results without flanges.

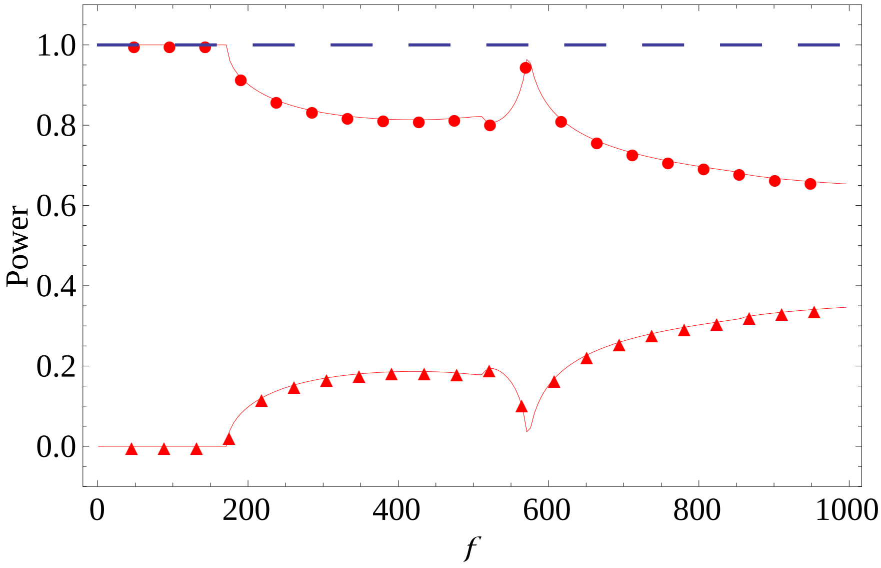

FIGURE 3.4: Power reflected (●), power transmitted (▲) and the law (3.33) of power balance (−−) against frequency for soft type boundary conditions with flanges for $N = 90$.

In Fig. 3.4, the reflected power decreases from maximum to 80%, whereas the sum of reflected and transmitted power remains identity. In contrast, the power propagation behavior in Fig. 3.5 is quite different than Fig. 3.4. It is because

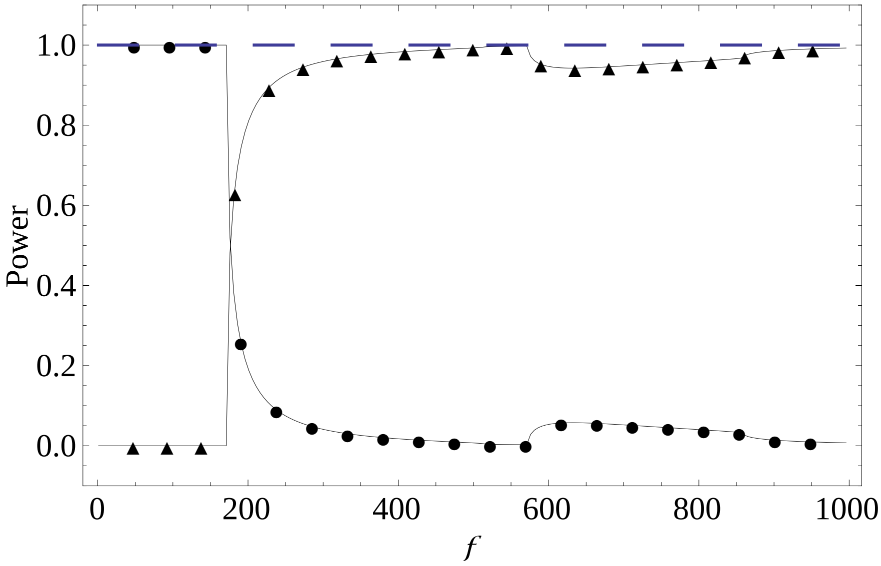

FIGURE 3.5: Power reflected (●), power transmitted (▲) and the law (3.33) of power balance (−−) against frequency for soft type boundary conditions without flanges for $N = 90$.

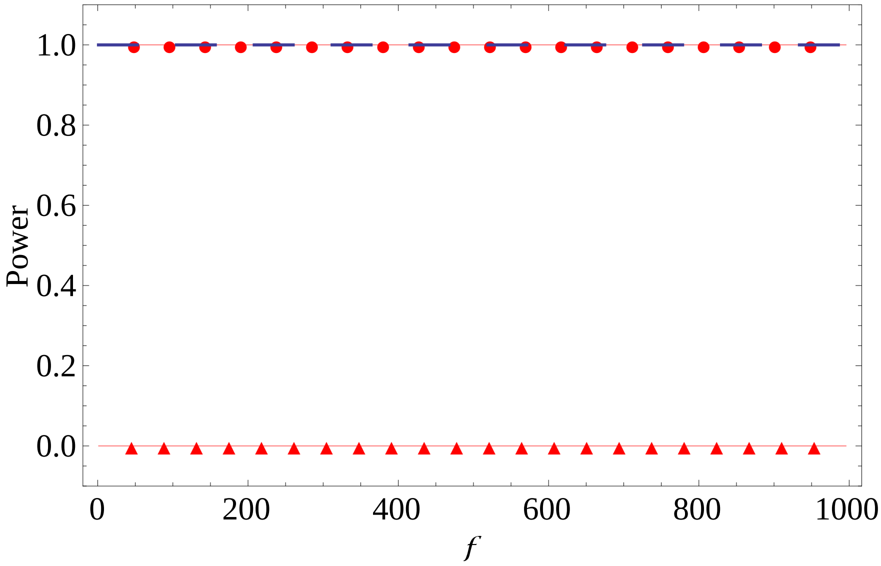

FIGURE 3.6: Power reflected (●), power transmitted (▲) and the law (3.33) of power balance (−−) against frequency for rigid type boundary conditions with flanges for $N = 90$.

of the absence of flanges, the reflected power goes to minimum after $f = 200$Hz and transmitted power behaves conversely. However, the sum of the reflected and transmitted powers is unity that successfully testifies the conserve power identity (3.33), as shown in both Figs. 3.4-3.5. Figs. 3.6-3.7 depict for the rigid (see Type.(c)) boundary conditions that are imposed on the walls of both inlet and

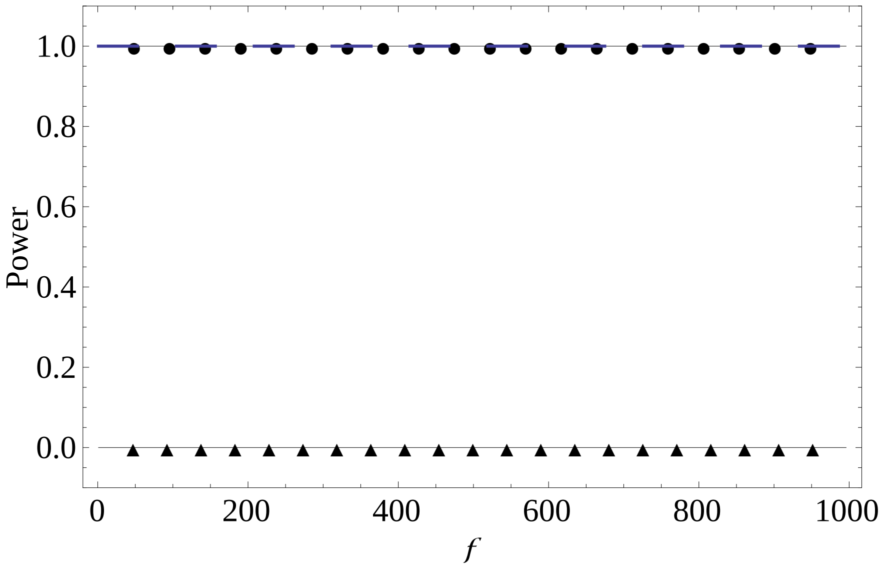

FIGURE 3.7: Power reflected (●), power transmitted (▲) and the law (3.33) of power balance (−−) against frequency for rigid type boundary conditions without flanges for $N = 90$.

outlet duct sections including flanges. Clearly, it is depicted that the maximum power is reflected in both of the case with and without flanges, as shown in Figs. 3.6-3.7. Also the sum of reflected and transmitted power remains unity.

3.1.4 Validation of the Method

The graphical results presented in last section 3.1.3 focused on the scattering analysis of powers against frequency for two different types of boundary conditions in the presence of the flanges and without flanges. In view of the nature of singularity in the velocity field, it is essential to validate the MM solution. Toward this end, it is verified that

(a) a sufficient number of terms have been retained while truncating (3.15) and (3.18) so that an adequate convergence of the modal coefficients can be ensured, and

(b) the coefficients contain correct information so that the matching conditions (3.14) and (3.17) can be reconstructed.

Accordingly, the real and imaginary parts of velocities and pressures are plotted at interface $x = 0$ for rigid boundaries of inlet duct wall and impedance boundaries for outlet duct walls in Fig. 3.15 and in Fig. 3.18 respectively. It can be observed that the real and imaginary parts of non-dimensional pressures and velocities are in excellent agreement along with the aperture at $x = 0$. Both pairs of curves almost overlap for $h_1 \leq y \leq h_2$ and velocities are zero in the domain $a < y < h_1$ and $h_2 < y < b$. This is true at all relevant frequencies. Thus, conditions from

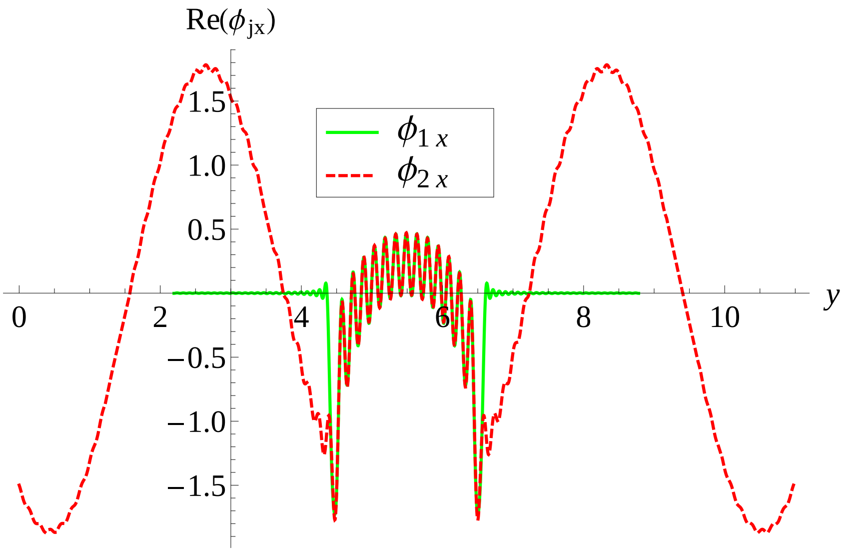

(a) Real part of velocities

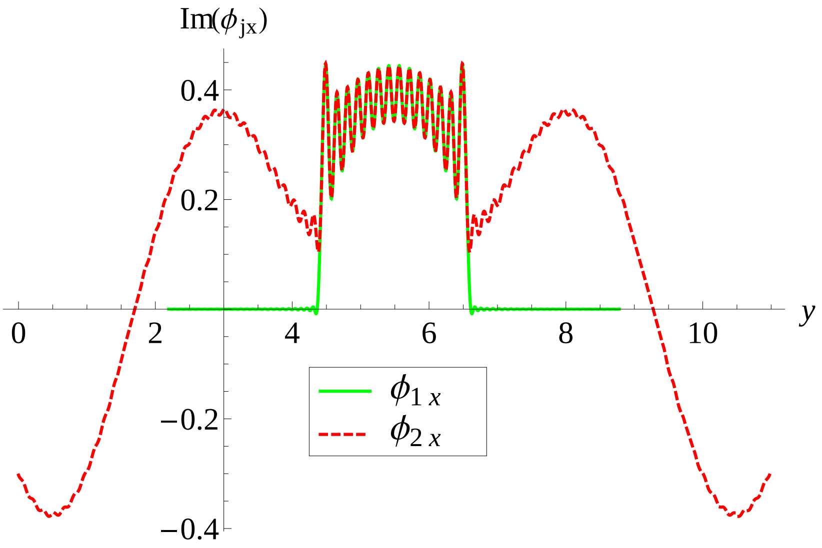

(b) Imaginary part of velocities.

FIGURE 3.8: Normal velocities vs. duct height at $x = 0$ in the presence of flanges, frequency 600Hz, and $N = 150$.

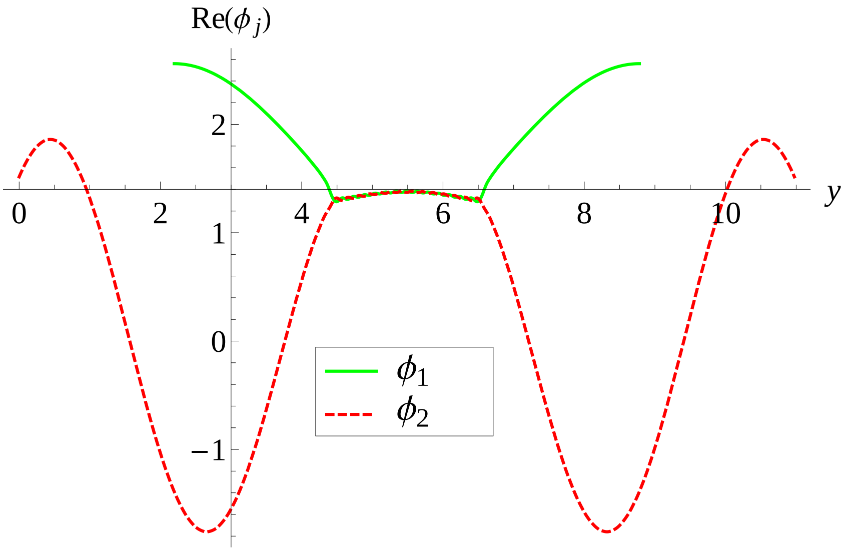

(a) Real part of pressures.

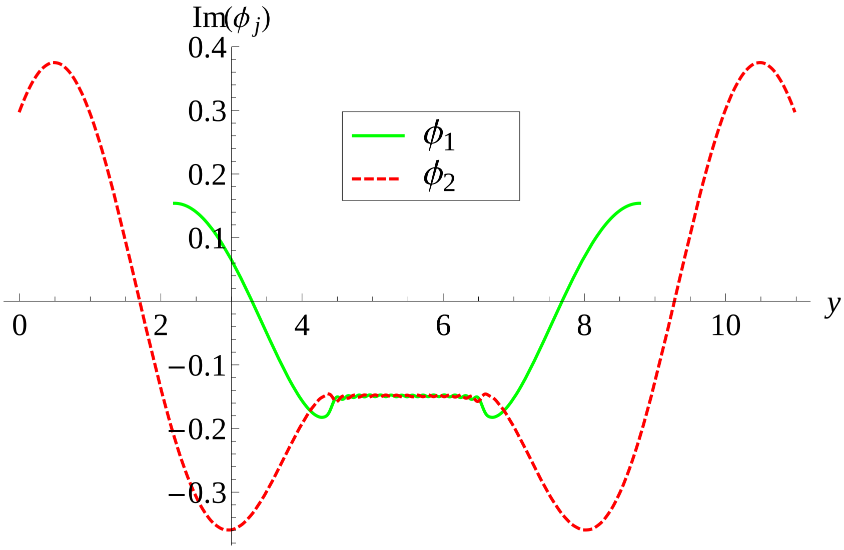

(b) Imaginary part of pressures.

FIGURE 3.9: Pressures vs. duct height at $x = 0$ in the presence of flanges, frequency 600Hz, and $N = 150$.

(3.14) and (3.17) are satisfied. The matching conditions are also met to the same accuracy at interfaces $x = 0$. Nevertheless, the two curves oscillate around their mean value and the amplitude of oscillation reduces significantly as y increases, except when $y \to h_1$ and $y \to h_2$. This is, in fact, due to the singular behavior of the velocity field at the corner of the two flangs, one is at $y = h_1$ and other is at $y = h_2$. It has been debated in great detail in, for instance [34]. In a nutshell, the reconstruction of the matching conditions completely justify the truncated MM approach and assert on the correctness of the performed algebra.

3.2 Canonical Problem 2

Consider a two-dimensional infinite waveguide containing two semi-infinite duct regions $-\infty < \bar{x} \leq 0$, $0 \leq \bar{y} \leq \bar{a}$ and $0 \leq \bar{x} < \infty$, $\bar{h}_1 \leq \bar{y} \leq \bar{b}$. These duct regions are bounded below by an acoustically rigid surfaces at $\bar{y} = 0$ and $\bar{y} = \bar{h}_1$, whilst bounded above by an elastic plate at $\bar{y} = \bar{a}$, $-\infty < \bar{x} \leq 0$ and $\bar{y} = \bar{b}$, $0 \leq \bar{x} < \infty$. Two duct regions are mutually joined by means of two vertical strips lying at $\bar{x} = 0$, $0 \leq \bar{y} < \bar{h}_2$ and $\bar{x} = 0$, $\bar{a} \leq \bar{y} < \bar{b}$. The material properties on the sides of the vertical strips are assumed to be different. The sides of vertical strips lying at $\bar{x} = 0^-$ are acoustically rigid while the sides aliened along $\bar{x} = 0^+$ are soft. The interior region of the waveguide is filled with a compressible fluid of density ρ and sound speed c, whereas, the exterior region is assumed to be in *vacuo*. The waveguide structure of the problem is shown in Fig. 3.10. As the time independent dimensionless fluid potential $\phi(x, y)$ satisfies the Helmholtz's equation with unit

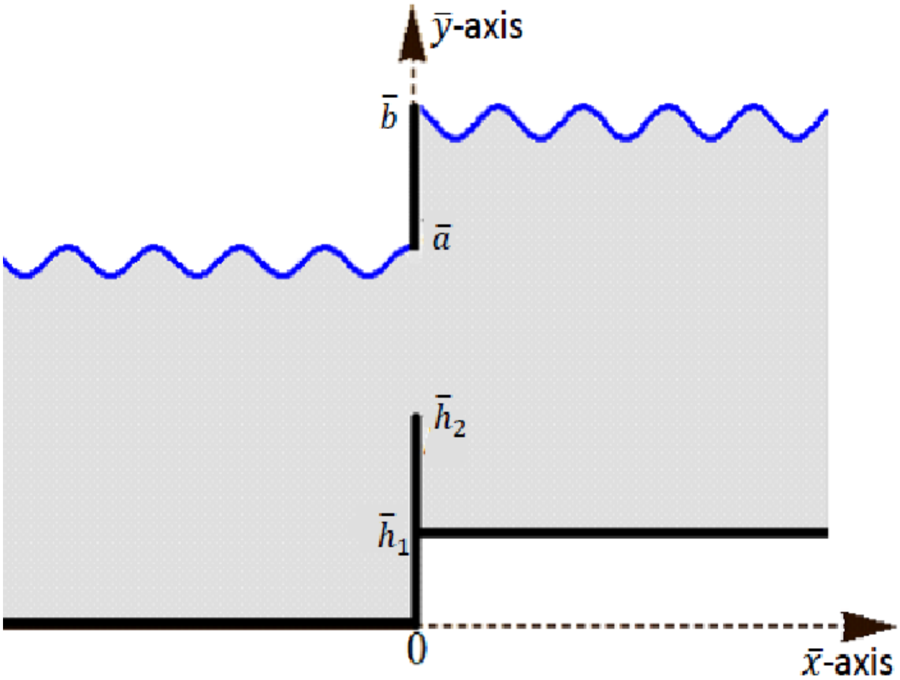

FIGURE 3.10: The physical configuration of the waveguide.

wave number, that is

$$\left(\nabla^2 + 1\right) \phi(x, y) = 0. \tag{3.36}$$

For the convenience the time independent fluid potential $\phi(x, y)$ for two duct region is expressed in terms of two different scattered fields as

$$\phi(x, y) = \begin{cases} \phi_1(x, y), & x \leq 0, \quad 0 \leq y \leq a, \\ \phi_2(x, y), & x \geq 0, \quad h_1 \leq y \leq b. \end{cases} \tag{3.37}$$

The rigid horizontal lower boundaries are defined as

$$\frac{\partial \phi_1(x, 0)}{\partial y} = 0, \quad \frac{\partial \phi_2(x, h_1)}{\partial y} = 0, \qquad x \in \mathbb{R}, \tag{3.38}$$

whilst the upper surfaces with flexible boundaries are defined by the following equation

$$\left(\frac{\partial^4}{\partial x^4} - \mu_1^4\right) \frac{\partial \phi_j}{\partial y} - \alpha_1 \phi_j = 0, \tag{3.39}$$

where for $j = 1$ and $j = 2$ the condition is applied at $y = a,\ x < 0$ and $y = b,\ x > 0$, respectively. Here the non-dimensional parameters μ_1 is in *vacuo* plate wavenumber and α_1 a fluid loading parameter defined by

$$\mu_1 = \sqrt[4]{\frac{12(1 - \upsilon^2)c^2 \rho_p}{h^2 k^2 E}} \qquad \text{and} \qquad \alpha_1 = \frac{12(1 - \upsilon^2)c^2 \rho}{h^3 k^3 E}, \tag{3.40}$$

where E is Young's modulus, ρ_p is the density of the plate and ν is Poisson's ratio. At $x = 0^-$, the rigid vertical flanged-strip is given by

$$\frac{\partial \phi_1}{\partial x} = 0, \qquad 0 < y < h_2, \tag{3.41}$$

whereas, at $x = 0^+$ the soft back of strip is defined as

$$\phi_2 = 0, \qquad y \in (h_1, h_2) \cup (a, b). \tag{3.42}$$

At the aperture $x = 0$, $h_2 < y < a$, the fluid pressure and normal component of velocities are continuous, that is

$$\phi_{1x}(0,y) = \begin{cases} 0, & 0 \le y \le h_1, \\ \phi_{2x}(0,y), & h_2 \le y \le a \end{cases} \tag{3.43}$$

and

$$\phi_2(0,y) = \begin{cases} 0, & h_1 \le y \le h_2, \\ \phi_1(0,y), & h_2 \le y \le a, \\ 0, & a \le y \le b. \end{cases} \tag{3.44}$$

It is well-studied concept that the mathematical model for structures involving flexible boundaries is no more well-posed unless some extra conditions are imposed to make it well-posed. The choice of these conditions depend on the order of flexible boundary, that is, the number of extra conditions is the half of the order of boundary condition [43]. Moreover these conditions are termed as "edge conditions" which ensure that how the flexible boundaries are connected vertically. Here, we will discuss the solution for three set of edge conditions; i) clamped edge conditions, ii) pin-jointed edge conditions and iii) pivoted edge conditions.

- **Acquisition of Solution**

It is well established that there exist many physical situations that can be modelled in terms of waveguides with higher order surfaces [56–59]. The mathematical models for waveguide structures having plannar boundaries are solvable using the standard WH technique. In such cases the eigensystem appeared to be SL and therefore separation of variables yields the simplest form of eigenfunction expansions that are orthogonal and linearly independent. However, for waveguide structures having geometric discontinuity (abrupt change in height) and comprising of higher order boundaries can be solved using MM approach. In such situations the eigensystem is non SL, obtained eigenfunctions are linearly dependent that do not satisfy the usual OR. In this way the appropriate orthogonality relations are developed by which the Fourier coefficients of eigenfunction expansions can explicitly be expressed in terms of known boundary data. Few extra conditions such as edge conditions are also used to ensure the uniqueness of the MM solution. The choice of these extra conditions certainly affects the scattered field thereby incorporating the physical behavior of scattering process. The detail study of edge condition is referred for instance to [70, 71, 99]. With this, the solution to the above stated problem can be achieved while taking the following footsteps; I) to obtain the eigenfunction expansion of duct modes; II) to obtain the related dispersion relations and appropriate orthogonality relations, III) to apply mode-matching at vertical interface and, IV) the implication of appropriate edge conditions.

3.2.1 Eigenfunction Expansion

Consider an incident wave of harmonic time dependence propagating from negative $x-axis$ towards $x=0$. The incident wave is considered with an arbitrary duct mode. At $x=0$ it will scatter into an infinite number of reflected and transmitted modes. In order to find the eigenfunction expansion in respective duct region (3.37), we use (3.36) along with (3.37), (3.38), (3.39), by using the usual process of separation of variables, the eigenfunction expansion of these scattered duct modes are given by

$$\phi_1(x,y)=F_\ell Y_{1\ell}(\gamma_\ell,y)e^{i\eta_\ell x}+\sum_{n=0}^{\infty}A_nY_{1n}(\gamma_n,y)e^{-i\eta_n x} \tag{3.45}$$

and

$$\phi_2(x,y)=\sum_{n=0}^{\infty}B_nY_{2n}(\beta_n,y)e^{i\nu_n x}, \tag{3.46}$$

where $Y_{1n}(\gamma_n,y)=\cosh(\gamma_n y)$ and $Y_{2n}(\beta_n,y)=\cosh[\beta_n(y-h_1)]$. Moreover, the first term in above (3.45) denotes the incident field. The forcing $F_\ell=\sqrt{\alpha/E_\ell\eta_\ell}$ (where the quantity E_ℓ will be defined later) is chosen for algebraic convenience and to scale the incident power at unity as well. The counter ℓ is considered to incorporate two different incident duct modes, that is, $\ell=0$ for fundamental mode incident whereas $\ell=1$ for the secondary mode incident. The quantities $\eta_n=\sqrt{1+\gamma_n^2}$ and $\nu_n=\sqrt{1+\beta_n^2}$ are the wave numbers of n^{th} reflected and transmitted modes, respectively.

3.2.2 Dispersion and Orthogonality Relations

It can be seen that condition (3.39) contains even order derivative which ensures the even order of corresponding characteristic polynomial [103]. Therefore, the eigen values γ_n and β_n; $(n = 0, 1, 2...)$ of the duct eigenfunction satisfy the following dispersion relations (for detail, referred by Section. 2.7), that is

$$\{(\gamma_n^2 + 1)^2 - \mu_1^4\}\gamma_n \sinh(\gamma_n a) - \alpha_1 \cosh(\gamma_n a) = 0 \tag{3.47}$$

and

$$\{(\beta_n^2 + 1)^2 - \mu_1^4\}\beta_n \sinh[\beta_n(b - h_1)] - \alpha_1 \cosh[\beta_n(b - h_1)] = 0. \tag{3.48}$$

The equations (3.47)-(3.48) can be solved numerically for γ_n and β_n. For the problems in which waveguide comprises of walls with soft, rigid or impedance type, the separation of variable renders the solution in a simple way. Also the corresponding eigenfunctions satisfy the standard OR. Albeit, the governing system is SL in nature. But system will be no more SL if waveguide comprises of flexible boundaries. In such circumstances the eigenfunctions do not satisfy standard OR. Thus, for such systems we have to explore the related orthogonal properties. The problem considered herein contain elastic plate bounded duct for $x \in (-\infty, 0) \cup (0, \infty)$ in which the eigenfunctions satisfy the generalized form of ORs for inlet and outlet duct regions (for detail, referred by Section. 2.7), that is

$$\begin{aligned} &\alpha_1 \int_0^a Y_1(\gamma_n, y)Y_1(\gamma_m, y)dy \\ &= E_n\delta_{mn} - (\gamma_m^2 + \gamma_n^2 + 2)Y_1^{'}(\gamma_m, a)Y_1^{'}(\gamma_n, a) \end{aligned} \tag{3.49}$$

and

$$\begin{aligned} &\alpha_1 \int_{h_1}^b Y_2(\beta_n, y)Y_2(\beta_m, y)dy \\ &= G_n\delta_{mn} - (\beta_m^2 + \beta_n^2 + 2)Y_2^{'}(\beta_m, (b - h_1))Y_2^{'}(\beta_n, (b - h_1)), \end{aligned} \tag{3.50}$$

respectively, where

$$E_m = \frac{\alpha_1 a}{2} + \frac{\alpha_1 Y_1(\gamma_m, a) Y_{1m}^{'}(\gamma_m, a)}{2\gamma_m^2} + 2[(\gamma_m^2 + 1) Y_1^{'}(\gamma_m, a)]^2 \tag{3.51}$$

and

$$\begin{aligned} G_m = \frac{\alpha_1(b-h_1)}{2} &+ \frac{\alpha_1 Y_2(\beta_m, (b-h_1)) Y_2^{'}(\beta_m, (b-h_1))}{2\beta_m^2} \\ &+2[(\beta_m^2 + 1) Y_2^{'}(\beta_m, (b-h_1))]^2. \end{aligned} \tag{3.52}$$

It is important to note that the eigenfunctions corresponding to the eigenvalues γ_n or β_n, $n = 0, 1, 2, ...$ are linearly dependent but contain well defined orthogonal properties for elastic plate bounded ducts. Having obtained well defined orthogonal properties, the scattered modes coefficients, (A_n, B_n) can be found by using the continuity conditions of pressure and normal velocity at matching interface along with appropriate edge conditions. This process is illustrated in the subsequent section.

3.2.3 Mode-Matching Solution

We opt MM across the interface to find the solution of above boundary value problem. In order to find the expression of reflected amplitudes, we use (3.45)-(3.46) into (3.43), it is straight forward to obtain

$$\begin{aligned} &F_\ell \eta_\ell Y_{1\ell}(\gamma_\ell, y) - \sum_{n=0}^{\infty} A_n \eta_n Y_{1n}(\gamma_n, y) \\ &= \begin{cases} 0, & 0 \le y \le h_2, \\ \sum_{n=0}^{\infty} B_n \nu_n Y_{2n}(\beta_n, y), & h_2 \le y \le b. \end{cases} \end{aligned} \tag{3.53}$$

On multiplying with $\alpha_1 Y_{1m}(\gamma_n, y)$, integrating from 0 to a and then using OR (3.49), we get the expression of reflected amplitudes, that is

$$A_m = F_\ell \delta_{m\ell} - \frac{Y_{1m}^{'}(\gamma_m, a)}{\eta_m E_m}\{e_1 + (\gamma_m^2 + 2)e_2\} - \frac{\alpha_1}{\eta_m E_m} \sum_{n=0}^{\infty} B_n \nu_n R_{mn}, \tag{3.54}$$

where

$$e_1 = -i\ \phi_{1xyyy}(0,a), \tag{3.55}$$

$$e_2 = -i\ \phi_{1xy}(0,a) \tag{3.56}$$

and

$$R_{mn} = \int_{h_2}^{a} Y_{1m}(\gamma_m, y) Y_{2n}(\beta_n, y) dy. \tag{3.57}$$

Similarly, we obtain the expression of transmitted amplitudes by substituting (3.45)-(3.46) into (3.44) along with appropriate orthogonality relation (3.50), that is

$$B_m = \frac{Y_{2m}^{'}(\beta_m, (b-h_1))}{G_m}\{e_3 + (\gamma_m^2 + 2)e_4\} + \frac{\alpha_1}{G_m}\{F_\ell R_{\ell m} + \sum_{n=0}^{\infty} B_n R_{nm}\}, \tag{3.58}$$

where

$$e_3 = \ \phi_{2yyy}(0,b) \tag{3.59}$$

and

$$e_4 = \ \phi_{2y}(0,b). \tag{3.60}$$

Here $e_1 - e_4$ are arbitrary constants that can be determined by using the edge conditions. Three sets of edge condition are considered here which we discuss in following cases.

3.2.4 Use of Edge Conditions

As in case of higher order field equation and boundary conditions, the ORs are likely to be non simple then there is inevitably a question of how to impose the corner conditions at the junction of discontinuity. Thus, the development of appropriate OR is not sufficient without a practical and convenient approach of imposing the edge conditions. In order to incorporate the clamped, pin-jointed and pivoted types of edge conditions, a simple procedure is demonstrated.

- **Clamped Edges:** For edges to be clamped, the elastic plate displacement and gradient are assumed as zero, that is,

$$\phi_{1y}(0,a)=0, \tag{3.61}$$

$$\phi_{1xy}(0,a)=0, \tag{3.62}$$

$$\phi_{2y}(0,b)=0, \tag{3.63}$$

$$\phi_{2xy}(0,b)=0. \tag{3.64}$$

From (3.62)-(3.63), it is directly to get $e_2=e_4=0$. Moreover, to determine e_1 we multiply (3.54) by $Y_{1m}^{'}(\gamma_m,a)$, taking sum over m upto ∞ and then use the edge condition (3.61), we obtain

$$e_1=\frac{2F_\ell Y_{1\ell}^{'}(\gamma_\ell,a)}{S_1}-\frac{\alpha_1}{S_1}\sum_{m=0}^{\infty}\sum_{n=0}^{\infty}\frac{B_n\nu_nR_{mn}Y_{1m}^{'}(\gamma_m,a)}{\eta_mE_m}, \tag{3.65}$$

where

$$S_1=\sum_{m=0}^{\infty}\frac{[Y_{1m}^{'}(\gamma_m,a)]^2}{\eta_mE_m}.$$

Likewise, to calculate e_3 we multiply (3.58) by $Y_{2m}^{'}(\beta_m,(b-h_1))$, taking sum over m upto ∞ and after using the edge condition (3.64), we found

$$e_3=-\frac{\alpha_1}{S_2}\sum_{m=0}^{\infty}\frac{\nu_mY_{2m}^{'}(\beta_m,(b-h_1))}{G_m}\{F_\ell R_{\ell m}+\sum_{n=0}^{\infty}B_nR_{nm}\}, \tag{3.66}$$

where

$$S_2=\sum_{m=0}^{\infty}\frac{\nu_m[Y_{2m}^{'}(\beta_m,(b-h_1))]^2}{G_m}.$$

Hence, we obtained the arbitrary constants e_1-e_4 for clamped edge conditions. In next, these arbitrary constant are also found for pin-jointed and pivoted edge conditions.

- **Pin-Jointed Edges:** In this condition we assume the zero displacement and the zero bending moment at the elastic plate edges, that is

$$\phi_{1y}(0,a) = 0, \tag{3.67}$$

$$\phi_{1xxy}(0,a) = 0, \tag{3.68}$$

$$\phi_{2y}(0,b) = 0, \tag{3.69}$$

$$\phi_{2xxy}(0,b) = 0. \tag{3.70}$$

Now on using the reflected mode coefficient (3.54) into (3.45), differentiating with respect to y and after utilizing the edge condition (3.67), we obtain

$$e_1S_1 + e_2S_3 = 2F_\ell Y_{1\ell}'(\gamma_\ell, a) - \alpha_1 \sum_{m=0}^{\infty}\sum_{n=0}^{\infty} \frac{B_n\nu_n R_{mn} Y_{1m}'(\gamma_m, a)}{\eta_m E_m}, \tag{3.71}$$

where

$$S_3 = \sum_{m=0}^{\infty} \frac{(\gamma_m^2+2)[Y_{1m}'(\gamma_m,a)]^2}{\eta_m E_m}.$$

In the similar fashion, the application of edge condition (3.68), yields

$$e_1S_4 + e_2S_5 = 2F_\ell \eta_\ell^2 Y_{1\ell}'(\gamma_\ell, a) - \alpha_1 \sum_{m=0}^{\infty}\sum_{n=0}^{\infty} \frac{B_n\nu_n \eta_n R_{mn} Y_{1m}'(\gamma_m, a)}{E_m}, \tag{3.72}$$

where

$$S_4 = \sum_{m=0}^{\infty} \frac{\eta_m[Y_{1m}'(\gamma_m,a)]^2}{E_m}$$

and

$$S_5 = \sum_{m=0}^{\infty} \frac{\eta_m(\gamma_m^2+2)[Y_{1m}'(\gamma_m,a)]^2}{E_m}.$$

The equation (3.69) directly yields to $e_4 = 0$, while the value of e_3 is found by multiplying (3.58) with $Y_{2m}'(\beta_m,(b-h_1))$, taking sum over m upto ∞ then imposing the edge condition (3.70), that is

$$e_3 = -\alpha_1 \sum_{m=0}^{\infty} \frac{\nu_m^2 Y_{2m}'(\beta_m,(b-h_1))}{G_m}\{F_\ell R_{\ell m} + \sum_{n=0}^{\infty} B_n R_{nm}\}. \tag{3.73}$$

Thus, to make sure the smooth convergence of summations in (3.73), we apply the Green's identities (2.90). For sake of this, the integral of R_{nm} is splitted as

$$\begin{aligned} R_{nm} = &\int_{h_1}^{b} Y_{1n}(\gamma_n, y)Y_{2m}(\beta_m, y)dy \\ &-\int_{h_1}^{h_2} Y_{1n}(\gamma_n, y)Y_{2m}(\beta_m, y)dy \\ &-\int_{a}^{b} Y_{1n}(\gamma_n, y)Y_{2m}(\beta_m, y)dy. \end{aligned} \tag{3.74}$$

On using the above value in (3.73), we arrive

$$\begin{aligned} e_3 = &-\alpha_1 F_\ell \sum_{m=0}^{\infty} \frac{\nu_m^2 Y_{2m}'(\beta_m,(b-h_1))}{G_m}\{\int_{h_1}^{b} Y_{1\ell}(\gamma_\ell, y)Y_{2m}(\beta_m, y)dy - T_{\ell m}\} \\ &-\alpha_1 \sum_{m=0}^{\infty}\sum_{n=0}^{\infty} \frac{B_n\nu_m^2 Y_{2m}'(\beta_m,(b-h_1))}{G_m}\int_{h_1}^{b} Y_{1n}(\gamma_n, y)Y_{2m}(\beta_m, y)dy \\ &+\alpha_1 \sum_{m=0}^{\infty}\sum_{n=0}^{\infty} \frac{B_n\nu_m^2 Y_{2m}'(\beta_m,(b-h_1))T_{nm}}{G_m}, \end{aligned} \tag{3.75}$$

where

$$T_{nm} = \int_{h_1}^{h_2} Y_{1n}(\gamma_n, y)Y_{2m}(\beta_m, y)dy + \int_{a}^{b} Y_{1n}(\gamma_n, y)Y_{2m}(\beta_m, y)dy.$$

Since, the application of Green's identities (2.90) in the domain $h_1 \leq y \leq b$, reveals

$$-\alpha_1 F_\ell \sum_{m=0}^{\infty} \frac{\nu_m^2 Y_{2m}'(\beta_m,(b-h_1))}{G_m}\int_{h_1}^{b} Y_{1\ell}(\gamma_\ell, y)Y_{2m}(\beta_m, y)dy = 0, \tag{3.76}$$

$$-\alpha_1 \sum_{m=0}^{\infty}\sum_{n=0}^{\infty} \frac{B_n\nu_m^2 Y_{2m}'(\beta_m,(b-h_1))}{G_m}\int_{h_1}^{b} Y_{1n}(\gamma_n, y)Y_{2m}(\beta_m, y)dy = 0. \tag{3.77}$$

On manipulating the values of (3.76)-(3.77) in the equation (3.75), we finally concludes to

$$e_3 = \alpha_1 \sum_{m=0}^{\infty} \frac{\nu_m^2 Y_{2m}'(\beta_m,(b-h_1))}{G_m}\{F_\ell T_{\ell m} + \sum_{n=0}^{\infty} B_n T_{nm}\}. \tag{3.78}$$

Now, we elaborate the pivoted type of edge condition for elastic plate.

- **Pivoted Edges:** The pivoted edge conditions are usually feasible only when $a = b$. These can be defined as

$$\phi_{jy}(0,b) = 0, \quad j = 1,2. \tag{3.79}$$

$$\phi_{1xy}(0,b) = \phi_{2yx}(0,b), \tag{3.80}$$

$$\phi_{1xxy}(0,b) = \phi_{2yxx}(0,b). \tag{3.81}$$

The above conditions can be used to calculate the values of constants $e_1 - e_4$. For that we reconstruct the scattered field potentials (3.45)-(3.46) on using(3.54) and (3.58). Now by using the edge conditions (3.79), it is straightforward to write $e_4 = 0$ and

$$e_1 S_1 + e_2 S_3 = 2F_\ell Y_{1\ell}'(\gamma_\ell, a) - \alpha_1 \sum_{m=0}^{\infty}\sum_{n=0}^{\infty} \frac{B_n \nu_n R_{mn} Y_{1m}'(\gamma_m, a)}{\eta_m E_m}. \tag{3.82}$$

However, the simplification of (3.80) by using the Green's identities (2.90) yields to

$$e_2 - e_3 S_2 = \alpha_1 \sum_{m=0}^{\infty}\sum_{n=0}^{\infty} \frac{B_n \nu_m Y_{1m}'(\gamma_m, b) Q_{mn}}{G_m}$$

$$+ \alpha_1 \sum_{m=0}^{\infty} \frac{\nu_m Y_{2m}'(\beta_m, (b-h_1))}{G_m} \{F_\ell R_{\ell m} + \sum_{n=0}^{\infty} B_n R_{nm}\}, \tag{3.83}$$

where

$$Q_{nm} = \int_0^{h_2} Y_{1n}(\gamma_n, y) Y_{2m}(\beta_m, y) dy. \tag{3.84}$$

Moreover, the equation (3.81) can be also simplified with constructing the Green's function which can be written as

$$e_1 S_4 + e_2 S_5 + e_3 = 2F_\ell \eta_\ell^2 Y_{1\ell}'(\gamma_\ell, a) - \alpha_1 \sum_{m=0}^{\infty}\sum_{n=0}^{\infty} \frac{B_n \nu_n \eta_n R_{mn} Y_{1m}'(\gamma_m, a)}{E_m}$$

$$+ \alpha_1 \sum_{m=0}^{\infty} \frac{\nu_m^2 Y_{2m}'(\beta_m, (b-h_1))}{G_m} \{F_\ell P_{\ell m} + \sum_{n=0}^{\infty} B_n P_{nm}\}, \tag{3.85}$$

where

$$P_{nm} = \int_{h_1}^{h_2} Y_{1n}(\gamma_n, y) Y_{2m}(\beta_m, y) dy. \tag{3.86}$$

Hence, we found arbitrary constants $e_1 - e_4$ for different sets of edge conditions. So, we have two infinite systems of algebraic equations defined by (3.54) and (3.58). These are truncated and solved numerically for each sets of edge conditions to determine the unknown amplitudes.

The truncated solution can be used to check the accuracy of presented algebra and distribution of energy flux. This not only validate the proposed solution but also provide a useful physical information about the boundary value problem. So, expression for energy flux is derived in next subsection.

3.2.5 Expression for Energy Flux and Power Balance

The expressions of energy flux for flexible waveguide bounded by elastic plates are determined in this section. In order to obtain the incident power through fluid ($P_i\rfloor_{\text{fluid}}$), we manipulate the incident field

$$\phi_{inc}(x, y) = F_\ell Y_{1\ell}(\gamma_\ell, y) e^{i\eta_\ell x}, \tag{3.87}$$

in (2.94), thus we have

$$P_i\rfloor_{\text{fluid}} = \text{Re}\left[\frac{1}{\alpha_1} F_\ell F_\ell^* \eta_\ell^* e^{i(\eta_\ell - \eta_\ell^*)x} \int_0^a Y_{1\ell}(\gamma_\ell, y) Y_{1\ell}(\gamma_\ell, y) dy\right]. \tag{3.88}$$

Since $F_\ell = \sqrt{\alpha_1/\eta_\ell G_\ell}$ and using OR (2.89) for $m = n = \ell$, after simplification, the incident power through fluid becomes

$$P_i\rfloor_{\text{fluid}} = \text{Re}\left[1 - \frac{1}{\alpha_1} F_\ell^2 \eta_\ell [Y_{1\ell}'(\gamma, a)]^2\right]. \tag{3.89}$$

In a similar way, we determine the incident power through plate ($P_i\rfloor_{plate}$) by substituting (3.87) into (2.96) and after simplification, the incident power traveling along the plate yields

$$P_i\rfloor_{\text{plate}} = \text{Re}\left[\frac{1}{\alpha_1}F_\ell^2\eta_\ell[Y_{1\ell}^{'}(\gamma,a)]^2\right]. \tag{3.90}$$

Consequently,

$$P_i\rfloor_{\text{fluid}} + P_i\rfloor_{\text{plate}} = 1. \tag{3.91}$$

Also, to find the reflected power through fluid ($P_r\rfloor_{\text{fluid}}$), the reflected field in the inlet duct region is represented as

$$\phi_{ref}(x,y) = \sum_{n=0}^{\infty} A_n Y_{1n}(\gamma_n,y)e^{-i\eta_n x}. \tag{3.92}$$

On substituting (3.92) into (2.94), the reflected power through fluid can be written as

$$P_r\rfloor_{\text{fluid}} = \text{Re}\left[\frac{1}{\alpha_1}\sum_{n=0}^{\infty}\sum_{m=0}^{\infty} A_n A_m^* \eta_m^* e^{-i(\eta_n-\eta_m^*)x}\int_0^a Y_{1n}(\gamma_n,y)Y_{1m}(\gamma_m,y)dy\right]. \tag{3.93}$$

On using OR (2.89) into (3.93), we get

$$P_r\rfloor_{\text{fluid}} = \text{Re}\left[\frac{1}{\alpha_1}\sum_{n=0}^{\infty} \mid A_n\mid^2 G_n\eta_n - \frac{1}{\alpha_1}\sum_{n=0}^{\infty}\mid A_n\mid^2 \eta_n[Y_{1n}^{'}(\gamma_n,a)]^2\right]. \tag{3.94}$$

As well as, the reflected field potential (3.92) along with (2.96) yields the reflected power through plate, that is

$$P_r\rfloor_{\text{plate}} = \text{Re}\left[\frac{1}{\alpha_1}\sum_{n=0}^{\infty}\mid A_n\mid^2 \eta_n[Y_{1n}^{'}(\gamma_n,a)]^2\right]. \tag{3.95}$$

As, the total reflected power is

$$P_r = P_r\rfloor_{\text{fluid}} + P_r\rfloor_{\text{plate}}. \tag{3.96}$$

Since, we acquire

$$P_r = \text{Re}\left[\frac{1}{\alpha_1}\sum_{n=0}^{\infty}\mid A_n\mid^2 \eta_n G_n\right]. \tag{3.97}$$

Similarly, we express the transmitted power for outlet duct section as

$$P_t = \mathrm{Re}\left[\frac{1}{\alpha_1}\sum_{n=0}^{\infty} \mid B_n \mid^2 \nu_n G_n\right]. \tag{3.98}$$

3.2.6 Numerical Results and Discussion

In this section, the obtained solution is truncated first, and then solved numerically for each set of edge conditions. In each case the non-SL system is suitably convergent [34, 36]. Thus we truncate (3.54) and (3.58) together with $e_1 - e_4$ upto $m = 0, 1, ...N - 1$ and then solve the retained system simultaneously. The reflected power and transmitted power in duct regions [36] are expressed in (3.97) and (3.98), respectively, which certifies the conserved power identity, that is

$$P_r + P_t = 1. \tag{3.99}$$

While carrying the numerical computation the elastic plate is chosen of aluminum, of thickness $\bar{h} = 0,0006m$ and density $\rho_p = 2700kgm^{-3}$; whereas, values of Young's modulus and Poisson's ratio are taken to be $E = 7.28 \times 10^10Nm^{-2}$ and $\upsilon = 0.34$. For each case considered here the speed of sound in air $c = 343ms^{-1}$ and density of air $\rho = 1.2043kgm^{-3}$ are taken from Kaye and Laby [104], whereas, the duct heights are fixed at $\bar{a} = 0.06m$ and $\bar{b} = 0.085m$. Now we can discuss the distribution of scattering power against frequency with different set of edge conditions. On taking $\ell = 0$ and $\ell = 1$ the fundamental (structure-borne) and secondary (fluid-borne) mode, respectively, can be used as an incident field. For the clamped set of edge conditions, reflected power (P_r), transmitted power (P_t) and their sum (P_r+P_t) against frequency (Hz) are shown in Figs. 3.11-3.14. These clearly follow that for structure-borne mode incident maximum of the power goes on reflection with and without flanged junction (solid curves in Figs. 3.11 & 3.13). On the other hand, for the fluid-borne mode incident which cuts-on at $f = 191Hz$, the transmitted power increases in the absence of flanged junction (dashed curves in Figs. 3.12 & 3.14). However, the sum of the reflected and transmitted powers (dotted lines) is unity that successfully testifies the conserve power identity (3.99).

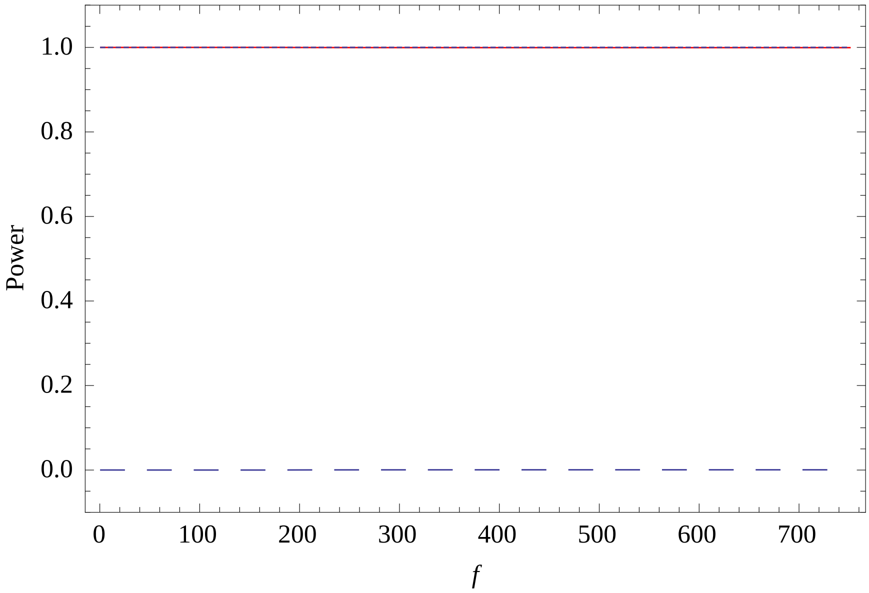

FIGURE 3.11: For structure-borne mode ($\ell = 0$), the P_r (solid), P_t (dashed) and the law (3.99) of power balance (dotted) are shown against frequency with flange.

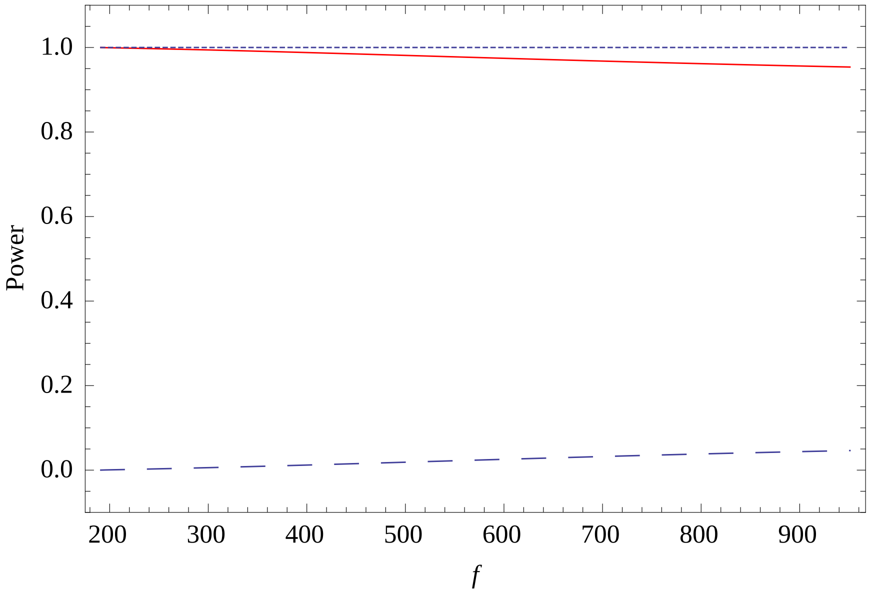

FIGURE 3.12: For fluid-borne mode ($\ell = 1$), the P_r (solid), P_t (dashed) and the law (3.99) of power balance (dotted) are shown against frequency with flange.

For Figs. 3.15-3.18 the power components are plotted for the pin-jointed set of edge conditions. The power propagation behavior for this set of edge conditions is most similar as the clamped set of edge conditions.

Figs. 3.19-3.22 depict the power propagation against frequency with pivoted set of edge conditions. For the structure-borne mode incident and in the presence

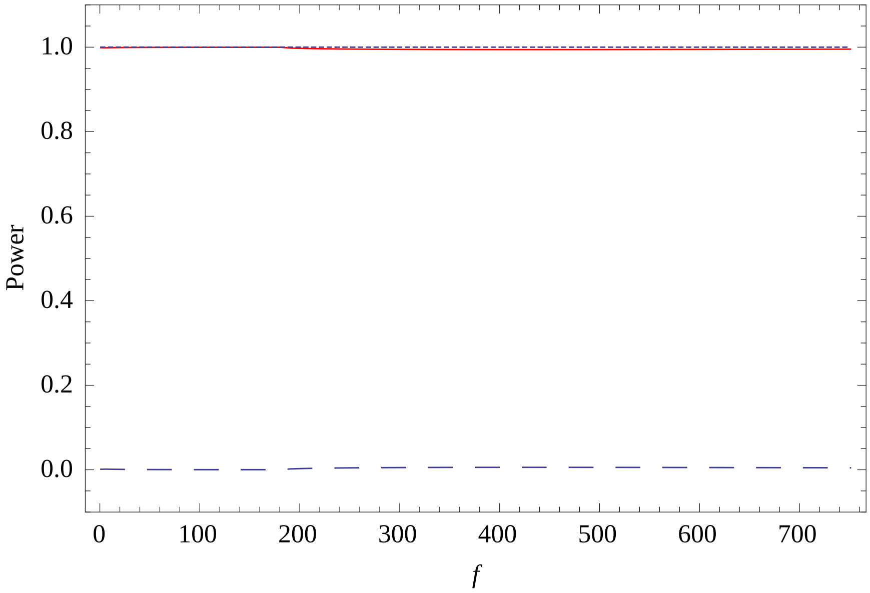

FIGURE 3.13: For structure-borne mode ($\ell = 0$), the P_r (solid), P_t (dashed) and the law (3.99) of power balance (dotted) are shown against frequency without flange.

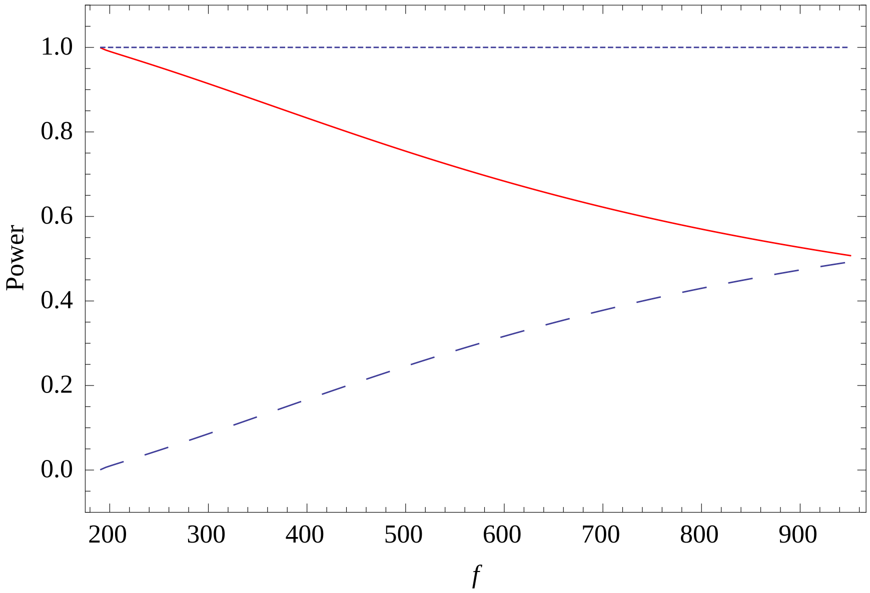

FIGURE 3.14: For fluid-borne mode ($\ell = 1$), the P_r (solid), P_t (dashed) and the law (3.99) of power balance (dotted) are shown against frequency without flange.

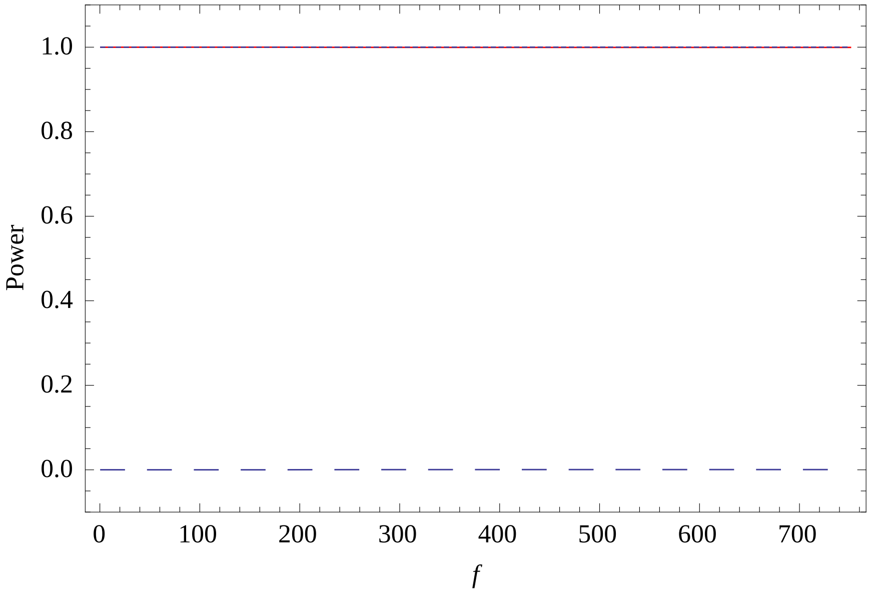

FIGURE 3.15: For structure-borne mode ($\ell = 0$), the P_r (solid), P_t (dashed) and the law (3.99) of power balance (dotted) are shown against frequency with flange.

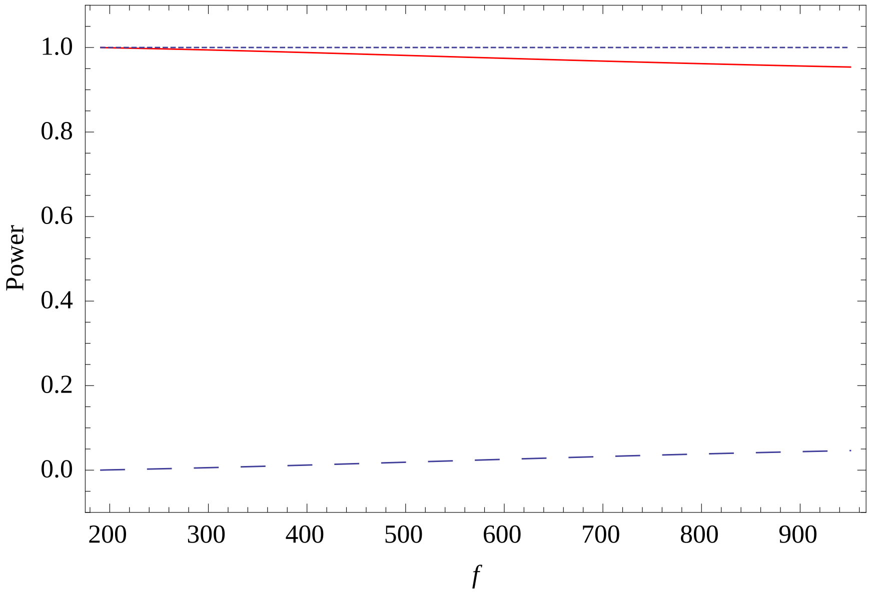

FIGURE 3.16: For fluid-borne mode ($\ell = 1$), the P_r (solid), P_t (dashed) and the law (3.99) of power balance (dotted) are shown against frequency with flange.

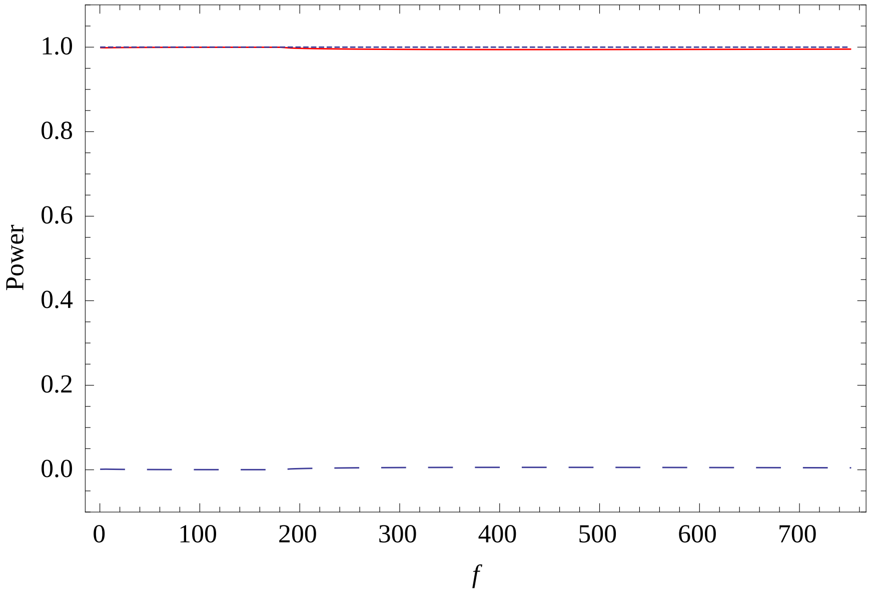

FIGURE 3.17: For structure-borne mode ($\ell = 0$), the P_r (solid), P_t (dashed) and the law (3.99) of power balance (dotted) are shown against frequency without flange.

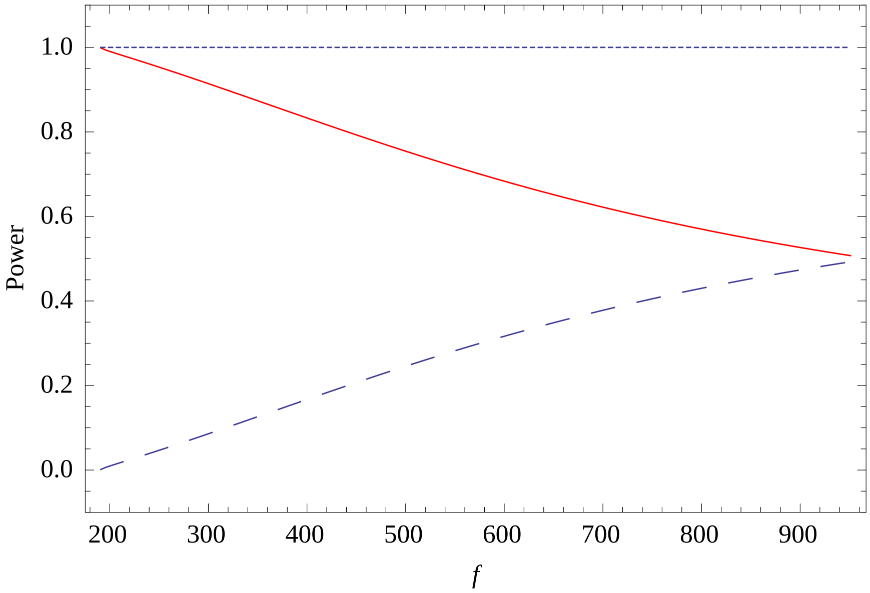

FIGURE 3.18: For fluid-borne mode ($\ell = 1$), the P_r (solid), P_t (dashed) and the law (3.99) of power balance (dotted) are shown against frequency without flange.

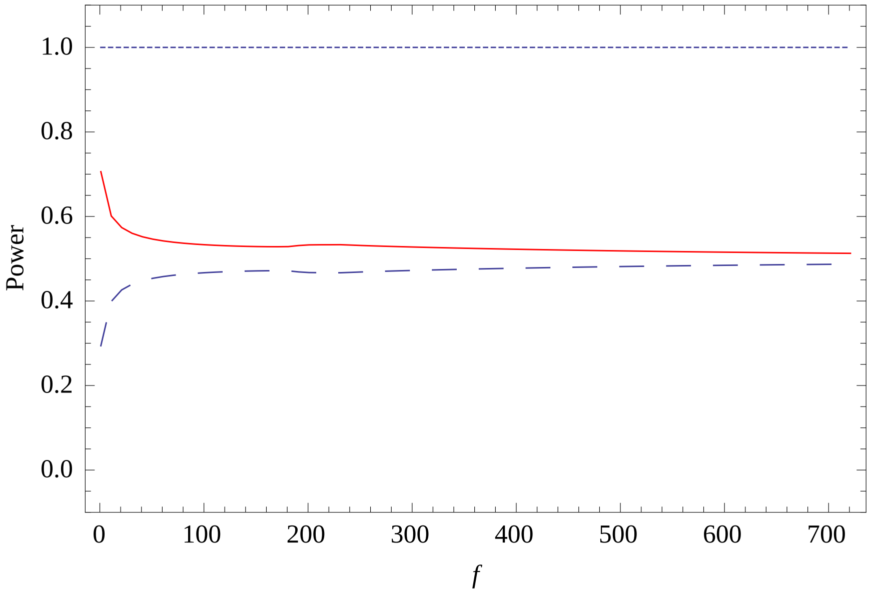

FIGURE 3.19: For structure-borne mode ($\ell = 0$), the P_r (solid), P_t (dashed) and the law (3.99) of power balance (dotted) are shown against frequency with flange.

of flanged junction, the reflected and transmitted powers tend to have identical power scattering in two duct regions over the variation of frequency (see Fig. 3.19). However, for the fluid-borne mode incident the reflected power decreases from the maximum to 80% as frequency varies from 191Hz to 953Hz (see Fig. 3.20). But, in the absence of flange, the power propagation behavior is quite different (see Figs. 3.21 & 3.22). As for the case of structure-borne mode incident with 1Hz $\leq f \leq$ 191Hz, the reflected power decreases steadily upto 70% of incident power and then goes on to maximum at cut-on frequency $f =$ 191Hz, but once it crosses the cut-on frequency the reflection decreases upto half of the total power. With this variation of frequency, the transmitted power behaves symmetrically in opposite direction but, of course, the sum of the reflected and transmitted power remains unity (see Fig. 3.21). On contrary for the fluid-borne mode incident the transmitted power increases from 20% to 80% with increasing values of frequency from 191Hz to 953Hz (see Fig. 3.22).

Now we reconstruct the continuity conditions at matching interface (3.43) and (3.44) by using the truncated solution. Figs. 3.23-3.26 show the real (Re) and imaginary (Im) parts of non-dimensional pressures and normal velocities at matching

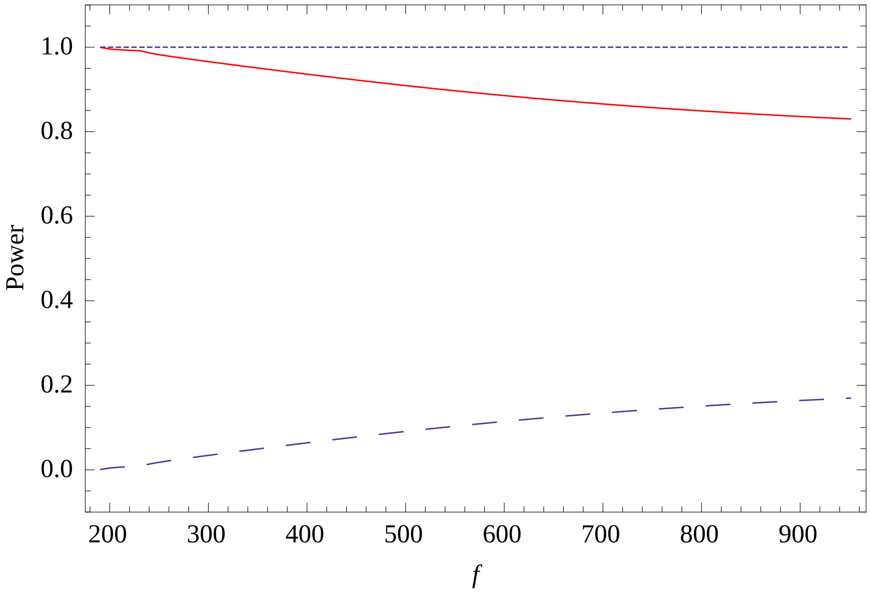

FIGURE 3.20: For fluid-borne mode ($\ell = 1$), the P_r (solid), P_t (dashed) and the law (3.99) of power balance (dotted) are shown against frequency with flange.

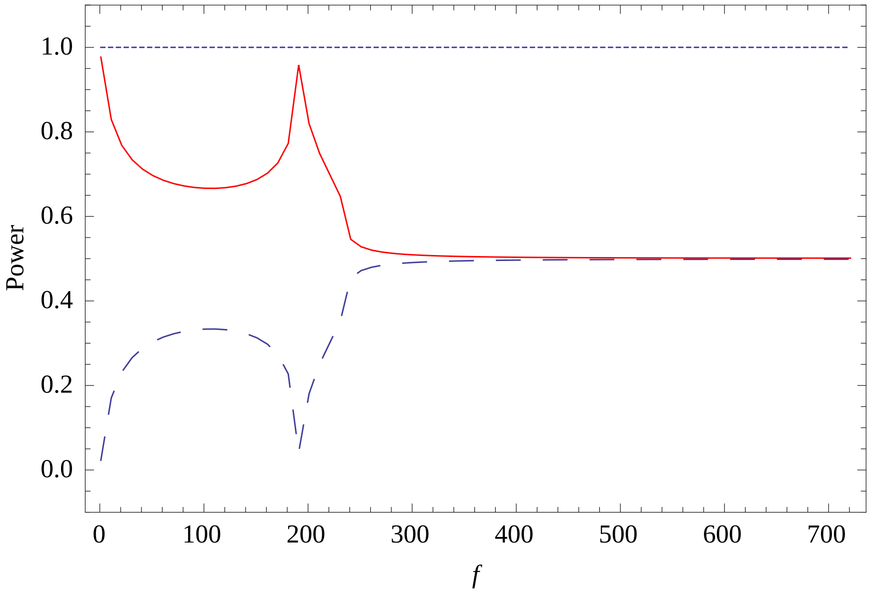

FIGURE 3.21: For structure-borne mode ($\ell = 0$), the P_r (solid), P_t (dashed) and the law (3.99) of power balance (dotted) are shown against frequency without flange.

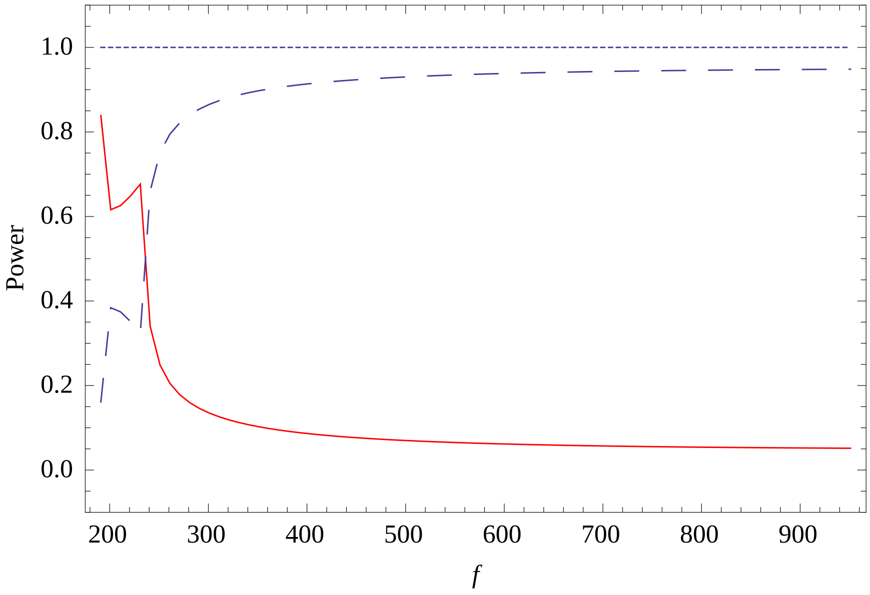

FIGURE 3.22: For fluid-borne mode ($\ell = 1$), the P_r (solid), P_t (dashed) and the law (3.99) of power balance (dotted) are shown against frequency without flange.

interface. From these figures it is evident that the pressures and normal velocities match exactly at $x = 0$, $h_2 \leq y \leq a$, whereas, real part of pressure, i.e, $\mathrm{Re}\{\phi_2(0, y)\} \to 0$ and imaginary part of pressure at $x = 0$, i.e, $\mathrm{Im}\{\phi_2(0, y)\} \to 0$, for $y \,\epsilon\, (h_1, h_2) \cup (a, b)$, (see Figs. 3.23 & 3.24) and similarly, $\mathrm{Re}\{\phi_{1x}(0, y)\} \to 0$ and $\mathrm{Im}\{\phi_{1x}(0, y)\} \to 0$, for $y \,\epsilon\, (0, h_1)$, (see Figs. 3.25 & 3.26). These are exactly the conditions given by equations (3.43) and (3.44).

In this chapter, we have studied the scattering analysis in two canonical problems by MM technique. The physical configuration of the first problem has been considered with rigid, soft and/or impedance type boundaries in the presence of upper and lower flanges at discontinuous junction. The resulted eigen-sub-system of modeled problem leads to SL category in which the standard OR is appropriate. The numerical experiments have been performed for different types of boundaries with or without flanges and significant effect in reflected and transmitted energies have been analyzed with and without flanges. In second problem, the scattering analysis has been studied through waveguide bounded by elastic plate in the presence of lower flange at discontinuity. The numerical analysis has been performed for clamped, pin-jointed and pivoted type of edge conditions for both fluid and structure borne mode incidents. The effect of scattering analysis has been observed same for both clamped and pin-jointed edge conditions for both structure and fluid borne mode incident, while reflected and transmitted energies have been observed inversely for the case of pivoted edge conditions.

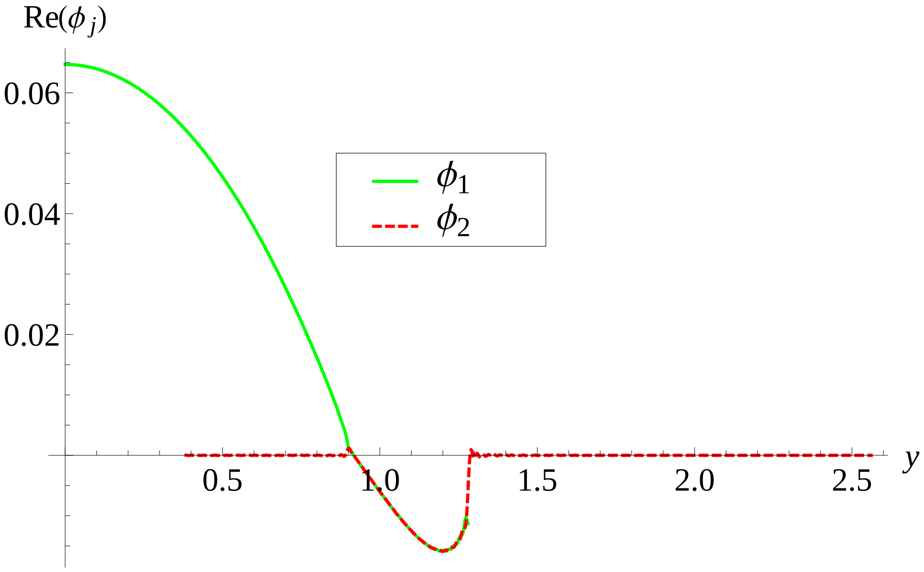

Figure 3.23: The real part of pressure vs. duct height at $x = 0$ in the presence of flanges, frequency 700Hz, and $N = 280$.

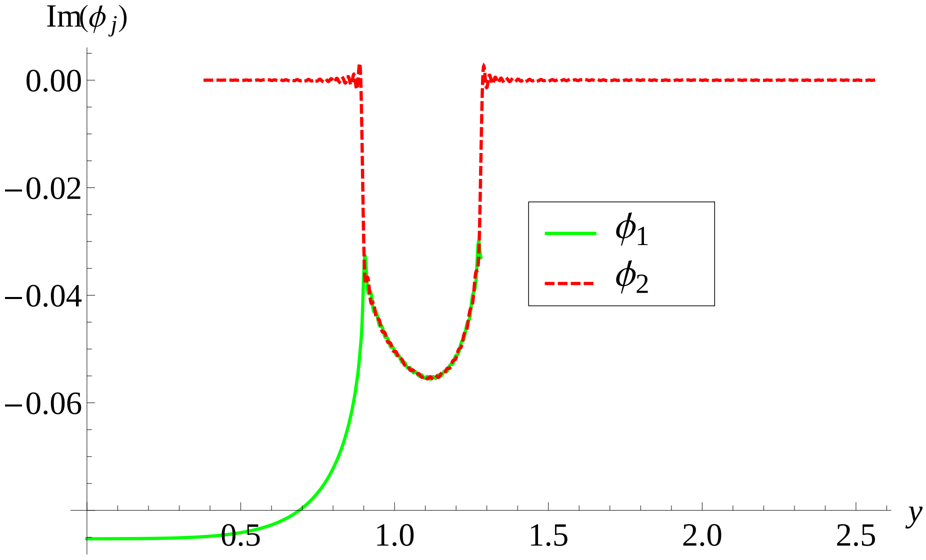

Figure 3.24: The imaginary part of pressure vs. duct height at $x = 0$ in the presence of flange, frequency 700Hz, and $N = 280$.

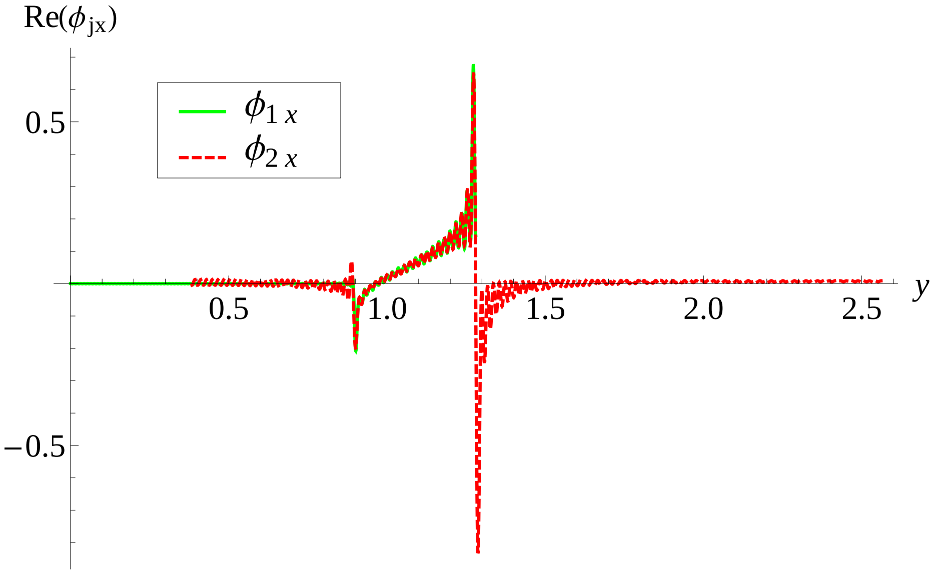

FIGURE 3.25: The real part of normal velocities vs. duct height at $x = 0$ in the presence of flange, frequency 700Hz, and $N = 280$.

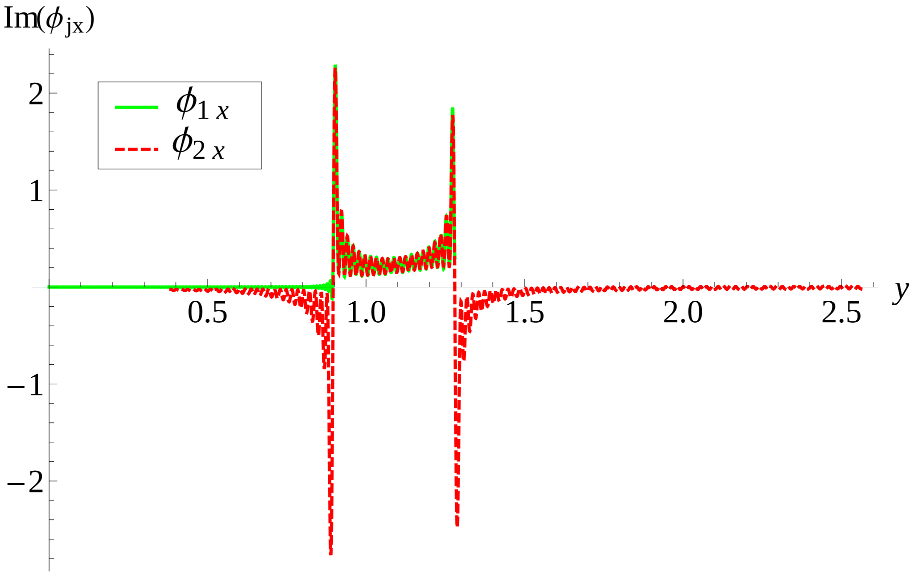

FIGURE 3.26: The imaginary part of normal velocities vs. duct height at $x = 0$ in the presence of flange, frequency 700Hz, and $N = 280$.

Chapter 4

Acoustic Analysis in Discontinuous Waveguide Bounded by Membranes

In this chapter, the attenuation of fluid-structure coupled modes of non-planar waveguide involving expansion chamber is analyzed. The physical problem is modeled to illustrate the scattering behavior of acoustic waves in a flexible waveguide composed of thin elastic membranes having edges or joints and structural discontinuities. The fluid-structure coupled waveforms scatter after interacting with the discontinuities and edges of the underlying structure. An appropriate choice of edges offers scattering or resonance processes, which also guide fluid-structure coupled waves. The MM technique together with LFA is used to determine velocity potentials. The guiding structure is then analyzed and validated through scattering energy or power functional by varying the dimensions of the expansion chamber and the wave frequency. The results are formulated and analyzed by tuning the device using an appropriate choice of edge conditions, dimension of expansion chamber, and wave frequencies, thereby validating the obtained solutions. These descriptions are very useful for the active control measure of structural vibrations.

This chapter is organized as follows: In Section. 4.1, the traveling waves forms for the duct modes together with appropriate orthogonality relations are illustrated. These are used in Section. 4.2, where the boundary value problem is solved using the MM technique. Section. 4.3 concerns the derivation of a LFA to the solution. In Section. 4.4, numerical results and discussions are provided.

4.1 Boundary Value Problem

This section provides the statement of the underlying waveguide problem configured in Fig. 4.1. The waveguide includes duct regions of different heights and comprises rigid boundaries along $\bar{y} = \bar{0}$, $\bar{a}$, $-\infty < \bar{x} < \infty$ and elastic membranes along $\bar{y} = \bar{b}$, $\bar{h}$, $-\infty < \bar{x} < \infty$. The duct regions are mutually joined at interfaces $\bar{x} = \pm\bar{L}$ by means of four rigid vertical surfaces lying along $\bar{0} \leq \bar{y} \leq \bar{a}$ and $\bar{b} \leq \bar{y} \leq \bar{h}$. The inside of the waveguide is filled with the compressible fluid of density ρ and sound speed c whilst the outside of it is set into *vacuo*. The boundary value problem (BVP) is formulated considering the structural and fluid-bornes modes which will propagate from negative x-direction towards $|\bar{x}| \leq \bar{L}$. Thus, the time independent dimensionless fluid potential ϕ satisfies the Helmholtz equation with unit wave number, that is

$$\left(\nabla^2 + 1\right) \phi(x, y) = 0. \tag{4.1}$$

The rigid and membranes boundaries in non-dimensional form are given by

$$\frac{\partial \phi(x,0)}{\partial y} = 0, \qquad \frac{\partial \phi(x,a)}{\partial y} = 0, \qquad -\infty < x < \infty, \tag{4.2}$$

$$\left(\frac{\partial^2}{\partial x^2} + \mu^2\right) \frac{\partial \phi(x,b)}{\partial y} + \alpha \phi(x,b) = 0 \qquad -\infty < x < \infty \tag{4.3}$$

and

$$\left(\frac{\partial^2}{\partial x^2}+\mu^2\right)\frac{\partial\phi(x,h)}{\partial y}+\alpha\phi(x,h)=0, \qquad -\infty<x<\infty, \tag{4.4}$$

respectively. Here, $\mu = c/c_m$ and $\alpha = \omega^2\rho/Tk^3$ represent the non-dimensional membrane wave number and the fluid loading parameter, respectively. Equations (4.1)-(4.4) yield the following eigenfunctions in respective waveguide regions

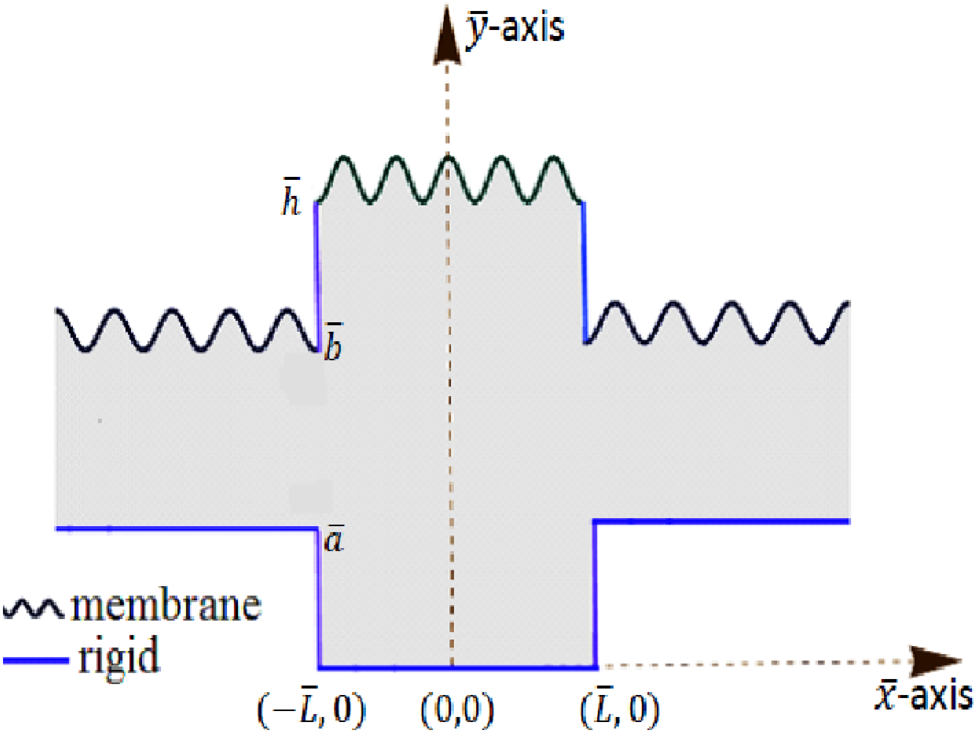

Figure 4.1: The physical configuration of the waveguide.

$$\begin{cases} Y_{1n}(y)=\cosh[\gamma_n(y-a)], & |x|>L, \quad a\le y\le b, \\ Y_{2n}(y)=\cosh(\beta_n y), & |x|<L, \quad 0\le y\le h, \end{cases} \tag{4.5}$$

where $Y_{1n}(y)$ and $Y_{2n}(y)$ represent the nth eigenfunctions in the inlet/outlet and expansion chamber of the waveguide, respectively. The corresponding eigenvalues (γ_n, β_n), $n = 0, 1, 2, ...,$ are the roots of the following characteristic equations

$$\begin{cases} \kappa_1(\gamma)=(\gamma^2+1-\mu^2)\gamma\sinh[\gamma(b-a)]-\alpha\cosh[\gamma(b-a)]=0, \\ \kappa_2(\beta)=(\beta^2+1-\mu^2)\beta\sinh(\beta h)-\alpha\cosh(\beta h)=0. \end{cases} \tag{4.6}$$

These roots exibhiting properties detailed in [99] are found numerically. We discuss here only the positive roots (i.e., those lying in the upper half of the complex beta/gamma plane axis which is deemed to include the positive real axis). It is found that there is always one real root, ($\gamma_0 > 0$, $\beta_0 > 0$) and an infinite number of imaginary roots.

The eigenfunctions $Y_{jn}(y), j = 1, 2$, satisfy the following generalized orthogonality relations

$$\alpha \int_a^b Y_{1n}(y)Y_{1m}(y)dy = G_n\delta_{mn} - Y_{1n}^{'}(b)Y_{1m}^{'}(b) \tag{4.7}$$

and

$$\alpha \int_0^h Y_{2n}(y)Y_{2m}(y)dy = E_n\delta_{mn} - Y_{2n}^{'}(h)Y_{2m}^{'}(h), \tag{4.8}$$

where the prime indicates differentiation with respect to y and δ_{mn} is the usual Kronecker delta. For the fluid-structure coupled modes the quantities G_n and E_n are found as

$$G_n = \frac{Y_{1n}^{'}(b)}{2\gamma_n}\frac{d}{d\gamma}\kappa_1(\gamma)|_{\gamma=\gamma_n} \tag{4.9}$$

and

$$E_n = \frac{Y_{2n}^{'}(h)}{2\beta_n}\frac{d}{d\beta}\kappa_2(\beta)|_{\beta=\beta_n}, \tag{4.10}$$

respectively.

4.2 Mode-Matching Solution

This section deals with the MM solution of equations (4.1) to (4.4) with the aid of generalized orthogonality relations (4.7) and (4.8). Consider an incident wave of harmonic time dependence with forcing $F_\ell = \sqrt{\alpha/G_\ell\eta_\ell}$, (where the subscript ℓ specifies the incident mode to be define later) is propagating from negative x-direction towards $|x| \leq L$. At interfaces $x = \pm L$, it will scatter into an infinite numbers of reflected and transmitted modes. The field potential $\phi(x, y)$ in different regions of waveguide is splitted and can be expressed as

$$\phi(x,y)=\begin{cases}\phi_1(x,y), & x\le -L, \quad a\le y\le b\\ \phi_2(x,y), & |x|\le L, \quad 0\le y\le h\\ \phi_3(x,y), & x\ge L, \quad a\le y\le b\end{cases}. \tag{4.11}$$

The eigenfunction expansion form of these field potentials is found as

$$\phi_1(x,y)=F_\ell Y_{1\ell}(y)e^{i\eta_\ell(x+L)}+\sum_{n=0}^{\infty}A_nY_{1n}(y)e^{-i\eta_n(x+L)}, \tag{4.12}$$

$$\phi_2(x,y)=\sum_{n=0}^{\infty}\left(B_ne^{-i\nu_nx}+C_ne^{i\nu_nx}\right)Y_{2n}(y) \tag{4.13}$$

and

$$\phi_3(x,y)=\sum_{n=0}^{\infty}D_nY_{1n}(y)e^{i\eta_n(x-L)}, \tag{4.14}$$

where $\eta_n=(\gamma_n^2+1)^{1/2}$ and $\nu_n=(\beta_n^2+1)^{1/2}$ denote the wave numbers of propagating modes in regions $|x|>L$ and $|x|<L$, respectively. Note that the first term in (4.12) represents the multimodal incident for structural borne ($\ell=0$) and fluid borne ($\ell=1$) incident. The coefficients (A_n, D_n) and (B_n , C_n) are the amplitudes of scattering modes in regions $|x|>L$ and $|x|<L$, respectively. These coefficients are unknowns to be found while using the continuity conditions of pressures and normal velocities across the interfaces. The continuity conditions of pressures at $x=\pm L$ are given by

$$\phi_1(-L,y)=\phi_2(-L,y), \qquad a\le y\le b, \tag{4.15}$$

$$\phi_2(L,y)=\phi_3(L,y), \qquad a\le y\le b. \tag{4.16}$$

Now on substituting (4.12)-(4.14) into (4.15) and (4.16) together with the use of OR (4.7) we get

$$A_m=-F_\ell\delta_{m\ell}+\frac{\gamma_m\sinh[\gamma_m(b-a)]e_1}{G_m}+\frac{\alpha}{G_m}\sum_{n=0}^{\infty}R_{mn}\{B_ne^{i\nu_nL}+C_ne^{-i\nu_nL}\}, \tag{4.17}$$

$$D_m=\frac{\gamma_m\sinh[\gamma_m(b-a)]}{G_m}e_2+\frac{\alpha}{G_m}\sum_{n=0}^{\infty}R_{mn}\{B_ne^{-i\nu_nL}+C_ne^{i\nu_nL}\}, \tag{4.18}$$

where

$$e_1 = F_\ell\gamma_\ell \sinh[\gamma_\ell(b-a)] + \sum_{n=0}^{\infty} A_n\gamma_n \sinh[\gamma_n(b-a)] \text{ and } e_2 = \sum_{n=0}^{\infty} D_n\gamma_n \sinh[\gamma_n(b-a)]$$

which are dependent sums to be determined using appropriate edge conditions and R_{mn} is defined by

$$R_{mn} = \frac{1}{\beta_n^2 - \gamma_m^2}\{\beta_n(-\sinh(a\beta_n) + \cosh[\gamma_m(a-b)]\sinh(\beta_n b)) \\ + \cosh(\beta_n b)\gamma_m \sinh[\gamma_m(a-b)]\}. \tag{4.19}$$

The addition and subtraction of equations (4.17) and (4.18) yield

$$\Psi_m^+ = -F_\ell\delta_{m\ell} + \frac{\gamma_m \sinh[\gamma_m(b-a)]}{G_m}U^- + \frac{2\alpha}{G_m}\sum_{n=0}^{\infty} R_{mn}\cos(\upsilon_n L)\chi_n^+ \tag{4.20}$$

and

$$\Psi_m^- = -F_\ell\delta_{m\ell} + \frac{\gamma_m \sinh[\gamma_m(b-a)]}{G_m}U^+ + \frac{2i\alpha}{G_m}\sum_{n=0}^{\infty} R_{mn}\sin(\upsilon_n L)\chi_n^-, \tag{4.21}$$

respectively, where $\Psi_m^\pm = (A_m \pm D_m)$, $\chi_n^\pm = (B_n \pm C_n)$ and $U^\pm = e_1 \pm e_2$. Similarly the continuity conditions of normal velocities at $x = \pm L$, are given by

$$\phi_{2x}(-L, y) = \begin{cases} 0, & 0 \le y \le a, \\ \phi_{1x}(-L, y), & a \le y \le b, \\ 0, & b \le y \le h \end{cases} \tag{4.22}$$

and

$$\phi_{2x}(L, y) = \begin{cases} 0, & 0 \le y \le a, \\ \phi_{3x}(L, y), & a \le y \le b, \\ 0, & b \le y \le h, \end{cases} \tag{4.23}$$

where $\phi_{ix} = \dfrac{\partial\phi_i}{\partial x}(i = 1, 2, 3)$. On substituting (4.12)-(4.14) into (4.22) and (4.23) and using the OR (4.8) results into the following equations, that are,

$$\chi_m^+ = \frac{\beta_m \sinh(\beta_m h)}{2iE_m\nu_m \sin(\nu_n L)}V^- - \frac{\alpha}{2iE_m\nu_m \sin(\nu_n L)}\left\{F_\ell \eta_\ell R_{0m} - \sum_{n=0}^{\infty} \Psi_n^+ \eta_n R_{nm}\right\} \tag{4.24}$$

and

$$\chi_m^- = \frac{\beta_m \sinh(\beta_m h)}{2E_m\nu_m \cos(\nu_n L)}V^+ - \frac{\alpha}{2E_m\nu_m \cos(\nu_n L)}\left\{F_\ell \eta_\ell R_{0m} - \sum_{n=0}^{\infty} \Psi_n^- \eta_n R_{nm}\right\}, \tag{4.25}$$

where $V^\pm = e_3 \pm e_4$ together with

$$e_3 = \sum_{n=0}^{\infty} \left(B_n e^{i\nu_n L} - C_n e^{-i\nu_n L}\right) \beta_n \nu_n \sinh(\beta_n h)$$

and

$$e_4 = \sum_{n=0}^{\infty} \left(B_n e^{-i\nu_n L} - C_n e^{i\nu_n L}\right) \beta_n \nu_n \sinh(\beta_n h)$$

are unknown sums to be determined with the help of appropriate edge conditions. The values of $V^\pm$ and $U^\pm$ describe the behavior of membranes at edges. In case of elastic membranes, we discuss only the choices of fixed (zero displacement) and simply supported (zero gradient) edges of membranes in the following subsections.

- **All Fixed Edges:** For this set of edge conditions, the displacements of membranes at edge points $(\pm L, b)$ and $(\pm L, h)$ are assumed to be zero, that is

$$\phi_{1y}(-L, b) = 0, \tag{4.26}$$

$$\phi_{2y}(\pm L, h) = 0, \tag{4.27}$$

$$\phi_{3y}(L, b) = 0. \tag{4.28}$$

  Now from (4.26) and (4.28), it is straightforward to write $U^\pm = 0$, as $e_1 = e_2 = 0$ whereas for $V^\pm$, we multiply (4.24) with $\beta_m \sinh(\beta_m h)\cos(\nu_m L)$ and (4.25) with $\beta_m \sinh(\beta_m h)\sin(\nu_m L)$, take summation over m from zero to infinty, and then using the edge conditions (4.27), we get

$$V^- = \frac{\alpha}{S_1}\sum_{m=0}^{\infty}\frac{\beta_m\sinh(\beta_m h)\cot(\nu_m L)}{E_m\nu_m}\left\{F_\ell\eta_\ell R_{0m} - \sum_{n=0}^{\infty}\Psi_n^+\eta_n R_{nm}\right\}, \tag{4.29}$$

$$V^+ = \frac{\alpha}{S_2}\sum_{m=0}^{\infty}\frac{\beta_m\sinh(\beta_m h)\tan(\nu_m L)}{E_m\nu_m}\left\{F_\ell\eta_\ell R_{0m} - \sum_{n=0}^{\infty}\Psi_n^-\eta_n R_{nm}\right\}, \tag{4.30}$$

where

$$S_1 = \sum_{m=0}^{\infty}\frac{\beta_m^2\sinh^2(\beta_m h)\cot(\nu_m L)}{E_m\nu_m}, \tag{4.31}$$

$$S_2 = \sum_{m=0}^{\infty}\frac{\beta_m^2\sinh^2(\beta_m h)\tan(\nu_m L)}{E_m\nu_m}. \tag{4.32}$$

- **All Simply Supported Edges:** In case of all edges to be simply supported, the gradient is assumed to be zero, that is

$$\phi_{1xy}(-L,b) = 0, \tag{4.33}$$

$$\phi_{2xy}(\pm L,h) = 0, \tag{4.34}$$

$$\phi_{3xy}(L,b) = 0. \tag{4.35}$$

The use of equation (4.34), clearly follows that $V^\pm = 0$, as $e_3 = e_4 = 0$. However, for $U^\pm$, we multiply (4.20)-(4.21) with $\eta_m\gamma_m\sinh[\gamma_m(b-a)]$, take summation over m from zero to infinity, and then apply the edge conditions (4.33) and (4.35) to get

$$\begin{aligned} U^- &= \frac{2F_\ell\gamma_\ell\eta_\ell\sinh[\gamma_\ell(b-a)]}{S_3} \\ &\quad -\frac{2\alpha}{S_3}\sum_{n=0}^{\infty}\chi_n^+\cos(\nu_n L)\sum_{m=0}^{\infty}\frac{\eta_m\gamma_m\sinh[\gamma_m(b-a)]R_{mn}}{G_m} \end{aligned} \tag{4.36}$$

and

$$\begin{aligned} U^+ &= \frac{2F_\ell\gamma_\ell\eta_\ell\sinh[\gamma_\ell(b-a)]}{S_3} \\ &\quad -\frac{2i\alpha}{S_3}\sum_{n=0}^{\infty}\chi_n^-\sin(\nu_n L)\sum_{m=0}^{\infty}\frac{\eta_m\gamma_m\sinh[\gamma_m(b-a)]R_{mn}}{G_m}, \end{aligned} \tag{4.37}$$

where

$$S_3 = \sum_{m=0}^{\infty} \frac{\eta_m \gamma_m^2 \sinh^2[\gamma_m(b-a)]}{G_m}. \tag{4.38}$$

- **Fixed at $(\pm L, b)$ and Simply Supported at $(\pm L, h)$:** In this case, we assume the zero displacement edge conditions on the membranes of inlet/outlet duct regions whereas the expansion chamber comprises zero gradient conditions, that is

  $$\phi_{1y}(-L, b) = 0, \tag{4.39}$$

  $$\phi_{2xy}(\pm L, h) = 0, \tag{4.40}$$

  $$\phi_{3y}(L, b) = 0. \tag{4.41}$$

  The implication of above equations give $U^{\pm} = 0$ and $V^{\pm} = 0$.

- **Simply Supported at $(\pm L, b)$ and Fixed at $(\pm L, h)$:** For this set of edge conditions, the elastic membranes of inlet/outlet duct regions comprise zero gradient at edges $(\pm L, b)$ whereas the membrane of the expansion chamber contains zero displacement at $(\pm L, b)$, that is

  $$\phi_{1xy}(-L, b) = 0, \tag{4.42}$$

  $$\phi_{2y}(\pm L, h) = 0, \tag{4.43}$$

  $$\phi_{3xy}(L, b) = 0. \tag{4.44}$$

  In view of above edge conditions, all the constants $U^{\pm}$ and $V^{\pm}$ are non-zero which are given by the expression defined in (4.29)-(4.30) and (4.36)-(4.37).

4.3 Low-Frequency Approximation

The MM solution of underlying problem is obtained subject to different edge conditions. We are interested to validate MM result in low frequency regime, thereby comparing with the LFA. The LFA solution relies on the number of modes that are allowed to propagate in duct regions. These modes are subjected to the physical conditions imposed on the walls and edges of the waveguide regions. Therefore, in case of LFA, the field potentials in waveguide regions may take the following forms as

$$\phi_1(x,y) \approx F_\ell \cosh[\gamma_\ell(y-a)]e^{i\eta_\ell(x+L)} + \sum_{n=0}^{J_1} A_n \cosh[\gamma_n(y-a)]e^{-i\eta_n(x+L)}, \quad (4.45)$$

$$\phi_2(x,y) \approx \sum_{n=0}^{J_2} \left(B_n e^{-i\nu_n x} + C_n e^{i\nu_n x}\right) Y_n(y) \quad (4.46)$$

and

$$\phi_3(x,y) \approx \sum_{n=0}^{J_1} D_n \cosh\{\gamma_n(y-a)\}e^{i\eta_n(x-L)}, \quad (4.47)$$

where J_1 and J_2 stand for the number of modes propagating in inlet/outlet and expansion chamber, respectively. The unknown coefficients are found by considering the continuity of mean pressures and velocities flux at interfaces, that is

$$\int_a^b \{\phi_1(-L,y) - \phi_2(-L,y)\}\, dy = 0, \quad (4.48)$$

$$\int_a^b \{\phi_{1x}(-L,y) - \phi_{2x}(-L,y)\}\, dy = 0, \quad (4.49)$$

$$\int_a^b \{\phi_3(L,y) - \phi_2(L,y)\}\, dy = 0, \quad (4.50)$$

$$\int_a^b \{\phi_{3x}(L,y) - \phi_{2x}(L,y)\}\, dy = 0 \quad (4.51)$$

and

$$\int_0^a \phi_{2x}(\pm L,y)dy = 0 \quad \text{and} \quad \int_b^h \phi_{2x}(\pm L,y)dy = 0. \quad (4.52)$$

On substituting (4.45)-(4.47) into (4.48)-(4.52), we get

$$\sum_{n=0}^{J_1} R_n A_n - \sum_{n=0}^{J_2} \left(Q_n B_n e^{i\nu_n L} + Q_n C_n e^{-i\nu_n L}\right) = \frac{F_\ell \sinh[\gamma_\ell(a-b)]}{\gamma_\ell}, \quad (4.53)$$

$$\sum_{n=0}^{J_1} \eta_n R_n A_n - \sum_{n=0}^{J_2} \left(\nu_n Q_n B_n e^{i\nu_n L} - \nu_n Q_n C_n e^{-i\nu_n L}\right) = \frac{\eta_\ell F_\ell \sinh[\gamma_\ell(a-b)]}{\gamma_\ell}, \quad (4.54)$$

$$\sum_{n=0}^{J_1} D_n R_n - \sum_{n=0}^{J_2} \left(Q_n B_n e^{-i\nu_n L} + Q_n C_n e^{i\nu_n L}\right) = 0, \tag{4.55}$$

$$\sum_{n=0}^{J_1} \eta_n D_n R_n - \sum_{n=0}^{J_2} \left(\nu_n Q_n B_n e^{-i\nu_n L} - \nu_n Q_n C_n e^{i\nu_n L}\right) = 0, \tag{4.56}$$

$$\sum_{n=0}^{J_2} \frac{i\nu_n \sinh(\beta_n a)}{\beta_n} \left\{B_n e^{i\nu_n L} - C_n e^{-i\nu_n L}\right\} = 0, \tag{4.57}$$

$$\sum_{n=0}^{J_2} \frac{i\nu_n \sinh(\beta_n a)}{\beta_n} \left\{B_n e^{-i\nu_n L} - C_n e^{i\nu_n L}\right\} = 0, \tag{4.58}$$

$$\sum_{n=0}^{J_2} \frac{i\nu_n \left\{\sinh(\beta_n b) - \sinh(\beta_n h)\right\}}{\beta_n} \left\{B_n e^{i\nu_n L} - C_n e^{-i\nu_n L}\right\} = 0 \tag{4.59}$$

and

$$\sum_{n=0}^{J_2} \frac{i\nu_n \left\{\sinh(\beta_n b) - \sinh(\beta_n h)\right\}}{\beta_n} \left\{B_n e^{-i\nu_n L} - C_n e^{i\nu_n L}\right\} = 0, \tag{4.60}$$

where $R_n = \dfrac{1}{\gamma_n}\left\{-\sinh\left[\gamma_n(a-b)\right]\right\}$ and $Q_n = -\dfrac{1}{\beta_n}\left\{\sinh(\beta_n a) - \sinh(\beta_n b)\right\}$. The system of equations for multiple types of connections is obtained as follows.

- **All Fixed Edges**

For this choice of edge conditions, we substitute (4.45)-(4.47) into (4.26)-(4.28), to obtain

$$\sum_{n=0}^{J_1} A_n \gamma_n \sinh\left[\gamma_n(b-a)\right] = -F_\ell \gamma_\ell \sinh\left[\gamma_\ell(b-a)\right], \tag{4.61}$$

$$\sum_{n=0}^{J_2} \left(B_n e^{-i\nu_n L} + C_n e^{i\nu_n L}\right) \beta_n \sinh(\beta_n h) = 0, \tag{4.62}$$

$$\sum_{n=0}^{J_2} \left(B_n e^{i\nu_n L} + C_n e^{-i\nu_n L}\right) \beta_n \sinh(\beta_n h) = 0 \tag{4.63}$$

and

$$\sum_{n=0}^{J_1} D_n \gamma_n \sinh\left[\gamma_n(b-a)\right] = 0. \tag{4.64}$$

In this way, equations (4.53)-(4.60) and (4.61)-(4.64) yield a system of linear algebraic equations after using LFA and considering all edges to be fixed.

- **All Simply Supported Edges**

On using (4.45)-(4.47) into equations (4.33)-(4.35)we found that

$$\sum_{n=0}^{J_1} A_n\eta_n\gamma_n \sinh\left[\gamma_n(b-a)\right] = F_\ell\eta_\ell\gamma_\ell \sinh[\gamma_\ell(b-a)], \tag{4.65}$$

$$\sum_{n=0}^{J_2} \left(B_n e^{i\nu_n L} - C_n e^{-i\nu_n L}\right) \nu_n\beta_n \sinh(\beta_n h) = 0, \tag{4.66}$$

$$\sum_{n=0}^{J_2} \left(B_n e^{-i\nu_n L} - C_n e^{i\nu_n L}\right) \nu_n\beta_n \sinh(\beta_n h) = 0 \tag{4.67}$$

and

$$\sum_{n=0}^{J_1} D_n\eta_n\gamma_n \sinh[\gamma_n(b-a)] = 0. \tag{4.68}$$

Equations (4.53)-(4.60) together with (4.65)-(4.68) form a system of linear algebraic equations for LFA. Similarly system of equations for LFA is obtained when inlet/outlet membranes are fixed while expansion chamber is simply supported and vice versa.

4.4 Numerical Results and Discussions

The linear algebraic systems are obtained throughout via MM technique and LFA are truncated and solved numerically. First we truncate infinite systems obtained through MM procedure along with each set of edge conditions upto $m = n = 0, 1, 2, ...N$ terms, and then solve the remaining systems to determine the values of unknown modal amplitudes (A_n, B_n, C_n, D_n), $n = 0, 1, 2, ...N$. It is useful to discuss the propagation of scattering energies in the inlet/outlet duct sections and the TL against frequency and the half-chamber length (for detail see article [95]). The aim here is to examine the scattering powers / energies and the TL to provide physical insight into the limitations of the model with different sets of edge conditions and to validate the MMT and LFA solutions with their relative merits. The P_r in the inlet duct and P_t in the outlet duct are given by [36]

$$P_r = \mathrm{Re}\left\{\frac{1}{\alpha}\sum_{n=0}^{\infty}|A_n|^2\eta_n G_n\right\} \tag{4.69}$$

and

$$P_t = \mathrm{Re}\left\{\frac{1}{\alpha}\sum_{n=0}^{\infty}|D_n|^2\eta_n G_n\right\}, \tag{4.70}$$

respectively. Note that the choice of F_ℓ enables us to scale P_i at unity, thus

$$P_r + P_t = 1, \tag{4.71}$$

which is the conserved power identity. The graphical results presented here are found from the truncated solutions with truncation parameter $N = 20$. The computational process is carried out by fixing the dimensional variables as the duct heights $\overline{a} = 0.085$m, $\overline{b} = 0.17$m and $\overline{h} = 0.25$m, length of expansion chamber $2\overline{L} = 2*0.425$m, the speed of sound $c = 343\text{ms}^{-1}$, density of air $\rho = 1.2043\text{Kgm}^{-2}$, membrane mass density $\rho_m = 0.2\text{Kgm}^{-2}$ and tension $T = 3250\text{Nm}^{-2}$. The scattering analysis of wave energies against frequency and half-chamber length is illustrated below.

4.4.1 Scattering Energies against Frequency

The scattering of energies against frequency (Hz) for the structure-borne mode incident ($\ell = 0$) and the fluid-borne mode incident ($\ell = 1$) are depicted in Figs. 4.2 and 4.3, respectively. The results obtained via MMT and LFA are plotted together for different sets of edge conditions which resulted a good agreement when structure-borne mode incident (see Fig. 4.2). However, when the fluid-borne mode is incident, a little variation in LFA results appears due to the occurrence of new cut-on modes at higher frequencies. The list of cut-on modes verses frequency for various duct regions is shown via Table. 4.1. From Figs. 4.2 and 4.3, it can be seen that the P_r and the P_t fluctuate inversely against frequency in somehow periodic manner. These variations are because of the trigonometric factor present in the

TABLE 4.1: Propagating Modes

Cut-on f(Hz)	Inlet-Outlet Region	Expansion Chamber Region
211	1	2
418	2	2
759	2	3
1395	2	4
2054	2	5
2116	3	5
2719	3	6
3388	3	7
4058	3	8
4091	4	8
4730	4	9

amplitudes of scattering energies defined by equations (4.24) and (4.25). However, the behavior becomes different due to the existence of compressional waves along the membrane boundaries and the leakage of sound while using different conditions at edges. Moreover, it is noted that the reflected energy drops to its maximum level with sharper dips at frequencies 16Hz, 91Hz, 158Hz, 322Hz and 389Hz, when all the edges are assumed fixed. But it is not evident for other sets of edge conditions (see Fig. 4.2).

Nevertheless, the propagation of cut-on modes is same for all the set of edge conditions but the variation of scattering energies is different for the different set of edge conditions. Nonetheless, the scattering behavior resembles when all edges are either fixed or fixed at $(\pm L, b)$ and simple supported at $(\pm L, h)$. But clearly it happens only if number of modes propagating in the inlet/outlet are equal to the number of modes propagating in the expansion chamber. For instance, the scattering behavior of Figs. 4.2(a) and 4.2(b) differ significantly in regime 211Hz to 418Hz when the structure-borne is propagating in the inlet/outlet whereas the

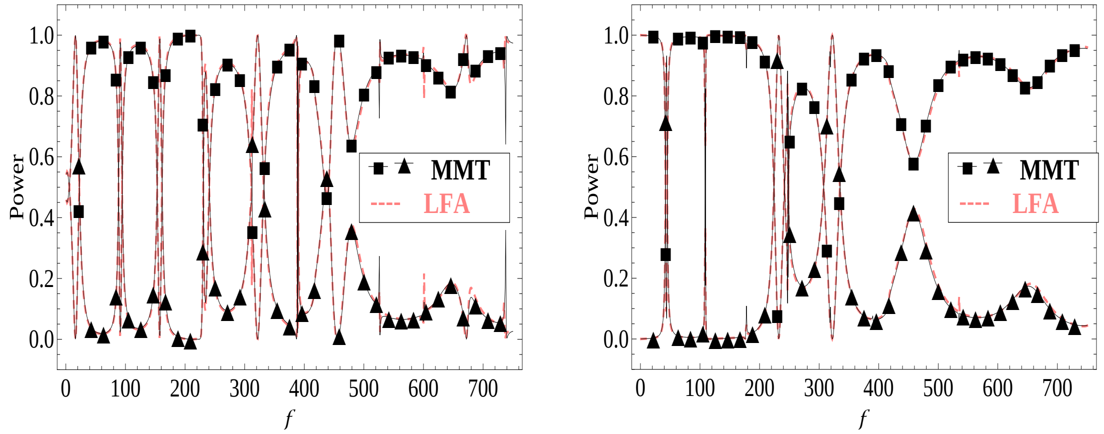

(a) All fixed edges.

(b) Fixed at$(\pm L, b)$ and simply supported at $(\pm L, h)$.

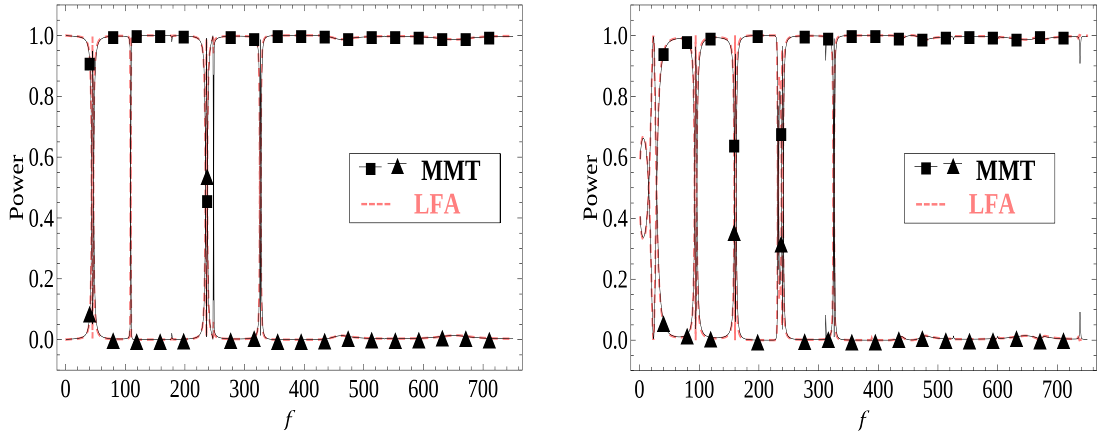

(c) All simply supported edges.

(d) Simply supported at $(\pm L, b)$ and fixed at $(\pm L, h)$.

FIGURE 4.2: For fundamental mode incident ($\ell = 0$): the reflected power (■) and the transmitted power (▲) against frequency with different set of edge conditions.

structure-borne and fluid-borne modes are propagating in the expansion chamber. Likewise, manifestation is observed for the rest of the cases of Figs. 4.2(c) and 4.2(d), whilst in case of simply supported edges at $(\pm L, b)$ the leakage of compressional wave is much higher, therefore more reflection is observed.

The results for the fluid-borne mode incident which cuts-on at frequency 418Hz are depicted in Fig. 4.3. Clearly, a sharp inversion in dips of scattering energies against frequency from 418Hz to 1250Hz for the various sets of edge conditions is portrayed. The fact is due to the shifting of energy from structure to fluid and vice versa, which is commonly caused by the advent of new cut-on modes in waveguide and is useful for the design of HVAC systems [95]. Nevertheless, by changing the

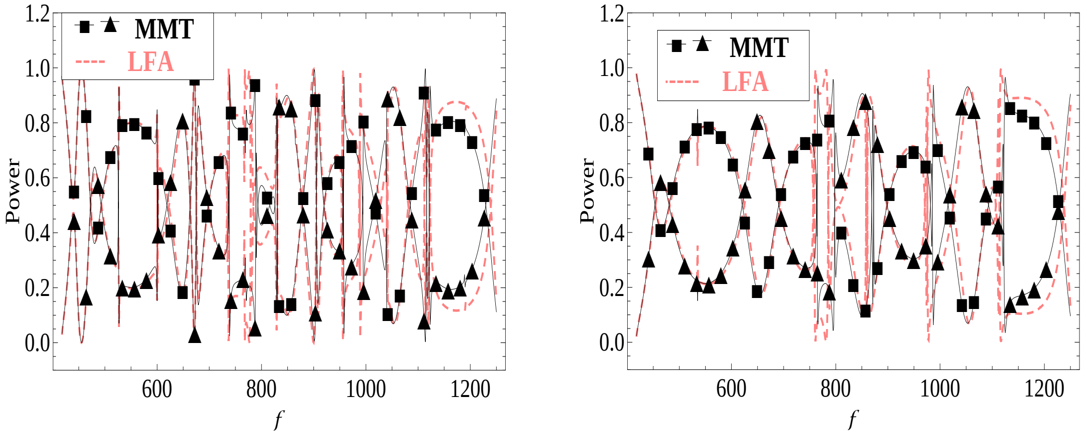

(a) All fixed edges.

(b) Fixed at $(\pm L, b)$ and simply supported at $(\pm L, h)$.

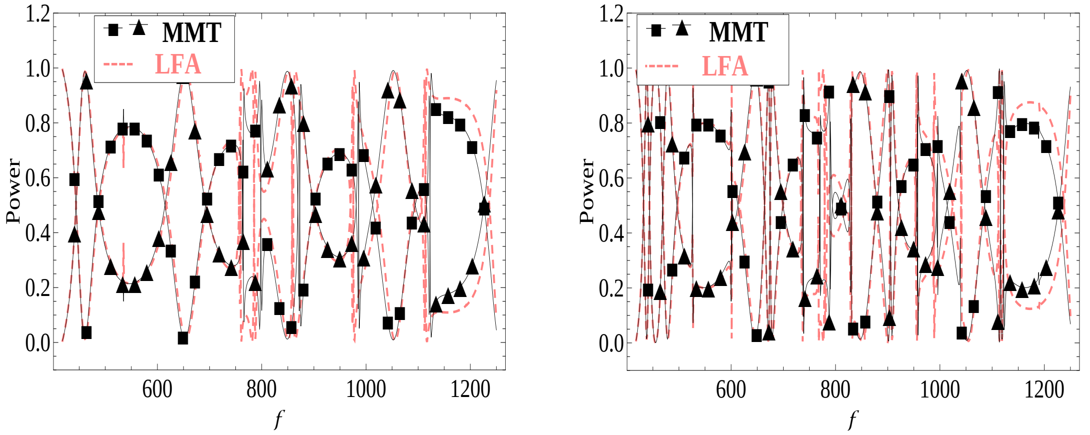

(c) All simply supported edges.

(d) Simply supported at $(\pm L, b)$ and fixed at $(\pm L, h)$.

Figure 4.3: For fluid mode incident ($\ell = 1$): the reflected power (■) and the transmitted power (▲) against frequency with different set of edge conditions.

physical connections of the elastic membranes at joints $(\pm L, b)$ and $(\pm L, h)$, a significant deviation in the propagating energies verses frequency is perceived (see Fig. 4.3). Moreover, the MMT and LFA curves coincide in low frequency regime only. However, if the frequency is increased the discrepancy in both curves is found (see Fig. 4.3). This occurs since the limited number of modes are being allowed in LFA case, but there appears new propagating modes on increasing frequency.

Beside, the use of optimal length of an expansion chamber in HVAC duct system is very important. The length of the device for the practical use must not be long or too short, because it may significantly alter the scattering energies (see for example [95]). Thus, the analysis of scattering energies against half-length of the expansion chamber is now discussed.

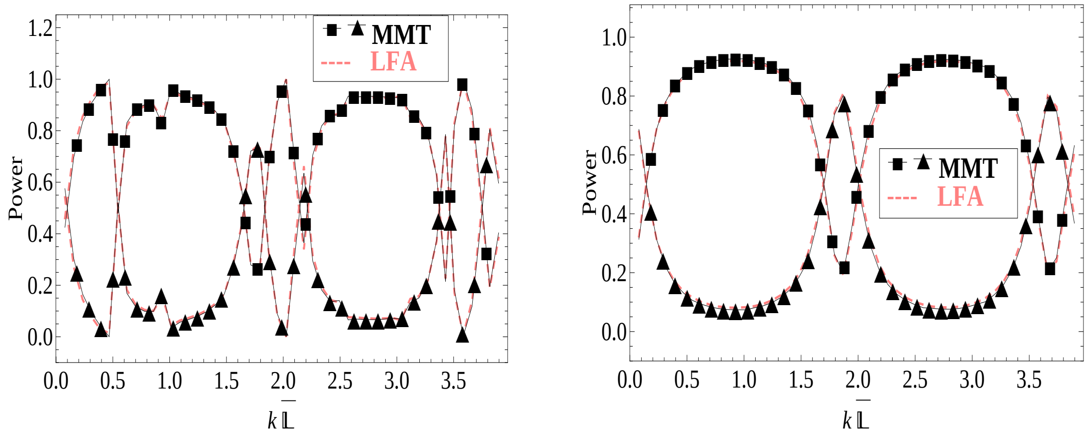

(a) All fixed edges.

(b) Fixed at $(\pm L, b)$ and simply supported at $(\pm L, h)$.

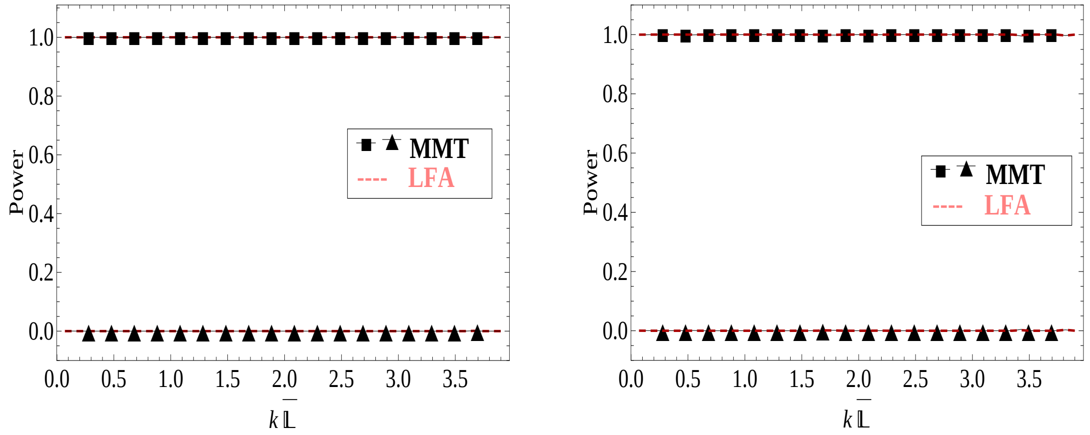

(c) All simply supported edges.

(d) Simply supported at $(\pm L, b)$ and fixed at $(\pm L, h)$.

FIGURE 4.4: For structure-borne mode incident ($\ell = 0$): the reflected power (■) and the transmitted power (▲) against silencer-half length with different set of edge conditions.

4.4.2 Scattering Energies against Half-Chamber Length

In Figs. 4.4 and 4.5, the P_r and the P_t against the half-length of the expansion chamber are depicted. The graphs are plotted at frequency $f = 426$ Hz, which is chosen to make sure that the fluid-borne mode incident becomes cut-on. The cut-ons of duct regions verses frequency are shown in Table 4.1, whilst, the remaining parameters are taken as same as for Fig. 4.2. Fig. 4.4 shows the graphs for different sets of edge conditions along with the structure-borne mode incident whereas the results for fluid-borne mode incident are shown in Fig. 4.5. Note that by changing the half-length of the expansion chamber, a significant variation in scattering energies is seen in Figs. 4.4(a) and 4.4(b), when the edges of membranes bounding the inlet and outlet duct regions are assumed to be fixed. Moreover, the energies (P_r and P_t) are inverted at the half-length of the chamber at 1.7, 2.2 and 3.8, respectively. However, the envisaged situation is not noticeable if the edges at $(\pm L, b)$ are kept simply supported. It occurs due to the leakage of compressional waves on edges when we assume the simply supported conditions at the edges $(\pm L, b)$ for structure-borne mode incident (see Fig. 4.4(c) and Fig. 4.4(d)).

On contrary, for the fluid-borne mode incident ($\ell = 1$), this behavior is not evident for the same sets of edge conditions (see Figs. 4.5(c) and 4.5(d)). It clearly follows that the transient of maximum energy is through fluid for the case of secondary mode incident, as discussed in [34, 87]. It is also demonstrated in Figs. 4.5(a) and 4.5(b) that the energy is totally reflected when the simply supported edge condition instead of fixed edges in the expansion chamber. Thus, by adjusting the half-length of the expansion chamber and/or by changing the edge conditions the device can be tuned. Hence, the analysis of scattering energies against the half-chamber length are presented in Figs.(4.4-4.5).

The length of the expansion chamber also plays an important role to measure the TL of the silencer/waveguide. As Lawrie and Guled [95] discussed the TL against frequency and the length of chamber for the reactive silencer. However, the performance of a HVAC silencer is usually measured by the TL as

$$\mathrm{TL} = -10 \log_{10}\left(\frac{P_t}{P_i}\right). \tag{4.72}$$

For modelled device, we define the aspect ratio by definig $R = 2\overline{L}/(\overline{h} - \overline{b})$ where $\overline{h} = \overline{b} + \overline{a}$. The low and very high value of this aspect ratio contains significant affect in the analysis of stopband, as disscussed by Huang [59]. To explain the stopband criteria we follow the procedure as adopted by Huang [59] by using the dimensionless form of spatial coordinates.

When we put two cavities together ($a = b$), the total volume occupied $V = 4L * a$ form a reference expansion chamber with expansion ratio: $1 + 2a = 1 + \sqrt{V}$ at $R = 2$. Now it is convenient to implement the criteria on TL to observe the better

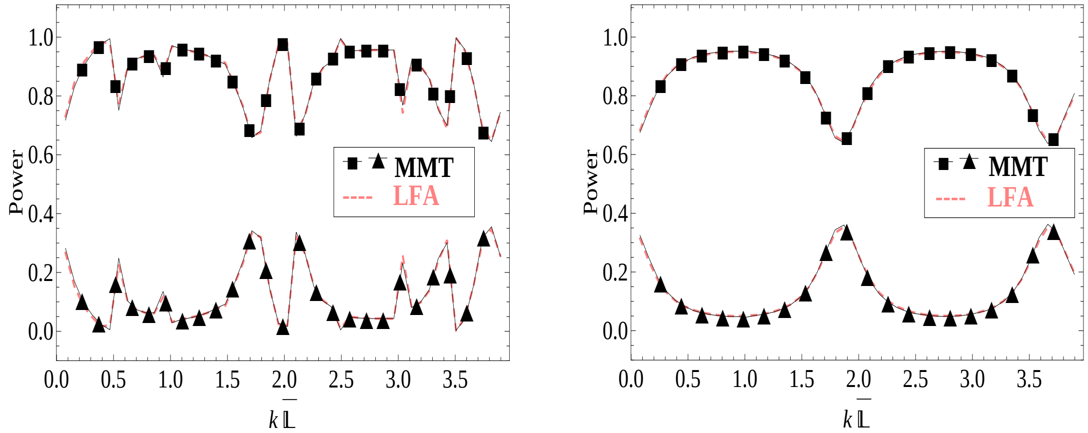

(a) All fixed edges.

(b) Fixed at $(\pm L, b)$ and simply supported at $(\pm L, h)$.

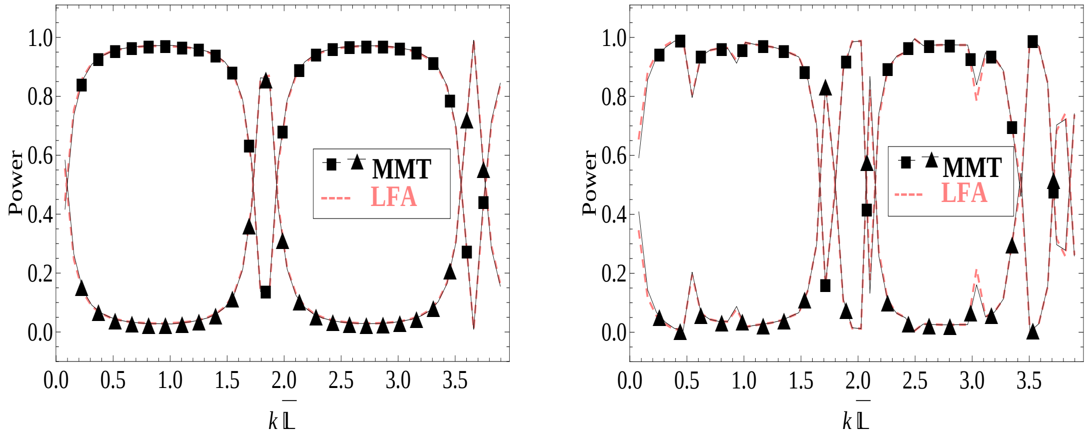

(c) All simply supported edges.

(d) Simply supported at $(\pm L, b)$ and fixed at $(\pm L, h)$.

FIGURE 4.5: For fluid-borne mode incident ($\ell = 1$): the reflected power (■) and the transmitted power (▲) against half-chamber length with different set of edge conditions.

performance of the device. For this, we set the volume of the device equal to three times of the actual volume, which yield the expansion ratio $1 + \sqrt{3V}$. Now by using the formula as given by [59]

$$\mathrm{TL}_{cr} = 10 \log_{10}[1 + \frac{1}{4}(a_3 - a_3^{-1})^2]. \tag{4.73}$$

Thus, TL_{cr} is found to be approximately 10 dB, when $V = 8$, $a = 1$, $L = 2$ and $a_3 = 1 + \sqrt{3V}$. Based on above information the analysis of TL against frequency and half-chamber length are now presented in next subsection.

4.4.3 Transmission-Loss against Frequency

The TL against frequency for different sets of edge conditions is shown in Figs. 4.6 and 4.7. Fig. 4.6 shows the variation of TL spectrum over the frequency regime 1Hz $\leq f \leq$ 1500 Hz in case of structure-borne mode incident. A good agreement is observed between MM solution and LFA. Also, it is noted that comparatively lesser TL is achieved in the frequency range (229-526) Hz for fixed edges at $(\pm L, b)$. It reveals that more pass-band occur in this range, as depicted in Fig. 4.6(a) and Fig. 4.6(b).

On the other hand, if we replace the fixed edge conditions at $(\pm L, b)$ with simply supported ends the pass-bands become stopband. Thus the TL is increased for simply supported ends conditions (see Figs. 4.6(c) and 4.6(d)). Moreover, the wider stopbands with simply supported ends at $(\pm L, b)$ are seen. However, when the simply supported ends at $(\pm L, h)$ are replaced with fixed ends, the noise attenuation closely resembles with that of all simply supported ends condition (see Fig. 4.6(c)) except the frequencies 770 Hz, 789 Hz, 790 Hz and 995 Hz.

For fluid-borne mode incident, the TL against frequency in the regime 418Hz $\leq f \leq$ 1500 Hz is shown in Fig. 4.7. Clearly, this mode is cut-on at $f = 418$ Hz. It is noted that two stopbands with bandwidth 1.02 and 1.03 for all fixed edges case are found (see Fig. 4.7(a)). These stopbands appear in the frequency range (1295Hz - 1330Hz) and (1353Hz - 1401Hz). Moreover, when we alter simply supported edges by fixed edges at $(\pm L, b)$, the TL spectrum of Fig. 4.7(d) also resembles with Fig. 4.7(a). On contrary to it, the stopband with bandwidth ratio 1.06 is seen in Fig. 4.7(c), for the fixed and simply supported edges case at $(\pm L, b)$ and $(\pm L, h)$, respectively. This stopband occur at the frequency range (1317Hz - 1399Hz). However, it is found that Fig. 4.7(c) resembles with Fig. 4.7(b) for all simply supported edges case.

At the end of the discussion, the analysis of transmission loss against half-chamber length is presented.

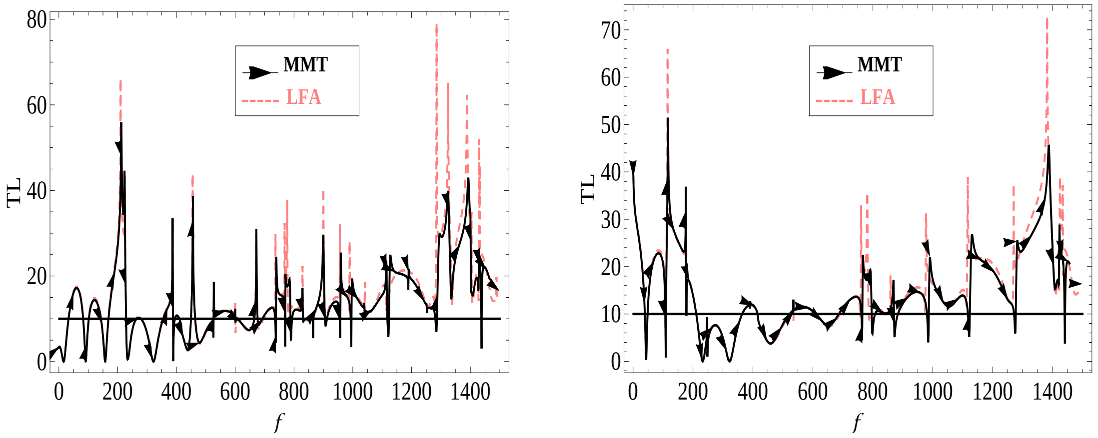

(a) All fixed edges.

(b) Fixed at $(\pm L, b)$ and simply supported at $(\pm L, h)$.

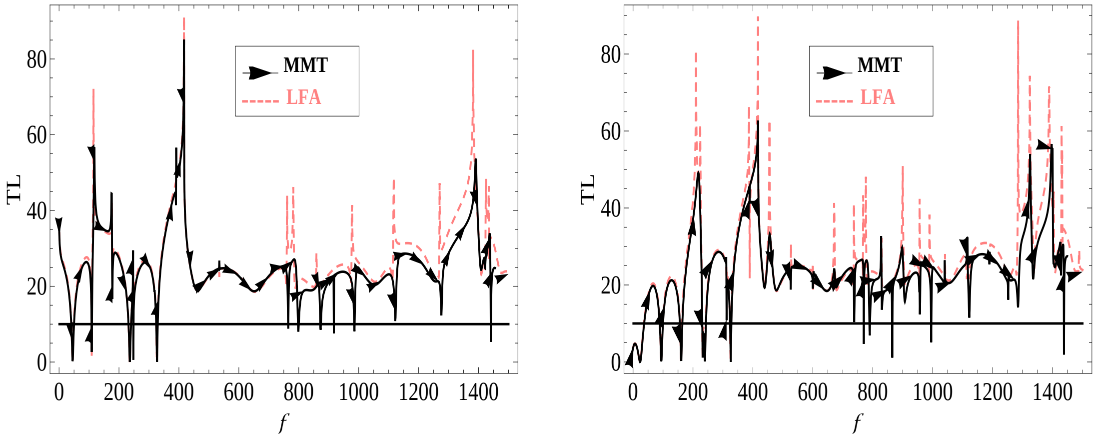

(c) All simply supported edges.

(d) Simply supported at $(\pm L, b)$ and fixed at $(\pm L, h)$.

FIGURE 4.6: For structure-borne mode incident ($\ell = 0$): the transmission loss components against frequency with different set of edge conditions.

4.4.4 Transmission-Loss against Half-Chamber Length

In Figs. 4.8 and 4.9, the TL against the half length of the chamber is discussed for the structure-borne mode incident ($\ell = 0$) and the fluid-borne mode incident ($\ell = 1$), respectively at $f = 426$. Note that for all fixed edges case (see Fig. 4.8(a)), the highest TL (37.83dB) occurs at non-dimensional length $L = 2.02$, which is exactly the point where the P_t is minimum as depicted in Fig. 4.4(a). Likewise the second and third highest peaks at the dimensionless length $L = 0.5$ and $L = 3.5$ appear at minimum P_t (see Fig. 4.8(a) and 4.4(a)). However, the TL is almost zero at length $L = 2.02$, when we change the fixed edges at $(\pm L, b)$ with the simply supported edge (Fig. 4.8(b)). This situation is exactly revealed in Fig.

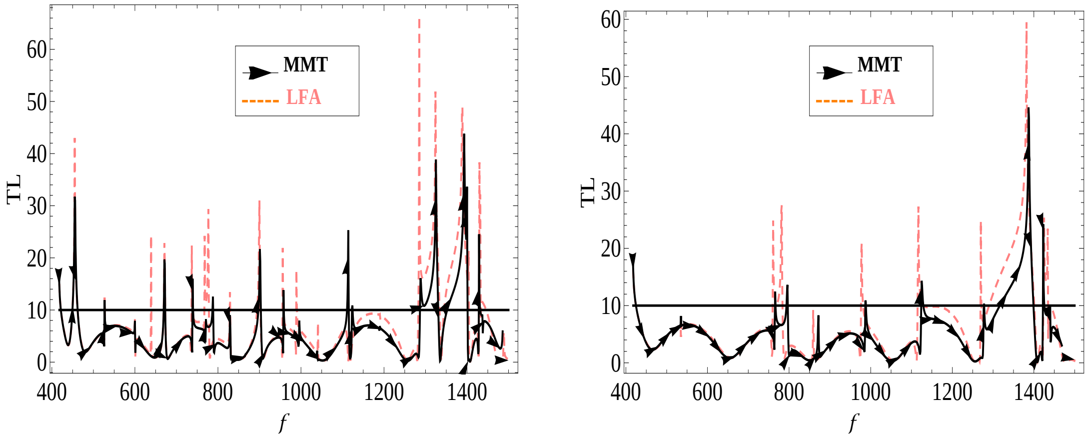

(a) All fixed edges.

(b) Fixed at $(\pm L, b)$ and simply supported at $(\pm L, h)$.

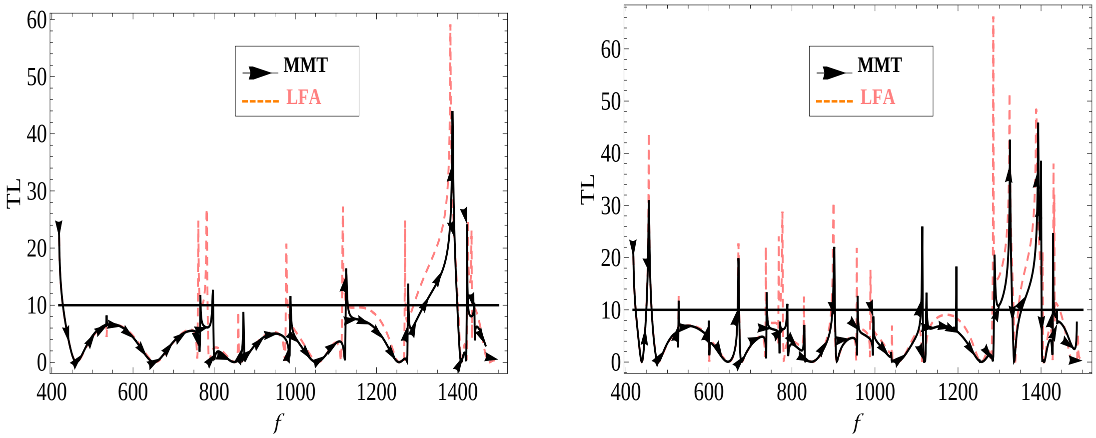

(c) All simply supported edges.

(d) Simply supported at $(\pm L, b)$ and fixed at $(\pm L, h)$.

FIGURE 4.7: For fluid-borne mode incident ($\ell = 1$): the transmission loss components against frequency for different set of edge conditions.

4.4(b), because at this point the P_r is maximum. It is observed that the TL curves of both Figs. 4.8(c) and 4.8(d) cover the TL criteria in whole regime at $f = 426$. This frequency shows that two propagating modes occurred in inlet, outlet and expansion chamber regions (see Table.1). But the peak values of TL as shown in Fig. 4.8(c) are greater than that of TL as shown in Fig. 4.8(d). The reason behind is the variation of edge conditions from all simply supported to fixed and simply supported. The analysis of TL curves shows that all simply supported edges case reveals more noise attenuation than fixed and simply supported edges.

The choice of appropriate edge conditions yields noise attenuation. For all fixed edges case and the fluid-borne mode incident (Fig. 4.9) the highest TL (25dB) occurs at $L = 3.5$, which is the point where the transmitted power P_t is minimum

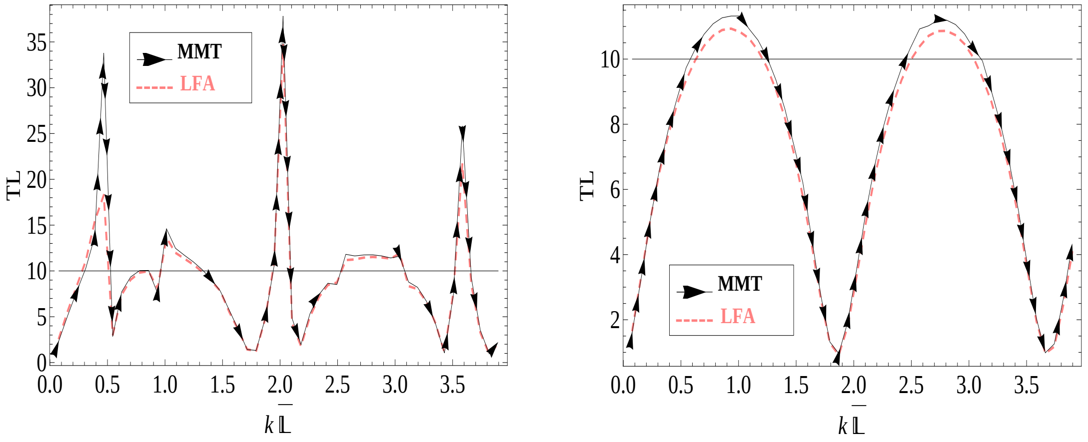

(a) All fixed edges. (b) Fixed at $(\pm L, b)$ and simply supported at $(\pm L, h)$.

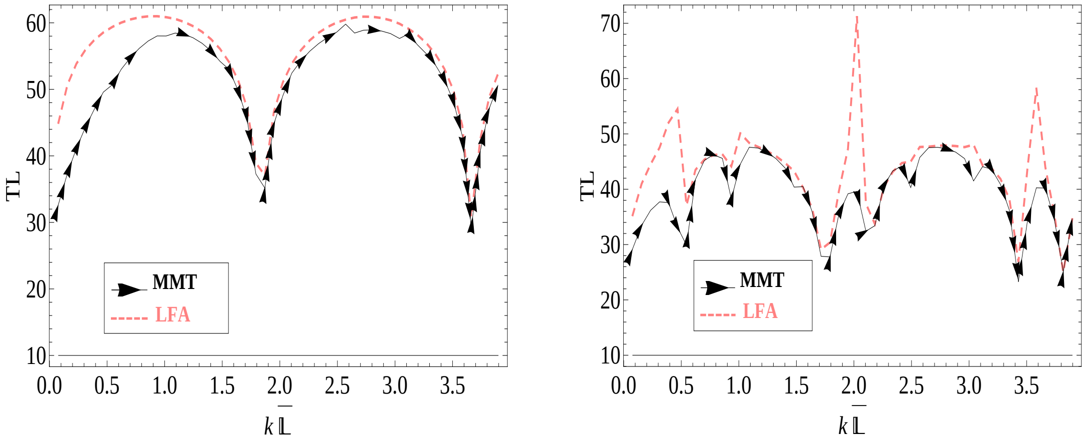

(c) All simply supported edges. (d) Simply supported at $(\pm L, b)$ and fixed at $(\pm L, h)$.

FIGURE 4.8: For structure-borne mode incident ($\ell = 0$): the transmission loss components against against silencer-half length with different set of edge conditions.

as referred in Fig. 4.5(a). Likewise, the rest fluctuation in peak values of TL for this case is according to the scattering powers curves are found in Fig. 4.5(a). On contrary to it, the TL goes to its minimum value at $L = 1.8$ and $L = 3.6$ when the case of fixed and simply supported edges is selected (see Figs. 4.9(b) and 4.9(c)). However, with a little variation in magnitude of transmission loss for all simply supported edges case it resembles with simply supported and fixed edges case. More TL is observed for simply supported edges than fixed edges, as depicted in Fig. 4.9(d). Clearly, a good agreement in TL curves obtained via MMT and LFA is seen in Figs. 4.8 and 4.9.

To validate MM solution the conditions at interfaces are matched graphically.

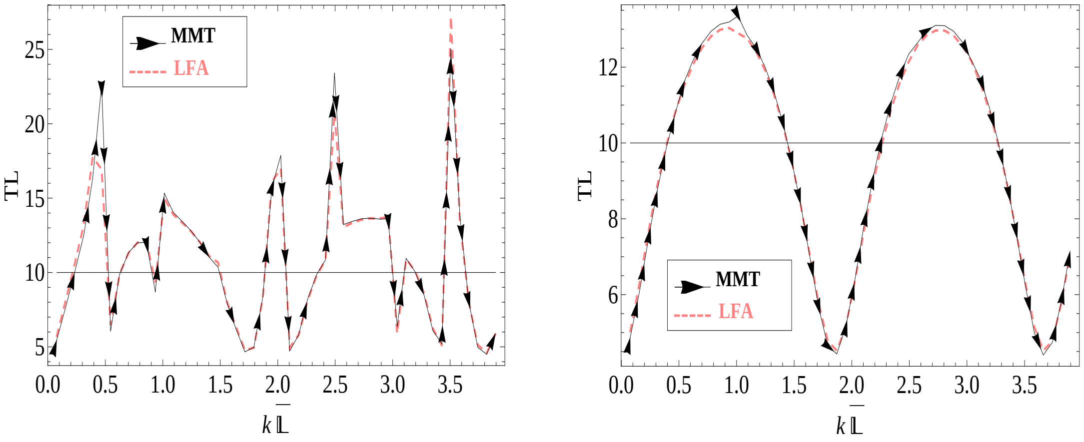

(a) All fixed edges.

(b) Fixed at $(\pm L, b)$ and simply supported at $(\pm L, h)$.

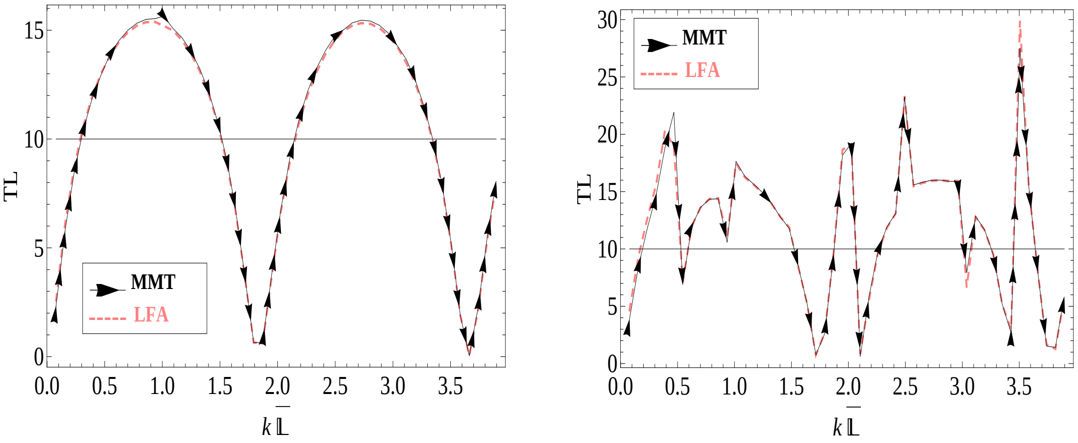

(c) All simply supported edges.

(d) Simply supported at $(\pm L, b)$ and fixed at $(\pm L, h)$.

FIGURE 4.9: For fluid-borne mode incident ($\ell = 1$): the transmission loss components against silencer-half length with different set of edge conditions.

It clearly validate the accuracy of truncated solution as well as the correction of performed algebra. Thus in Figs. 4.10-4.12, the real and imaginary parts of normal velocities and pressures are plotted at interfaces, $x = L$, and $x = -L$ respectively. From Figs. 4.10 and 4.11, it can be seen that the real and imaginary parts of non dimensional pressures and normal velocities show excellent agreement.

Both pairs of curves overlie for $a \leq y \leq b$ and normal velocities are zero, for $0 < y < a$ and $b < y < h$. Thus, conditions from equations (4.15) and (4.22) are fully satisfied. This is true as all relevant frequencies and the matching conditions are met to the same accuracy at interfaces $x = -L$. In Figs. 4.12(a) and 4.12(b), real and imaginary parts of nondimensional pressures overlie at (L, y), indicating

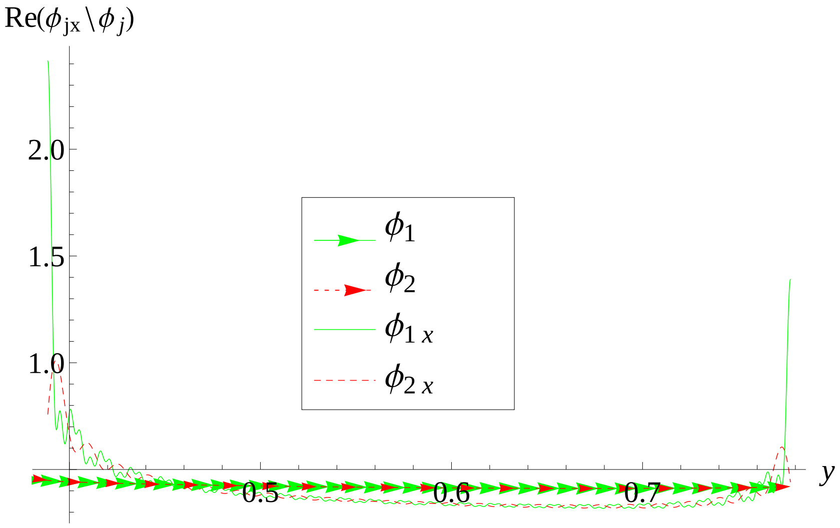

FIGURE 4.10: The real parts of normal velocity and pressure against duct height at interface $x = -L$ for edge conditions; fixed at $(-L, b)$ and simply supported at $(-L, h)$ with $f = 250$ Hz, $\overline{a} = 0.085m$, $\overline{b} = 0.17m$, $\overline{h} = 0.255m$ and $N = 150$

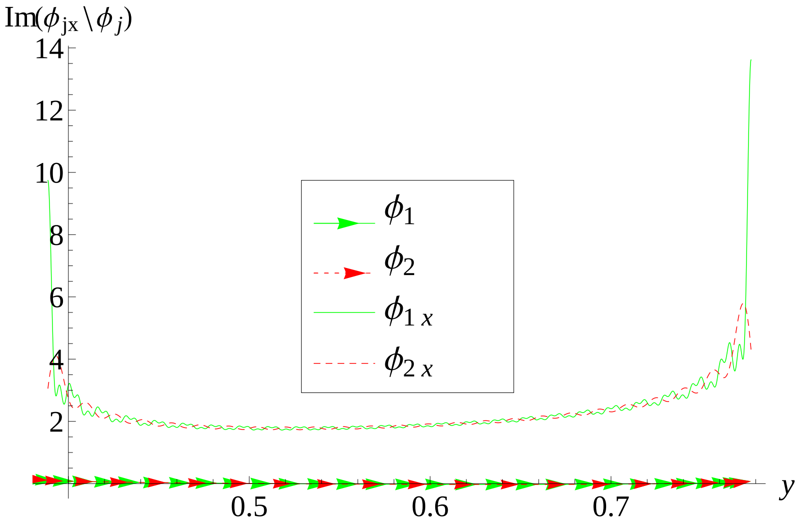

FIGURE 4.11: The imaginary parts of normal velocity and pressure against duct height at interface $x = -L$ for edge conditions; fixed at $(-L, b)$ and simply supported at $(-L, h)$ with $f = 250$ Hz, $\overline{a} = 0.085m$, $\overline{b} = 0.17m$, $\overline{h} = 0.255m$ and $N = 150$

excellent agreement. Furthermore, real and imaginary parts of the normal velocities are zero for $0 < y < a$ and $b < y < h$. For $a < y < b$ the normal velocities at (L, y) are in close agreement. Hence, equations (4.16) and (4.23) are fully satisfied. Although the two curves oscillate around their mean value and the amplitude of oscillation reduces significantly as y increases, except close to the corners.

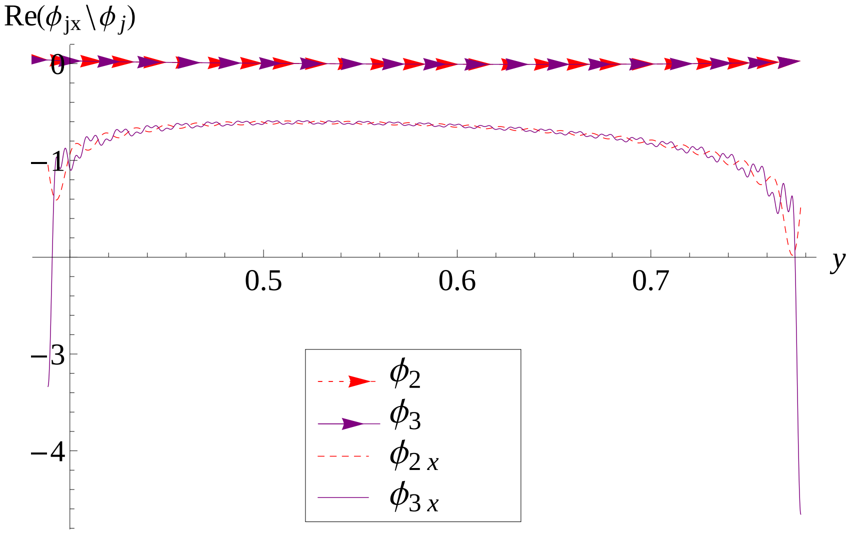

(a)

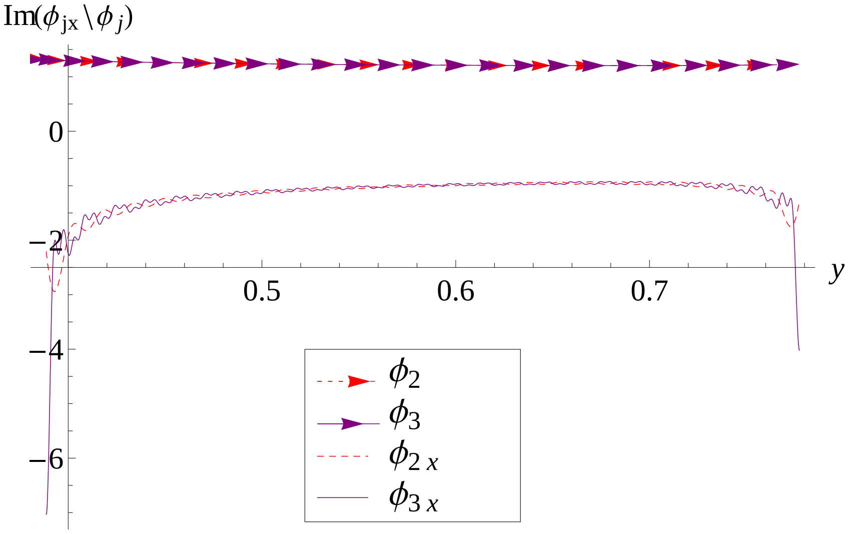

(b)

FIGURE 4.12: The real (a) and imaginary (b) parts of normal velocity and pressure against duct heights at interface $x = L$ for edge conditions; fixed at (L, b) and simply supported (L, h) with $f = 250$ Hz, $\overline{a} = 0.085m$, $\overline{b} = 0.17m$, $\overline{h} = 0.255m$ and $N = 150$

Chapter 5

Acoustic Analysis in Waveguide with Plates Boundaries and Lined Flanges

The analysis of fluid-structure coupled waveforms and their attenuation in a flexible waveguide is carried out in this chapter. The physical configuration contains expansion chamber connected with extended inlet/outlet by means of vertical lined flanges. The governing boundary value problem is solved by using MM technique. The associated eigen expansions of field potentials include non-orthogonal eigenfunctions and the related eigen-sub-systems are classified in non-SL category, whereby the use of generalized orthogonal characteristics has ensured the point-wise convergence of solution. The LFA which relies on the limited propagating modes is developed, and is compared with MM solution. Furthermore, the numerical experiments are provided to analyze the effects of absorbent linings and edge conditions on the attenuation of flexural modes. The guiding structure is exited with the structure-born mode incident as well as the fluid-born mode incident.

The chapter is organized as follows. In Section. 5.1, the BVP is formulated and the properties of flexural modes are explained. The MM solution is constructed in Section. 5.2, and LFA is established in Section. 5.3. The numerical results and discussion are provided in Section. 5.4.

5.1 Boundary Value Problem

The two-dimensional, infinite flexible waveguide comprising rigid base at $\bar{y} = 0$, $-\infty < \bar{x} < \infty$ and elastic plates at $\bar{y} = \bar{a}$, $|\bar{x}| > \bar{L}$ and $\bar{y} = \bar{b}$ $|\bar{x}| < \bar{L}$, where $\bar{b} > \bar{a}$, is assumed. Two vertical flanged strips at $\bar{x} = \pm\bar{L}$, $\bar{d} \leq \bar{y} \leq \bar{b}$ connect mutually the outside regions $|\bar{x}| > \bar{L}$, $\bar{0} < \bar{y} < \bar{a}$ with the central region $|\bar{x}| < \bar{L}$, $\bar{0} < \bar{y} < \bar{b}$ forming the inlet/outlet and the expansion chamber, respectively. An absorbent lining is introduced along the vertical strips inside of the expansion chamber. The inside of the waveguide is filled with the compressible fluid of density ρ and sound speed c whilst the outer side is in *vacuo*. Note that the overbars with variables denote the dimensional setting of coordinates. The physical configuration of the waveguide is shown in Fig. 5.1. The BVP is formulated by exiting the structure

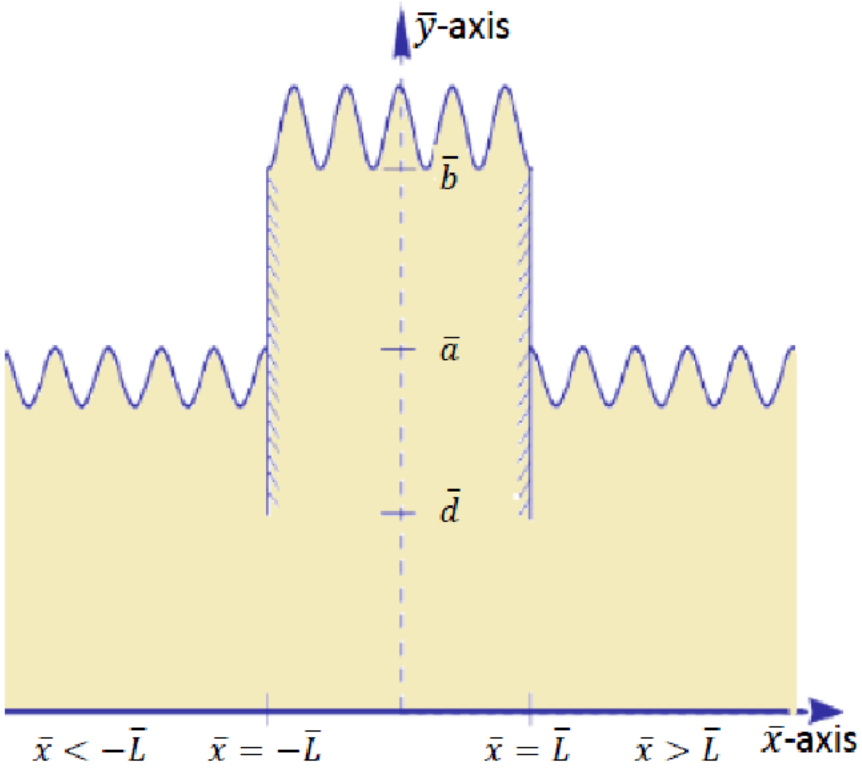

FIGURE 5.1: The physical configuration of the waveguide, wherein the wavy boundaries represent elastic plates.

through the duct mode of region $\bar{x} < -\bar{L}$, $\bar{0} < \bar{y} < \bar{a}$ which will propagate from negative $\bar{x}$-direction towards $|\bar{x}| < \bar{L}$. The absorbent surface, referred by Section. 2.3.1, in terms of dimensionless velocity potential is given by

$$\phi + i\zeta \mathbf{n} \cdot \nabla \phi = 0, \tag{5.1}$$

where $\zeta = (\rho c)^{-1} Z$ represents the dimensionless specific impedance of the lining. Thus, the time independent dimensionless fluid potential ϕ satisfies the Helmholtz's equation with unit wave number, that is

$$\left(\nabla^2 + 1\right) \phi = 0. \tag{5.2}$$

The acoustically rigid and elastic plate boundary conditions [75] in non-dimensional form are

$$\frac{\partial \phi}{\partial y} = 0, \qquad y = 0, \qquad -\infty < x < \infty \tag{5.3}$$

and

$$\left(\frac{\partial^4}{\partial x^4} - \mu_1^4\right) \frac{\partial \phi}{\partial y} - \alpha_1 \phi = 0, \qquad y = a, b, \qquad -\infty < x < \infty, \tag{5.4}$$

respectively. The quantities

$$\mu_1 = \left(\frac{12(1-\nu^2)c^2\rho_p}{k^2h^2E}\right)^{1/4} \qquad \text{and} \qquad \alpha_1 = \frac{12(1-\nu^2)c^2\rho}{k^3h^3E}, \tag{5.5}$$

represent the plate wavenumber and fluid loading parameters, respectively. Here E Young's modulus, ρ_p plate density, ν Poisson's ratio and h is the thickness of the plate. From (5.2)-(5.4), the eigenfunctions in regions $|x| > L, 0 \le y \le a$ (inlet/outlet) and $|x| < L, 0 \le y \le b$ (expansion chamber) are obtained $Y_1(\gamma_n, y) = \cosh(\gamma_n y)$ and $Y_2(\beta_n, y) = \cosh(\beta_n y)$, respectively. The corresponding eigenvalues $\gamma(\beta)$ be the roots of characteristic equations

$$\left((\varrho^2+1)^2 - \mu^4\right) \varrho \sinh(\varrho p) - \alpha_1 \cosh(\varrho p) = 0, \tag{5.6}$$

where $\varrho = \gamma$ when elastic plates lie along $p = a$ and $\varrho = \beta$ when elastic plate is situated at $p = b$. These roots are found numerically. The computation of all roots is essential for the successful implementation of MM approach. The root finding algorithms such as Newton's method or Secant's method largely depend upon the propriety of initial guesses, which at low Helmholtz numbers, can be identified by taking the low frequency approximations of the characteristic equations (5.6). Then the Argument Principle may be employed to check all roots in specified complex plane have been found successfully. The properties of such roots in details may be found in [99]. We consider only the positive roots (those roots lying in the upper half of the complex $\gamma(\beta)$ plane axis, which is deemed to include the positive real axis). It is found that there is always one real root, ($\gamma_0 > 0$, $\beta_0 > 0$) and an infinite number of imaginary roots, (γ_n, β_n), $n = 1, 2, 3, ...$, which are labeled in ascending order on imaginary axis. Also there exist pairs of complex roots for certain ranges of frequency. Such pairs appear when the imaginary plate mode tends to cut-off duct modes. The plots of the first 10 roots of the characteristic equation for the inlet/outlet duct of height 0.06m at a frequency of 4 Hz and for the expansion chamber of height 0.085m at 3Hz are shown in Fig. 5.2. These complex pairs of γ and β can be obtained by solving the equation [34]

$$i\mu = \sqrt{1 - \frac{n^2\pi^2}{k^2\bar{a}^2}} \qquad \text{and} \qquad i\mu = \sqrt{1 - \frac{n^2\pi^2}{k^2\bar{b}^2}}, \quad \text{for} \quad n = 1, 2, 3..., \tag{5.7}$$

respectively. These roots are arranged according to the magnitude of imaginary part in ascending order such that γ^*(or β^*) is followed by $-\gamma^*$(or $-\beta^*$).

To achieve the convergent system, the use of generalized orthogonality conditions is indispensable. Accordingly, we may get the generalized orthogonality relations

$$\alpha_1 \int_0^a Y_1(\gamma_n, y) Y_1(\gamma_m, y) dy = E_n \delta_{mn} - (\gamma_m^2 + \gamma_n^2 + 2) Y_1^{'}(\gamma_m, a) Y_1^{'}(\gamma_n, a) \tag{5.8}$$

and

$$\alpha_1 \int_0^b Y_2(\beta_n, y) Y_2(\beta_m, y) dy = G_n \delta_{mn} - (\beta_m^2 + \beta_n^2 + 2) Y_2^{'}(\beta_m, b) Y_2^{'}(\beta_n, b), \tag{5.9}$$

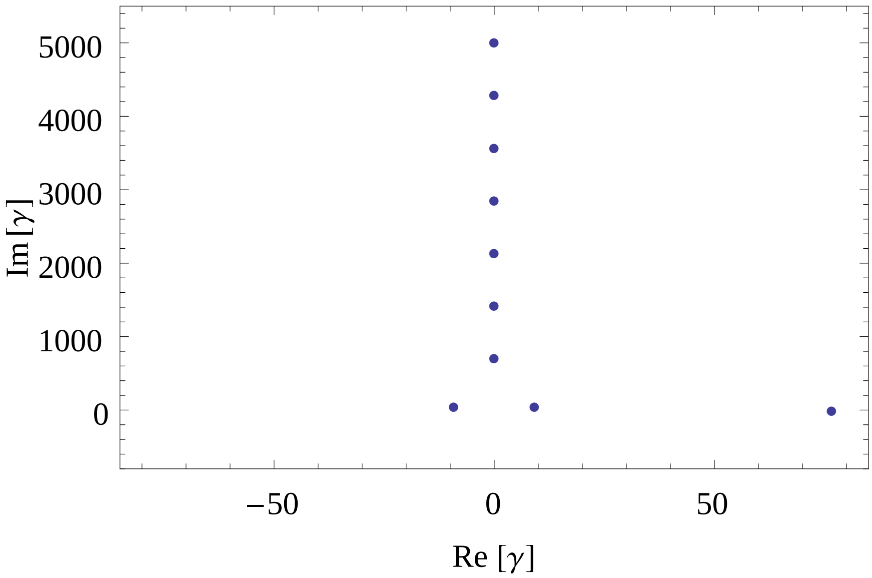

(a)

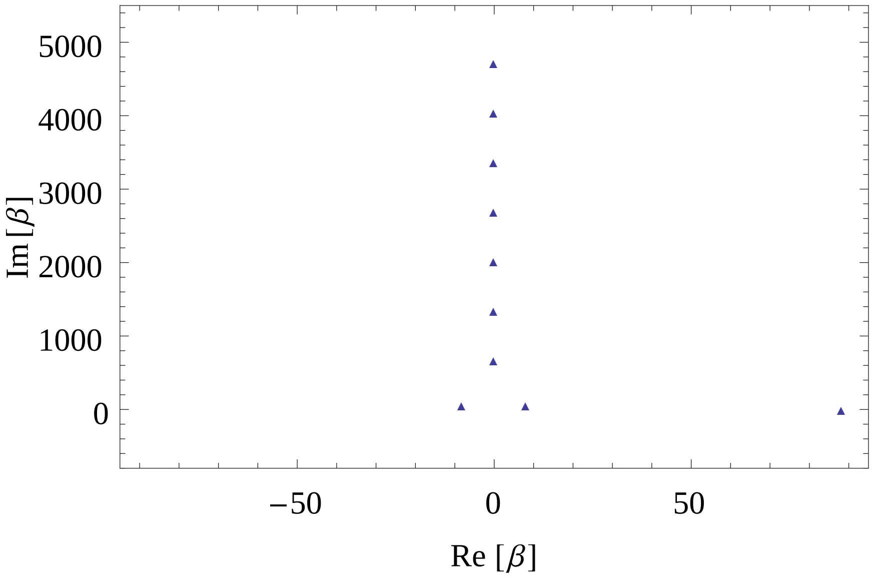

(b)

FIGURE 5.2: The first 10 roots of the characteristic equations: (a) is plotted at $f = 4$Hz with $\bar{a} = 0.06$m, (b) is plotted at $f = 3$Hz with $\bar{b} = 0.085$m.

where

$$E_m = \frac{\alpha_1 a}{2} + \frac{\alpha Y_1(\gamma_m, a) Y_{1m}^{'}(\gamma_m, a)}{2\gamma_m^2} + 2[(\gamma_m^2 + 1)Y_1^{'}(\gamma_m, a)]^2 \tag{5.10}$$

and

$$G_m = \frac{\alpha_1 b}{2} + \frac{\alpha Y_2(\beta_m, b) Y_2^{'}(\beta_m, b)}{2\beta_m^2} + 2[(\beta_m^2 + 1)Y_2^{'}(\beta_m, b)]^2. \tag{5.11}$$

Moreover it is worthwhile to comment before the solution presented, that mode-matching models the stronger singularities appearing at the corner of flange in velocity flux. The behavior of fluid potential at the singular point is already comprehensively addressed in the article [34].

5.2 Mode-Matching Solution

The MM solution of BVP developed in Section 5.1 is presented in this section. The time-independent fluid potentials for each duct region can be expressed as

$$\phi(x,y)=\begin{cases}\phi_1(x,y), & x\le -L, \quad 0\le y\le a\\ \phi_2(x,y), & |x|\le L, \quad 0\le y\le b\\ \phi_3(x,y), & x\ge L, \quad 0\le y\le a\end{cases}. \tag{5.12}$$

For the inlet, expansion chamber and outlet ducts, eigenfunction expansion for the fluid potentials takes the form

$$\phi_1(x,y)=F_\ell Y_1(\gamma_\ell,y)e^{i\eta_\ell(x+L)}+\sum_{n=0}^{\infty}A_nY_1(\gamma_n,y)e^{-i\eta_n(x+L)}, \tag{5.13}$$

$$\phi_2(x,y)=\sum_{n=0}^{\infty}\left(B_ne^{-i\nu_nx}+C_ne^{i\nu_nx}\right)Y_2(\beta_n,y), \tag{5.14}$$

$$\phi_3(x,y)=\sum_{n=0}^{\infty}D_nY_1(\gamma_n,y)e^{i\eta_n(x-L)}, \tag{5.15}$$

where $\{A_n,B_n,C_n,D_n\}$, $n=1,2,3...$ are the complex amplitudes of the n^{th} reflected and transmitted modes. Note that the first term on right hand side of the equation (5.13) indicates the incident field having forcing F_ℓ, wherein, index ℓ representing the incident force to be fundamental mode or higher mode. The quantities η_n and ν_n are the wave numbers and are defined in terms of eigenvalues as $\eta_n=(\gamma_n^2+1)^{1/2}$ and $\nu_n=(\beta_n^2+1)^{1/2}$, for $n=0,1,2,\ldots$. In order to find the amplitudes of the reflected and transmitted fields, we use the velocity flux conditions at interfaces, that yield

$$\int_0^a \phi_{1x}(-L,y)Y_1(\gamma_m,y)dy = \int_0^d \phi_{2x}(-L,y)Y_1(\gamma_m,y)dy \tag{5.16}$$

and

$$\int_0^a \phi_{3x}(L,y)Y_1(\gamma_m,y)dy = \int_0^d \phi_{2x}(L,y)Y_1(\gamma_m,y)dy. \tag{5.17}$$

Note that (5.16) and (5.17) relate the acoustic velocities of inlet and outlet regions to the acoustic velocity of central region at $x = \pm L$, that govern the formulations of symmetric and anti-symmetric mode amplitudes. These amplitude are obtained by substituting (5.13)-(5.15) into (5.16) and (5.17), then normalizing with the aid of the orthogonality relation (5.8), after simplification we may get

$$A_m = F_\ell\delta_{m\ell} - \Omega_m\{e_1 + (\gamma_m^2+2)e_2\}$$

$$+ \frac{\alpha_1}{\eta_m E_m}\sum_{n=0}^{\infty}\nu_n R_{nm}\left(B_n e^{i\nu_n L} - C_n e^{-i\nu_n L}\right), \tag{5.18}$$

$$D_m = \Omega_m\{e_3 + (\gamma_m^2+2)e_4\} - \frac{\alpha_1}{\eta_m E_m}\sum_{n=0}^{\infty}\nu_n R_{nm}\left(B_n e^{-i\nu_n L} - C_n e^{i\nu_n L}\right), \tag{5.19}$$

where,

$$\Omega_m = \frac{\Delta_{1m}}{\eta_m} \qquad \text{with} \qquad \Delta_{1m} = \frac{\gamma_m \sinh(\gamma_m a)}{E_m}, \tag{5.20}$$

$$e_1 = -i\phi_{1xyyy}(-L,a),\; e_2 = -i\phi_{1xy}(-L,a),\; e_3 = -i\phi_{3xyyy}(L,a),\; e_4 = -i\phi_{3xy}(L,a)$$

and

$$R_{nm} = \int_0^d \cosh(\beta_n y)\cosh(\gamma_m y)dy. \tag{5.21}$$

Now by adding (5.18) and (5.19), we find

$$A_m + D_m = F_\ell\delta_{m\ell} - \Omega_m\{(e_1-e_3) + (\gamma_m^2+2)(e_2-e_4)\}$$

$$+ \frac{2i\alpha_1}{\eta_m E_m}\sum_{n=0}^{\infty}\nu_n R_{nm}\sin(\nu_n L)\left(B_n + C_n\right). \tag{5.22}$$

Likewise, the subtraction of (5.18) from (5.19), leads to the following equation, that is,

$$\begin{aligned} A_m - D_m = F_\ell \delta_{m\ell} - \Omega_m\{(e_1 + e_3) + (\gamma_m^2 + 2)(e_2 + e_4)\} \\ + \frac{2\alpha_1}{\eta_m E_m} \sum_{n=0}^{\infty} \nu_n R_{nm} \cos(\nu_n L)\,(B_n - C_n)\,. \end{aligned} \tag{5.23}$$

Considering $\Psi_m^{\pm} = (A_m \pm D_m)$, $\chi_n^{\pm} = (B_n \pm C_n)$, $U_1^{\pm} = e_1 \mp e_3$ and $U_2^{\pm} = e_2 \mp e_4$ in (5.22) and (5.23), we finally achieve

$$\Psi_m^{+} = F_\ell \delta_{m\ell} - \{U_1^{+} + (\gamma_m^2 + 2)U_2^{+}\}\Omega_m + \frac{2i\alpha_1}{\eta_m E_m} \sum_{n=0}^{\infty} \nu_n R_{nm} \sin(\nu_n L)\chi_n^{+} \tag{5.24}$$

and

$$\Psi_m^{-} = F_\ell \delta_{m\ell} - \{U_1^{-} + (\gamma_m^2 + 2)U_2^{-}\}\Omega_m + \frac{2\alpha_1}{\eta_m E_m} \sum_{n=0}^{\infty} \nu_n R_{nm} \cos(\nu_n L)\chi_n^{-}, \tag{5.25}$$

respectively. The quantities $\Psi_m^{\pm} = (A_m \pm D_m)$ and $\chi_n^{\pm} = (B_n \pm C_n)$ denote the amplitudes of symmetric/anti-symmetric modes propagating in respective side regions and central regions that yield the amplitudes of modes propagating towards the positive and negative directions of the waveguide through expressions

- $A_m = \frac{1}{2}(\Psi_m^{+} + \Psi_m^{-})$ and $D_m = \frac{1}{2}(\Psi_m^{+} - \Psi_m^{-})$,
- $B_m = \frac{1}{2}(\chi_m^{+} + \chi_m^{-})$ and $C_m = \frac{1}{2}(\chi_m^{+} - \chi_m^{-})$.

Likewise, the pressure flux conditions at interfaces may take the form

$$\begin{aligned} \int_0^b \phi_2(-L, y) Y_2(\beta_m, y) dy = \int_0^d \phi_1(-L, y) Y_2(\beta_m, y) dy \\ - \frac{\zeta}{i} \int_d^b \phi_{2x}(-L, y) Y_2(\beta_m, y) dy \end{aligned} \tag{5.26}$$

and

$$\begin{aligned} \int_0^b \phi_2(L, y) Y_2(\beta_m, y) dy = \int_0^d \phi_3(L, y) Y_2(\beta_m, y) dy \\ + \frac{\zeta}{i} \int_d^b \phi_{2x}(L, y) Y_2(\beta_m, y) dy. \end{aligned} \tag{5.27}$$

Accordingly, (5.26) and (5.27) link the acoustic pressure of central region to the acoustic pressures of inlet and outlet regions at $x = \pm L$, and that may lead to the values of amplitudes of symmetric and anti-symmetric modes propagating in the central region. These are found by invoking (5.13)-(5.15) into (5.26) and (5.27), and normalizing with the help of OR (5.9), after some rearrangement, we have

$$\begin{aligned} B_m e^{i\nu_m L} + C_m e^{-i\nu_n L} = \Delta_{2m}\{e_5 + (\beta_m^2 + 2)e_6\} + \frac{\alpha_1}{G_m}\{F_\ell R_{m\ell} + \sum_{n=0}^{\infty} R_{mn} A_n\} \\ -\frac{\alpha_1 \zeta}{iG_m}\sum_{n=0}^{\infty} \nu_n\, T_{mn}(B_n e^{i\nu_n L} - C_n e^{-i\nu_n L}) \end{aligned} \tag{5.28}$$

and

$$\begin{aligned} B_m e^{-i\nu_m L} + C_m e^{i\nu_n L} = \Delta_{2m}\{e_7 + (\beta_m^2 + 2)e_8\} + \frac{\alpha_1}{G_m}\sum_{n=0}^{\infty} R_{mn} D_n \\ +\frac{\alpha_1 \zeta}{iG_m}\sum_{n=0}^{\infty} \nu_n\, T_{mn}(B_n e^{-i\nu_n L} - C_n e^{i\nu_n L}), \end{aligned} \tag{5.29}$$

where

$$\Delta_{2m} = \frac{\beta_m \sinh(\beta_m b)}{G_m}, \tag{5.30}$$

$$e_5 = \phi_{2yyy}(-L, b), \quad e_6 = \phi_{2y}(-L, b),$$

$$e_7 = \phi_{2yyy}(L, b), \quad e_8 = \phi_{2y}(L, b)$$

and

$$T_{mn} = \int_d^b \cosh(\beta_m y)\cosh(\beta_n y)dy. \tag{5.31}$$

However, the addition and subtraction of (5.28) and (5.29) reveal

$$\begin{aligned} B_m + C_m = \frac{\Delta_{2m}}{2\cos(\nu_m L)}\left\{(e_5 + e_7) + (\beta_m^2 + 2)(e_6 + e_8)\right\} \\ +\frac{\alpha_1}{2G_m \cos(\nu_m L)}\{F_\ell R_{m\ell} + \sum_{n=0}^{\infty} R_{mn}(A_n + D_n)\} \\ -\frac{\alpha_1 \zeta}{iG_m \cos(\nu_m L)}\{\sum_{n=0}^{\infty} \nu_n \sin(\nu_n L)\, T_{mn}(B_n + C_n)\} \end{aligned} \tag{5.32}$$

and

$$\begin{aligned} B_m - C_m = & \frac{\Delta_{2m}}{2i\sin(\nu_m L)}\left\{(e_5 - e_7) + (\beta_m^2 + 2)(e_6 - e_8)\right\} \\ & + \frac{\alpha_1}{2iG_m \sin(\nu_m L)}\{F_\ell R_{m0} + \sum_{n=0}^{\infty} R_{mn}(A_n - D_n)\} \\ & - \frac{\alpha_1 \zeta}{iG_m \sin(\nu_m L)}\{\sum_{n=0}^{\infty} \nu_n \cos(\nu_n L)\ T_{mn}(B_n - C_n)\}, \end{aligned} \tag{5.33}$$

respectively. Let us choose, the parameters $\chi_n^{\pm} = (B_n \pm C_n)$, $V_1^{\pm} = e_5 \pm e_7$ and $V_2^{\pm} = e_6 \pm e_8$ in (5.32) and (5.33), thus we obtain

$$\begin{aligned} \chi_m^{+} = & \frac{1}{2\cos(\nu_m L)}(V_1^{+} + (\beta_m^2 + 2)V_2^{+})\ \Delta_{2m} \\ & + \frac{1}{2\cos(\nu_m L)}\{\frac{\alpha_1}{G_m}(\Theta_m^{+}(R) + 2i\zeta \sum_{n=0}^{\infty} \nu_n \sin(\nu_n L)\ T_{mn}\ \chi_n^{+})\} \end{aligned} \tag{5.34}$$

and

$$\begin{aligned} \chi_m^{-} = & \frac{1}{2i\sin(\nu_m L)}(V_1^{-} + (\beta_m^2 + 2)V_2^{-})\Delta_{2m} \\ & + \frac{1}{2i\sin(\nu_m L)}\{\frac{\alpha_1}{G_m}(\Theta_m^{-}(R) + 2\zeta \sum_{n=0}^{\infty} \nu_n \cos(\nu_n L)\ T_{mn}\ \chi_n^{-})\}, \end{aligned} \tag{5.35}$$

respectively, where

$$\Theta_m^{\pm}(R) = F_\ell R_{m\ell} + \sum_{n=0}^{\infty} R_{mn}\Psi_n^{\pm}. \tag{5.36}$$

It is worthwhile noted that the additional unknowns $\{U_i^{\pm}, V_i^{\pm}\}$ for $i = 1, 2$ describe the behavior of plates at edges that are determined from the physical conditions on edges or joints. For elastic plates to be clamped, pin jointed or pivoted on edges the evaluation of these constants is discussed in accompanying subsections.

5.2.1 Clamped Edges

In case of clamped edges, the displacement and gradient are assumed to be zero, that is

$$\phi_{1y}(-L,a) = 0 = \phi_{3y}(L,a), \tag{5.37}$$

$$\phi_{1xy}(-L,a) = 0 = \phi_{3xy}(L,a), \tag{5.38}$$

$$\phi_{2y}(\pm L,b) = 0, \tag{5.39}$$

$$\phi_{2xy}(-L,b) = 0 = \phi_{2xy}(L,b). \tag{5.40}$$

These equations help to determine the values of additional constants $\{U_i, V_i\}$. Thus, the application of these equations yield $U_2^{\pm} = V_2^{\pm} = 0$, whereas, to achieve $U_1^{\pm}$, the multiplication of (5.24)-(5.25) with $\gamma_m \sinh(\gamma_m a)$ results

$$\begin{aligned}\Delta_{1m}E_m\Psi_m^{+} = \Delta_{1m}E_mF_\ell\delta_{m\ell} - \Omega_m^2E_m\eta_m\{U_1^{+} + (\gamma_m^2+2)U_2^{+}\}\\ +2i\alpha_1\Omega_m\sum_{n=0}^{\infty}\nu_nR_{nm}\sin(\nu_nL)\chi_n^{+},\end{aligned} \tag{5.41}$$

$$\begin{aligned}\Delta_{1m}E_m\Psi_m^{-} = \Delta_{1m}E_mF_\ell\delta_{m\ell} - \Omega_m^2E_m\eta_m\{U_1^{-} + (\gamma_m^2+2)U_2^{-}\}\\ +2\alpha_1\Omega_m\sum_{n=0}^{\infty}\nu_nR_{nm}\cos(\nu_nL)\chi_n^{-}.\end{aligned} \tag{5.42}$$

However, by using (5.13)-(5.15) into edge conditions (5.37) one finds

$$F_\ell\Delta_{1\ell}E_\ell + \sum_{n=0}^{\infty}\Delta_{1n}E_nA_n = 0, \tag{5.43}$$

$$\sum_{n=0}^{\infty}\Delta_{1n}E_nD_n = 0. \tag{5.44}$$

The addition and subtraction of (5.43) and (5.44) result

$$\sum_{n=0}^{\infty}\Delta_{1n}E_n\Psi_n^{\pm} = -F_\ell\Delta_{1\ell}E_\ell. \tag{5.45}$$

Now by taking summation over m from zero to infinity of (5.41) and (5.42), and then substituting (5.45), we accomplish

$$U_1^{-} = \frac{2}{S_1}\{F_\ell\Delta_{1\ell}E_\ell + \alpha_1\sum_{m=0}^{\infty}\sum_{n=0}^{\infty}\Omega_m\nu_nR_{nm}\cos(\nu_nL)\chi_n^{-}\} \tag{5.46}$$

and

$$U_1^+ = -\frac{2}{S_1}\{F_\ell\Delta_{1\ell}E_\ell + \alpha_1 i\sum_{m=0}^{\infty}\sum_{n=0}^{\infty}\Omega_m\nu_n R_{nm}\sin(\nu_n L)\chi_n^+\}. \tag{5.47}$$

Likewise, to determine $V_1^\pm$ the multiplication of $\Delta_{2m}G_m\nu_m\sin(\nu_m L)$ with (5.34)-(5.35), taking summation over m from zero to infinity, and then imposing edge conditions (5.40), finally conclude to

$$V_1^+ = -\frac{\alpha_1}{2S_2}\sum_{m=0}^{\infty}\Delta_{2m}\nu_m\tan(\nu_m L)\{\Theta_m^+(R) + 2i\zeta\sum_{n=0}^{\infty}\nu_n\sin(\nu_n L)T_{mn}\chi_n^+\} \tag{5.48}$$

and

$$V_1^- = -\frac{\alpha_1}{2iS_3}\sum_{m=0}^{\infty}\Delta_{2m}\nu_m\cot(\nu_m L)\{\Theta_m^-(R) + 2\zeta\sum_{n=0}^{\infty}\nu_n\cos(\nu_n L)T_{mn}\chi_n^-\}, \tag{5.49}$$

where

$$S_1 = \sum_{m=0}^{\infty}\Omega_{1m}^2 E_m\eta_m, \quad S_2 = \frac{1}{2}\sum_{m=0}^{\infty}\Delta_{2m}^2 G_m\nu_m\tan(\nu_m L)$$

and

$$S_3 = \frac{1}{2i}\sum_{m=0}^{\infty}\Delta_{2m}^2 G_m\nu_m\cot(\nu_m L).$$

5.2.2 Pin-Jointed Edges

For pin-jointed edge conditions, we assume zero displacement as well as zero bending moment over the edges, that reveal

$$\phi_{1y}(-L,a) = 0 = \phi_{3y}(L,a), \tag{5.50}$$

$$\phi_{1xxy}(-L,a) = 0 = \phi_{3yxx}(L,a), \tag{5.51}$$

$$\phi_{2y}(\pm L,b) = 0, \tag{5.52}$$

$$\phi_{2xxy}(-L,b) = 0 = \phi_{2yxx}(L,b). \tag{5.53}$$

From (5.52) it is found that $V_2^\pm = 0$, whereas, to obtain $U_1^\pm$, $U_2^\pm$, we multiply $\sum_{m=0}^{\infty}\Delta_{1m}E_m$ with (5.24) and $\sum_{m=0}^{\infty}\Delta_{1m}E_m\eta_m^2$ with (5.25), then by utilizing edge conditions (5.50) and (5.51), we achieve.

$$S_1U_1^+ + S_4U_2^+ = -2F_\ell\Delta_{1\ell}E_\ell - 2\alpha_1 i\sum_{m=0}^{\infty}\sum_{n=0}^{\infty}\Omega_m R_{nm}\chi_n^+\nu_n\sin(\nu_n L), \tag{5.54}$$

$$S_5U_1^+ + S_6U_2^+ = -2F_\ell\eta_\ell^2\Delta_{1\ell}E_\ell - 2\alpha_1 i\sum_{m=0}^{\infty}\sum_{n=0}^{\infty}\eta_m^2\Omega_m R_{nm}\chi_n^+\nu_n\sin(\nu_n L), \tag{5.55}$$

$$S_1U_1^- + S_4U_2^- = 2F_\ell\Delta_{1\ell}E_\ell + 2\alpha_1\sum_{m=0}^{\infty}\sum_{n=0}^{\infty}\Omega_m R_{nm}\chi_n^-\nu_n\cos(\nu_n L), \tag{5.56}$$

$$S_5U_1^- + S_6U_2^- = 2F_\ell\eta_\ell^2\Delta_{1\ell}E_\ell + 2\alpha_1\sum_{m=0}^{\infty}\sum_{n=0}^{\infty}\eta_m^2\Omega_m R_{nm}\chi_n^-\nu_n\cos(\nu_n L), \tag{5.57}$$

where

$$S_4 = \sum_{m=0}^{\infty}\Omega_m^2 E_m\eta_m(\gamma_m^2+2),\ \ S_5 = \sum_{m=0}^{\infty}\Delta_{1m}^2 E_m\eta_m \ \text{ and } S_6 = \sum_{m=0}^{\infty}\Delta_{1m}^2 E_m\eta_m(\gamma_m^2+2).$$

Now by solving (5.54) and (5.55) simultaneously give $\{U_1^+, U_2^+\}$ and likewise by solving (5.56) and (5.57) yield $\{U_1^-, U_2^-\}$. However, to get $V_1^\pm$, we multiply (5.34) with $\sum_{m=0}^{\infty}\Delta_{2m}G_m\nu_m^2\cos(\nu_m L)$ then using (5.53), it is found

$$V_1^+ = \alpha_1\sum_{m=0}^{\infty}\Delta_{2m}\nu_m^2\Theta_m^+(R) + 2i\alpha_1\zeta\sum_{m=0}^{\infty}\sum_{n=0}^{\infty}\Delta_{2m}\nu_m^2\nu_n\sin(\nu_n L)\ \chi_n^+\ T_{mn}. \tag{5.58}$$

On using the value of $\Theta_m^+(R)$ from (5.36), it is straightforward to obtain

$$\begin{aligned} V_1^+ = {} & \alpha_1 F_\ell\sum_{m=0}^{\infty}\Delta_{2m}\nu_m^2 R_{m\ell} + \alpha_1\sum_{m=0}^{\infty}\sum_{n=0}^{\infty}\Delta_{2m}\nu_m^2\Psi_n^+ R_{mn} \\ & + 2i\alpha_1\zeta\sum_{m=0}^{\infty}\sum_{n=0}^{\infty}\Delta_{2m}\nu_m^2\nu_n\sin(\nu_n L)\ \chi_n^+\ T_{mn}. \end{aligned} \tag{5.59}$$

Now to ensure the smooth convergence of summations appearing in (5.58), the use of the Green's identity (2.90) is crucial. Accordingly our problem, we fix the setting in equations (2.90)-(2.91) as $j = 1,\ \varrho = \gamma,\ p = a,\ \kappa = E$ for inlet/outlet duct region and $j = 2,\ \varrho = \beta,\ p = b,\ \kappa = G$ for expansion chamber. For this, the integrals of R_{mn} and T_{mn} may be splitted as

$$R_{mn} = \int_0^b \cosh(\beta_m y)\cosh(\gamma_n y)dy - \int_d^b \cosh(\beta_m y)\cosh(\gamma_n y)dy \tag{5.60}$$

and

$$T_{mn} = \int_0^b \cosh(\beta_m y)\cosh(\beta_n y)dy - \int_0^d \cosh(\beta_m y)\cosh(\beta_n y)dy. \tag{5.61}$$

By using these values, (5.58) can be expressed as

$$\begin{aligned} V_1^+ = \alpha_1 F_\ell \sum_{m=0}^{\infty} \Delta_{2m}\nu_m^2\{\int_0^b \cosh(\beta_m y)\cosh(\gamma_\ell y)dy - P_{m\ell}\} \\ +\alpha_1 \sum_{n=0}^{\infty}\sum_{m=0}^{\infty} \Delta_{2m}\nu_m^2\Psi_n^+\{\int_0^b \cosh(\beta_m y)\cosh(\gamma_n y)dy - P_{mn}\} \\ +2i\alpha_1\zeta \sum_{m=0}^{\infty}\sum_{n=0}^{\infty} \Delta_{2m}\nu_m^2\nu_n\sin(\nu_n L)\chi_n^+\{\int_0^b \cosh(\beta_m y)\cosh(\beta_n y)dy - Q_{mn}\}, \end{aligned} \tag{5.62}$$

where

$$P_{mn} = \int_d^b \cosh(\beta_m y)\cosh(\gamma_n y)dy \tag{5.63}$$

and

$$Q_{mn} = \int_0^d \cosh(\beta_m y)\cosh(\beta_n y)dy. \tag{5.64}$$

However, form the Green's identity (2.90) in the domain $0 \le y \le b$, it is noted that

$$\sum_{m=0}^{\infty} \Delta_{2m}\nu_m^2 \int_0^b \cosh(\beta_m y)\cosh(\gamma_\ell y)dy = 0, \tag{5.65}$$

$$\sum_{n=0}^{\infty} \Psi_n^+ \sum_{m=0}^{\infty} \Delta_{2m}\nu_m^2 \int_0^b \cosh(\beta_m y)\cosh(\gamma_n y)dy = 0, \tag{5.66}$$

$$\sum_{n=0}^{\infty} \nu_n\sin(\nu_n L)\chi_n^+ \sum_{m=0}^{\infty} \Delta_{2m}\nu_m^2 \int_0^b \cosh(\beta_m y)\cosh(\beta_n y)dy = 0. \tag{5.67}$$

Hence, on making use of (5.65)-(5.67), (5.62) yields

$$V_1^+ = -\alpha_1 \sum_{m=0}^{\infty} \nu_m^2\Delta_{2m}\{\Theta_m^+(P) + 2i\zeta \sum_{n=0}^{\infty} \nu_n\sin(\nu_n L)Q_{mn}\chi_n^+\}. \tag{5.68}$$

In a similar fashion, we find the value of V_1^-, that is

$$V_1^- = -\alpha_1 \sum_{m=0}^{\infty} \nu_m^2\Delta_{2m}\{\Theta_m^-(P) - 2\zeta \sum_{n=0}^{\infty} \nu_n\cos(\nu_n L)Q_{mn}\chi_n^-\}, \tag{5.69}$$

where

$$P_{mn} = \int_d^b \cosh(\beta_m y)\cosh(\gamma_n y)dy \qquad \text{and} \quad Q_{mn} = \int_0^d \cosh(\beta_m y)\cosh(\beta_n y)dy.$$

5.2.3 Pivoted Edges

For pivoted edges we assume zero displacement and continuous gradient and bending moment at finite edges of the plates. Physically, the conditions are realistic only if $y = a = b$ and comprise formulation as follows [34]

$$\phi_{1y}(-L, y) = 0 = \phi_{3y}(L, y), \tag{5.70}$$

$$\phi_{1xy}(-L, y) = \phi_{2yx}(-L, y), \tag{5.71}$$

$$\phi_{3xy}(L, y) = \phi_{2yx}(L, y), \tag{5.72}$$

$$\phi_{2y}(\pm L, y) = 0, \tag{5.73}$$

$$\phi_{1xxy}(-L, y) = \phi_{2yxx}(-L, y), \tag{5.74}$$

$$\phi_{3xxy}(L, y) = \phi_{2yxx}(L, y). \tag{5.75}$$

From (5.73), we find $V_2^{\pm} = 0$, however, to get the values of $U_1^{\pm}, U_2^{\pm}, V_1^{\pm}$, we multiply the factors $\sum_{m=0}^{\infty} \eta_m \Delta_{1m} E_m$ with (5.24) and (5.25), $2i\sum_{m=0}^{\infty} \Delta_{2m} G_m \nu_m \sin(\nu_m L)$ with (5.34) and $2\sum_{m=0}^{\infty} \Delta_{2m} G_m \nu_m \cos(\nu_m L)$ with (5.35), then the imposition of the edge conditions (5.71)- (5.72) and (5.74) -(5.75) along with Green's functions identities (2.90)-(2.93). Eventually, the following systems of equations are found

$$\begin{aligned} S_2V_1^+ + S_7U_2^+ = {} & -\frac{\alpha_1}{2}\sum_{m=0}^{\infty} \nu_m \tan(\nu_m L)\Delta_{2m}\Theta_m^+(R) \\ & -\alpha_1 \sum_{m=0}^{\infty}\sum_{n=0}^{\infty} \chi_n^+ \nu_n \sin(\nu_n L)\{\Delta_{1m}P_{nm} + i\zeta\Delta_{2m}\nu_m \tan(\nu_m L)T_{mn}\}, \end{aligned} \tag{5.76}$$

$$\begin{aligned} S_5U_1^+ + S_6U_2^+ - V_1^+ = {} & -2F_\ell \eta_\ell^2 \Delta_{1\ell} E_\ell + \alpha_1 \sum_{m=0}^{\infty} \nu_m^2 \Delta_{2m}\Theta_m^+(P) \\ & -2\alpha_1 \sum_{m=0}^{\infty}\sum_{n=0}^{\infty} \chi_n^+ \nu_n \sin(\nu_n L)\{i\eta_m \Delta_{1m} R_{nm} - i\zeta\nu_m^2 \Delta_{2m} Q_{mn}\}, \end{aligned} \tag{5.77}$$

$$\begin{aligned}S_3V_1^- + S_8U_2^- &= -\frac{\alpha_1}{2i}\sum_{m=0}^{\infty}\nu_m\cot(\nu_mL)\Delta_{2m}\Theta_m^-(R)\\ &-\alpha_1\sum_{m=0}^{\infty}\sum_{n=0}^{\infty}\chi_n^-\nu_n\cos(\nu_nL)\{\Delta_{1m}P_{nm} - i\zeta\Delta_{2m}\nu_m\cot(\nu_mL)T_{mn}\}\end{aligned} \tag{5.78}$$

and

$$\begin{aligned}S_5U_1^- + S_6U_2^- + V_1^- &= 2F_\ell\eta_\ell^2\Delta_{1\ell}E_\ell - \alpha_1\sum_{m=0}^{\infty}\nu_m^2\Delta_{2m}\Theta_m^-(P)\\ &+2\alpha_1\sum_{m=0}^{\infty}\sum_{n=0}^{\infty}\chi_n^-\nu_n\cos(\nu_nL)\{\eta_m\Delta_{1m}R_{nm} - \zeta\Delta_{2m}\nu_m^2Q_{mn}\},\end{aligned} \tag{5.79}$$

where

$$S_7 = -\frac{1}{2i}\sum_{m=0}^{\infty}\Delta_{1m}^2\gamma_m^2E_m \qquad \text{and} \quad S_8 = -\frac{1}{2}\sum_{m=0}^{\infty}\Delta_{1m}^2\gamma_m^2E_m.$$

The simultaneous solution of (5.54) and (5.76)-(5.77) reveals $\{U_1^+, U_2^+, V_1^+\}$, and (5.56) and (5.78)-(5.79) yield $\{U_1^-,\, U_2^-, V_1^-\}$. Hence, two systems of infinite equations defined by (5.24) and (5.25) are obtained. These can be truncated and solved numerically for different set of edge conditions to determine the unknown amplitudes.

5.3 Low-Frequency Approximation

It is useful to be able to compare the results obtained via MM approach and thus for this purpose, an approximate solution LFA is developed. Therefore, the field potentials in duct regions are approximated as

$$\phi_1(x,y) \approx F_\ell Y_1(\gamma_\ell, y)e^{i\eta_\ell(x+L)} + \sum_{n=0}^{J_1}A_nY_1(\gamma_n, y)e^{-i\eta_n(x+L)}, \tag{5.80}$$

$$\phi_2(x,y) \approx \sum_{n=0}^{J_2}\left(B_ne^{-i\nu_nx} + C_ne^{i\nu_nx}\right)Y_2(\beta_n, y), \tag{5.81}$$

$$\phi_3(x,y) \approx \sum_{n=0}^{J_3}D_nY_1(\gamma_n, y)e^{i\eta_n(x-L)}, \tag{5.82}$$

where J_1, J_2 and J_3 stand for the number of modes propagating the inlet region, expansion chamber and outlet region, respectively. The values of J_1, J_2 and J_3 must be in accordance with geometrical and imposed conditions. The coefficients A_n, $n = 0, 1....J_1$, $\{B_n, C_n\}$, $n = 0, 1, ...J_2$ and D_n, $n = 0, 1....J_3$ are unknowns. These are found by considering the continuity conditions of mean pressure and velocity flux at interfaces. The continuity conditions of mean pressures expressed by

$$\int_0^d \{\phi_1(-L, y) - \phi_2(-L, y)\}\, dy = 0 \tag{5.83}$$

and

$$\int_0^d \{\phi_3(L, y) - \phi_2(L, y)\}\, dy = 0 \tag{5.84}$$

lead to

$$\sum_{n=0}^{J_1} \Upsilon(\gamma_n, d)\Psi_n^+ - 2\sum_{n=0}^{J_2} \Upsilon(\beta_n, d)\cos(\nu_n L)\chi_n^+ = F_\ell \Upsilon(\gamma_\ell, d) \tag{5.85}$$

and

$$\sum_{n=0}^{J_1} \Upsilon(\gamma_n, d)\Psi_n^- - 2i\sum_{n=0}^{J_2} \Upsilon(\beta_n, d)\sin(\nu_n L)\chi_n^- = F_\ell \Upsilon(\gamma_\ell, d) \tag{5.86}$$

respectively, where

$$\Upsilon(x, y) = x^{-1} \sinh(xy), \tag{5.87}$$

if $x = \gamma_n$ represents the inlet/outlet duct region and $x = \beta_n$ denotes the expansion chamber region. Similarly, the velocities flux conditions at interfaces defined by

$$\int_0^d \{\phi_{1x}(-L, y) - \phi_{2x}(-L, y)\}\, dy = 0, \tag{5.88}$$

$$\int_0^d \{\phi_{3x}(L, y) - \phi_{2x}(L, y)\}\, dy = 0, \tag{5.89}$$

yield the following systems of equations

$$\sum_{n=0}^{J_3}\Upsilon(\gamma_n,d)\eta_n\Psi_n^+ - 2\sum_{n=0}^{J_2}\Upsilon(\beta_n,d)\nu_n\cos(\nu_nL)\chi_n^- = \eta_\ell F_\ell\Upsilon(\gamma_\ell,d) \tag{5.90}$$

and

$$\sum_{n=0}^{J_3}\Upsilon(\gamma_n,d)\eta_n\Psi_n^- - 2i\sum_{n=0}^{J_2}\Upsilon(\beta_n,d)\nu_n\sin(\nu_nL)\chi_n^+ = \eta_\ell F_\ell\Upsilon(\gamma_\ell,d). \tag{5.91}$$

However, the surfaces bounding vertically the regions at $|x| > L$ are rigid, therefore, the normal velocities along these surfaces satisfy

$$\int_d^a \phi_{1x}(-L,y)\ dy = 0 \qquad \text{and} \qquad \int_d^a \phi_{3x}(L,y)\ dy = 0, \tag{5.92}$$

which lead to

$$\sum_{n=0}^{J_1}(\Upsilon(\gamma_n,a)-\Upsilon(\gamma_n,d))\eta_n\Psi_n^\pm = F_\ell\eta_\ell(\Upsilon(\gamma_\ell,a)-\Upsilon(\gamma_\ell,d)), \tag{5.93}$$

where $J_1 = J_3$. However, the inner surfaces of the flange facing into the region at $|x| < L$ contain impedance type flux conditions, that is

$$\int_d^b \{\phi_2(-L,y) - i\zeta\phi_{2x}(-L,y)\}\ dy = 0 \tag{5.94}$$

and

$$\int_d^b \{\phi_2(L,y) + i\zeta\phi_{2x}(L,y)\}\ dy = 0, \tag{5.95}$$

which reveal

$$\sum_{n=0}^{J_2}(\Upsilon(\beta_n,b)-\Upsilon(\beta_n,d))\left(\cos(\nu_nL) - i\zeta\nu_n\sin(\nu_nL)\right)\chi_n^+ = 0 \tag{5.96}$$

and

$$\sum_{n=0}^{J_2}(\Upsilon(\beta_n,b)-\Upsilon(\beta_n,d))\left(i\sin(\nu_nL) - \zeta\nu_n\cos(\nu_nL)\right)\chi_n^- = 0. \tag{5.97}$$

respectively. Furthermore, the effects of edge conditions are assimilated in subsequent subsections.

5.3.1 Clamped Edges

For clamped edges, the equations (5.37)-(5.40) in association with the approximated field potentials (5.80)-(5.82) give

$$\sum_{n=0}^{J_1} \Delta_{1n} E_n \Psi_n^{\pm} = -F_\ell \Delta_{1\ell} E_\ell, \tag{5.98}$$

$$\sum_{n=0}^{J_2} \Delta_{2n} G_n \cos(\nu_n L) \chi_n^{+} = 0, \tag{5.99}$$

$$\sum_{n=0}^{J_2} \Delta_{2n} G_n \sin(\nu_n L) \chi_n^{-} = 0, \tag{5.100}$$

$$\sum_{n=0}^{J_1} \Delta_{1n} E_n \eta_n \Psi_n^{\pm} = -F_\ell \eta_\ell \Delta_{1\ell} E_\ell, \tag{5.101}$$

$$\sum_{n=0}^{J_2} \Delta_{2n} G_n \nu_n \sin(\nu_n L) \chi_n^{+} = 0, \tag{5.102}$$

and

$$\sum_{n=0}^{J_2} \Delta_{2n} G_n \nu_n \cos(\nu_n L) \chi_n^{-} = 0. \tag{5.103}$$

For this set of edge conditions we set $J_1 = J_2 = J_3 = 3$ and compute the unknown modal coefficients $\{A_n, B_n, C_n, D_n\}$ through solving (5.85)-(5.86), (5.90)-(5.91), (5.93) and (5.96)-(5.103) simultaneously.

5.3.2 Pin-Jointed Edges

For this set of edge conditions, (5.51) and (5.53) together with (5.80)-(5.82) lead to the following equations

$$\sum_{n=0}^{J_1}\Delta_{1n}E_n\eta_n^2\Psi_n^{\pm}=-F_\ell\eta_\ell^2\Delta_{1\ell}E_\ell, \tag{5.104}$$

$$\sum_{n=0}^{J_2}\Delta_{2n}G_n\nu_n^2\cos(\nu_nL)\chi_n^{+}=0 \tag{5.105}$$

and

$$\sum_{n=0}^{J_2}\Delta_{2n}G_n\nu_n^2\sin(\nu_nL)\chi_n^{-}=0. \tag{5.106}$$

Again we set $J_1=J_2=J_3=3$ and solve (5.85)-(5.86), (5.90)-(5.91), (5.93), (5.96)-(5.100) and (5.104)-(5.106) simultaneously for unknown modal coefficients $\{A_n,B_n,C_n,D_n\}$.

5.3.3 Pivoted Edges

In case of pivoted edges, the conditions (5.71)-(5.72) and (5.74)-(5.75) in association with the approximated field potentials (5.80)-(5.82) yield

$$\sum_{n=0}^{J_1}\eta_n\Delta_{1n}E_n\Psi_n^{+}-2\sum_{n=0}^{J_2}\Delta_{2n}G_n\nu_n\cos(\nu_nL)\chi_n^{-}=-F_\ell\eta_\ell\Delta_{1\ell}E_\ell, \tag{5.107}$$

$$\sum_{n=0}^{J_1}\eta_n\Delta_{1n}E_n\Psi_n^{-}-2i\sum_{n=0}^{J_2}\Delta_{2n}G_n\nu_n\sin(\nu_nL)\chi_n^{+}=-F_\ell\eta_\ell\Delta_{1\ell}E_\ell, \tag{5.108}$$

$$\sum_{n=0}^{J_1}\eta_n^2\Delta_{1n}E_n\Psi_n^{+}-2\sum_{n=0}^{J_2}\Delta_{2n}G_n\nu_n^2\cos(\nu_nL)\chi_n^{+}=-F_\ell\eta_\ell^2\Delta_{1\ell}E_\ell \tag{5.109}$$

and

$$\sum_{n=0}^{J_1}\eta_n^2\Delta_{1n}E_n\Psi_n^{-}-2i\sum_{n=0}^{J_2}\Delta_{2n}G_n\nu_n^2\sin(\nu_nL)\chi_n^{-}=-F_\ell\eta_\ell^2\Delta_{1\ell}E_\ell. \tag{5.110}$$

Consequently by solving (5.85)-(5.86), (5.90)-(5.91), (5.93), (5.96)-(5.100) and (5.107)-(5.110) the unknown modal coefficients $\{A_n,B_n,C_n,D_n\}$ are found, where $J_1=J_2=J_3=3$.

5.4 Numerical Results and Discussion

The graphical results presented in this section are obtained through the truncated form of MM solution having truncation parameter N. The numerical experiments are performed by fixing the specific impedance $\zeta = \xi + i\chi$ to fibrous sheet with parameters $\xi = 2.1,\ \chi = 2.5$ and to perforated sheet with values $\xi = 2.1,\ \chi = 2.5$. The regimes of parameters as given in [100] that specify the fibrous and perforated coatings are $\xi = 0.5, -1 < \chi < 3$, and $0 < \xi < 3, -1 < \chi < 3$, respectively. The power absorbed (P_{abs}) due to the layer of lining [102] can be given as

$$P_{abs} = P_i - P_r - P_t. \tag{5.111}$$

The expressions for P_r in the inlet region and the P_t in the outlet region can be determined by using the definition given by [34] and that are found

$$P_r = \operatorname{Re}\left\{\frac{1}{\alpha_1}\sum_{n=0}^{\infty}|A_n|^2 E_n \eta_n\right\} \tag{5.112}$$

and

$$P_t = \operatorname{Re}\left\{\frac{1}{\alpha_1}\sum_{n=0}^{\infty}|D_n|^2 E_n \eta_n\right\}, \tag{5.113}$$

where the incident power is being scaled at unity. However, the performance of a HVAC silencer [95] is usually measured by the TL as

$$\mathrm{TL} = -10\log_{10}\left(\frac{P_t}{P_i}\right). \tag{5.114}$$

For numerical computation the elastic plates of aluminum having thickness $\bar{h} = 0.0006$ m and density $\rho_p = 2700$ kgm^{-3} are assumed. The values of Young's modulus and Poisson's ratio are $E = 7.2 \times 10^{10}$ Nm^{-2} and $\upsilon = 0.34$, respectively, while, sound speed $c = 344$ ms^{-1} and density of air $\rho_a = 1.2$ kgm^{-3} remain fixed [34]. Two different incident fields are considered; the structural-borne fundamental mode ($\ell = 0$) and the fluid-borne second mode ($\ell = 1$). The later case include only the results obtained via MM technique. The TL against frequency with and without cavity inclusion is discussed in following two cases.

5.4.1 Case 1: $b > a > d$

The graphical results of TL verses frequency in the presence of chamber cavity (which refers $b > a > d$) with two different sets of edge conditions and two types porous lining are shown in Fig. 5.3. The graphs in Fig. 5.3(a) reveal the case when a perforated type sheet ($\xi = 2.1,\ \chi = 2.5$) is assumed along the surface of vertical flanges in the the expansion chamber, whereas, the dimensions of waveguide are fixed with $\bar{a} = 0.06$m, $\bar{b} = 0.085$m, $\bar{d} = 0.045$m and $\bar{L} = 0.02$m. The TL against frequency with geometrical setting containing all clamped or all pin-jointed edge conditions is shown in Fig. 5.3 while the system being radiated through the structure borne mode incident. Accordingly, maximum energy propagates along the structure and a stop-band produced in regime 2Hz $\leq f \leq$ 190Hz suppresses as the next mode of inlet duct becomes cut-on at $f = 191$ Hz which is basically the fluid-borne mode. Nevertheless, when both modes start propagating the TL starts increasing with increasing frequencies. It clearly reveals more reflection and absorption with the participation of additional modes.

Now by changing the edge conditions from all clamped to all pin-jointed more leakage in compressional waves due zero bending moment at edges occurs, thereby yields enhancement of TL as compared with the magnitude of TL with clamped edges (Fig. 5.3(a)). Moreover a good agreement in MM technique and LFA results is found in frequency regime $f \leq$ 600Hz. In Fig. 5.3(b) fibrous sheet is assumed instead of perforated lining by taking $\xi = 0.5,\ \chi = 0.5$. More absorption with this type of lining is obtained for both (clamped & pin-jointed edges) with similar pattern of TL. Also extra leakage of compressional waves with pin-jointed conditions is clearly evident. However, the MM and LFA solutions dissimulate on some frequency ranges, (see Fig. 5.3(b)). The fact is due to the inability of LFA to cater the information around the complex eigen values. The occurrence of such eigen values is depicted in (5.7) and comprehensively debated in [34].

Fig. 5.4 depicts the TL results when the structure is radiated through the fluid-borne mode incident whereas, the dimensional duct heights are fixed as: $\bar{a} = 0.1$m, $\bar{b} = 0.15$m, $\bar{d} = 0.06$m and half-length of expansion chamber $\bar{L} = 0.25$m. Moreover,

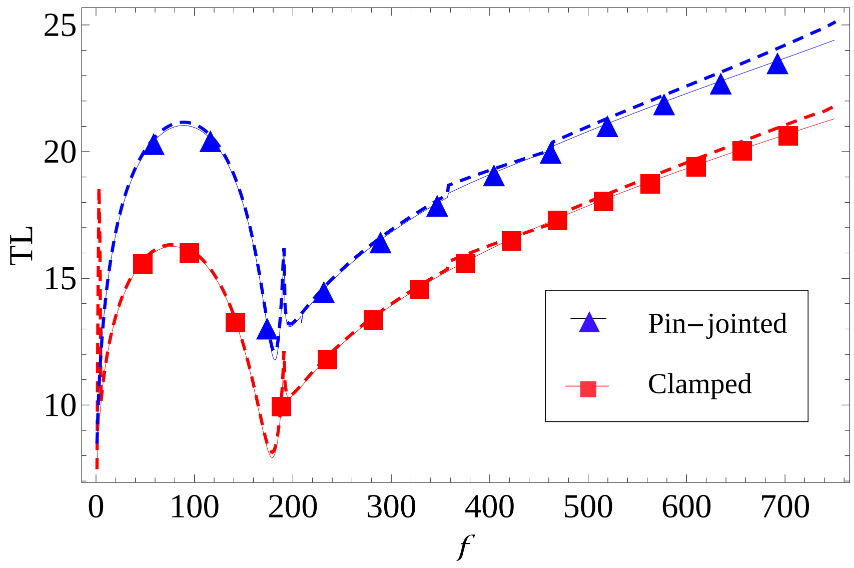

(a)

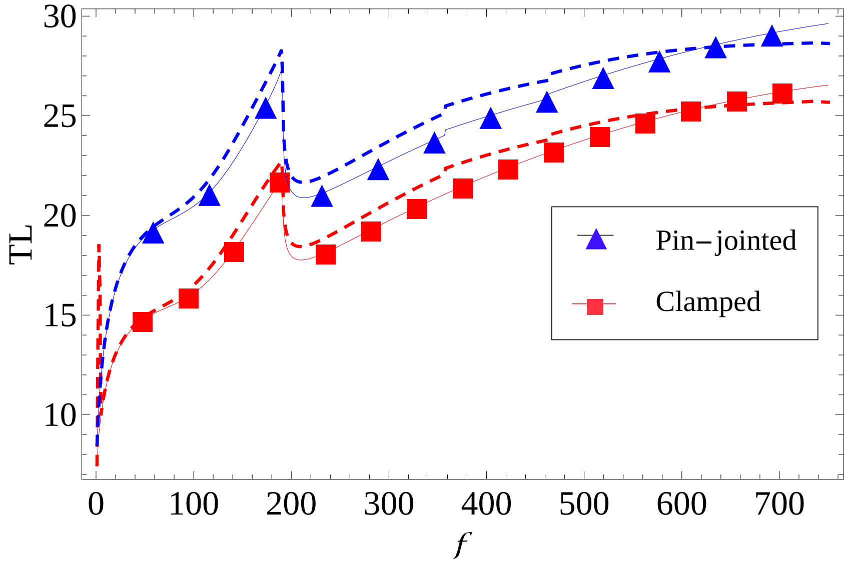

(b)

FIGURE 5.3: The transmission loss against frequency for fundamental mode incident ($\ell = 0$) Via LFA $(---)$ and MM (■▲) with (N = 40): (a) perforated lining and (b) fibrous lining.

the absorbent parameters for fibrous lining are assumed to have: $\xi = 0.5$, $\chi = 0.5$, while for perforated lining contains values: $\xi = 2.1$, $\chi = 2.5$. The curves of Fig. 5.4 are displayed with the frequency range 148Hz $\leq f \leq$ 1500Hz. The starting frequency $f =$ 148Hz is chosen such as to make sure that the fluid-born mode incident becomes cut-on. The results show that the all clamped and all pin-joint edge conditions have no apparent effect on the acoustical performance

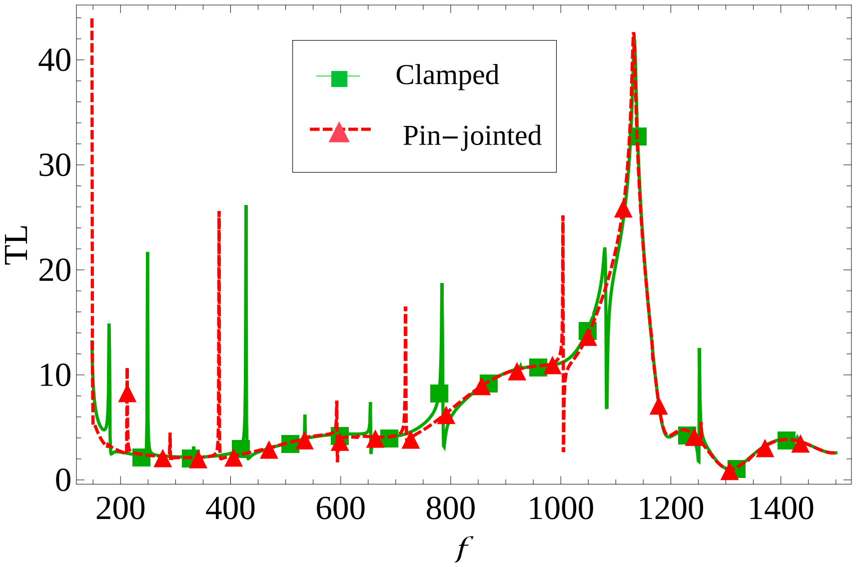

(a)

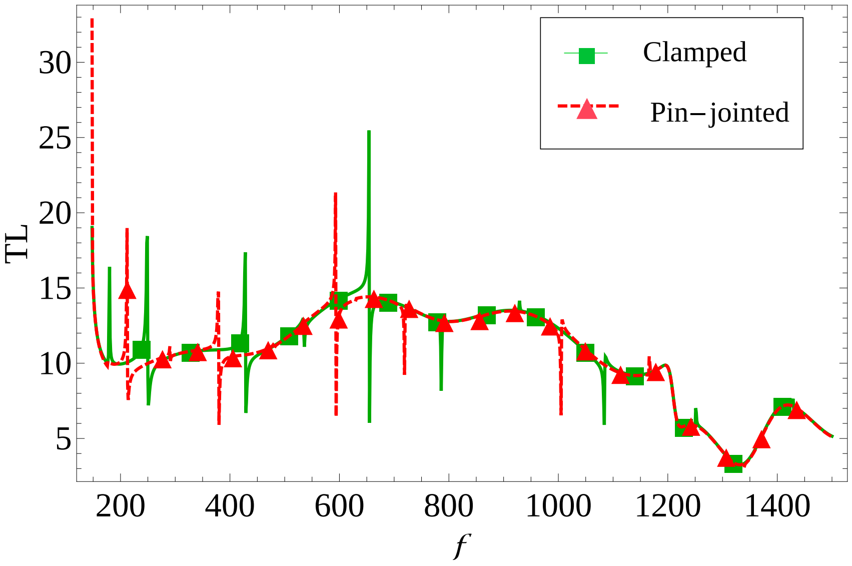

(b)

FIGURE 5.4: The transmission loss against frequency for fluid-borne mode incident ($\ell = 1$) with N=90: (a) perforated lining and (b) fibrous lining.

of the waveguide. Since with the fluid-borne mode case most of the energy is transferred through the fluid and thus, the all clamped and all pin-jointed curves overlie. Moreover, more absorption with fibrous type lining than perforated lining is obtained. Nevertheless a sharp stop-band occurred in regime 1009Hz $\leq f \leq$ 1171Hz with perforated lining over the point whereby the secondary mode of the expansion chamber starts propagating.

TABLE 5.1: Case: 1 ($b > a > d$), the power components verses N for $\ell = 0$ with $\bar{a} = 0.06$m, $\bar{b} = 0.085$m, $\bar{d} = 0.045$m, $\bar{L} = 0.02$m, $f = 250$Hz.

Absorbent Lining	Edge Conditions	N	P_r	P_t	P_{abs}
Perforated	Clamped	20	0.918068	0.057352	0.0245803
($\chi = 2.1,\ \xi = 2.5$)		25	0.918064	0.0573664	0.0245699
		30	0.91818	0.0575092	0.0243113
	Pin-Jointed	20	0.956881	0.0296523	0.0134671
		25	0.956768	0.0297077	0.0135245
		30	0.956921	0.0297639	0.0133154
Fibrous	Clamped	40	0.946937	0.0141735	0.0388892
($\chi = 0.5,\ \xi = 0.5$)		45	0.946847	0.0140359	0.0391169
		50	0.94727	0.01441382	0.0385923
	Pin-Jointed	15	0.972715	0.0067222	0.0205629
		20	0.970781	0.00704184	0.0221771
		25	0.972783	0.00688863	0.0203283

TABLE 5.2: Case: 1 ($b > a > d$), the power components verses N for $\ell = 1$ with $\bar{a} = 0.1$m, $\bar{b} = 0.15$m, $\bar{d} = 0.06$m, $\bar{L} = 0.25$m, $f = 250$Hz.

Absorbent Lining	Edge Conditions	N	P_r	P_t	P_{abs}
Perforated	Clamped	90	0.64793	0.26464	0.087430
($\chi = 2.1,\ \xi = 2.5$)		95	0.648503	0.264904	0.086593
		100	0.648908	0.265095	0.085997
	Pin-Jointed	90	0.164322	0.595649	0.240029
		95	0.164107	0.536246	0.239647
		100	0.163895	0.596716	0.239390
Fibrous	Clamped	65	0.620859	0.127816	0.251325
($\chi = 0.5,\ \xi = 0.5$)		70	0.620091	0.127863	0.252046
		75	0.619321	0.12787	0.252809
	Pin-Jointed	65	0.227142	0.105486	0.667372
		70	0.226639	0.105577	0.667784
		75	0.226163	0.10563	0.668206

Furthermore, the P_r, P_t and P_{abs} for different types of edge conditions and the properties of absorbent material against the variation of number of terms N are displayed in Tables. 5.1 and 5.2. To collect data of Table. 5.1, the dimensional variable are taken as: $\bar{a} = 0.06$m, $\bar{b} = 0.085$m, $\bar{d} = 0.045$m and $\bar{L} = 0.02$m and frequency is fixed at $f = 250$Hz. Note that Table. 5.1 shows the results when structure-borne mode is incident whilst Table. 5.2 displays the results with fluid-borne mode incident. The number of terms are varied to confirm adequate convergence of presented results. From Table. 5.1, it can be seen that maximum of energy is reflected. The amount of reflection not only depends upon the edge conditions of this physical problem but also the material properties of the absorbent material. For instance greater amount of energy is reflected with fibrous material and all pin-jointed conditions as compared to other settings (see Table. 5.1).

Likewise to produce the data of Table. 5.2, the dimensional variable are assumed as: $\bar{a} = 0.1$m, $\bar{b} = 0.15$m, $\bar{d} = 0.06$m and $\bar{L} = 0.25$m at $f = 250$Hz. Note that when fluid-borne mode is incident, the reflection is decreased but absorption is increased. More absorption with all pin-jointed and fibrous case is revealed than all other setting. For this case the convergence is achieved with increasing truncation parameter $N = 90$ (see Table. 5.2). The fact is due to the case of singularity at the tips of flange in fluid-borne mode case. Fig. 5.5 shows the reflected and transmitted powers against the truncation parameter N with $f = 250$Hz. Only the results with all clamped edge conditions and fibrous absorbent lining are displayed. Fig. 5.5(a) and Fig. 5.5(b) show respectively the curves of the fundamental or structure-borne mode incident ($\ell = 0$) along with dimensional parameters $\bar{a} = 0.06$m, $\bar{b} = 0.085$m, $\bar{d} = 0.045$m and $\bar{L} = 0.02$m and of the fluid-borne mode incident ($\ell = 1$) together with parameters $\bar{a} = 0.1$m, $\bar{b} = 0.15$m, $\bar{d} = 0.06$m and $\bar{L} = 0.25$m. Clearly, the systems converge more rapidly for the structure born mode incident (see Fig. 5.5(a)) than the fluid-borne mode incident (see Fig. 5.5(b)). In these tables the reflection, transmission and absorption of energy flux are shown. The unit energy flux provided to the system is transformed to reflected, transmitted and absorbed energies. From the conservation law of energy, the sum of reflected,

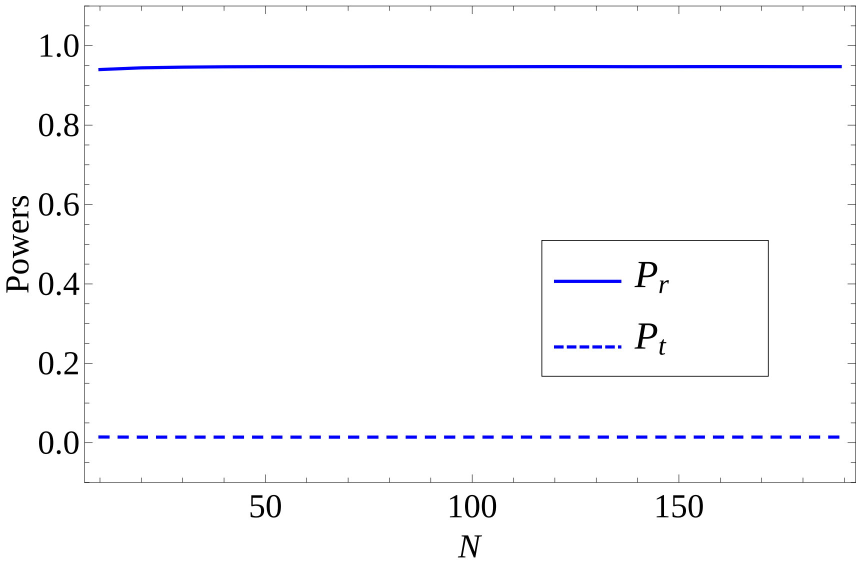

(a)

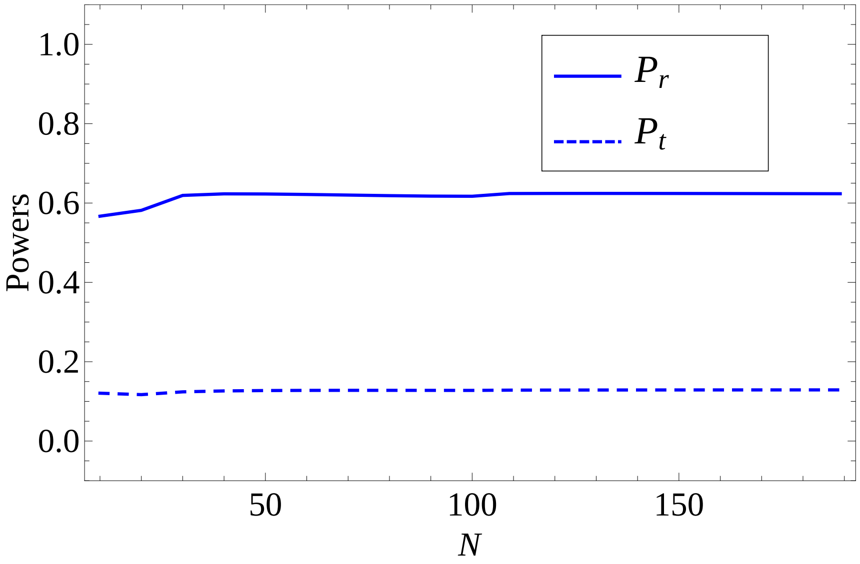

(b)

FIGURE 5.5: Powers (P_r and P_t) against parameters (N) at $f = 250$ Hz in the presence of fibrous absorbent lining with clamped edges: (a) $\ell = 0$, (b) $\ell = 1$.

transmitted and absorbed energies should be equal to provides unit incident energy. This can be regarded as standard base line.

5.4.2 Case 2: $a = b$ and $a > d$

In this case the computations are performed for planar waveguide by fixing the dimensional heights $\bar{a} = \bar{b} = 0.06$m, $\bar{d} = 0.045$m and half-length of expansion chamber $\bar{L} = 0.02$m. The TL results against frequency with clamped, pin-jointed and pivoted edge conditions for perforated ($\xi = 2.1,\ \chi = 2.5$) and fibrous ($\xi = 0.5,\ \chi = 0.5$) absorbent linings are shown in Fig. 5.6. For the perforated type of absorbent coating along the flanges (Fig. 5.6(a)) a sharp decrements is observed at $f = 191$ Hz which is the first cut-on mode of inlet/outlet duct region. However, once this duct mode starts propagating, the TL increases by increasing frequency for clamped and pin-jointed conditions.

Nevertheless, this situation is not depicted with pivoted edge conditions which are physical only when ($\bar{a} = \bar{b}$). The reason behind is the transformation of extra energy along the boundaries and a leakage of comperssional waves at the edges. Highest leakage occurs in pin-jointed case rather than clamped and pivoted cases which is as expected due to zero bending moment with pin-jointed edge conditions. Moreover, an excellent agreement between MM and LFA results for perforated case is achieved. However, a slight variation among the LFA and MM curves comprising fibrous absorbent lining for all clamped and all pin-jointed edge conditions is found (see Fig. 5.6(b)). This variation is because of the inability of LFA to cater the information about the complex eigenvalues on higher frequencies. Since a limited number of modes have been allowed to propagate in LFA.

Fig. 5.7 shows the results with fluid-borne mode incident found by fixing the dimensional lengths at: $\bar{a} = \bar{b} = 0.15$m, $\bar{d} = 0.06$m and $\bar{L} = 0.02$m. The absorbent parameters for fibrous lining are assumed to have: $\xi = 0.5,\ \chi = 0.5$, while for perforated lining contain values: $\xi = 2.1,\ \chi = 2.5$. The graphs are plotted at frequency $f = 120$ Hz which is chosen such as to make sure that the fluid-borne mode incident becomes cut-on. The results show that the clamped, pin-jointed and pivoted edge conditions have no apparent effect on the acoustical performance of the device due to transformation of maximum energy via fluid. A sharp peak is appeared at $f = 1160$ Hz over the point whereby the second mode of the expansion chamber begins propagating for all types of edge conditions (see Fig. 5.7). After this cut-on, the attenuation decreases with increasing frequency.

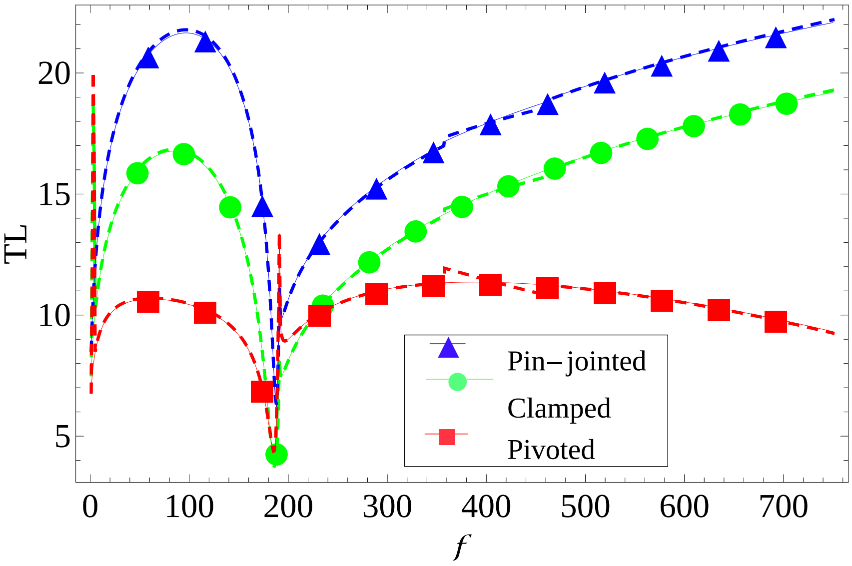

(a)

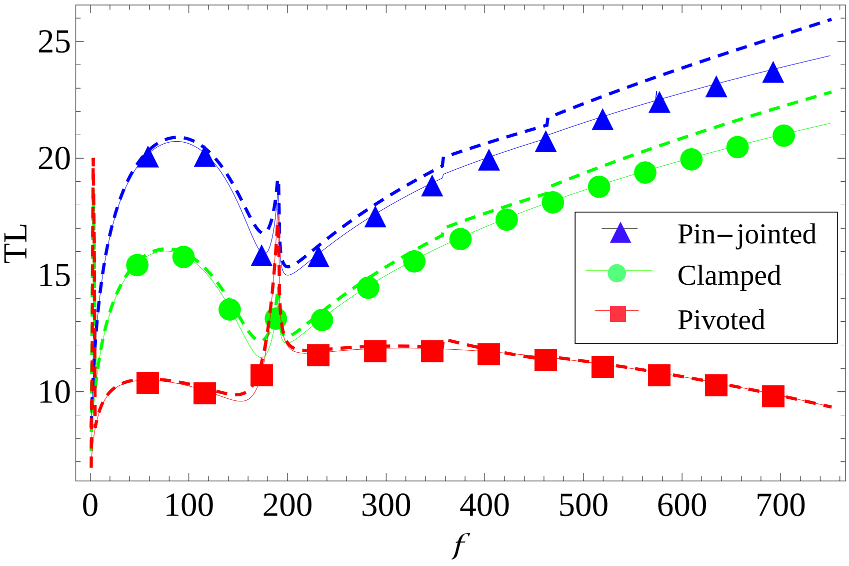

(b)

FIGURE 5.6: The transmission loss against frequency for fundamental mode incident ($\ell = 0$) Via LFA (− − −) and MM (■ • ▲) with N=20: (a) perforated lining and (b) fibrous lining.

Now the P_r, P_t and P_{abs} for different types of edge conditions and the properties of absorbent material against the variation of number of terms N are displayed in Tables. 5.3 and 5.4. The numerical data in Table. 5.3 is achieved by considering the dimensional parameters: $\bar{a} = \bar{b} = 0.06$m, $\bar{d} = 0.045$m and $\bar{L} = 0.02$m at $f = 250$Hz with fundamental-borne mode incident. From Table. 5.3, it can be seen that maximum of energy is reflected. Also the amount of energy reflection not only

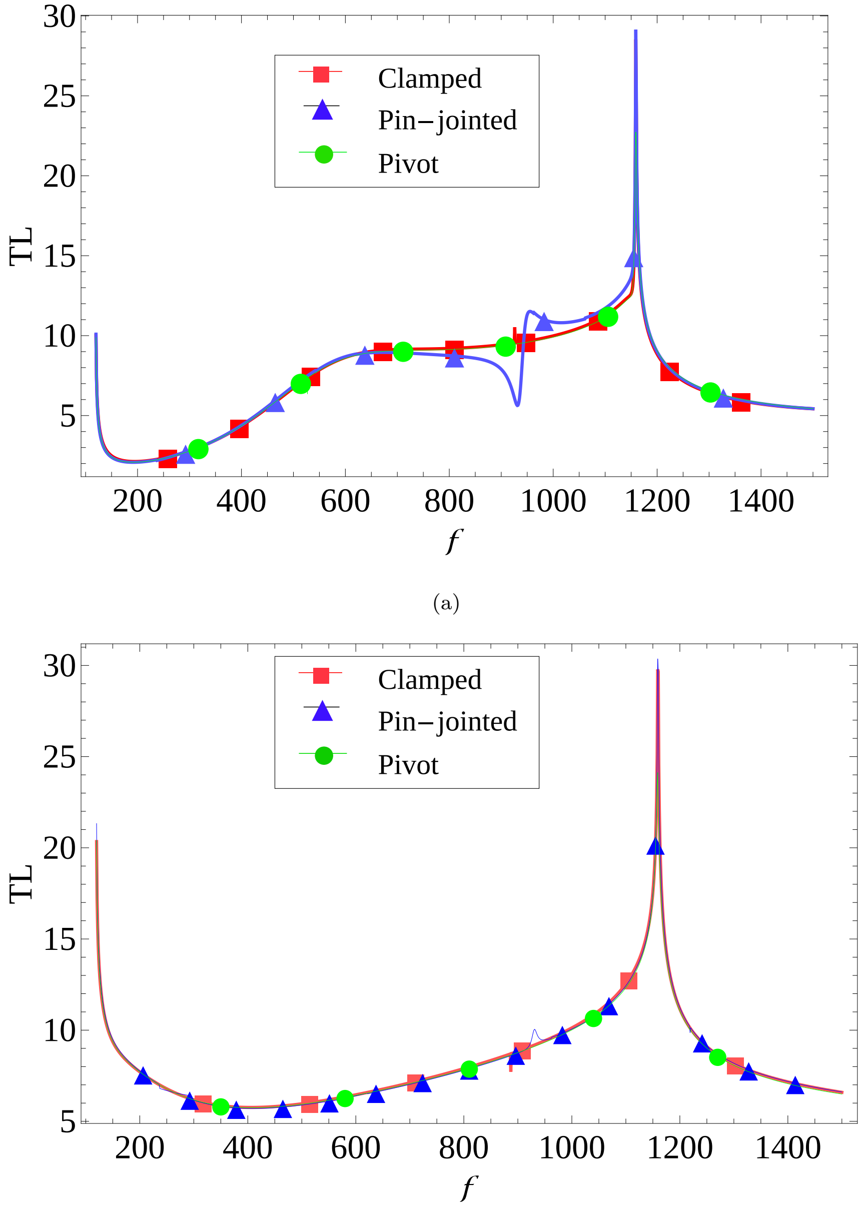

(a)

(b)

FIGURE 5.7: The transmission loss against frequency for fluid-borne mode incident ($\ell = 1$) with N=90: (a) perforated lining and (b) fibrous lining.

depends upon the edge conditions of the physical problem but also depends upon the material properties of the absorbent material. For instance greater amount of energy is reflected with both absorbent material and all pin-jointed conditions as compared to other settings (see Table. 5.3).

Similarly for fluid-borne mode incident, Table. 5.4 is presented with clamped, pin-jointed and pivoted edge conditions by assuming fibrous and perforated coatings.

Table 5.3: Case: 2 ($a = b, a > d$), the power components verses N for $\ell = 0$ with $\bar{a} = \bar{b} = 0.06$m, $\bar{d} = 0.045$m, $\bar{L} = 0.02$m, $f = 250$Hz.

Absorbent Lining	Edge Conditions	N	P_r	P_t	P_{abs}
Perforated	Clamped	20	0.910338	0.0783934	0.0112683
($\chi = 2.1,\ \xi = 2.5$)		25	0.910324	0.0780739	0.0116022
		30	0.910307	0.0782425	0.0114507
	Pin-Jointed	20	0.952691	0.0410675	0.0062419
		25	0.952596	0.0409087	0.0064957
		30	0.952634	0.0409857	0.0063801
	Pivoted	15	0.900367	0.0890946	0.0105381
		20	0.901634	0.0902692	0.0080964
		25	0.901428	0.0900829	0.0084891
Fibrous	Clamped	15	0.922148	0.0434187	0.0344329
($\chi = 0.5,\ \xi = 0.5$)		20	0.922005	0.0428381	0.0351570
		25	0.922584	0.0434597	0.0339568
	Pin-Jointed	15	0.959085	0.0222686	0.0186464
		20	0.958981	0.0219269	0.0190926
		25	0.959416	0.0222872	0.0182966
	Pivoted	15	0.908655	0.0669801	0.0243652
		20	0.908319	0.0666611	0.0250196
		25	0.909237	0.0669478	0.0238150

The dimensional lengths $\bar{a} = \bar{b} = 0.15$m, $\bar{d} = 0.06$ m and $\bar{L} = 0.02$m remain fixed, where $f = 250$ Hz. It is noted that almost zero reflection and maximum absorption regardless of edge conditions and absorbent characteristics is found. However, with fibrous lining relatively more absorption than perforated lining is revealed (see Table. 5.4).

Fig. 5.8 shows the reflected and transmitted powers against the truncation parameter N, where $f = 250$Hz. Only the results with all clamped edge conditions and fibrous absorbent lining are displayed. Fig. 5.8(a) and Fig. 5.8(b) show respectively the curves of the fundamental or structure-borne mode incident ($\ell = 0$) along with

TABLE 5.4: Case: 2 ($a = b, a > d$), the power components verses N for $\ell = 1$ with $\bar{a} = \bar{b} = 0.15$m, $\bar{d} = 0.06$m, $\bar{L} = 0.02$m, $f = 250$Hz.

Absorbent Lining	Edge Conditions	N	P_r	P_t	P_{abs}
Perforated	Clamped	90	0.0733949	0.604349	0.322256
($\chi = 2.1,\ \xi = 2.5$)		95	0.0732667	0.605375	0.321359
		100	0.0731403	0.606207	0.320653
	Pin-Jointed	90	0.0625319	0.609751	0.327717
		95	0.0624963	0.610716	0.326787
		100	0.0624561	0.611496	0.326048
	Pivoted	35	0.062084	0.596332	0.341584
		40	0.0607462	0.594692	0.344562
		45	0.0600641	0.591413	0.348523
Fibrous	Clamped	75	0.384793	0.206054	0.409153
($\chi = 0.5,\ \xi = 0.5$)		80	0.383845	0.20604	0.410115
		85	0.383068	0.206044	0.410888
	Pin-Jointed	75	0.381379	0.210389	0.408232
		80	0.380551	0.210372	0.409755
		85	0.379871	0.210374	0.409077
	Pivoted	55	0.388673	0.206399	0.404928
		60	0.387344	0.20626	0.406396
		65	0.386083	0.206165	0.407752

dimensional parameters $\bar{a} = 0.06$m, $\bar{b} = 0.085$m, $\bar{d} = 0.045$m and $\bar{L} = 0.02$m, and of the fluid-borne mode incident ($\ell = 1$) together with parameters $\bar{a} = \bar{b} = 0.15$m, $\bar{d} = 0.06$m and $\bar{L} = 0.25$m. Clearly, the systems converge more rapidly for the structure born mode incident (see Fig. 5.8(a)) than the fluid-borne mode incident (see Fig. 5.8(b)).

It is useful to reconstruct the matching conditions by using the truncated form of MM solution. It validates the truncated solution as well as confirm the accuracy of performed algebra. In Figs. 5.9 and 5.10, the real and imaginary parts of dimensionless normal velocities and pressures are plotted at interface $x = -L$ respectively (likewise can be shown at $x = L$). From figures it can be seen that

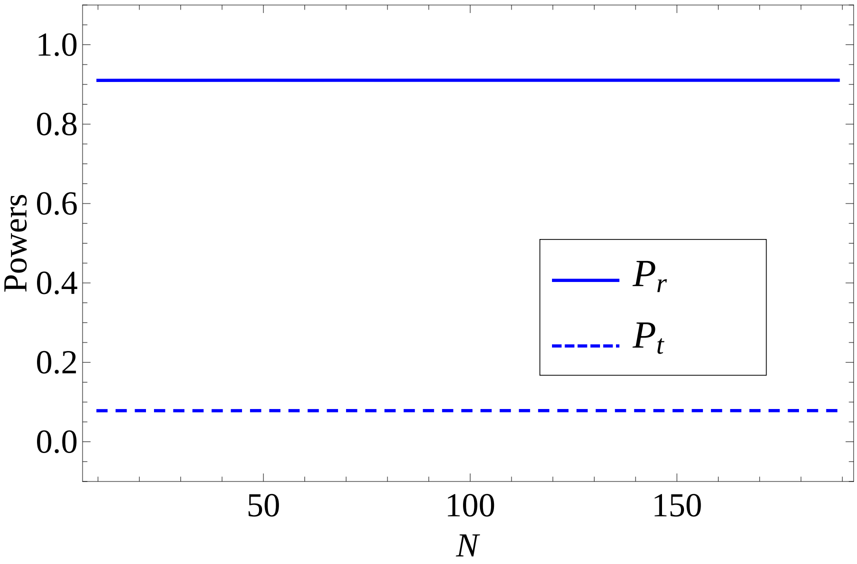

(a)

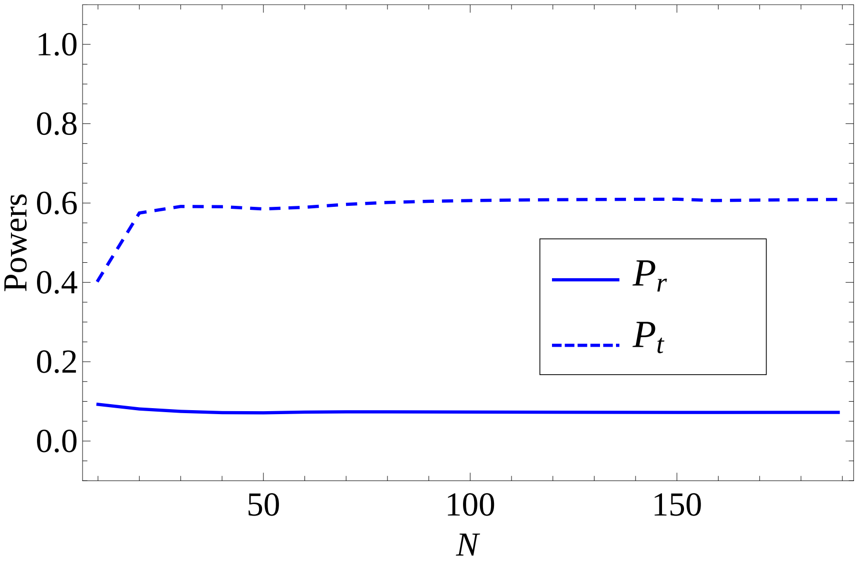

(b)

FIGURE 5.8: Powers (P_r and P_t) against parameters (N) at f = 250 Hz in the presence of perforated absorbent lining with clamped edges: (a) $\ell = 0$, (b) $\ell = 1$.

the curves for real as well as imaginary parts of normal velocities and pressures overlie when $0 \leq y \leq d$. However the normal velocity curves are zero while $0 < y < a$. Thus, the matching conditions (5.16) and (5.26) are fully satisfied. Nevertheless, two curves oscillate around their mean value and the amplitude of oscillation reduces significantly as y increases, except close to the corners $y = d$ and b.

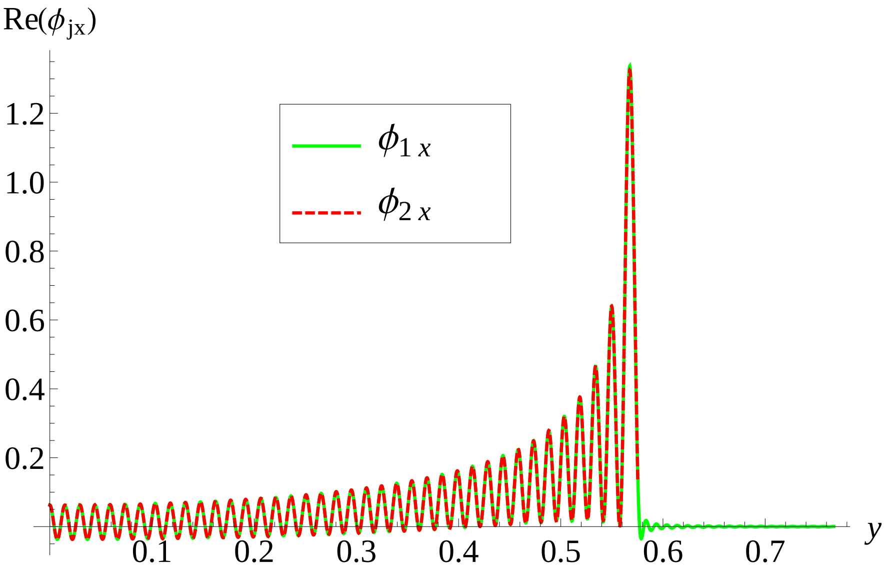

(a) Real part of velocities at $(-L, y)$

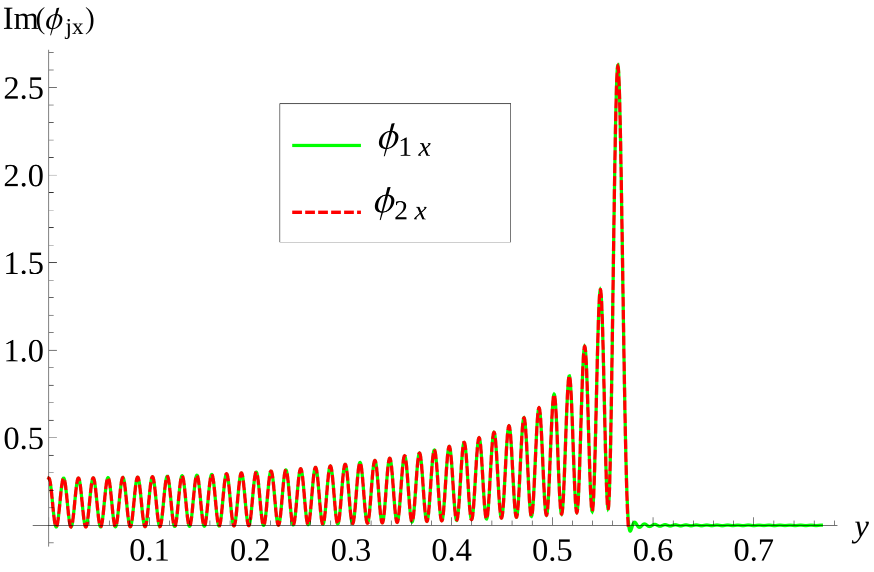

(b) Imaginary part of velocities.

FIGURE 5.9: The real and imaginary parts of normal velocities against duct height at $(-L, y)$ for clamped edge condition in the presence of absorbent lining (fibrous) with $f = 700$ Hz, $\overline{a} = 0.06$m, $\overline{b} = 0.085$m, $\overline{d} = 0.45$m and $N = 150$.

In this chapter, we have studied the scattering analysis through a waveguide bounded by elastic plates in the presence of lined flanges. The physical configuration comprises expansion chamber that is connected with the elastic plates bounded inlet and outlet through lined flanges. The governing boundary value problems are solved by using MM approach and LFA. From the numerical experiment it is found that the absorbent lining along the flanges and edge conditions significantly affect the attenuation of structure as well as fluid-borne excitation.

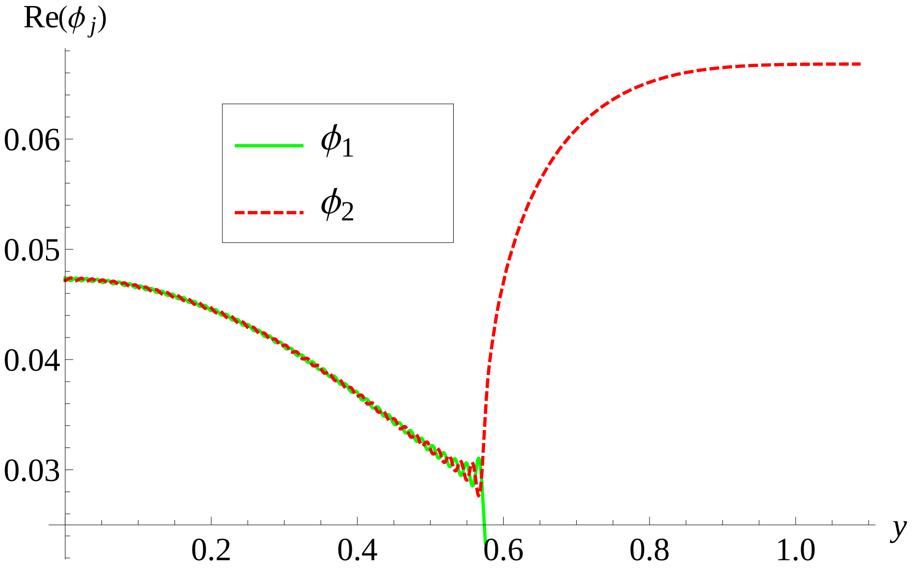

(a) Real part of pressures.

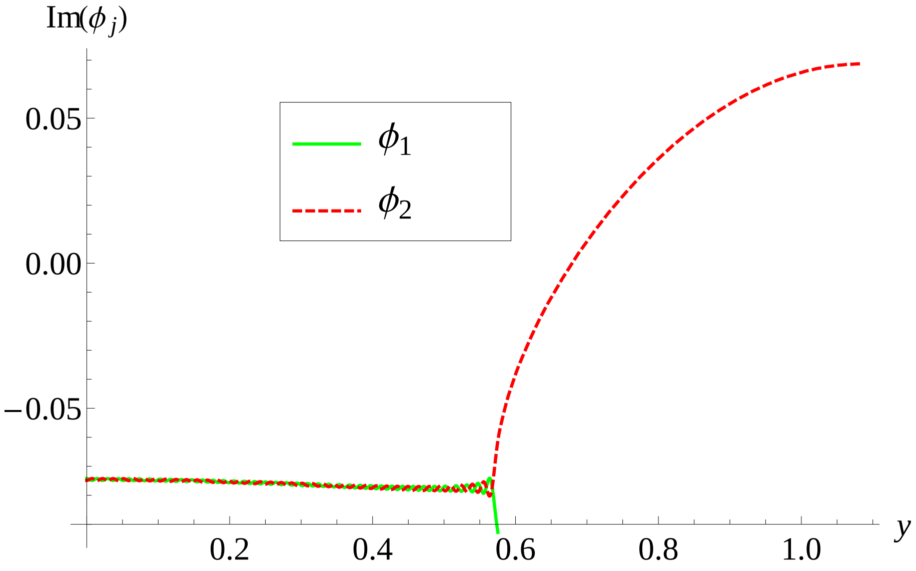

(b) Imaginary part of pressures.

FIGURE 5.10: The real and imaginary parts of pressures against duct height at $(-L, y)$ for clamped edge condition in the presence of absorbent lining (fibrous) with $f = 700$ Hz, $\overline{a} = 0.06$m, $\overline{b} = 0.085$m, $\overline{d} = 0.45$m and $N = 150$.

Chapter 6

Acoustic Analysis in Waveguide with Plates-Membrane Boundaries

In this chapter, the traveling waveform of a flexible waveguide bounded by elastic plates with an inserted expansion chamber having flanges at two junctions and a finite elastic membrane atop is investigated through a MM technique. The modeled problem is governed by Helmholtz's equation together with Dirichlet and higher order boundary conditions. An acoustically absorbent lining is placed along the inner sides of the flanges at the junctions while their outer sides are kept rigid. Moreover, the edge conditions are imposed to define the physical behavior of elastics membrane and plates at finite edges. The configuration is exited with the structure as well as fluid-born mode. The influence of the imposed edge conditions at the connections of the plates and the prescribed incident forcing on the TL along the duct is elaborated. Specifically, the effects of edge conditions on the TL of structure-borne vibrations and fluid-borne noise are specified. The performance of LFA is compared with the benchmark MM method with relative merits. Apposite numerical simulations are also performed to substantiate the validity of the MM technique.

The contents hereinafter are organized as follows. The mathematical formulation of the problem is furnished in Section. 6.1. The MM solution is rendered in Section. 6.2. In Section. 6.3, the LFA is derived. Numerical results are presented in Section. 6.4.

6.1 Boundary Value Problem

Consider a two-dimensional, rectangular flexible waveguide filled with a compressible fluid having density ρ and sound speed c. The lower boundary of the waveguide lying along $\bar{y} = 0$ for $\bar{x} \in \mathbb{R}$ is assumed acoustically rigid. The upper walls consist of elastic plates at height $\bar{y} = \bar{a}$ for $|\bar{x}| > \bar{L}$ and elastic membrane at height $\bar{y} = \bar{b}$ for $|\bar{x}| < \bar{L}$ with $\bar{b} > \bar{a}$ and $\bar{L} > 0$. The finite ends of the elastic plates are connected at $\bar{y} = \bar{a}$ with two vertical strips elongated along $\bar{x} = \pm\bar{L}$ for $\bar{d} \leq \bar{y} \leq \bar{b}$. The upper ends of the strips are joined with each other by means of the finite elastic membrane at $\bar{y} = \bar{b}$ with $|\bar{x}| < \bar{L}$, forming an expansion chamber region $(|\bar{x}| \leq \bar{L}, \bar{0} < \bar{y} < \bar{b})$, and the inlet and outlet duct regions $(|\bar{x}| \geq \bar{L}, \bar{0} < \bar{y} < \bar{a})$.

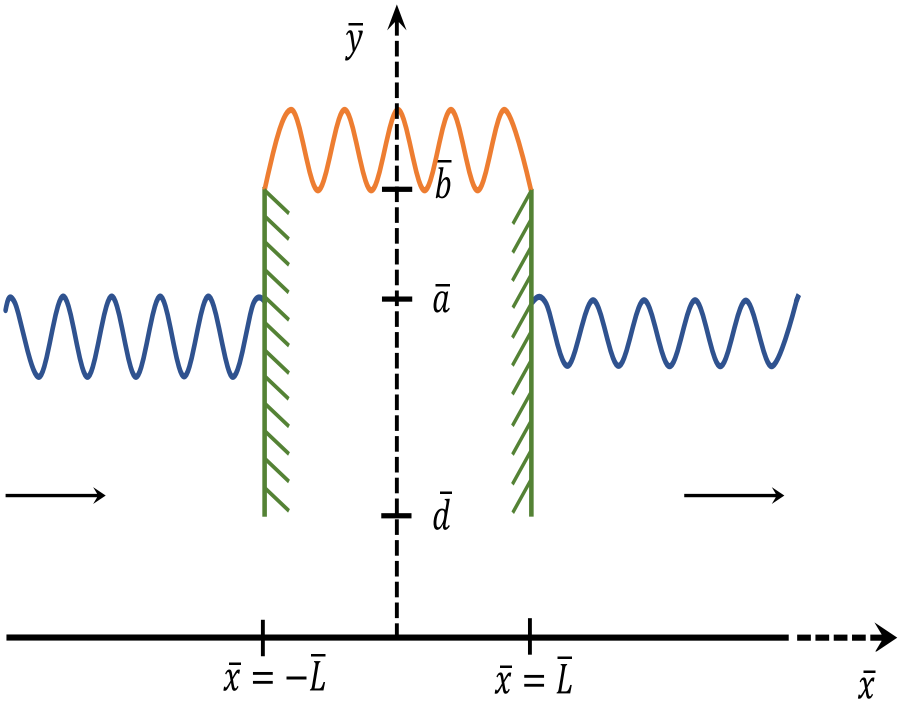

FIGURE 6.1: Flexible waveguide.

The absorbent linings of a porous material are taken along the inner sides of the vertical strips whereas the outer sides of the strips facing towards inlet and outlet are kept acoustically rigid. The geometrical configuration is shown in Fig. 6.1. The impedance condition for the absorbent material is same as of the boundary value problem of Section. 5.1, that is defined as

$$\phi + i\zeta \mathbf{n} \cdot \nabla \phi = 0, \tag{6.1}$$

where $\zeta = (\rho c)^{-1} Z$ represents the dimensionless specific impedance of the lining. The structure is excited from inlet region by a structure or fluid-borne mode which will be scattered and/or absorbed upon interaction with geometric discontinuities and material properties of the chamber. In order to study the scattering characteristics, a boundary value problem is formulated. Towards this end, the time-harmonic dimensionless fluid potential $\phi(x, y)$ satisfies the Helmholtz's equation

$$\left(\nabla^2 + 1\right) \phi = 0, \tag{6.2}$$

with a unit wave-number. The dimensionless normal component of fluid velocity vanishes at the rigid base, that is,

$$\frac{\partial \phi}{\partial y} = 0, \qquad \text{for all } (x, y) \in \mathbb{R} \times \{0\}. \tag{6.3}$$

The dimensionless form of the membrane connecting the flanges from the top is given by

$$\left(\frac{\partial^2}{\partial x^2} + \mu^2\right) \frac{\partial \phi}{\partial y} + \alpha \phi = 0 \qquad \text{for all } (x, y) \in (-L, L) \times \{b\}, \tag{6.4}$$

where μ is membrane wave-number and α is fluid-loading parameter. Moreover, all parameters about membrane boundary conditions have already been explained in Subsection. 2.3.2. However, the upper elastic plate boundaries of inlet and outlet duct sections are same as of the previous problem of Section. 5.1, that is written in dimensionless form as

$$\left(\frac{\partial^4}{\partial x^4} - \mu_1^4\right)\frac{\partial \phi}{\partial y} - \alpha_1 \phi = 0 \qquad \text{for all } (x, y) \in (\mathbb{R} \setminus [-L, L]) \times \{a\}. \tag{6.5}$$

In order to describe the traveling wave formulation in inlet, outlet, and expansion chamber, the eigen-functions of the associated duct regions can be found by using (6.2)-(6.4), as

$$\begin{cases} Y_{1n}(y) = \cosh(\gamma_n y), & |x| > L, \quad 0 \leq y \leq a, \\ Y_{2n}(y) = \cosh(\beta_n y), & |x| < L, \quad 0 \leq y \leq b. \end{cases} \tag{6.6}$$

The eigenvalues (γ_n, β_n), for $n \in \mathbb{N} \cup \{0\}$, are the roots of the characteristic equations

$$\begin{cases} \left((\gamma_n^2 + 1)^2 - \mu_1^4\right)\gamma_n \sinh(\gamma_n a) - \alpha_1 \cosh(\gamma_n a) = 0, \\ \left(\beta_n^2 + 1 - \mu^2\right)\beta_n \sinh(\beta_n b) - \alpha \cosh(\beta_n b) = 0. \end{cases} \tag{6.7}$$

These roots are determined numerically. Towards this end, any standard numerical scheme, such as, Newton-Raphson or scant method, may be invoked. For the propagation of vibrational waves in the positive $x-$direction and/or for an exponential decay as $x \to +\infty$, first the real roots and then the complex roots are incorporated by increasing the imaginary part. In fact, the real roots correspond to the vibrational modes which propagate in the positive $x-$direction (i.e., the *propagating modes*) whereas the imaginary roots correspond to the vibration modes which decay with distance from the interface (i.e., the *evanescent modes*). There is always one real root ($\gamma_0 > 0$, $\beta_0 > 0$) accompanied by an infinity of imaginary roots, $(\gamma_n, \beta_n)_{n \in \mathbb{N}}$, labeled in ascending order on imaginary axis as depicted in Fig. 6.2. First 10 roots of the dispersion relations in (6.7) are displayed. Figs. 6.2(a) and 6.2(b) reflect the roots, respectively, in the inlet/outlet duct mode regions with duct height 0.06m and in the expansion chamber region bounded by elastic membrane at the height 0.085m at frequency 430Hz. There exist pairs of complex roots for certain ranges of frequency in the inlet and outlet duct regions. Such pairs appear when the imaginary plate mode tends to cut-off duct modes (see Fig. 6.2(a)).

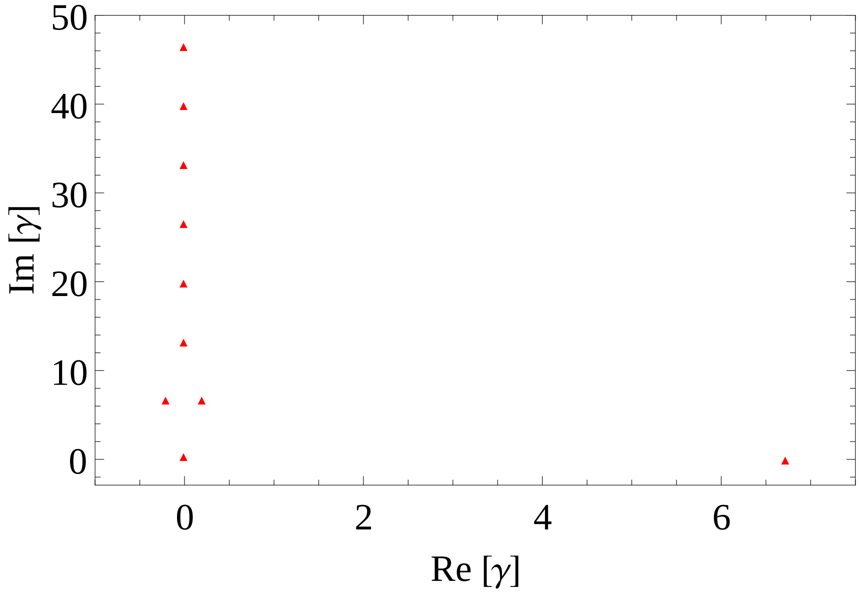

(a) Inlet and outlet duct regions

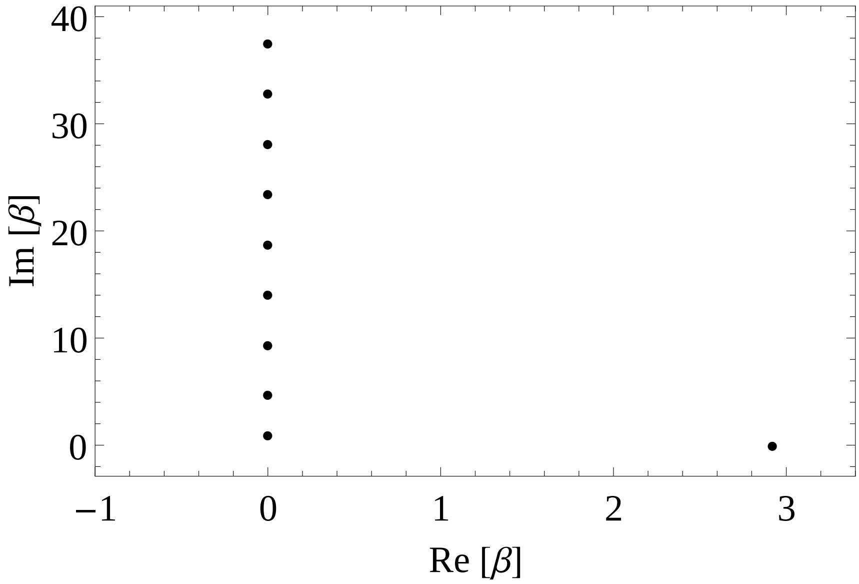

(b) Expansion chamber

FIGURE 6.2: First 10 roots of the characteristic equation (6.7) at $f = 430$Hz with $\bar{a} = 0.06$m and $\bar{b} = 0.085$m.

These complex pairs of γ can be obtained by solving the equation [34]

$$i\mu_1 = \sqrt{1 - \frac{n^2\pi^2}{k^2\bar{a}^2}}, \qquad n \in \mathbb{N}, \tag{6.8}$$

where $\bar{a}$ is the dimensional height of the duct. Such roots are arranged according to the magnitude of the imaginary part in ascending order such that γ^* is followed by $-\gamma^*$. It is important to note that the corresponding eigen-system is non-Sturm-Liouville in nature, whereby the development and use of generalized orthogonal characteristics is indispensable (see, for instance, [32]). The generalized OR for inlet/outlet and expansion chamber are found to be

$$\alpha_1 \int_0^a Y_{1n}(y)Y_{1m}(y)dy = G_n\delta_{mn} - (\gamma_m^2 + \gamma_n^2 + 2)Y_{1n}^{'}(a)Y_{1m}^{'}(a), \quad n, m \in \mathbb{N} \cup \{0\}, \tag{6.9}$$

$$\alpha \int_0^b Y_{2n}(y)Y_{2m}(y)dy = E_n\delta_{mn} - Y_{2n}^{'}(b)Y_{2m}^{'}(b), \quad n, m \in \mathbb{N} \cup \{0\}, \tag{6.10}$$

respectively. Here, the prime denotes differentiation with respect to y and δ_{mn} is the Kronecker's delta. Moreover, the quantities G_m and E_m are given by

$$G_m = \frac{\alpha_1 a}{2} + \frac{\alpha_1 Y_{1m}(a)Y_{1m}^{'}(a)}{2\gamma_m^2} + 2[(\gamma_m^2 + 1)Y_{1m}^{'}(a)]^2, \tag{6.11}$$

$$E_m = \frac{\alpha b}{2} + \left(\frac{3\beta_m^2 + 1 - \mu_2^2}{2\beta_m^2}\right)[Y_{2m}^{'}(b)]^2. \tag{6.12}$$

Now the MM solution is rendered in next section.

6.2 Mode-Matching Solution

Let us express the fluid potential $\phi(x, y)$ for inlet, outlet, and expansion chamber, respectively, as

$$\begin{aligned} &\left\{\phi^-(x,y), \quad x \le -L,\ 0 \le y \le a\right\}, \\ &\left\{\phi^+(x,y), \quad x \ge L,\ 0 \le y \le a\right\}, \\ &\{\phi^c(x,y), \quad |x| \le L,\ 0 \le y \le b\}. \end{aligned}$$

Then, by virtue of the eigen-function expansion, we have

$$\phi^{-}(x,y) = F_\ell Y_{1\ell}(y)e^{i\eta_\ell(x+L)} + \sum_{n=0}^{\infty} A_n Y_{1n}(y)e^{-i\eta_n(x+L)}, \tag{6.13}$$

$$\phi^{c}(x,y) = \sum_{n=0}^{\infty} \left(B_n e^{-i\nu_n x} + C_n e^{i\nu_n x}\right) Y_{2n}(y), \tag{6.14}$$

$$\phi^{+}(x,y) = \sum_{n=0}^{\infty} D_n Y_{1n}(y)e^{i\eta_n(x-L)}. \tag{6.15}$$

Here, $\{A_n, B_n, C_n, D_n\}_{n\in\mathbb{N}\cup\{0\}}$ are the complex amplitudes of the propagating modes. The first term on the right hand side of (6.13) indicates the incident field with forcing F_ℓ. The index ℓ takes on the value 0 or 1 for a structure-borne or a fluid-borne incident mode, respectively. The quantities η_n and ν_n are defined as

$$\eta_n = \sqrt{\gamma_n^2+1} \quad \text{and} \quad \nu_n = \sqrt{\beta_n^2+1} \qquad \text{for } n \in \mathbb{N}\cup\{0\}.$$

In order to find the amplitudes of the reflected and transmitted fields, the velocity flux conditions at interfaces are invoked, which yield

$$\int_0^a \phi_x^{\pm}(\pm L, y)Y_{1m}(y)dy = \int_0^d \phi_x^{c}(\pm L, y)Y_{1m}(y)dy. \tag{6.16}$$

On substituting (6.13)-(6.15) into (6.16) and simplifing the result using OR (6.9), one gets

$$\Psi_m^{\pm} = F_\ell\delta_{m\ell} - \frac{\gamma_m \sinh(\gamma_m a)}{\eta_m G_m}\left(U_1^{\pm} + (\gamma_m^2+2)U_2^{\pm}\right) + \frac{2\alpha_1}{\eta_m G_m}\sum_{n=0}^{\infty}\nu_n R_{nm}\Lambda^{\pm}(\nu_n L)\chi_n^{\pm}, \tag{6.17}$$

where

$$\Psi_m^{\pm} = (A_m \pm D_m), \quad \chi_n^{\pm} = (B_n \pm C_n),$$
$$\Lambda^{+}(x) = i\sin(x), \quad \Lambda^{-}(x) = \cos(x),$$
$$U_1^{\pm} = e_1 \mp e_3, \qquad U_2^{\pm} = e_2 \mp e_4,$$

with $\quad e_1 = -i\,\phi^{-}_{xyyy}(-L,a),\ e_2 = -i\,\phi^{-}_{xy}(-L,a),\ e_3 = -i\,\phi^{+}_{xyyy}(L,a),$

and

$$e_4 = -i\, \phi^{+}_{xy}(L,a).$$

The constants R_{nm} in (6.17) are given by

$$R_{nm} = \frac{1}{\beta_n^2 - \gamma_m^2}\Big(\beta_n \cosh(\gamma_m d)\sinh(\beta_n d)) - \gamma_m \cosh(\beta_n d)\sinh(\gamma_m d)\Big),$$
$$n, m \in \mathbb{N} \cup \{0\}. \qquad (6.18)$$

Similarly, the pressure flux conditions at interfaces render

$$\int_0^b \phi^c(\pm L, y) Y_{2m}(y)dy = \int_0^d \phi^{\pm}(\pm L, y) Y_{2m}(y)dy \pm \frac{\zeta}{i}\int_d^b \phi^c_x(\pm L, y) Y_{2m}(y)dy. \qquad (6.19)$$

On substituting (6.13)-(6.15) into (6.19), simplifying the resultants with the help of OR (6.10), and after fairly easy manipulations, one arrives at

$$\chi^{\pm}_m = \frac{\beta_m \sinh(\beta_m b)}{2E_m \Lambda^{\mp}(\nu_m L)} V^{\pm}_1 + \frac{\alpha}{2E_m \Lambda^{\mp}(\nu_m L)}\left\{F_\ell R_{m0} + \sum_{n=0}^{\infty} R_{mn}\Psi^{\pm}_n\right\}$$

$$+ \frac{\alpha\zeta}{E_m \Lambda^{\mp}(\nu_m L)}\left\{\sum_{n=0}^{\infty} \nu_n \Lambda^{\pm}(\nu_m L)\; T_{mn}\; \chi^{\pm}_n\right\}, \qquad (6.20)$$

with

$$T_{mn} := \int_d^b \cosh(\beta_m y)\cosh(\beta_n y)dy, \quad n, m \in \mathbb{N} \cup \{0\},$$
$$V^{\pm}_1 := e_5 \pm e_6, \quad e_5 := \phi^c_y(-L, b), \quad e_6 := \phi^c_y(L, b).$$

Remark that $U^{\pm}_k$ and $V^{\pm}_k$, for $k = 1, 2$, are still unknown. They describe the behavior of the vibrating plates and membrane at finite edges. Towards this end, appropriate edge conditions are imposed depending upon the types of connections of the elastic plates or membrane on the edges. These connections and the corresponding edge conditions are discussed in subsequent subsections.

6.2.1 Clamped Plates and Fixed Membrane

When the edges of the elastic plates are clamped, the displacement and the gradient are zero, therefore,

$$\phi_y^{\pm}(\pm L, a) = 0, \tag{6.21}$$

$$\phi_{xy}^{\pm}(\pm L, a) = 0. \tag{6.22}$$

On the other hand, the displacement of the membrane is zero when its edges are fixed, that is,

$$\phi_y^{c}(\pm L, b) = 0. \tag{6.23}$$

It is straightforward that $U_2^{\pm} = V_1^{\pm} = 0$ thanks to (6.22) and (6.23). In order to find $U_1^{\pm}$, multiply (6.17) with $\gamma_m \sinh(\gamma_m a)$, take summation over $m \in \mathbb{N} \cup \{0\}$, and invoke edge conditions (6.21) to get

$$U_1^{\pm} = \mp \frac{2F_\ell \gamma_\ell \sinh(\gamma_\ell a)}{S_1} \mp \frac{2\alpha_1}{S_1} \sum_{m=0}^{\infty} \sum_{n=0}^{\infty} \frac{\gamma_m \nu_n R_{nm} \Lambda^{\pm}(\nu_m L) \sinh(\gamma_m a) \chi_n^{\pm}}{G_m \eta_m}, \tag{6.24}$$

where

$$S_1 = \sum_{m=o}^{\infty} \frac{\gamma_m^2 \sinh^2(\gamma_m a)}{G_m \eta_m}. \tag{6.25}$$

6.2.2 Clamped Plates and Free Membrane

When the edges of the elastic plates are clamped but the joints of the membrane are free, the only change from the previous case is observed in zero-displacement condition (6.23) which is now replaced with a zero-gradient condition, i.e.,

$$\phi_{xy}^{c}(\pm L, b) = 0. \tag{6.26}$$

In this case, $V_1^{\pm}$ can be found by multiplying (6.20) with $\beta_m \nu_m \sinh(\beta_m b) \sin(\nu_m L)$, taking summation over $m \in \mathbb{N} \cup \{0\}$, and finally invoking (6.26). It turns out that

$$\begin{aligned}V_1^{\pm} =& -\frac{\alpha_1}{S^{\pm}}\sum_{m=0}^{\infty}\frac{\nu_m\beta_m\sinh(\beta_m b)\Upsilon^{\pm}(\nu_m L)}{2E_m}\left\{F_\ell R_{m0}+\sum_{n=0}^{\infty}R_{mn}\Psi_n^{\pm}\right\}\\ &-\frac{\zeta\alpha_1}{S^{\pm}}\sum_{m=0}^{\infty}\sum_{n=0}^{\infty}\frac{\nu_m\beta_m\nu_n\sinh(\beta_m b)\Upsilon^{\pm}(\nu_m L)T_{mn}\chi_n^{\pm}}{E_m},\end{aligned} \tag{6.27}$$

where

$$S^{+}=\sum_{m=0}^{\infty}\frac{\nu_m\beta_m^2\sinh^2(\beta_m b)\tan(\nu_m L)}{2E_m}\text{ and }S^{-}=-i\sum_{m=0}^{\infty}\frac{\nu_m\beta_m^2\sinh^2(\beta_m b)\cot(\nu_m L)}{2E_m}.$$

6.2.3 Pin-Jointed Plates and Fixed Membrane

In case of pin-jointed edges of the plates, the displacement and the bending moment are assumed to be zero, i.e.,

$$\phi_y^{\pm}(\pm L,a)=0, \tag{6.28}$$

$$\phi_{xxy}^{\pm}(\pm L,a)=0 \tag{6.29}$$

and for fixed membrane edges,

$$\phi_y^{c}(\pm L,b)=0. \tag{6.30}$$

It can be immediately seen that $V_1^{\pm}=0$ thanks to (6.30). In order to find $U_1^{\pm}$ and $U_2^{\pm}$, multiply (6.17) with $\gamma_m\sinh(\gamma_m a)$, take summation over $m\in\mathbb{N}\cup\{0\}$, and invoke edge conditions (6.28) and (6.29), respectively, to get

$$S_1U_1^{\pm}+S_2U_2^{\pm}=\mp 2F_\ell\gamma_\ell\sinh(\gamma_\ell a)\mp 2\alpha_1\sum_{m=,n=0}^{\infty}\frac{\gamma_m\nu_nR_{nm}\chi_n^{\pm}\Lambda^{\pm}(\nu_nL)\sinh(\gamma_m a)}{G_m\eta_m}, \tag{6.31}$$

$$S_3U_1^{\pm}+S_4U_2^{\pm}=\mp 2F_\ell\eta_\ell^2\gamma_\ell\sinh(\gamma_\ell a)\mp 2\alpha_1\sum_{m,n=0}^{\infty}\frac{\eta_m\gamma_m\nu_nR_{nm}\chi_n^{\pm}\Lambda^{\pm}(\nu_nL)\sinh(\gamma_m a)}{G_m}. \tag{6.32}$$

Here, S_1 is given in (6.25) and

$$S_2 = \sum_{m=0}^{\infty} \frac{\gamma_m^2(\gamma_m^2+2)\sinh^2(\gamma_m a)}{G_m \eta_m},$$
$$S_3 = \sum_{m=0}^{\infty} \frac{\eta_m \gamma_m^2 \sinh^2(\gamma_m a)}{G_m}$$

and

$$S_4 = \sum_{m=0}^{\infty} \frac{\eta_m \gamma_m^2(\gamma_m^2+2)\sinh^2(\gamma_m a)}{G_m}.$$

6.2.4 Pin-Jointed Plates and Free Membrane

In this case, the set of edge conditions (6.26), (6.28), and (6.29) are considered, which in tern furnish the equations (6.27), (6.31), and (6.32) for the unknown constants. Thus, two infinite systems of equations defined by (6.17) are obtained. They are truncated and, subsequently, solved simultaneously together with the associated set of edge conditions for determining the unknown amplitudes.

6.3 Low-Frequency Approximation

In this section, the LFA is developed for the considered BVP to compare the obtained results via MM technique. So, the field potentials in respective duct region can be written as

$$\phi^-(x,y) \approx F_\ell Y_{1\ell}(y)e^{i\eta_\ell(x+L)} + \sum_{n=0}^{J_1} A_n Y_{1n}(y)e^{-i\eta_n(x+L)}, \tag{6.33}$$

$$\phi^c(x,y) \approx \sum_{n=0}^{J_2} \left(B_n e^{-i\nu_n x} + C_n e^{i\nu_n x}\right) Y_{2n}(y), \tag{6.34}$$

$$\phi^+(x,y) \approx \sum_{n=0}^{J_3} D_n Y_{1n}(y)e^{i\eta_n(x-L)}, \tag{6.35}$$

where, $J_1, J_2, J_3 \in \mathbb{N} \cup \{0\}$ stand for the number of modes propagating in the inlet duct region, expansion chamber, and outlet duct region, respectively. The coefficients $\{A_n\}_{n=0}^{J_1}$, $\{B_n, C_n\}_{n=0}^{J_2}$, and $\{D_n\}_{n=0}^{J_3}$, by abuse of notation, are unknown amplitudes in low-frequency approximation. They are found by taking into account the continuity of mean pressures and velocity fluxes at interfaces, i.e., by taking into account the conditions

$$\int_0^d \left\{\phi^{\pm}(\pm L, y) - \phi^c(\pm L, y)\right\} dy = 0, \tag{6.36}$$

$$\int_0^d \left\{\phi_x^{\pm}(\pm L, y) - \phi_x^c(\pm L, y)\right\} dy = 0. \tag{6.37}$$

On substituting (6.33)-(6.35) into (6.36)-(6.37) and after fairly easy manipulation, one gets

$$\sum_{n=0}^{J_1} \frac{\sinh(\gamma_n d)}{\gamma_n} \Psi_n^{\pm} - 2\sum_{n=0}^{J_2} \frac{\sinh(\beta_n d)\Lambda^{\mp}(\nu_n L)}{\beta_n} \chi_n^{\pm} = \frac{F_\ell \sinh(\gamma_\ell d)}{\gamma_\ell}, \tag{6.38}$$

$$\sum_{n=0}^{J_3} \frac{\eta_n \sinh(\gamma_n d)}{\gamma_n} \Psi_n^{\pm} - 2\sum_{n=0}^{J_2} \frac{\nu_n \sinh(\beta_n d)\Lambda^{\mp}(\nu_n L)}{\beta_n} \chi_n^{\mp} = \frac{\eta_n F_\ell \sinh(\gamma_\ell d)}{\gamma_\ell}. \tag{6.39}$$

Let us now consider the geometrical configuration that comprises flanges and structural discontinuity at interfaces $x = \pm L$. The outside of the flanges lying in duct regions $|x| > L$ (for $J_1 = J_3$) are acoustically rigid and thus, the normal velocity fluxes are zero, i.e.,

$$\int_d^a \phi_x^{\pm}(\pm L, y)\, dy = 0. \tag{6.40}$$

This yields

$$\sum_{n=0}^{J_1} \frac{\eta_n(\sinh(\gamma_n a) - \sinh(\gamma_n d))}{\gamma_n} \Psi_n^{\pm} = F_\ell \frac{\eta_\ell(\sinh(\gamma_\ell a) - \sinh(\gamma_\ell d))}{\gamma_\ell}. \tag{6.41}$$

On the other hand, the insides of the flanges in the section $|x| < L$ contain an acoustically absorbent lining and therefore, the impedance type flux conditions hold, i.e.,

$$\int_d^b \{\phi^c(\mp L, y) \pm \frac{\zeta}{i}\phi_x^c(\mp L, y)\}\, dy = 0. \tag{6.42}$$

On substituting (6.34) into (6.42), and after some rearrangements, one arrives at

$$\sum_{n=0}^{J_2} \frac{(\sinh(\beta_n b) - \sinh(\beta_n d))\,(\Lambda^{\mp}(\nu_n L) - \Lambda^{\pm}\nu_n \sin(\nu_n L))}{\beta_n}\chi_n^{\pm} = 0. \tag{6.43}$$

To include the behavior on the edges of the plates in the inlet and outlet regions, and of the membrane in the expansion chamber, the role of different sets of edge conditions is discussed in the subsequent subsections.

6.3.1 Clamped Plates and Fixed Membrane

For the plates to have clamped edges along with fixed edges of the membrane, the set of edge conditions defined by (6.21)-(6.23) are considered. They lead to the relations

$$\sum_{n=0}^{J_1} \gamma_n \sinh(\gamma_n a)\Psi_n^{\pm} = -F_\ell \gamma_\ell \sinh(\gamma_\ell a), \tag{6.44}$$

$$\sum_{n=0}^{J_1} \gamma_n \eta_n \sinh(\gamma_n a)\Psi_n^{\pm} = -F_\ell \eta_n \gamma_\ell \sinh(\gamma_\ell a), \tag{6.45}$$

$$\sum_{n=0}^{J_2} \beta_n \sinh(\beta_n b)\Lambda^{\mp}(\nu_n L)\chi_n^{\pm} = 0. \tag{6.46}$$

Therefore, in order to obtain the modal coefficients $\{A_n\}_{n=0}^{J_1}$, $\{B_n, C_n\}_{n=0}^{J_2}$, and $\{D_n\}_{n=0}^{J_3}$, equations (6.38), (6.39), (6.41), (6.43)-(6.46) are solved simultaneously by setting appropriate values of J_1, J_2 and J_3. In this investigation, their values are taken as $J_1 = 3$, $J_2 = 5$, and $J_3 = 3$.

6.3.2 Clamped Plates and Free Membrane

For this choice of edges, the edge condition defined by (6.26) yields

$$\sum_{n=0}^{J_2} \nu_n \beta_n \sinh(\beta_n b)\Lambda^{\pm}(\nu_n L)\chi_n^{\pm} = 0. \tag{6.47}$$

Thus, a new system of equations is obtained by replacing (6.46) with (6.47) in the system of equations discussed in Subsection 6.3.1 for finding the unknown modal coefficients.

6.3.3 Pin-Jointed Plates and Fixed Membrane

For this edge condition, Eq. (6.29) leads to

$$\sum_{n=0}^{J_1} \gamma_n \eta_n^2 \sinh(\gamma_n a)\Psi_n^{\pm} = -F_\ell \eta_n^2 \gamma_\ell \sinh(\gamma_\ell a). \tag{6.48}$$

By replacing (6.45) with (6.48) in the system of equations discussed in Subsection 6.3.1, the finite system of equations for this set of edge conditions is obtained.

6.3.4 Pin-Jointed Plates and Free Membrane

For pin-jointed plates and a free membrane, the finite system of equations consists of (6.38)-(6.39), (6.41), (6.43), (6.44), (6.47), (6.48), which provides the unknown modal coefficients. Once again, $J_1 = 3$, $J_2 = 5$, and $J_3 = 3$ are chosen for solving the aforementioned system of simultaneous equations.

6.4 Numerical Results and Discussions

In this section, numerical results are provided and discussed. Towards this end, the appropriate values of the relevant parameters are specified as in [34, 102]. The relevant duct heights are fixed as $\bar{a} = 0.06$m, $\bar{b} = 0.085$m, and $\bar{d} = 0.045$m and the length of the expansion chamber is set to $2\bar{L} = 2 * 0.25$m for all numerical computations. The plates are taken to be of aluminum with thickness $\bar{h} = 6 \times 10^{-4}$m, density $\rho_p = 2700\text{kg/m}^3$, Young's modulus $E = 7.2 \times 10^{10}\text{N/m}^2$, and Poisson's ratio $\upsilon = 0.34$. The sound speed, density of the air, density of the membrane, and membrane tension are taken to be $c = 344\text{m/s}$, $\rho_a = 1.2\ \text{kg/m}^3$, $\rho_m = 0.2\text{Kg/m}^2$, and $T = 3250\text{N/m}^2$, respectively.

The values of the acoustical impedance in dimensionless form $\zeta = \xi + i\chi$ is entertained for two types of absorbent sheets [100]

(a) fibrous sheet with parameters $\xi = 0.5$ and $1 < \chi < 3$,

(b) perforated sheet with parameters $0 < \xi < 3$ and $1 < \chi < 3$.

As the absorbed power due to lining is given

$$P_{\text{abs}} = P_i - P_r - P_t \tag{6.49}$$

and the expressions for the reflected power in the inlet duct and the transmitted power in the outlet duct are found to be

$$P_r = \text{Re}\left\{ \frac{1}{\alpha_1} \sum_{n=0}^{\infty} |A_n|^2 \eta_n G_n \right\}, \tag{6.50}$$

$$P_t = \text{Re}\left\{ \frac{1}{\alpha_1} \sum_{n=0}^{\infty} |D_n|^2 \eta_n G_n \right\}, \tag{6.51}$$

where, the incident power is scaled at unity. All the numerical results presented herein are obtained by truncating the MM solutions with a truncation parameter referred to as N. Two different incident fields; the structural-borne vibrations ($\ell = 0$) and the fluid-borne vibration ($\ell = 1$), are considered.

To discuss the convergence of the truncated systems, Tables. 6.1 and 6.2 are prepared for different choices of the edge conditions, modes $\ell = 0$, 1, and frequency $f = 250\text{Hz}$. The numerical results of the absorbed power P_{abs} versus the truncation parameter N are presented for different values of the fibrous and perforated sheets. It is seen in Table. 6.1 that when the inlet duct is radiated through the structure-borne mode ($\ell = 0$), energy transfers along the walls and relatively less amount of energy is absorbed. On the other hand, if the duct is radiated with fluid-borne mode ($\ell = 1$) the majority of the energy is transferred via fluid and the

Table 6.1: Truncation number versus absorbed power for structure-borne mode incident ($\ell = 0$).

Edge Conditions	N	$P_{\text{abs}} = 1 - P_r - P_t$			
		Fibrous		Perforated	
		0.5+0.1i	0.5+2.9i	0.1+0.1i	0.1+2.5i
Clamped Plates	80	0.0521773	0.00952322	0.0343930	0.0029397
&	85	0.0522568	0.00937831	0.0337881	0.0029313
Fixed Membrane	90	0.0522549	0.00936252	0.0340617	0.0029183
Clamped Plates	25	0.0365528	0.00206605	0.0381136	0.0006067
&	30	0.0360314	0.00215696	0.0400469	0.0005983
Free Membrane	35	0.0364426	0.00230593	0.0381713	0.0007283
Pin-Jointed Plates	30	0.0267293	0.00508255	0.0183089	0.0015871
&	35	0.0269054	0.00513628	0.0170755	0.0016385
Fixed Membrane	40	0.0268891	0.00502636	0.0177238	0.0015781
Pin-Jointed Plates	20	0.0180893	0.00139099	0.0205259	0.0003505
&	25	0.0187166	0.00107404	0.0195307	0.0003165
Free Membrane	30	0.0183633	0.00112350	0.0207883	0.0003072

use of absorbent material along the walls has impact on absorption. By changing the edge conditions there is no significant variation in absorption. However, by changing the material properties of absorbent surface from fibrous to perforated the deviation in absorption is notable (see Table. 6.2). To show the convergence of truncated solution the reflection, transmission and absorption are showed against the number of terms N. Also, by changing the type of edge conditions as well as the properties of absorbent material, a variation in absorbed energy is revealed. Thus, the fluid-borne mode is found to be more operative than structure-borne mode by using the attenuating materials. Nevertheless, the systems converge rapidly enough for both of these exciting modes to truncate for two decimal places.

TABLE 6.2: Truncation number versus absorbed power for fluid-borne mode incident ($\ell = 1$).

Edge Conditions	N	$P_{\text{abs}} = 1 - P_r - P_t$			
		Fibrous		Perforated	
		0.5+0.1i	0.5+2.9i	0.1+0.1i	0.1+2.5i
Clamped Plates	80	0.507006	0.0924401	0.330628	0.0286081
&	85	0.507670	0.0913518	0.325817	0.0285506
Fixed Membrane	90	0.507608	0.0912399	0.328155	0.0284502
Clamped Plates	80	0.353525	0.0215676	0.378864	0.0058656
&	85	0.354431	0.0193289	0.374057	0.0056811
Free Membrane	90	0.354326	0.0191013	0.376703	0.0055204
Pin-Jointed Plates	80	0.516257	0.0982221	0.331943	0.0306523
&	85	0.516944	0.0971697	0.327079	0.0306029
Fixed Membrane	90	0.516876	0.0970555	0.329467	0.0305001
Pin-Jointed Plates	80	0.354068	0.0213310	0.380888	0.0058048
&	85	0.354984	0.0191420	0.376014	0.0056240
Free Membrane	90	0.354874	0.0189212	0.378727	0.0054677

6.4.1 Transmission-Loss Analysis

As the TL in terms of the reflected and transmitted powers is

$$\text{TL} := -10\log_{10}\left(\frac{P_t}{P_i}\right). \tag{6.52}$$

In this subsection, the TL results are presented to analyze the noise and vibration effect with fibrous and perforated type sheets:

(a) by varying the values of the surface impedance for both types of absorbent materials for a fixed choice of edge conditions of the plates and membrane, and

(b) by varying the edge conditions of the plates and the membrane for a fixed choice of sheet type (fibrous or perforated).

It is specified that the TL results obtained via MM technique are compared with LFA only for the structure-borne mode incident ($\ell = 0$).

6.4.1.1 Effect of Absorbent Linning

The graphs of the TL versus frequency are depicted in Figs. 6.3-6.6 for two different choices of the fibrous and perforated absorbent linings along the vertical flanges of the expansion chamber. The edges of the plates in inlet and outlet duct regions of the waveguide are assumed to be clamped.

Figs. 6.3–6.4 reveal the cases when the system is radiated with a structure-borne mode incident ($\ell = 0$) with fixed or free edges of the membrane in the expansion chamber. For Fig. 6.3, two different fibrous linings with impedance $0.5 + 0.1i$ and $0.5 + 2.9i$ are considered. Similarly, for Fig. 6.4, the perforated linings are chosen with impedance $0.1 + 0.1i$ and $0.1 + 2.5i$. Moreover, the results are plotted for both the MM solutions with appropriate truncation and the LFA solutions.

It is observed in Fig. 6.3 that there is significantly higher acoustic attenuation for the value $0.5 + 0.1i$ than $0.5 + 2.9i$ of the impedance. By changing the nature of the edge connection of the membrane from fixed to free, more leakage in the compression part of the wave is observed (refer to Figs. 6.3(a)–6.3(b)). The TL significantly increases at a higher frequency regime for fibrous lining with impedance $0.5 + 0.1i$ than $0.5 + 2.9i$. Exactly the same observations can be made for the cases presented in Fig. 6.4 when the perforated linings are chosen with impedance $0.1 + 0.1i$ and $0.1 + 2.5i$.

Remark that the power for structure-borne mode incident did not significantly absorb in both cases with different sets of edge conditions and linings, as indicated in Table: 6.1. The first cut-on occurred at $f = 191$Hz which has not affected the TL. Although, the MM and LFA solutions are found to be in good agreement in Fig. 6.3, there are some differences for the choices of parameters $0.1 + 0.1i$ and $0.1 + 2.5i$ in Fig. 6.4 at relatively high-frequency ranges. This is, in fact, due to the inability of LFA to cater to the information around the complex eigenvalues.

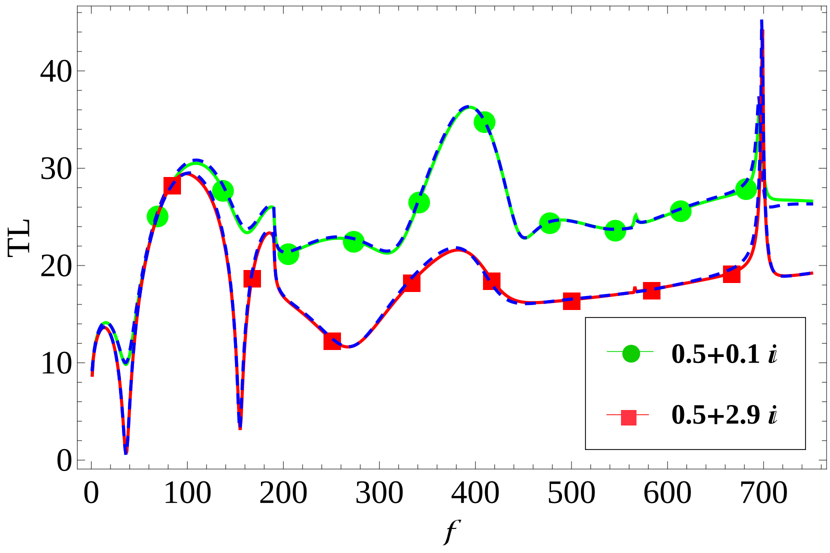

(a) Fixed membrane edges

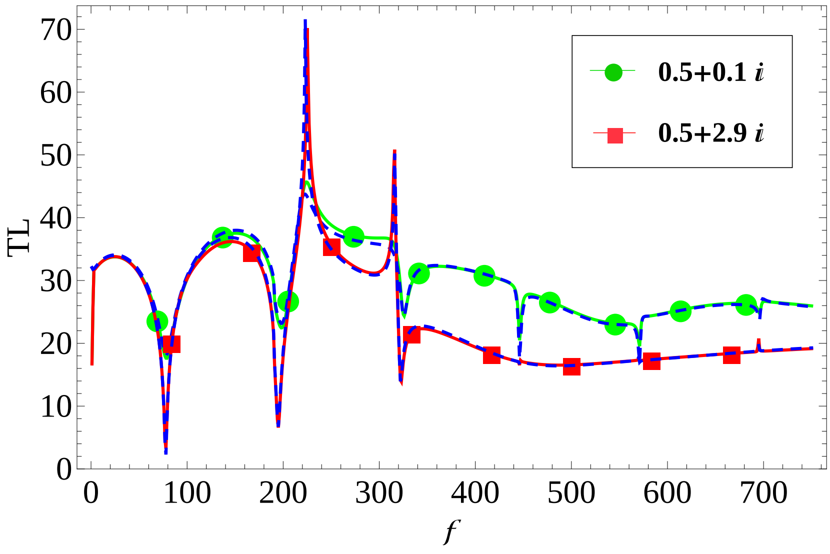

(b) Free membrane edges

FIGURE 6.3: Transmission-loss vs. frequency for fibrous linings, structure-borne mode incident ($\ell = 0$), and $N = 90$. Comparison of LFA (dashed) and MM (squares and bullets).

Figs. 6.5 – 6.6 depict the TL for the frequency range 191Hz $\leq f \leq$ 900Hz when the structure is radiated by a fluid-borne mode incident. For Fig. 6.5, the impedance values are chosen to be $0.5 + 0.1i$ and $0.5 + 2.9i$ whereas for Fig. 6.6 the pair consists of $0.1 + 0.1i$ and $0.1 + 2.5i$. The starting frequency, $f = 191$Hz, is chosen to make sure that the fluid-borne mode incident becomes cut-on.

The results show that the fibrous material with different values has an apparent

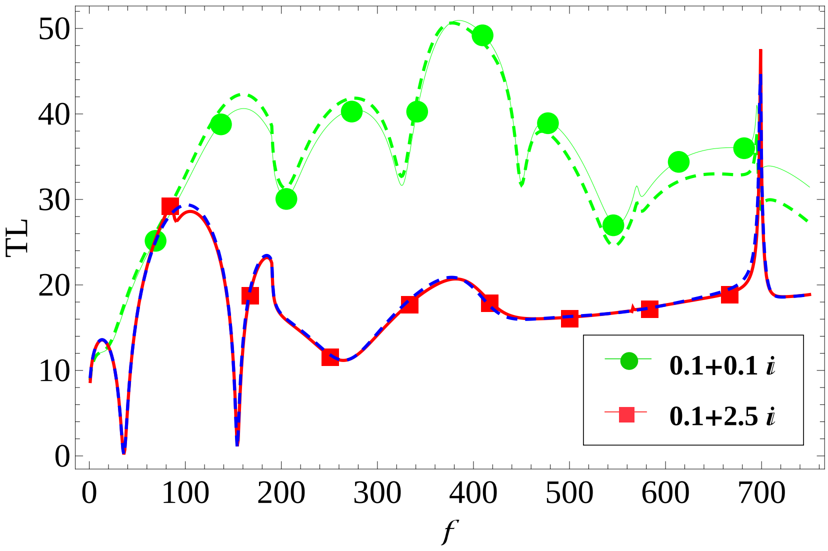

(a) Fixed membrane edges

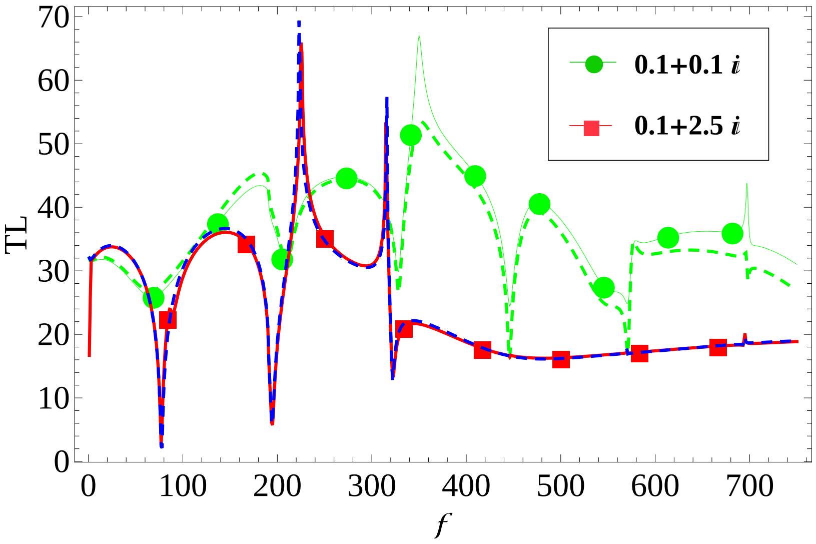

(b) Free membrane edges

FIGURE 6.4: Transmission-loss vs. frequency for perforated lining, structure-borne incident ($\ell = 0$), and $N = 90$. Comparison of LFA (dashed) and MM (squares and bullets).

effect on the acoustical performance of the waveguide. This is due to the fluid-borne mode case wherein most of the energy is absorbed with different fibrous sheets through the fluid. The TL increases when the value of the impedance decreases with both fixed and free membrane edges, as shown in Figs. 6.5–6.6. Table. 6.2 suggests a maximum absorbed power P_{abs} with the fibrous sheet $0.5 + 0.1i$, clamped plates, and fixed edges of the membrane in the expansion chamber.

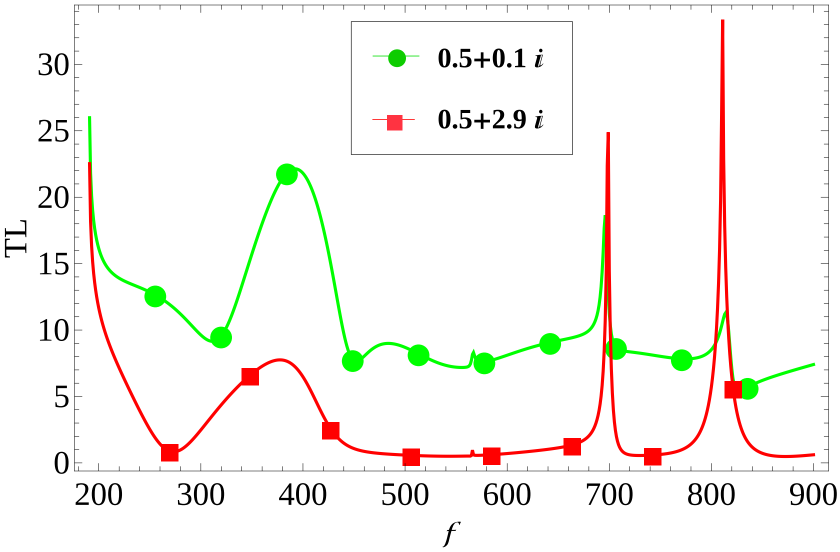

(a) Fixed membrane edges

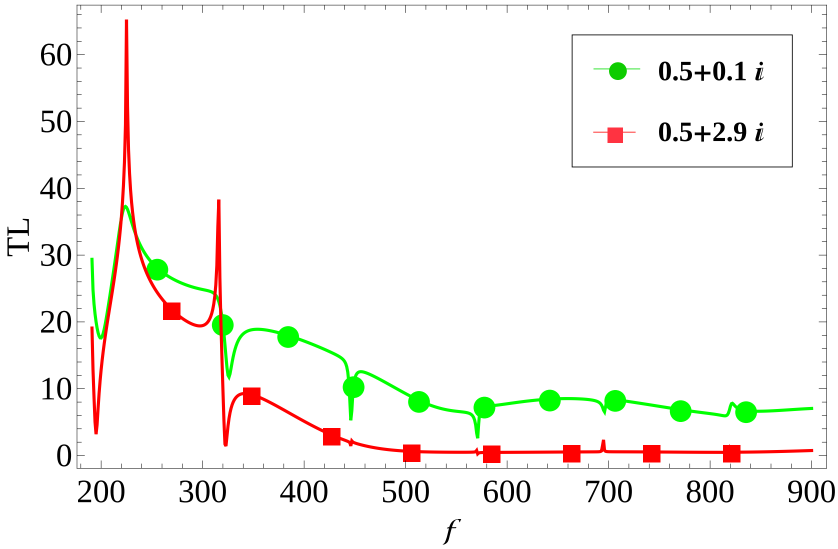

(b) Free membrane edges

FIGURE 6.5: The transmission-loss vs. frequency for fibrous lining, fluid-borne mode incident ($\ell = 1$), and $N = 90$.

6.4.1.2 Effect of Edge Conditions

The graphs of the TL versus frequency with different edge conditions are plotted in Fig. 6.7 and Fig. 6.8 when structure-borne ($\ell = 0$) and fluid-borne mode ($\ell = 1$) are incident, respectively. The numerical results are presented for a fibrous type sheet with $\xi = 0.5$, $\chi = 0.1$ along the vertical flanges of the expansion chamber.

The graphs in Fig. 6.7(a) reveal the apparent effect on the acoustical performance

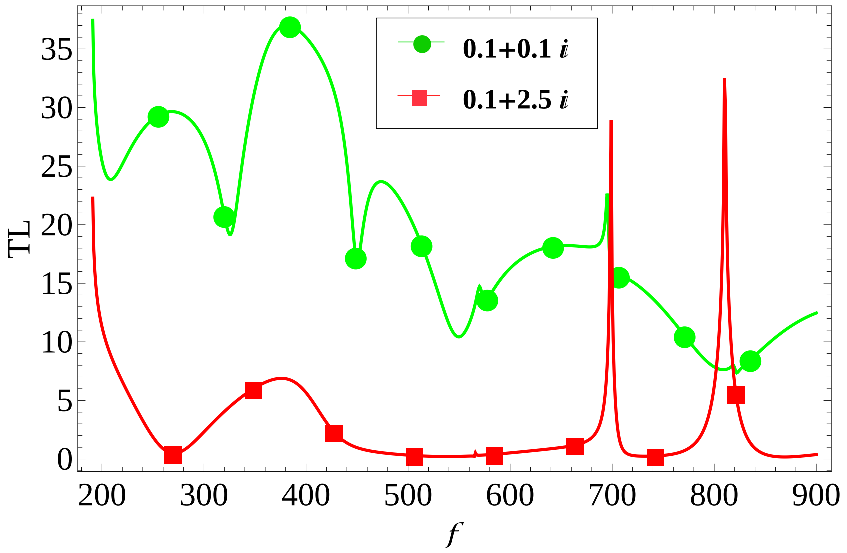

(a) Fixed membrane edges

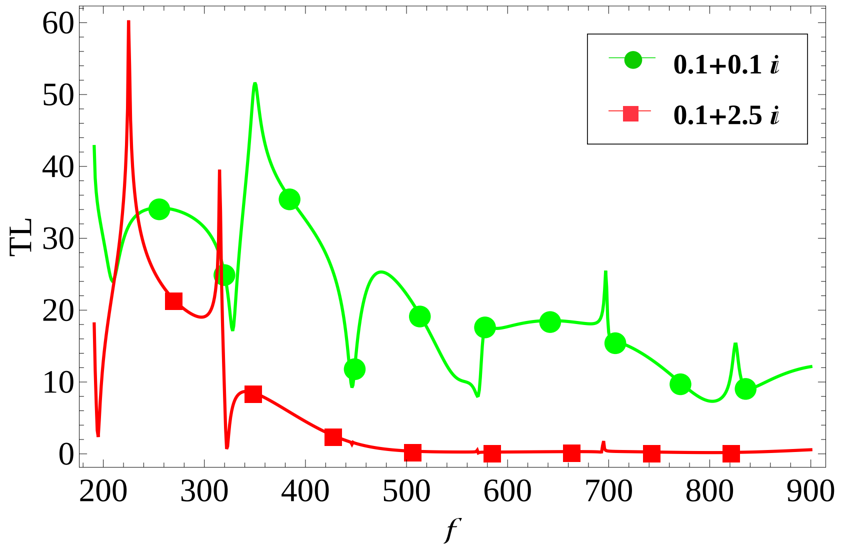

(b) Free membrane edges

FIGURE 6.6: Transmission-loss vs. frequency for different edge conditions with perforated lining, fluid-borne incident ($\ell = 1$), and $N = 90$.

of the waveguide when edges of the plates in the inlet and outlet duct region are clamped or pin-jointed while the membrane edges are assumed fixed in the expansion chamber. It is observed that there is more leakage in the compression part of the waves with pin-jointed edges (wherein the bending moment is also zero) than clamped edges. The magnitude of the TL is increased with pin-jointed edges as compared to that with clamped edges. In contrast to the case of fixed membrane edges, the pattern of the TL differs with the free membrane edges and the peak value of the TL is obtained at 210Hz, as delineated in Fig. 6.7(b). In the case of pin-jointed edges in inlet and outlet, the magnitude of the TL increases relative to that in the clamped edges case. This is due to the structure-borne mode incidence wherein most of the energy is transferred through the structure. Moreover, relatively less absorption with fibrous type lining is achieved (see, e.g., Table. 6.1). However, the MM and LFA solutions are found to be in good agreement.

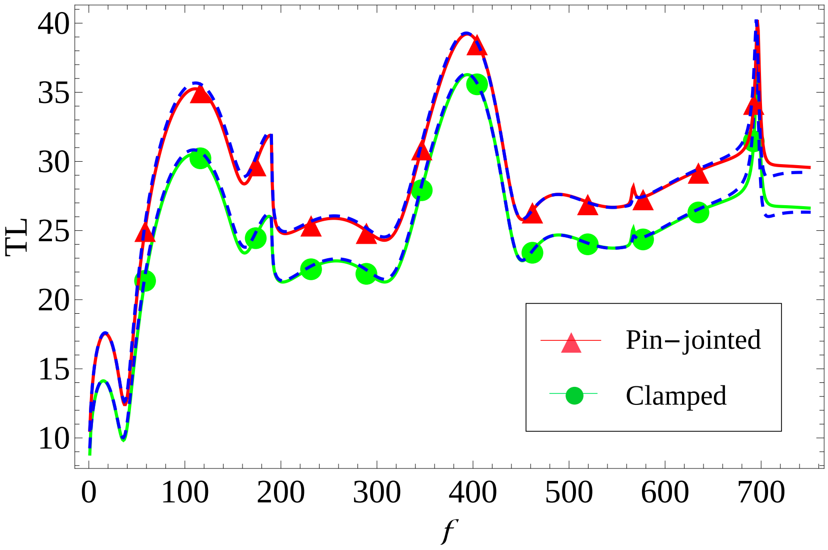

(a) Fixed membrane edges

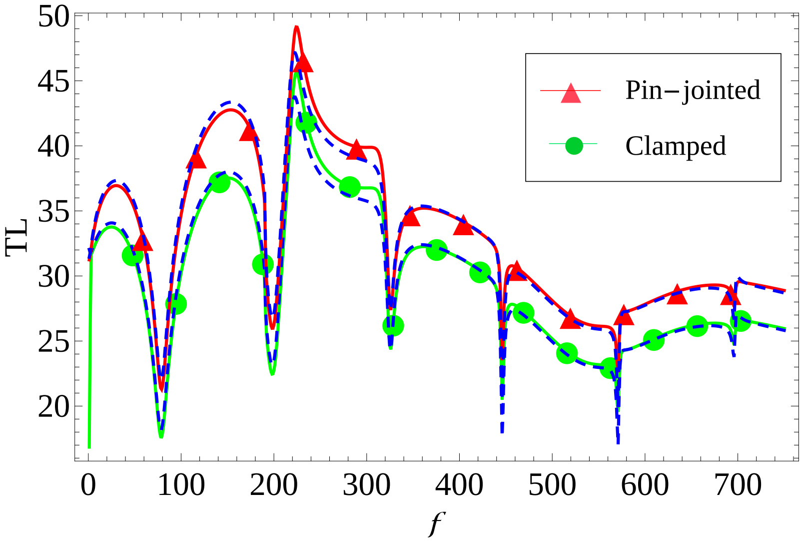

(b) Free membrane edges

FIGURE 6.7: Transmission-loss vs. frequency with structure-borne mode incident ($\ell = 0$) and fibrous lining ($\xi = 0.5$, $\chi = 0.1$).

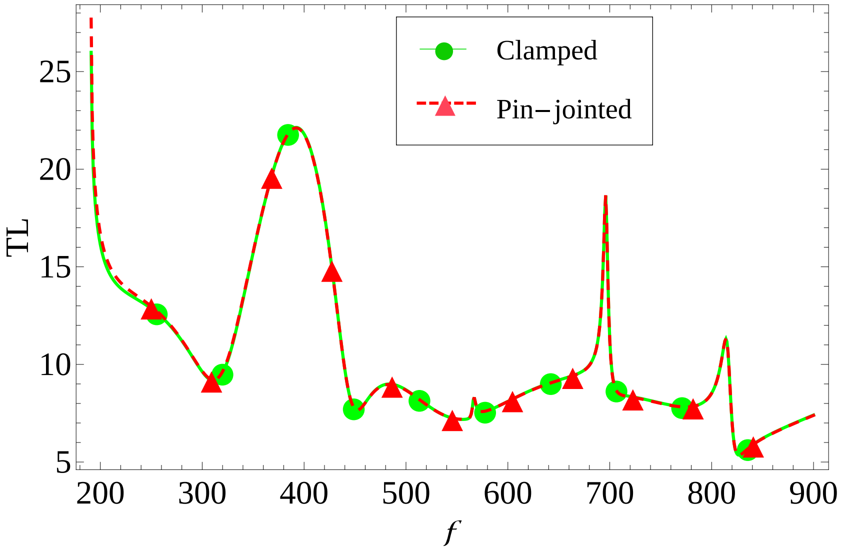

(a) Fixed membrane edges

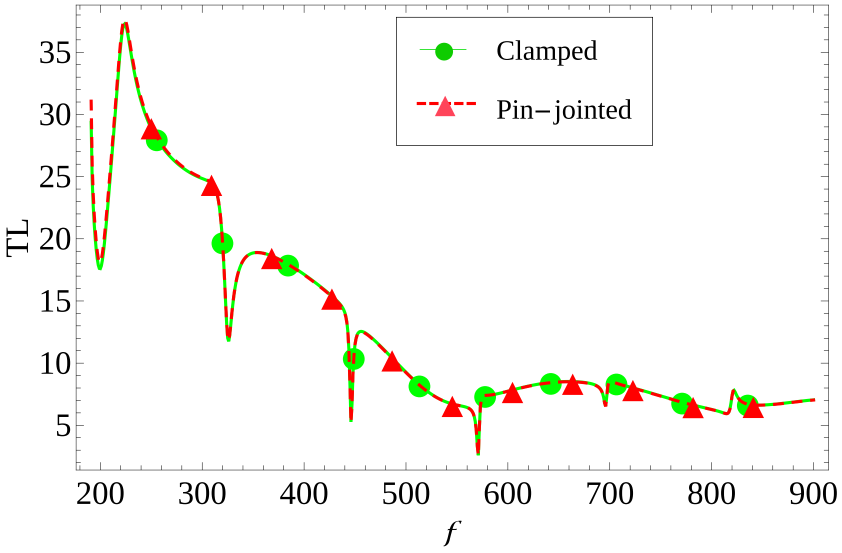

(b) Free membrane edges

FIGURE 6.8: Transmission-loss vs. frequency with fluid-borne mode incident ($\ell = 1$), regime $191\text{Hz} \leq f \leq 900\text{Hz}$, and fibrous lining ($\xi = 0.5$, $\chi = 0.1$).

Fig. 6.8 depicts the TL when the structure is radiated by a fluid-borne mode incident and the absorbent parameters for fibrous lining are taken as $\xi = 0.5$ and $\chi = 0.1$. The frequency range is taken as $191\text{Hz} \leq f \leq 900\text{Hz}$.

The results show that the clamped and pin-joint edge conditions in inlet and outlet duct regions have no apparent effect on the acoustical performance of the waveguide. This is due to the fluid-borne mode case wherein most of the energy is transferred through the fluid. Moreover, relatively high absorption is observed with fibrous type lining for the pin-jointed plates and fixed membrane edges (see Table. 6.2). However, a *stop-band* occurred in regime 300Hz$\leq f \leq$ 450Hz because of the fixed membrane edges (see Fig. 6.8(a)). The stop-band disappears in the case of free edges (see Fig. 6.8(b)). Moreover, the peak value of the TL is observed in the low-frequency regime.

The case of a perforated type sheet with $\xi = 0.1$, $\chi = 2.5$ is treated in Figs. 6.9–6.10 when structure-borne and fluid-borne modes are incident, respectively. Analogous conclusions can be drawn from Fig 6.9 in the case of $\ell = 0$. In the case $\ell = 1$, a pass-band occurred in frequency regime 300 Hz$\leq f \leq$ 450Hz because of fixed membrane edges, which is transformed into a stop-band in regime 200 Hz$\leq f \leq$ 300Hz for free membrane edges (see Fig. 6.10).

6.4.2 Validation of the Method

The graphical results presented in Subsection 6.4.1 focused on the analysis of transmission-loss for two different incident fields and two different sets of edge conditions in the presence of the absorbent linings. In view of the nature of singularity in the velocity field, it is essential to validate the MM solution. Toward this end, it is verified that

(a) a sufficient number of terms have been retained while truncating (6.17) and (6.20) so that an adequate convergence of the modal coefficients can be ensured, and

(b) the coefficients contain correct information so that the matching conditions (6.16) and (6.19) can be reconstructed.

Accordingly, the real and imaginary parts of velocities and pressures are plotted at interface $x = -L$ with clamped edges in Fig. 6.11 and in Fig. 6.12 respectively. It can be observed that the real and imaginary parts of non-dimensional pressures and velocities are in excellent agreement along with the aperture at $x = -L$. Both pairs of curves almost overlap for $0 \leq y \leq d$ and velocities are zero when $d < y < a$.

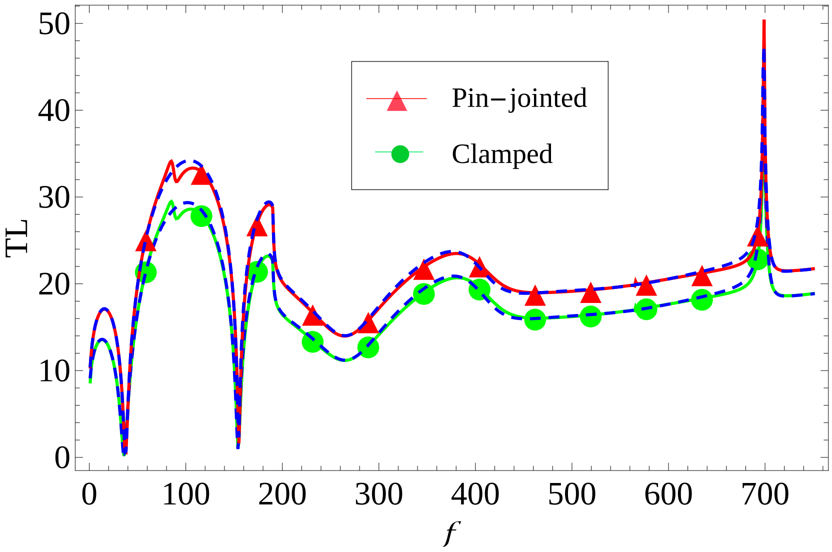

(a) Fixed membrane edges

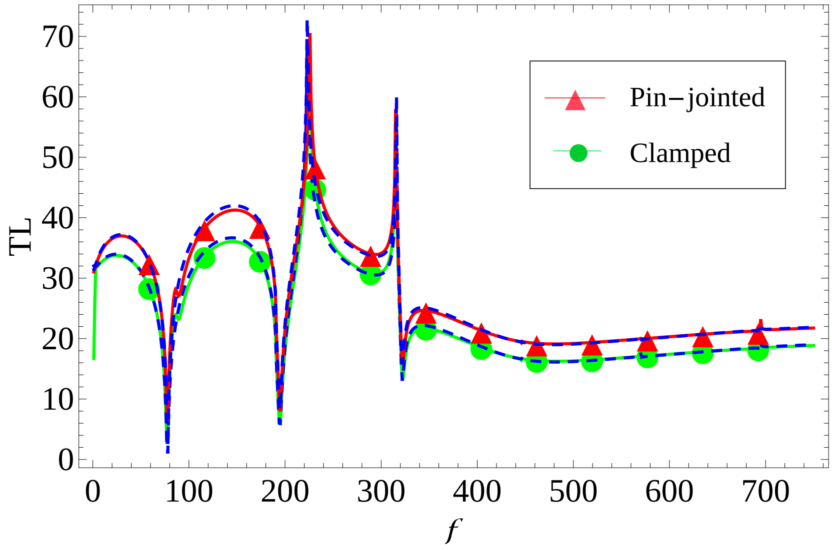

(b) Free membrane edges

FIGURE 6.9: Transmission-loss vs. frequency with structure-borne mode incident ($\ell = 0$) and perforated lining ($\xi = 0.1$, $\chi = 2.5$).

This is true at all relevant frequencies. Thus, conditions from (6.16) and (6.19) are satisfied. The matching conditions are also met to the same accuracy at interfaces $x = -L$. Nevertheless, the two curves oscillate around their mean value and the amplitude of oscillation reduces significantly as y increases, except when $y \to d$. This is, in fact, due to the singular behavior of the velocity field at the corner $y = d$. It is worthwhile mentioning that analogous graphs can be delineated and similar conclusions hold for the interface $x = L$ and/or different sets of edge conditions.

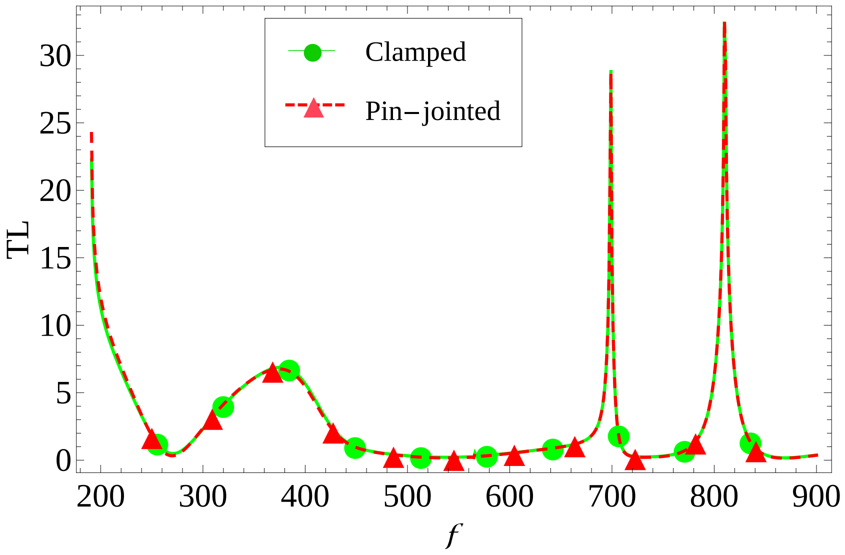

(a) Fixed membrane edges

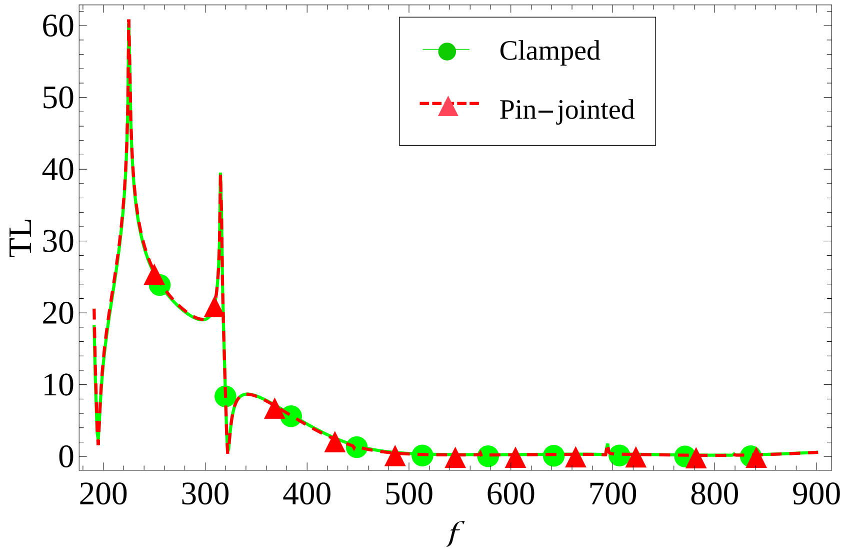

(b) Free membrane edges

FIGURE 6.10: Transmission-loss vs. frequency with fluid-borne mode incident ($\ell = 1$), regime 191Hz $\leq f \leq$ 900Hz, and perforated lining ($\xi = 0.1$, $\chi = 2.5$).

In a nutshell, the convergence results of the truncated amplitudes versus the truncation parameter N furnished in Tables 6.1–6.2 along with the reconstruction of the matching conditions completely justify the truncated MM approach and assert on the correctness of the performed algebra.

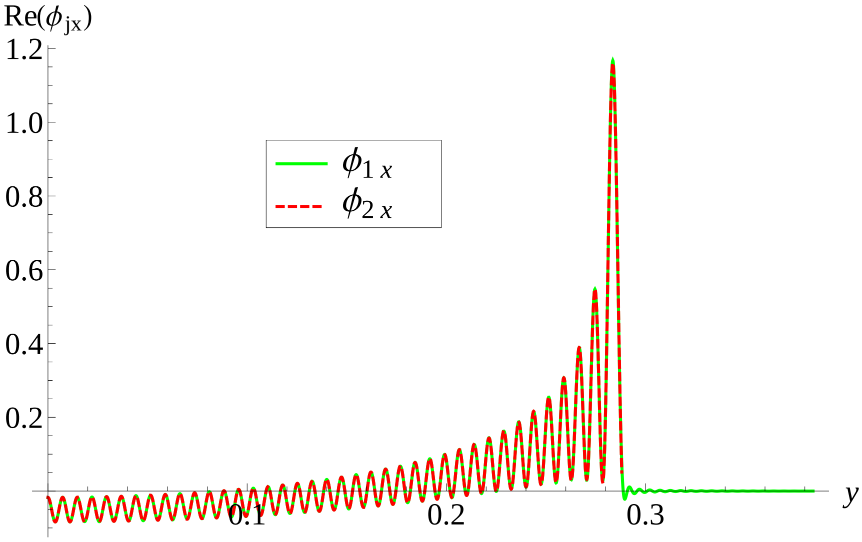

(a) Real part of velocities vs. duct height at $x = -L$

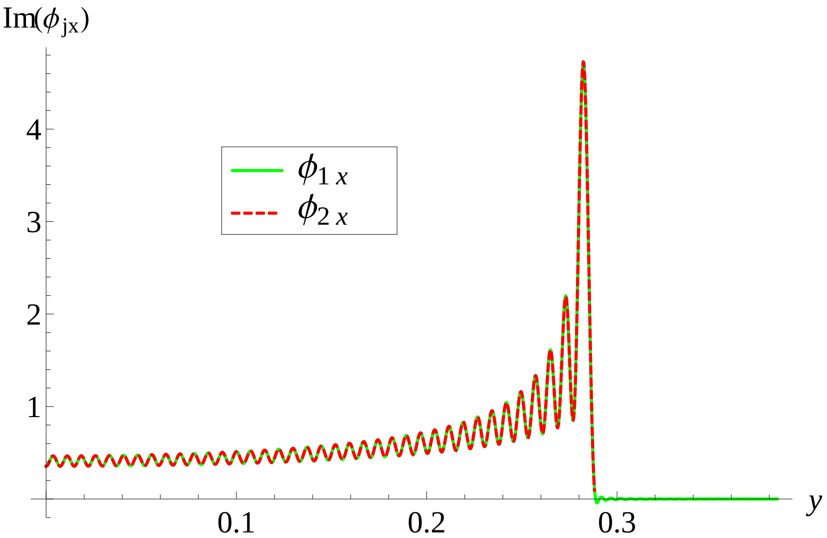

(b) Imaginary part of velocities vs. duct height at $x = -L$

FIGURE 6.11: Normal velocities vs. duct height at $x = -L$ for clamped edges and absorbent lining (fibrous), frequency 700Hz, and $N = 150$.

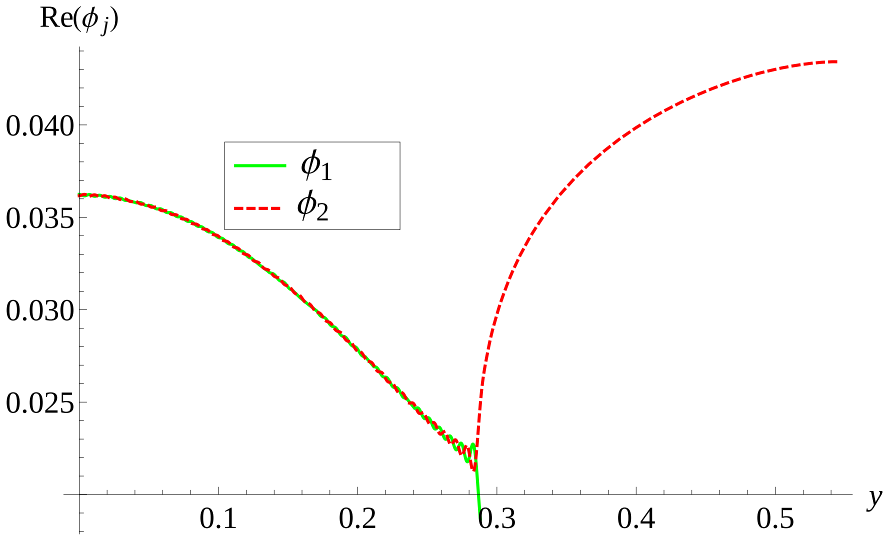

(a) Real part of pressures vs. duct height at $x = -L$.

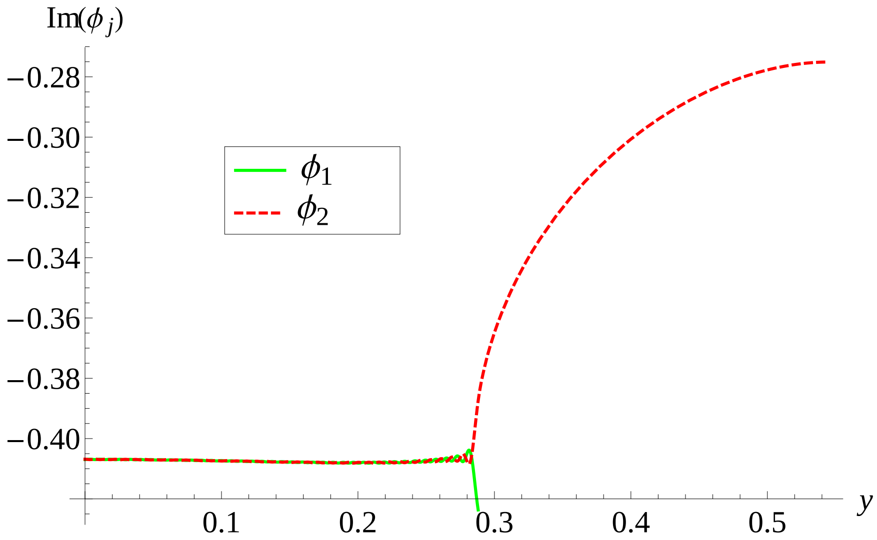

(b) Imaginary part of pressures vs. duct height at $x = -L$

FIGURE 6.12: Pressures vs. duct height at $x = -L$ for clamped edges and absorbent lining (fibrous), frequency 700Hz, and $N = 150$.

Chapter 7

Summary and Conclusion

In this thesis the analysis of scattering problems involving different boundary conditions and structural discontinuities is presented. The model problems contain boundary conditions of Dirichlet, Neumann, Robin and/or higher order boundary category and are governed by Helmholtz equation. The MM technique is applied to solve the governing boundary value problems. In low frequency regime the LFA is developed and compared with MM technique through numerical results.

The chapter wise summary of the present study are enclosed in this chapter. Chapter 1 depicts the state of the art relevant to the current study along with the avant-garde. The fundamental concepts that are necessary to understand the scattering analysis of acoustic wave in different waveguide structure, the derivation of linear acoustic wave equation along with different types of boundary conditions for different waveguide models have been discussed in Chapter 2. Also, the standard and generalized orthogonality relations have been explored on the basis of physical models in the category of either SL or non SL systems in this chapter.

In Chapter 3, the coupled wave scattering analysis in non-planar waveguide structure with different bounding properties like rigid, soft, impedance and wave bearing boundaries such as elastic plate has been studied by using MM approach. The primary focus is the scattering of the incident mode by the flanged junction and, in particular, the effect that different edge conditions have on this process. It is worthwhile mentioned that the case of a fully rigid flange is significantly more challenging requiring, for example, a matrix WH approach. Despite the use of the zero pressure condition, it is concluded that current problem offers much information both about scattering at a flange and about MM approaches. It is observed that the choice of appropriate edge conditions and the incident forcing term expressively affect the scattered field as well as the transmission through structure-borne as compared to fluid-borne vibration. It is also revealed that the power distribution is greatly affected by the attenuated regions and abrupt changes in height of duct. In the end the MM solution is well supported through number of validation points.

In Chapter 4, the attenuation of acoustic modes in a waveguide bounded by an elastic membrane and involving cavities radiating structure or fluid-borne incidence modes has been discussed using a MM solution and LFA. The uniqueness of the underlying problem has been ensured by the choice of physical edge conditions. The essential difficulties encountered while finding the roots of dispersion relations in the expansion chamber region have been tackled carefully. The energy functional has been obtained to observe wave scattering behavior in all duct regions. Through graphical illustration, we made the following conclusions.

For the structure-borne incident mode, a good agreement in scattering energies is observed for both MM and LFA solutions. However, the results do not hold at higher frequencies because of limitations on the selection of propagating modes. It is also noted that the attenuation of modes is linked with the dimensions and material properties of the duct regions; however, the cut-on limits are independent of edge conditions. Moreover, the variation of edge conditions significantly affects the scattering energies and TL as a function of frequency, as well as the dimensions of the bounding cavities. For instance, for all simply supported edges, and for edges simply supported at (L, b) and fixed at (L, h), the TL curves TL_{cr} are achieved as a function of the half-length of the expansion chamber for almost the whole frequency range. Similarly, the widest stop band is observed in the range $330 - 1400Hz$ for the simply supported edge conditions of the inlet or outlet and the expansion chamber. It is revealed that the choice of edge conditions, the selection of the cavity dimensions, and the bounding material properties helped to produce the attenuated regions and to minimize structural vibrations. Furthermore, the MM solution is validated physically and mathematically through the satisfaction of the conserved power identity and reconstruction of matching conditions at the interfaces, respectively.

In Chapter 5, a detailed analysis of fluid-structure coupled waveforms of duct modes and their attenuation in a flexible waveguide has been carried out. The physical configuration includes expansion chamber connected with extended inlet/outlet by means of vertical lined flanges. The BVP is formulated by radiating the inlet region with structure or fluid-borne mode incident which passes through outlet after interaction with the chamber. The MM solution has been developed whereby eigen expansion forms of field potentials of duct modes are associated with the dispersion relations. These dispersion relations are computed for the eigenvalues of flexural modes which appeared as real, imaginary and/or complex number forms. The corresponding eigenfunctions are non-orthogonal and the systems are of non-SL category, whereby, the use of generalized characteristics developed recently [99], yield the accurate solution of the problem. However, the absorbent linings lying along the vertical surfaces of the flanges are incorporated in the matching conditions of pressure modes, when the differential system is recasted into the linear algebraic systems of equations. These equations involve additional constants which are found through edge conditions. Nevertheless, the convergence of sums appeared during the assimilation of edge conditions is ensured through the usage of Green's function (2.93). Furthermore, the numerical experiments are performed to analyze the effects of absorbent linings and edge conditions on the attenuation of flexural modes. The guiding structure is exited by the structure-born mode or fluid-born mode, and the results are presented graphically. It is observed that when the structure-born mode is made incident the device can be tuned through the variation of edge conditions. The pin-jointed connections are found more effective than clamped or free edge conditions. Nevertheless, the use of absorbent linings is not much effective for structure-borne mode incident. However, a significant absorption of fluid-borne mode incident is revealed by this lining. On the other the role of edge conditions for fluid-born mode incident is not much notable. Likewise the variation of silencer geometries also effect the attenuation for structure-borne mode incident as well as fluid-borne mode incident. Furthermore, a good agreement between the results obtained via MM technique and LFA is achieved.

In Chapter 6, the scattering of fluid-structure coupled waves by geometric discontinuities, comprising flanges and/or a change in height, in a two-dimensional duct, has been studied. The physical problem containing incident radiations of structure-borne mode or fluid-borne mode is solved by using an established MM approach. A variety of numerical results have been presented for various sets of edge conditions and different properties of sound-absorbent material. It is found that the MM technique accompanied by the generalized orthogonal characteristics does not only provide an appropriate solution of the problem involving flexible boundaries but also helps to impose extra conditions for accommodating the physical behavior at edges. These edges may be clamped or pin-jointed for elastic plates and fixed or free for elastic membranes. Four different combinations of the envisaged edge conditions have been considered to analyze the TL versus frequency together with different choices of absorbent material. It is noted that the use of edge conditions affects significantly the attenuation of structure-borne mode incident vibrations whilst the usage of attenuating material along the flanges accomplishes the attenuation of the fluid-borne mode vibrations. Moreover, the rate of noise attenuation depends upon the choices of the specific impedance as well as the types of edge conditions. Furthermore, the results obtained by both techniques (LFA and MM) are found in good agreement.

Future work

Future work would be to extend by considering the insertion of double expansion chambers in flexible panels bounded by elastic membranes and plates in the presence of mean flow by using MM approach.

Bibliography

[1] H. Levine and J. Schwinger, "On the radiation of sound from an unflanged circular pipe", *Journal of Sound and Vibration*, vol. 73, no. 4, pp. 383, 1948.

[2] J. B. Keller, "Geometric theory of diffraction", *Journal of the Optical Society of America*, vol. 52, no. 2, pp. 116-130, 1962.

[3] P. A. Cannell, "Edge scattering of aerodynamic sound by a lightly loaded elastic half-plane", *Proceeding of the Royal Society of London A*, vol. 347, no. 1649, pp. 213-238, 1975.

[4] P. H. Masterman and P. J. B. Clarricoats, "Computer field-matching solution of waveguide transverse discontinuities", *Proceedings of the Institution of Electrical Engineers*, vol. 118, no. 1, pp. 51-63, 1971.

[5] R. Munt, "Acoustic radiation properties of a jet pipe with subsonic jet flow: I. The cold jet reflection coefficient", *Journal of Sound and Vibration*, vol. 142, no. 3, pp. 413-436, 1990.

[6] E. Brambley, "Fundamental problems with the model of uniform flow over acoustic linings", *Journal of Sound and Vibration*, vol. 322, no. 4-5, pp. 1026-1037, 2009.

[7] N. S. Dickey, A. Selamet, J. M. Novak, "Multi-pass perforated tube silencers: A computational approach", *Journal of Sound and Vibration*, vol. 211, no. 3, pp. 435-447, 2001.

[8] A. McAlpine and M. Wright, “Acoustic scattering by a spliced turbofan inlet duct liner at supersonic fan speeds”, *Journal of Sound and Vibration*, vol. 292, no. 3-5, pp. 911-934, 2006.

[9] R. Munt, “Acoustic transmission properties of a jet pipe with subsonic jet flow: I. The cold jet reflection coefficient”, *Journal of Sound and Vibration*, vol. 142, no. 3, pp. 413-436, 1990.

[10] A. H. Nayfeh, J. E. Kaiser, and D. P. Telionis, “Acoustics of aircraft engine duct systems”, *AIAA Journal*, vol. 13, no. 2, pp. 130-153, 1975.

[11] J. Wall, “Dynamics study of an automobile exhaust system”, Ph.D. dissertation, *Blekinge Institute of Technology*, 2003.

[12] B. Veitch and N. Peake, “Models for acoustic propagation through turbofan exhaust flows”, *13th AIAA/CEAS Aeroacoustics Conference* (*28th AIAA Aeroacoustics Conference*), pp. 35-43, 2007.

[13] M. A. Swinbanks, “The active control of sound propagation in long ducts”, *Journal of Sound and Vibration*, vol. 27, no. 3, pp. 411-436, 1973.

[14] S. Laugesen, “Active control of multi-modal propagation of tonal noise in ducts”, *Journal of Sound and Vibration*, vol. 195, no. 1, pp. 33-56, 1996.

[15] V. Martin, A. Cummings, and C. Gronier, “Discrimination of coupled structural/acoustical duct modes by active control: principles and experimental results”, *Journal of Sound and Vibration*, vol. 274, pp. 583–603, 2004.

[16] A. Preumont, “Vibration control of active structures: an introduction”, *Springer*, vol. 246, 2018.

[17] K. Natarajan, and L. Venkatakrishnan, “Influence of launch platform cutouts on flow and acoustic behavior of rocket exhaust”, *The Journal of the Acoustical Society of America*, vol. 140, no. 4, pp. 3042-3042, 2016.

[18] I. Klotz, “Recycling rockets”, *Aerospace America*, vol. 55, no. 8, pp. 32–37, 2017.

[19] B. R. Wyerman, “A theoretical and experimental study of acoustic propagation in multisectioned circular ducts”, Ph.D. dissertation, *Pennsylvania State University*, 1976.

[20] N. S. Dickey, A. Selamet and J. M. Novak, “Multi-pass perforated tube silencers: A computational approach”, *Journal of Sound and Vibration*, vol. 211, no. 3, pp. 435-447, 1998.

[21] T. Bravo and C. Maury, “Sound attenuation and absorption by micro-perforated panels backed by anisotropic fibrous materials: Theoretical and experimental study”, *Journal of Sound and Vibration*, vol. 425, no. 3, pp. 189-207, 2018.

[22] R. J. Astley and A. Cummings, “A finite element scheme for attenuation in ducts lined with porous material: comparison with experiment”, *Journal of Sound and Vibration*, vol. 116, no. 2, pp. 239-263, 1987.

[23] S. W. Rienstra, “Fundamentals of duct acoustics”, *Von Karman Institute Lecture Notes*, 2015.

[24] Y. Auregan, “On the use of a stress-impedance model to describe sound propagation in a lined duct with grazing flow”, *The Journal of the Acoustical Society of America*, vol. 143, no. 5, pp. 2975-2979, 2018.

[25] P. Morse and K. Ingard, “Encyclopedia of Physics”, *Acoustics I. SpringerVerlag, Berlin*, 1961.

[26] J. B. Lawrie and I. D. Abrahams, “A brief historical perspective of the Wiener-Hopf technique”, *Journal of Engineering Mathematics*, vol. 59, no. 4, pp. 351-358, 2007.

[27] A. D. Rawlins, “Wave propagation in a bifurcated impedance-lined cylindrical waveguide”, *Journal of Engineering Mathematics*, vol. 59, no. 4, pp. 419-435, 2007.

[28] A. D. Rawlins, "Two waveguide trifurcation problems", *Mathematical Proceedings of the Cambridge Philosophical Society*, vol. 121, no. 3, pp. 555-573, 1997.

[29] T. Nawaz, M. Afzal and R. Nawaz, "The scattering analysis of trifurcated waveguide involving structural discontinuities", *Advances in Mechanical Engineering*, vol. 11, no. 7, pp. 1-10, 2019.

[30] M. Ayub, M. H. Tiwana, and A. B. Mann, "Influence of acoustic dominant mode propagation in a trifurcated lined duct with different impedances", *Physica Scripta*, vol. 81, no. 3, pp. 035402, 2010.

[31] M. Hassan and M. Naz, "Reflection coefficient of a dominant mode in a pentafurcated duct", *Boundary Value Problems*, vol. 2017, no. 1, pp. 1-17, 2017.

[32] J. B. Lawrie and I. D. Abrahams, "An orthogonality relation for a class of problems with high-order boundary conditions; applications in sound/structure interaction", *The Quarterly Journal of Mechanics and Applied Mathematics*, vol. 52, no. 2, pp. 161-181, 1999.

[33] J. Satti, M. Afzal, and R. Nawaz, "Scattering analysis of a partitioned wave-bearing cavity containing different material properties", *Physica Scripta*, vol. 94, no. 11, pp. 1-22, 2019.

[34] R. Nawaz and J. B. Lawrie, "Scattering of a fluid-structure coupled wave at a flanged junction between two flexible waveguides", *The Journal of the Acoustical Society of America*, vol. 134, no. 3, pp. 1939-1949, 2013.

[35] R. Nawaz, M. Afzal, and M. Ayub, "Acoustic propagation in two-dimensional waveguide for membrane bounded ducts", *Communications in Nonlinear Science and Numerical Simulation*, vol. 20, no. 2, pp. 421-433, 2015.

[36] D. Warren, J. Lawrie, and I. Mohamed, "Acoustic scattering in waveguides that are discontinuous in geometry and material property", *Wave Motion*, vol. 36, no. 2, pp. 119-142, 2002.

[37] B. Veitch and N. Peake, "Acoustic propagation and scattering in the exhaust flow from coaxial cylinders", *Journal of Fluid Mechanics*, vol. 613, pp. 275-307, 2008.

[38] I. Abrahams, "Radiation and scattering of waves on an elastic half-space; a non-commutative matrix Wiener-Hopf problem", *Journal of the Mechanics and Physics of Solids*, vol. 44, no. 12, pp. 2125-2154, 1996.

[39] A. Büyükaksoy and B. Polat, "A bifurcated waveguide problem", *ARI-An International Journal for Physical and Engineering Sciences*, vol. 51, no. 3, pp. 196-202, 1999.

[40] S. Shafique, M. Afzal, and R. Nawaz, "On mode-matching analysis of fluid-structure coupled wave scattering between two flexible waveguides", *Wave Motion*, vol. 95, no. 6, pp. 581-589, 2017.

[41] S. Shafique, M. Afzal, and R. Nawaz, "On the attenuation of fluid-structure coupled modes in a non-planar waveguide", *Mathematics and Mechanics of Solids*, vol. 25, no. 10, pp. 1831–1850, 2020.

[42] M. Afzal, J. U. Satti, and R. Nawaz, "Scattering characteristics of non-planar trifurcated waveguides", *Meccanica*, vol. 55, pp. 1-12, 2020.

[43] J. B. Lawrie, "Comments on a class of orthogonality relations relevant to fluid-structure interaction," *Meccanica*, vol. 47, no. 3, pp. 783-788, 2012.

[44] J. B. Lawrie and J. Kaplunov "Edge waves and resonance on elastic structures: an overview", *Mathematics and Mechanics of Solids*, vol. 17, no. 1, pp. 4-16, 2012.

[45] K. Peat, "The acoustical impedance at the junction of an extended inlet or outlet duct", *Journal of Sound and Vibration*, vol. 150, no. 1, pp. 101-110, 1991.

[46] A. Selamet and Z. Ji, "Acoustic attenuation performance of circular expansion chambers with extended inlet/outlet," *Journal of Sound and Vibration*, vol. 223, no. 2, pp. 197-212, 1999.

[47] A. Selamet, F. Denia, and A. Besa, “Acoustic behavior of circular dual-chamber mufflers”, *Journal of Sound and Vibration*, vol. 265, no. 5, pp. 967-985, 2003.

[48] Z. Ji, “Acoustic attenuation performance analysis of multi-chamber reactive silencers”, *Journal of Sound and Vibration*, vol. 283, no. 1-2, pp. 459-466, 2005.

[49] J. W. Lee and Y. Y. Kim, “Topology optimization of muffler internal partitions for improving acoustical attenuation performance”, International journal for numerical methods in engineering, vol. 80, no. 4, pp. 455-477, 2009.

[50] J. W. Lee and G. W. Jang, “Topology design of reactive mufflers for enhancing their acoustic attenuation performance and flow characteristics simultaneously”, *International Journal for Numerical Methods in Engineering*, vol. 91, no. 5, pp. 552-570, 2012.

[51] X. Wang and C. M. Mak, “Wave propagation in a duct with a periodic Helmholtz resonators array”, *The Journal of the Acoustical Society of America*, vol. 131, no. 2, pp. 1172-1182, 2012.

[52] S. H. Seo and Y. H. Kim, “Silencer design by using array resonators for low frequency band noise reduction”, *The Journal of the Acoustical Society of America*, vol. 118, no. 4, pp. 2332-2338, 2005.

[53] E. Dowell and H. Voss, “The effect of a cavity on panel vibration”, *AIAA journal*, vol. 1, no. 2, pp. 476-477, 1963.

[54] R. Ford and M. McCormick, “Panel sound absorbers”, *Journal of Sound and Vibration*, vol. 10, no. 3, pp. 411-423, 1969.

[55] J. Kang and H. Fuchs, “Predicting the absorption of open weave textiles and micro-perforated membranes backed by an air space”, *Journal of Sound and Vibration*, vol. 220, no. 5, pp. 905-920, 1999.

[56] L. Huang, “A theoretical study of duct noise control by flexible panels”, *The Journal of the Acoustical Society of America*, vol. 106, no. 4, pp. 1801-1809, 1999.

[57] L. Huang, Y. Choy, R. So, and T. Chong, “Experimental study of sound propagation in a flexible duct”, *The Journal of the Acoustical Society of America*, vol. 108, no. 2, pp. 624-631, 2000.

[58] L. Huang, “Modal analysis of a drum-like silencer”, *The Journal of the Acoustical Society of America*, vol. 112, no. 5, pp. 2014-2025, 2002.

[59] L. Huang, “Parametric study of a drum-like silencer”, *Journal of Sound and Vibration*, vol. 269, no. 3-5, pp. 467-488, 2004.

[60] P. I. Galich, N. X. Fang, M. C. Boyce, and S. Rudykh, “Elastic wave propagation in finitely deformed layered materials,” *Journal of the Mechanics and Physics of Solids*, vol. 98, pp. 390-410, 2017.

[61] M. Ayub, M. Tiwana, and A. Mann, “Propagation of sound in a duct with mean flow”, *Communications in Nonlinear Science and Numerical Simulation*, vol. 14, no. 9-10, pp. 3578-3590, 2009.

[62] M. Ayub, M.H. Tiwana, and A.B. Mann, “Acoustic diffraction in a trifurcated waveguide with mean flow”, *Communications in Nonlinear Science and Numerical Simulation*, vol. 15, no. 12, pp. 3939-3949, 2010.

[63] R. Scott, “The propagation of sound between walls of porous material”, *Proceedings of the Physical Society*, vol. 58, no. 4, p. 358-368, 1946.

[64] A. Demír and A. Büyükaksoy, “Transmission of sound waves in a cylindrical duct with an acoustically lined muffler”, *International Journal of Engineering Science*, vol. 41, no. 20, pp. 2411-2427, 2003.

[65] B. Nilsson and O. Brander, “The propagation of sound in cylindrical ducts with mean flow and bulk-reacting lining. I- Modes in an infinite duct”, *IMA Jouranl of Applied Mathematics*, vol. 26, no. 3, pp. 269-298, 1980.

[66] B. Nilsson and O. Brander, "The propagation of sound in cylindrical ducts with mean flow and bulk-reacting lining. II- Bifurcated ducts", *IMA Jouranl of Applied Mathematics*, vol. 26, no. 4, pp. 381-410, 1980.

[67] B. Nilsson and O. Brander, "The propagation of sound in cylindrical ducts with mean flow and bulk-reacting lining. III- Step discontinuities", *IMA Jouranl of Applied Mathematics*, vol. 27, no. 1, pp. 105-131, 1981.

[68] B. Nilsson and O. Brander, "The propagation of sound in cylindrical ducts with mean flow and bulk-reacting lining. IV- Several interacting discontinuities", *IMA Jouranl of Applied Mathematics*, vol. 27, no. 3, pp. 263-289, 1981.

[69] A. Demír and A. Büyükaksoy, "Wiener-Hopf approach for predicting the transmission loss of a circular silencer with a locally reacting lining", *International Journal of Engineering Science*, vol. 43, no. 5-6, pp. 398-416, 2005.

[70] A. N. Norris and G. Wickham, "Acoustic diffraction from the junction of two at plates", *Proceedings of the Royal Society of London. Series A: Mathematical and Physical Sciences*, vol. 451, no. 1943, pp. 631-655, 1995.

[71] P. Brazier-Smith, "The acoustic properties of two co-planar half-plane plates", *Proceedings of the Royal Society of London. A. Mathematical and Physical Sciences*, vol. 409, no. 1836, pp. 115-139, 1987.

[72] L. Tkacheva, "The diffraction of surface waves by a floating elastic plate at oblique incidence", *Journal of Applied Mathematics and Mechanics,* vol. 68, no. 3, pp. 425-436, 2004.

[73] B. Erbas and I. D. Abrahams, "Scattering of sound waves by an infinite grating composed of rigid plates", *Wave Motion*, vol. 44, no. 4, pp. 282-303, 2007.

[74] B. Noble, "Methods based on the Wiener-Hopf technique for the solution of partial differential equations", 1958.

[75] A. Grant and J. Lawrie, “Propagation of fluid-loaded structural waves along a duct with smoothly varying bending characteristics”, *Quarterly Journal of Mechanics and Applied Mathematics*, vol. 53, no. 2, pp. 299-321, 2000.

[76] I. D. Abrahams and G. Wickham, “On the scattering of sound by two semi infinite parallel staggered plates-i. explicit matrix Wiener-Hopf factorization”, *Proceedings of the Royal Society of London. A. Mathematical and Physical Sciences*, vol. 420, no. 1858, pp. 131-156, 1988.

[77] I. Abrahams and G. Wickham, “General Wiener-Hopf factorization of matrix kernels with exponential phase factors”, *SIAM Journal on Applied Mathematics*, vol. 50, no. 3, pp. 819-838, 1990.

[78] I. D. Abrahams, “On the solution of Wiener-Hopf problems involving noncommutative matrix kernel decompositions”, *SIAM Journal on Applied Mathematics*, vol. 57, no. 2, pp. 541-567, 1997.

[79] I. D. Abrahams, “The application of Pade approximants to Wiener-Hopf factorization”, *IMA Journal of Applied Mathematics*, vol. 65, no. 3, pp. 257-281, 2000.

[80] N. Peake and I. D. Abrahams, “Sound radiation from a semi-infinite lined duct”, *Wave Motion*, vol. 92, pp. 102-407, 2020.

[81] H. Chung and C. Fox, “Calculation of wave-ice interaction using the Wiener-Hopf technique”, *New Zealand J. Math*, vol. 31, no. 1, pp. 1-18, 2002.

[82] D. V. Evans and T. V. Davies, “Wave-ice interaction”, *Stevens Inst of Tech Hoboken NJ Davidson Lab, Tech. Rep.*, 1968.

[83] M. Hassan, “Wave scattering by soft-hard three spaced waveguide”, *Applied Mathematical Modelling*, vol. 38, no. 17-18, pp. 4528-4537, 2014.

[84] A. D. Rawlins, “A trifurcated waveguide problem”, *Brunel University Mathematics Technical Papers collection*, pp.1-22, 1994.

[85] M. Hassan, M. H. Michael, A. Bashir, and M. Sumbul, "Mode matching analysis for wave scattering in triple and pentafurcated spaced ducts", *Brunel University Mathematics Technical Papers collection*, vol. 39, no. 11, pp. 3043-3057, 2016.

[86] M. Afzal, R. Nawaz, M. Ayub, and A. Wahab, "Acoustic scattering in flexible waveguide involving step discontinuity", *PloS one*, vol. 9, no. 8, pp. 1-9, 2014.

[87] M. Afzal, M. Ayub, R. Nawaz, and A. Wahab, "Mode-matching solution of a scattering problem in flexible waveguide with abrupt geometric changes", *American Mathematical Society*, vol. 660, pp. 113-29, 2016.

[88] J. B. Lawrie and M. Afzal, "Acoustic scattering in a waveguide with a height discontinuity bridged by a membrane: a tailored Galerkin approach", *Journal of Engineering Mathematics*, vol. 105, no. 1, pp. 99-115, 2017.

[89] R. Nawaz, A. U. Jan, and M. Afzal, "Fluid-structure coupled wave scattering in a flexible duct at the junction of planar discontinuities", *Advances in Mechanical Engineering*, vol. 9, no. 7, pp. 1-11, 2017.

[90] M. Afzal, and S. Shafique, "Attenuation analysis of flexural modes with absorbent lined flanges and different edge conditions", *The Journal of the Acoustical Society of America*, vol. 148, no. 1, pp. 85-99, 2020.

[91] A. Cummings and I. J. Chang, "Sound attenuation of a finite length dissipative flow duct silencer with internal mean flow in the absorbent", *Journal of Sound and Vibration*, vol. 127, no. 1, pp. 1-17, 1988.

[92] K. Peat, "A transfer matrix for an absorption silencer element", *Journal of Sound and Vibration*, vol. 146, no. 2, pp. 353-360, 1991.

[93] R. Kirby, "Simplified techniques for predicting the transmission loss of a circular dissipative silencer", *Journal of Sound and Vibration*, vol. 243, no. 3, pp. 403-426, 2001.

[94] S. Panigrahi and M. Munjal, "Comparison of various methods for analyzing lined circular ducts", *Journal of Sound and Vibration*, vol. 285, no. 4-5, pp. 905-923, 2005.

[95] J. B. Lawrie and I. M. Guled, "On tuning a reactive silencer by varying the position of an internal membrane", *The Journal of the Acoustical Society of America*, vol. 120, no. 2, pp. 780-790, 2006.

[96] T. Sahoo, T. L. Yip, and A. T. Chwang, "Scattering of surface waves by a semi-infinite floating elastic plate", *Physics of Fluids*, vol. 13, no. 11, pp. 3215-3222, 2001.

[97] R. V. Churchill, "Fourier series and boundary value problems", 1941.

[98] N. N. Lebedev, I. P. Skalskaya and Y. S. Uflyand. Worked problems in applied mathematics, *Dover*, *New York*, 1979.

[99] J. B. Lawrie, "On eigenfunction expansions associated with wave propagation along ducts with wave-bearing boundaries", *IMA Journal of Applied Mathematics*, vol. 72, no. 3, pp. 376-394, 2007.

[100] A. D. Rawlins, "Radiation of sound from an unflanged rigid cylindrical duct with an acoustically absorbing internal surface", *Proceeding of Royal Society London*, vol. 361, pp. 65-91, 1978.

[101] L. E. Kinsler, A. R. Frey, A. B. Coppens and J. V. Sanders, "Fundamentals of acoustics (4th edition)", 1999.

[102] J. B. Lawrie and R. Kirby, "Mode-matching without root-finding: Application to a dissipative silencer", *The Journal of the Acoustical Society of America*, vol. 119, no. 4, pp. 2050-2061, 2006.

[103] W. Frommhold and F. P. Mechel. "Simplified methods to calculate the attenuation of silencers", *Journal of Sound and Vibration*, vol. 141, no. 1, pp.103-125, 1990.

[104] G. W. Kaye and T. H. Laby, "Tables of Physical and Chemical Constants (15th Ed.)", *Longman Scientific and Technical, UK*, 1986.